

.....
Functional Photocatalytic Surfaces for Selective
Adsorption and Detection of Organic Pollutants
.....

Dissertation

zur Erlangung des akademischen Grades eines
Doktors der Ingenieurwissenschaften (Dr.-Ing.)
der Christian-Albrechts-Universität

vorgelegt von

.....
Herrn M.Sc. Josiah Ngenev SHONDO

aus

Dan-anacha-Nigeria

Jahr
Kiel 2023

1st Examiner: **Prof. Dr. Franz Faupel**

Chair for Multicomponent Materials
Faculty of Engineering, Kiel University

2nd Examiner: **Prof. Dr. Lorenz Kienle**

Chair for Synthesis and Real Structures
Faculty of Engineering, Kiel University

3rd Examiner: **Prof. Dr. Rainer Adelung**

Functional Nanomaterials Chair
Faculty of Engineering, Kiel University

Examination Committee Chair: **Prof. Dr. Stephan Wulfinghoff**

Computational Materials Science
Faculty of Engineering, Kiel University

Date of Disputation: **May 26, 2023**

*.....for generations yet unborn, to inspire them to relentlessly seek knowledge,
push the boundaries of what is possible, and make water safe for all.....*

Acknowledgement

It is with great pleasure and gratitude that I express my appreciation to the Petroleum Technology Development Fund (PTDF) of Nigeria and the German Academic Exchange Service (DAAD) for providing financial support that made it possible for me to pursue my doctoral studies. Their contribution has been invaluable in helping me advance my academic goals and career.

I want to extend my heartfelt appreciation to my esteemed supervisors, Prof. Dr. Franz Faupel and Prof. Dr. Oral Cenk Aktas, for their exceptional guidance and unwavering support throughout my research journey. Their profound knowledge, extensive experience, broad vision, and insightful comments have been invaluable to my growth as a researcher, and I am privileged to have learned under their mentorship. I am honored to have been a part of the Chair for Multicomponent Materials research group, and I will always cherish the experience.

I am also grateful to Dr. Thomas Strunskus and Prof. Dr. Klaus Rätzke for their invaluable suggestions and profound understanding of chemistry and physics. Their support has been much appreciated.

I would like to sincerely thank Dipl.-Ing Stefan Rehders for his exceptional technical assistance throughout my research. His expertise and dedication have been instrumental in the success of my experimental works, and without his contributions, much of this work would not have been possible.

In a special manner, I express my gratitude to Dr. Salih Veziroglu, my subgroup leader (Nano Energy & Surface Engineering), for his support and productive discussions that have aided in improving our research. I also appreciate the collaborative efforts and insightful discussions with Dr. Stefan Schröder and Dr. Alexander Vahl. I am also grateful to our secretary, Ms. Sieglinde Kastaun for her administrative support.

Furthermore, I am grateful to Assoc. Prof. Dr. Jacek Fiutowski, Prof. Dr. Horst-Günter Rubahn, and Prof. Dr. Yogendra Kumar Mishra for their collaborative work and for performing the Helium Ion Microscopy (HIM) analysis used in this dissertation. Their contributions have been invaluable.

I am grateful to Dr. Nancy Smith from the Welcome Center for International Researchers and Scholars at Kiel University for her constant support in providing us with relevant information on immigration, accommodation, work, and other related matters.

Also, I am grateful for the support of my Ph.D. Colleagues and friends, Chima Kalu, Tim Tjardts, Blessing Adejube, Torge Hartig, Igor Barg, Jonas Drewes, Maximilian Heiko Burk, Dr. Wiebke Reichstein, Joshua Christopher, Mercy Obado Ochieng, Chukwuka Ojiugwo, Donnet Rose Odhiambo and all those not mentioned, I am deeply grateful for your exceptional support and encouragement. It has been my pleasure to collaborate and discuss with you all.

Finally, my deepest appreciation goes to my family, especially my mother, Patricia Iorhembra Shondo, for her emotional, moral, and spiritual support. I am also grateful to my siblings and relatives for their unwavering support throughout my research career. Without their love and support, this dissertation would not have been possible.

Abstract

The industrial revolution has brought about a significant increase in water pollution, which poses a danger to both aquatic life and human health. To combat this issue, various technologies have been developed to remove contaminants, such as oil, from water. One of the most promising methods is the use of surfaces with unique wettability properties, such as superhydrophobicity and superhydrophilicity. These surfaces work by promoting the formation of the Cassie-Baxter state, which reduces the surface area where liquid and solid meet, resulting in high apparent contact angles and low contact angle hysteresis. However, creating these special wettability surfaces requires a deep understanding of factors like surface chemistry and roughness. Understanding these factors is crucial to designing structured surfaces that can attain the Cassie-Baxter state and be used in oil-water separation. In this dissertation, we explore the use of surfaces with unique wettability properties for removing oil contamination from water, a critical issue in industrial development. We focus on three main ideas: modifying the thin film surface with a hierarchically structured design to improve surface wettability properties, designing, and fabricating a multifunctional surface that provides highly selective oil sorption and clean-up capability, and fabricating a 4N-in-1 hybrid substrate for ultra-sensitive and reliable photo-induced-enhanced Raman spectroscopy. **In Publication 1**, a novel method ‘the fabrication of hierarchical Au nanostructures on TiO₂ film by a two-step photocatalytic reduction process’ was introduced. While the first photocatalytic deposition in a mixture of HAuCl₄ and non-ionic surfactant led to the formation of flower-like Au microstructures on TiO₂, second photocatalytic deposition within a highly acidic HAuCl₄ solution triggered the growth of needle-like sharp Au nanostructures selectively on former Au microstructures. Such a dual scale topography on TiO₂ enhanced the hydrophilicity significantly. After the surface modification (ODP-SAM) such hydrophilic nanostructures exhibited superhydrophobicity. Prepared surface stays stable under extreme temperature conditions and therefore it can be applied for harsh outdoor uses including self-cleaning and anti-icing applications. In addition, the photocatalytic nature of Au-TiO₂ hybrid layer allows superhydrophilic-superhydrophobic patterning (selective photocatalytic deposition of Au micro- and nanostructures), which may find applications in cell growth technologies, spotting of biomolecules, fluid microchips and microreactors. **In Publication 2**, the ‘3-in-1’ concept, which leads to a superhydrophobic and photocatalytically surface, was introduced. This concept combines (i) photocatalytic thin film (TiO₂), (ii) micro- and nanostructuring (Ag nanoplates), and (iii) low surface energy coating (V₃D₃) via iCVD. Not only p-V₃D₃ coating, but also the unique surface topography composed of flowerlike Ag nanoplates and columnar TiO₂ structures seems to promote the superhydrophobicity of the prepared surface. iCVD led to a highly conformal p-V₃D₃ coating retaining the surface topography on TiO₂, which is crucial to achieve an extreme non-wetting regime. Additionally, due to its siloxane backbone, the p-V₃D₃ layer exhibited high stability against the UV irradiation and atomic oxygen exposure (photodegradation). The superhydrophobic (water CA > 160°) and photocatalytically active p-V₃D₃/Ag/TiO₂ surface shows high selectivity to the oil adsorption, which may lead to several functional applications in oil–water separation, microfluidics, self-cleaning, and water harvesting technologies. **In Publication 3**, 4N-in-1 hybrid substrate concept (nanocolumnar structures, nano crack network, nanoscale mixed oxide phases, and nanometallic structures)

was introduced. Basically, 4N-in-1 hybrid substrate (AgTiO_2) acts an ultrasensitive and reliable photoinduced enhanced Raman spectroscopy (PIERS) active platform. Upon UV irradiation, a PIERS enhancement up to 50 times (in comparison to conventional surface enhanced Raman spectroscopy (SERS) intensity) was achieved. In addition to improved Raman signal, 4N-in-1 hybrid substrate provides a high detection sensitivity which may be attributed to the activation capability at an extremely low incident photon energy and prolonged relaxation time. Moreover, 4N-in-1 hybrid substrate exhibits a superior photocatalytic degradation performance, allowing its reuse at least for 18 cycles without any loss of PIERS activity. 4N-in-1 hybrid substrate concept can be combined with any type of Raman spectroscopy (by simply integrating a UV light source), and this may trigger new applications for biomedicine, forensic, and security field.

Kurzfassung

Die industrielle Revolution hat zu einer erheblichen Zunahme der Wasserverschmutzung geführt, die sowohl eine Gefahr für das aquatische Leben als auch für die menschliche Gesundheit darstellt. Um dieses Problem zu bekämpfen, wurden verschiedene Technologien entwickelt, um Verunreinigungen wie Öl aus dem Wasser zu entfernen. Eine der vielversprechendsten Methoden ist die Verwendung von Oberflächen mit einzigartigen Benetzbarkeitseigenschaften wie Superhydrophobie und Superhydrophilie. Diese Oberflächen arbeiten durch die Förderung der Bildung des Cassie-Baxter-Zustands, der die Oberfläche reduziert, an der Flüssigkeit und Feststoff aufeinandertreffen, was zu hohen scheinbaren Kontaktwinkeln und niedrigem Kontaktwinkelhysteresis führt. Die Schaffung dieser speziellen Benetzbarkeitsoberflächen erfordert jedoch ein tiefes Verständnis von Faktoren wie Oberflächenchemie und Rauheit. Das Verständnis dieser Faktoren ist entscheidend für das Design strukturierter Oberflächen, die den Cassie-Baxter-Zustand erreichen und zur Öl-Wasser-Trennung verwendet werden können. In dieser Dissertation untersuchen wir die Verwendung von Oberflächen mit einzigartigen Benetzbarkeitseigenschaften zur Entfernung von Ölverschmutzungen aus Wasser, einem wichtigen Thema in der industriellen Entwicklung. Wir konzentrieren uns auf drei Hauptideen: die Modifizierung der Dünnschichtoberfläche mit einem hierarchisch strukturierten Design, um die Oberflächenbenetzbarkeitseigenschaften zu verbessern, das Design und die Herstellung einer multifunktionalen Oberfläche, die eine hochselektive Ölsorption und Reinigungsfähigkeit bietet, und die Herstellung eines 4N-in-1-Hybridsubstrats für eine ultraempfindliche und zuverlässige photoinduzierte Raman-Verstärkungsspektroskopie. **In der Veröffentlichung 1** wurde eine neue Methode zur Herstellung hierarchischer Au-Nanostrukturen auf TiO₂-Filmen durch einen zweistufigen photo-katalytischen Reduktionsprozess vorgestellt. Durch die erste photo-katalytische Abscheidung in einer Mischung aus HAuCl₄ und nicht-ionischem Tensid entstanden blütenartige Au-Mikrostrukturen auf TiO₂, während die zweite photo-katalytische Abscheidung in einer stark sauren HAuCl₄-Lösung das Wachstum nadelförmiger scharfer Au-Nanostrukturen auf den vorherigen Au-Mikrostrukturen auslöste. Eine solche duale Skalentopographie auf TiO₂ verbesserte die Hydrophilie signifikant. Nach der Oberflächenmodifikation (ODP-SAM) zeigten solche hydrophilen Nanostrukturen eine superhydrophobe Eigenschaft. Die hergestellte Oberfläche bleibt unter extremen Temperaturbedingungen stabil und kann daher für raue Außenanwendungen wie Selbstreinigung und Antieisbeschichtung eingesetzt werden. Darüber hinaus ermöglicht die photo-katalytische Natur der Au-TiO₂-Hybrid-Schicht eine Superhydrophilie-Superhydrophobie-Musterung (selektive photo-katalytische Abscheidung von Au-Mikro- und Nanostrukturen), die Anwendungen in der Zellwachstumstechnologie, der Spotting von Biomolekülen, in Mikrofluidik-Chips und Mikroreaktoren finden könnte. **In der Veröffentlichung 2** wurde das "3-in-1"-Konzept vorgestellt, das zu einer superhydrophoben und photo-katalytisch aktiven Oberfläche führt. Dieses Konzept kombiniert (i) eine photo-katalytische dünne Schicht (TiO₂), (ii) Mikro- und Nanostrukturierung (Ag-Nanoplatte) und (iii) eine Beschichtung mit niedriger Oberflächenenergie (V₃D₃) über iCVD. Nicht nur die p-V₃D₃-Beschichtung, sondern auch die einzigartige Oberflächentopographie, bestehend aus blütenartigen Ag-Nanoplatte und säulenförmigen TiO₂-Strukturen, scheint die Superhydrophobie der hergestellten Oberfläche zu fördern. iCVD führte zu einer hoch konformen p-V₃D₃-Beschichtung, die die Oberflächentopographie auf TiO₂ beibehält, was für eine extreme Nichtbenetzung unerlässlich ist. Darüber hinaus zeigte die p-V₃D₃-Schicht aufgrund ihres Siloxanrückgrats eine hohe Stabilität gegen UV-Strahlung und atomaren Sauerstoff (Photodegradation). Die superhydrophobe (Wasser-KA > 160°) und photo-katalytisch aktive p-V₃D₃/Ag/TiO₂-Oberfläche zeigt eine hohe Selektivität für die ÖladSORPTION, was zu mehreren funktionalen Anwendungen in der Öl-Wasser-Trennung, der Mikrofluidik, der Selbstreinigung und der Wassergew. **Im Veröffentlichung 3** wurde das Konzept des 4N-in-1-Hybridsubstrats (Nanospaltenstruktur, Nanorissnetzwerk, Nanoskalierte gemischte

Oxidphasen und Nanometallstrukturen) vorgestellt. Grundsätzlich wirkt das 4N-in-1-Hybridsubstrat (AgTiO_2) als ultrasensibles und zuverlässiges PIERS-Aktivplattform. Durch UV-Bestrahlung wurde eine PIERS-Verbesserung um das 50-fache im Vergleich zur konventionellen SERS-Intensität erreicht. Neben einem verbesserten Raman-Signal bietet das 4N-in-1-Hybridsubstrat eine hohe Nachweissensitivität, die auf die Aktivierungsfähigkeit bei extrem niedriger einfallender Photonenenergie und verlängerter Relaxationszeit zurückgeführt werden kann. Darüber hinaus zeigt das 4N-in-1-Hybridsubstrat eine überragende photocatalytische Abbauleistung, die eine Wiederverwendung für mindestens 18 Zyklen ohne Verlust der PIERS-Aktivität ermöglicht. Das Konzept des 4N-in-1-Hybridsubstrats kann mit jeder Art von Raman-Spektroskopie kombiniert werden (durch einfache Integration einer UV-Lichtquelle), was neue Anwendungen für die Biomedizin, die Forensik und den Sicherheitsbereich auslösen kann.

Declaration of Authenticity

I, Josiah N. Shondo, hereby declare that this dissertation and related research are independently authored and authored by me. This work complies to the DFG recommendations for ensuring good scientific practice. All content and ideas that come directly or indirectly from external sources are clearly marked.

This dissertation has not been published or submitted to any other examining body, and all related research written and published in peer-reviewed journals are clearly recognized as such.

1. [Josiah Shondo](#), Salih Veziroglu, Dominik Stefan, Yogendra Kumar Mishra, Thomas Strunskus, Franz Faupel, Oral Cenk Aktas. Tuning wettability of TiO₂ thin film by photocatalytic deposition of 3D flower- and hedgehog-like Au nano- and microstructures *Applied Surface Science* 537 (2021) 147795
2. [Josiah Shondo](#), Salih Veziroglu, Tim Tjardts, Jacek Fiutowski, Stefan Schröder, Yogendra Kumar Mishra, Thomas Strunskus, Horst-Günter Rubahn, Franz Faupel, and Oral Cenk Aktas Selective Adsorption and Photocatalytic Clean-Up of Oil by TiO₂ Thin Film Decorated with p-V₃D₃ Modified Flowerlike Ag Nanoplates *Adv. Mater. Interfaces* 2022, 2102126
3. [Josiah Shondo](#), Salih Veziroglu, Tim Tjardts, Jacek Fiutowski, Stefan Schröder, Yogendra Kumar Mishra, Thomas Strunskus, Horst-Günter Rubahn, Franz Faupel, and Oral Cenk Aktas Selective Adsorption and Photocatalytic Clean-Up of Oil by TiO₂ Thin Film Decorated with p-V₃D₃ Modified Flowerlike Ag Nanoplates *Adv. Mater. Interfaces* 2022, 2102126 (**Inside Front Cover**)
4. [Josiah Shondo](#), Salih Veziroglu, Tim Tjardts, Tamim Bin Sarwar, Yogendra Kumar Mishra, Franz Faupel, and Oral Cenk Aktas. Nanoscale Synergetic Effects on Ag–TiO₂ Hybrid Substrate for Photoinduced Enhanced Raman Spectroscopy (PIERS) with Ultra-Sensitivity and Reusability. *Small* 2022, 2203861
5. [Josiah Shondo](#), Salih Veziroglu, Tim Tjardts, Tamim Bin Sarwar, Yogendra Kumar Mishra, Franz Faupel, and Oral Cenk Aktas. Nanoscale Synergetic Effects on Ag–TiO₂ Hybrid Substrate for Photoinduced Enhanced Raman Spectroscopy (PIERS) with Ultra-Sensitivity and Reusability. *Small* 2022, 2203861 (**Inside Front Cover**)

Additional Publications within Ph.D period

...In addition to to my PhD research, I also collaborate on other projects as follows:

6. Salih Veziroglu, Marie Ullrich, Majid Hussain, Jonas Drewes, [Josiah Shondo](#), Thomas Strunskus, Jost Adam, Franz Faupel, Oral Cenk Aktas. Plasmonic and non-plasmonic contributions on photocatalytic activity of Au-TiO₂ thin film under mixed UV–visible light *Surface & Coatings Technology* (2020)
7. S. Veziroglu, J. Hwang, J. Drewes, I. Barg, [J. Shondo](#), T. Strunskus, O. Polonskyi, F. Faupel, O.C. Aktas. PdO nanoparticles decorated TiO₂ film with enhanced photocatalytic and self-cleaning properties. *Materials Today Chemistry* 16 (2020) 100251
8. Gina Odochi Ihekwe, [Josiah Ngenev Shondo](#), Kingsley Ikechukwu Orisekeh , Godwin Mong Kalu-Uka, Iheoma Chigoziri Nwuzor , Azikiwe Peter Onwualu. Characterization of certain Nigerian clay minerals for water purification and other industrial applications. *Heliyon* 6 (2020) e03783

I declare that no academic degree has been withdrawn from me.

SignaturePlace/date.....

Table of Contents

Acknowledgement	i
Abstract	ii
Kurzfassung	iv
Declaration of Authenticity.....	vi
Additional Contributions within the Ph.D period.....	vi
Table of Contents.....	viii
1. Introduction.....	1
2. Theoretical Background.....	6
2.1. Surface Wettability and Separation of Pollutants through Wettability Contrast	6
2.2. Dependence of Surface Wettability on Topography and Surface Roughness	6
2.2.1. Wenzel's Model	6
2.2.2. Cassie-Baxter's Model	7
2.3. Effect of Shape and Geometry of Surface Features on Surface Wettability	8
2.4. Effect of Surface Chemistry on Wettability	8
2.4.1. Surface Energy	8
2.4.2. Effect of Functional Groups (Surface Chemical State) on Wettability	9
2.5. Surface Modification	10
2.5.1. Wet Chemical Surface Modification Methods	10
2.5.2. Dry Surface Modification Methods	10
2.5.2.1. Sputtering	11
2.5.2.2. Reactive Magnetron Sputtering	11
2.5.3. Chemical Vapor Deposition	12
2.5.3.1. Initiated Chemical Vapor Deposition	13
2.5.4. An Alternative Surface Modification Method: Photocatalytic Surface Patterning	15
2.6. Pollutants Separation Based on Wettability	15
2.6.1. Mechanisms of Oil-Water Separation Based on Surface Wettability	16
2.7. Photocatalytic Decomposition and Clean-up of Organic Pollutants	17
2.7.1. Photocatalysis	17
2.7.2. Fundamental Principle of Photocatalytic Reactions	18
2.7.3. Metal Oxide Photocatalysts	18
2.7.4. Titanium (IV) Oxide as Photocatalyst	19
2.7.4.1. Electronic Structures of TiO ₂	19
2.7.4.2. Formation of Oxygen Vacancies in TiO ₂	19
2.7.5. Photocatalytic Thin Films	20
2.7.6. Photocatalytic Decomposition of Pollutants	20
2.7.6.1. Mechanism of Photocatalytic Degradation of Organic Pollutants in Wastewater ..	21
2.8. Self- Cleaning Surfaces	22
2.8.1. Self-Cleaning Superhydrophobic Surfaces	22
2.8.2. Self-Cleaning Superhydrophilic Surfaces	23
2.8.3. Photocatalytic Self-Cleaning Surfaces	23
2.8.4. Photocatalytic Thin Films for Clean-up of Oil-like Organic Molecules	24
2.9. Detection of Organic Pollutants	24
2.9.1. Raman Scattering	25
2.9.2. Mechanism of SERS	26
2.9.2.1. Electromagnetic Mechanism of SERS	26
2.9.2.2. Chemical Mechanism of SERS	27
2.9.3. Mechanism of PIERS	28
2.9.3.1. Substrate Effect	28
2.9.3.2. Irradiation Effect	29
2.9.3.3. Relaxation Effect	29
3. Tuning wettability of TiO ₂ thin film by photocatalytic deposition of 3D flower- and hedgehog-like Au nano- and microstructures	31

4. Selective Adsorption and Photocatalytic Clean-Up of Oil by TiO ₂ Thin Film Decorated with p-V ₃ D ₃ Modified Flowerlike Ag Nanoplates	43
5. Nanoscale Synergetic Effects on Ag–TiO ₂ Hybrid Substrate for Photoinduced Enhanced Raman Spectroscopy (PIERS) with Ultra-Sensitivity and Reusability	65
6. Conclusion and Outlook	89
List of Figures	91
References.....	92

CHAPTER ONE

1. Introduction

Since each chapter has its own introduction, this section aims to describe the scope of the thesis in a broader sense. First, an overview of environmental pollution will be given, specifically focusing on oil-water pollution. Afterwards, oil pollution recovery and remediation strategies will be discussed briefly. This thesis emphasizes a novel oil-water separation approach based on the wettability contrast and the photocatalytic decomposition of oil-like organic pollutants. In addition, an innovative method which allows the detection of oil and oil-like organic pollutants at trace amounts is covered within this thesis.

As the world population continues to increase, our impact on the whole ecosystem also increases tremendously. But even as we continue to enjoy human-environment interaction^[1], the scale of anthropogenic activity is destabilizing the age-long ecological equilibrium^[2]. Today, increasing human activities such as fossil fuel burning, mining, refining, exploration, construction, mechanization, and transportation have brought serious environmental pollution problems^[3]. Environmental pollution is not a new issue, but it remains mankind's greatest challenge and the leading cause of diseases and mortality^[4]. However, despite the global attention to the pollution, the impact is still being felt due to its severe long-term consequences. Basically, the pollution can be described as uncontrolled the release of toxic substances (solids, liquids, or gases) into the environment that adversely affect human health and other living things. While the pollution can be named in different forms, such as light pollution^[5], plastic pollution^[6], and noise pollution^[7], mainly it can be classified into three main groups: air pollution^[8], soil pollution^[9], and water pollution^[10]. This thesis focuses on the oil-water contamination.

"Water is life, and clean water means health," said Audrey Hepburn^[11]. Literally, this statement means that water is an invaluable life-sustaining force that every living organism depends on to survive, live, produce, or even transport. Notwithstanding, human development and everyday activities have led to an increase in water pollution globally. Water pollution is a major concern due to the increasing demand for water in agriculture, industry, and households. 90% of the world's water is used in agricultural and industrial activities^[12-14], generating 80% of the untreated wastewater^[13] with various degrees of pollutants that have devastating effects on human health, aquatic life, infrastructure, and the environment^[15,16]. For example, toxic chemicals such as benzene, toluene, dichloromethane, hexadecane, and polycyclic aromatic hydrocarbons are released into water sources during oil exploration and refining or oil spills^[17-19]. This leads to oil-water pollution, a global problem due to its devastating effects on the local environment^[20].

Oil pollution is often caused by oil spills during transportation, exploration, and production^[21]. The environmental impact of oil spills is a complex phenomenon influenced by various factors, including the volume and composition of the spilled oil, the location of the spill in relation to the shoreline, and the availability of scientific data prior to, during, and after the event. When oil spills occur in aquatic environments, the oil typically floats on the surface due to its lower density compared to water and the lack of cohesion between the oil and water molecules. This can lead to the formation of persistent and toxic oil slicks on the water surface. To mitigate these effects, various techniques have been developed to remove spilled oil from water, including mechanical, chemical, and biological treatments. Each approach utilizes different techniques to eliminate oil from the water and make the environment safe.

Mechanical methods are considered as one of the most eco-friendly ways to clean up the oil-water pollution, as they do not rely on chemicals. Some of the most commonly used mechanical methods for

marine oil spill remediation include oil booms, skimmers, oil-water separators, and sorbents^[18,22–24]. Oil booms are used to prevent the spread of oil and to concentrate it for the recovery^[21]. They are designed to float on the surface of the water and come in various shapes and sizes, ranging from small and simple setups for small spills in isolated waters to large and complex setups for offshore spills that require large vessels, cranes, and auxiliary equipment to operate. The critical factor in determining the effectiveness of oil booms is their ability to contain or prevent the spread of oil, which is largely influenced by the properties of the boom and the water movement and sea conditions^[25]. Skimmers, on the other hand, are physical or mechanical devices used to remove oil from the water surface, typically in conjunction with oil containment and recovery booms^[25]. The design of a skimmer is dependent on the viscosity of the oil and the prevailing water condition (since a skimmer is supposed to float on the surface of the water). However, ripple effects from wind, waves, and ocean currents often affect skimmers, which can reduce their effectiveness, especially in rough water conditions.

Sorbents are oleophilic materials that sorb the oil and repel the water. There are three classes of sorbents in general: organic (agricultural waste), mineral (vermiculite, zeolites, activated carbon, and organic clays), and synthetic (polypropylene and polyurethane), which differ in recyclability, wettability, density, geometry, and sorption capacity (these determine their use can be cumbersome and time-consuming)^[26–28]. In addition, increasing oil and emulsion densities over time will significantly reduce the buoyancy differential between the spill and the seawater and consequently reduce the buoyancy of sorbents. In addition, changes in emulsion viscosity resulting from oil evaporation and emulsification disrupt the effectiveness of the sorbent.

When traditional methods such as booms, skimmers, and absorbents are unable to tackle an oil spill, dispersal agents can be used as an alternative clean-up solution^[29]. These agents consist of two main components: a surfactant and a solvent. When these agents are sprayed onto the oil slick, the interfacial tension between the oil and the water is reduced, promoting the formation of finely divided oil droplets. One of most used agents is Corexit EC9500A^[30], which is sprayed to break down the oil by increasing the surface area of each oil molecule, creating micro and nanodroplets. This makes it easier for microbes to degrade the oil by bonding with the water, effectively cleaning up the spill. However, the application of chemical dispersants, specifically Corexit EC9500A, as a response strategy during the Deepwater Horizon oil spill in the Gulf of Mexico 2010 has raised environmental concerns^[31]. Studies have shown that the Corexit EC9500A dispersant can harm marine organisms and impede the natural biodegradation process of the spilled oil^[31,32]. Furthermore, the efficacy of Corexit EC9500A in effectively mitigating the impacts of oil spills has been the subject of ongoing research and debate within the scientific community^[32,33].

The biological method of oil spill remediation involves using microorganisms, such as the bacteria and the fungi, to break down and degrade the oil^[34]. This method is a natural and environmentally friendly approach to clean up oil spills. The process begins by introducing a population of specifically adapted microorganisms to degrade the type of oil that has been spilled^[34]. These microorganisms consume the oil as a food source, breaking it down into simpler compounds such as water, carbon dioxide, and biomass. The microorganisms continue to grow and multiply, consuming more and more of the oil until it is fully degraded^[35]. This method can be used in various ways, including applying microorganisms directly to the surface of the oil spill, using bioremediation agents to stimulate the growth of native microorganisms, or using bioreactors to speed up the degradation process^[33,35,36]. One of the advantages of the biological method is that it is a natural and sustainable approach that does not require harsh chemicals or heavy machinery. Additionally, it can be used in remote or sensitive areas where other methods may not be feasible. However, the biological method can be slow and ineffective for large

spills or certain types of oil. It also requires careful monitoring and management to ensure that the microorganisms do not harm other organisms or the environment.

Separation membrane techniques are considered also as efficient methods for treatment of oil-water mixtures due to their simple operational process and are widely used in industrial applications^[23,37,38]. However, the separation efficiency with conventional membranes is severely limited since the separation of stable emulsions is traditionally achieved with small pores^[39,40]. In addition, membrane fouling problems and poor recyclability limit their application for the emulsion separation^[41-43].

In recent years, the research on the role of the surface wettability in oil-water separation has attracted much attention due to its ability to foster the selectivity, the stability, and high separation efficiency^[44-47]. Wettability is an inherent property of a solid surface that has a direct relationship between the contact angle (CA) and the surface energy (simply the CA decreases with the surface energy)^[48,49]. Therefore, materials with unique wettability properties, such as superhydrophobic, superhydrophilic, superoleophobic, and superoleophilic, can be fabricated and designed by tailoring the structure and surface energy^[50-54]. If the material has different wetting properties for oil and water, such as superhydrophobicity and superoleophilicity or superhydrophilicity and superoleophobicity, this can help to realize the selective separation of oil-water mixtures^[55]. Based on this idea, various materials with wettability contrasts have been developed and successfully applied in oil-water separation^[46,47,56,57]. Materials with superhydrophobicity and superoleophilicity can selectively filter or absorb the oil from oil-water mixtures^[52]. Likewise, materials with the opposite wettability, superhydrophilicity, and superoleophobicity can also absorb the water selectively from an oil-water mixture^[58]—more detail on oil-water separation based on wettability contrast is given in Chapter 2.

Despite advancements in the oil-water separation and removal of organic pollutants in water, still, several critical concerns remain. For example, the surface contamination, fouling, and reusability can lead to an irreversible separation efficiency and a severe decrease in flux^[59]. In this regard, the photocatalysis has been widely explored to decompose and clean up organic pollutants in water and on surfaces^[60]. Photocatalytic reactions lead to the catalytic decomposition of organic pollutants under the illumination^[61]. Photocatalytic reactions generally proceed through the generation of charge carriers upon the light absorption, the transport of charge carriers to the surface of the photocatalyst, and the reaction with target molecules^[62]. Various semiconductors have been explored as photocatalysts including titanium dioxide (TiO₂), zinc oxide (ZnO), and cadmium sulfide (CdS) to decompose organic pollutants,^[63-65]. The photocatalytic decomposition of organic pollutants follows a similar mechanism to conventional photocatalytic reactions (e.g., formation of reactive species). When a semiconductor photocatalyst absorbs the light, the charge carriers (excited by the light) move towards the catalyst surface and participate in redox reactions. Therefore, the decomposition of an organic pollutant is governed by four main factors: (i) the organic pollutant should be adsorbed on the catalyst surface for reactions; (ii) the active carriers should be sufficient; (iii) the intermediate products of the decomposed pollutant should be rapidly desorbed; and (iv) the catalysts should be stable throughout the process. Among various semiconductor photocatalysts, TiO₂ has been broadly studied due to its superior photoactivity, low toxicity, chemical and biological inertness, low cost, and corrosion resistance^[66].

In the use of TiO₂ in photocatalytic decomposition of organic pollutants, the reactivity is linked to the free radicals or reactive oxygen formed, which react and break down the targeted pollutants into lower molecular weight products and eventually mineralize them into more specific and non-toxic products, H₂O, CO₂, and mineral acids^[67]. The reactive oxygen species such as hydroxyl radical (HO[•]), superoxide anion radical (O₂^{•-}), hydroperoxyl radical (HO₂[•]), and singlet oxygen (¹O₂) are primarily formed during ultraviolet (UV) irradiation of TiO₂ photocatalyst^[68]. The hydroxyl radicals generated from the positive

holes of TiO₂ on the catalyst surface after water photolysis are nonselective oxidizing species with strong oxidation potential (+2.80 V) that react swiftly to most organic compounds with rate constants on the order of 10⁶–10¹⁰ M⁻¹ s⁻¹[69]. In general, the efficiency of the pollutant removal process depends on the generated hydroxyl radicals and their reactions with organic pollutants at and/or close to the TiO₂ surface. Therefore, the surface adsorption and reactivity of the target compounds with HO• are the main factors in the UV-promoted photocatalytic TiO₂ degradation of organic compounds.

Early detection of the contaminants (pollutants) at very low levels and concentrations is as important as separating and purifying the water from these pollutants, and it is essential to conduct proactive measurements to prevent oil spills and other related incidents. In recent years, there has been a growing interest in developing economical and credible methods for detecting, monitoring, and accurately determining the ultra-trace concentrations of organic pollutants in water^[70]. Most analytical laboratory techniques can meet the sensitivity and selectivity requirements but suffer from the need for skilled and trained personnel and expensive instrumentation for the analysis. In addition, time-consuming extraction and sample preparation steps are always critical issues. Also, most of the analytical laboratory techniques are not suitable for the remote water and environmental pollution monitoring on-site. There is a need for inexpensive, flexible, and reliable analysis tools to monitor pollution. Recently, keen attention has been given to the development of chemical sensors to encounter the limitations of classical analysis protocols^[71]. However, the practical application of chemical sensors is often hampered by their inadequate selectivity in multicomponent media (rather than isolated analytes). While various indication mechanisms can be exploited to develop chemical sensors, optical sensing methods hold the most promise for meeting organic pollutant sensitivity requirements^[72]. Optical sensing is a multipurpose tool that includes a range of techniques: fluorescence, absorption, reflection, refractive index, surface plasmon resonance, and colorimetry^[73]. Among these techniques, surface plasmon resonance or Raman scattering is arguably one of the most sensitive, selective, and robust analytical platforms^[74,75].

Similar to Infra-Red (IR) based absorption spectroscopy, Raman spectroscopy probes the vibrational energy levels of molecules. The Raman effect occurs when a photon interacts with the vibrational energy levels of a molecule (scattering)^[76]. For plasmonic metallic structures, the scattering effect is even higher due to the interaction of the localized surface plasmon generated at the metal surface with the vibrational levels of the molecule^[74]. The amplified (due to its plasmonic nature) electromagnetic field induces a dipole in the molecule, which is adsorbed on the metal surface, leads to an enormously enhanced Raman signal^[77]. Conclusively, since the scattering effect takes place in the local fields of metallic plasmonic structures (mostly metallic nanoparticles, nanowires, etc.), it leads to strongly enhanced Raman signals of the molecules attached to (and/or nearby) the metallic surface. More details on surface-enhanced Raman scattering (SERS) and photo-induced enhanced Raman scattering (PIERS) and the design of nanosensors for ultra-sensitive detection of organic contaminants at trace amounts are given in Chapter 2. The scope of the work is presented as follows:

Chapter 2: The basics of the wettability of solid surfaces is discussed by considering the theoretical background. In particular, the effect of surface roughness, shape, geometry, and distribution of surface structures, surface morphology on the wettability is covered in detail. The role of surface chemistry, surface energy, and functional groups on wetting is explained briefly. Additionally, the surface treatment methods (mechanical methods, chemical methods, and UV/laser-assisted methods), coatings/thin films, chemical surface modification methods, surface functionalization techniques (e.g., self-assembled monolayer and vapor phase modification), and photocatalytic surface patterning/structuring are covered. Afterwards the photocatalysis and (focusing especially on metal oxides, titanium dioxide, and photocatalytic thin films) and the decomposition of pollutants by the photocatalysis are explained. The decomposition of organic materials and the mineralization, self-

cleaning surfaces, photocatalytic cleaning of oil-like organic molecules, and monitoring of the decomposition process by photocatalysis are also discussed briefly. In addition, the detection of organic pollutants through chemical and optical methods are also covered within this chapter. Last, surface-enhanced Raman scattering (SERS) and photoinduced enhanced Raman scattering (PIERS) are reviewed.

Chapter 3: (Reprint of publication 1) This chapter explains a two-step approach for the preparation of hierarchical Au needle clusters (HAuNCs) on highly active TiO₂ thin film. Herein, a systematic study presents tuning the wettability of TiO₂ thin films by the photocatalytic deposition of 3D flower- and hedgehog-like HAuNCs and self-assembled monolayers. In addition, the photocatalytic patterning approach was explored to induce a wettability contrast on the surface (superhydrophobic and superhydrophilic regions).

Chapter 4: (Reprint of publication 2) This chapter presents the selective adsorption and the photocatalytic oil clean-up by the TiO₂ thin film decorated with poly(1,3,5-trimethyl-1,3,5-trivinyl cyclotrisiloxane) (p-V₃D₃) modified flowerlike Ag nanoplates. A novel “three-in-one (3-in-1)” surface, which is composed of (i) a highly photocatalytic layer, (ii) micro- and nanostructures, and (iii) a low surface energy layer, is introduced. First, the TiO₂ photocatalytic layer is prepared by magnetron sputtering. Then flowerlike Ag nanoplates are photocatalytically deposited on the sputtered TiO₂ layer. Last a thin layer of p-V₃D₃ is over-coated.

Chapter 5: (Reprint of Publication 3) This chapter explains nanoscale synergetic effects on Ag–TiO₂ hybrid substrate for photoinduced enhanced Raman spectroscopy (PIERS) with ultra-sensitivity and reusability. 4N-in-1 hybrid substrate concept (nanocolumnar structures, nanocrack network, nanoscale mixed oxide phases, and nanometallic structures) for ultra-sensitive and reliable photo-induced-enhanced Raman spectroscopy (PIERS) and photocatalytic clean-up of analytes.

Chapter 6 presents the “Conclusions and Outlook” part. Here, a comprehensive summary of obtained results with a brief outline of planned future research work is provided.

CHAPTER TWO

2. Theoretical Background

2.1. Surface Wettability and Separation of Pollutants Through Wettability Contrast

Surface wettability is a unique surface phenomenon that is observed in a variety of daily biological and industrial practices^[78–80]. It is a macroscopic process that involves the interactions of three states of matter (solid, liquid, and gas) and is very susceptible to surface properties at the nanoscale or/and even at the molecular scale^[81]. Chemical and as well as physical properties govern the wettability of a solid surface. The wettability of a solid surface by a liquid is typically analyzed by contact angle (CA) measurement ($0^\circ < \theta \leq 180^\circ$), from which the surface energy of the solid can be estimated^[49]. The values of CA indicate whether a surface is hydrophobic or hydrophilic. For example, if the CA of a solid surface is less than 90° ($CA < 90^\circ$), it is termed as hydrophilic. Oppositely a surface with a CA higher than 90° ($CA > 90^\circ$) is called as hydrophobic^[82]. However, there are extreme cases where the solid surface can be fully wetted by a liquid ($CA \approx 0^\circ$), termed as superhydrophilic (in case of water) or superoleophilic (in case of oil). On the other hand, when a surface completely repels the liquid, it is said to be superhydrophobic (in case of water) or superoleophobic (in case of oil) ($CA > 150^\circ$), both offering interesting scientific challenges and practical applications^[52,54]. Learning from living organisms in nature, such as lotus leaves^[83], water strider legs^[84], springtails^[78], Namib desert beetle^[85], butterfly wings^[86], and bird feather^[87], synthetic surfaces of wettable and non-wettable properties have been engineered for various applications^[44,88–93]. To achieve wettable and non-wettable surfaces for practical applications, the material selection is a critical issue (discussed in more detail later). To this end, basic qualitative aspects of the wetting are emphasized in this chapter rather than focusing on mathematical models.

2.2. Dependence of Surface Wettability on Topography and Surface Roughness

The deviation from an ideal surface (atomically homogeneous and smooth) may arise due to surface heterogeneities, such as topography, roughness, dislocations, different crystal systems (crystal planes), and other physicochemical surface defects^[94]. The topography of a solid surface defines the roughness and the size, the geometry, and the distribution of surface features^[95]. All these topographical details have been shown to affect the surface wettability^[82]. This was first investigated by Wenzel (eq.2.1)

2.2.1. Wenzel's Model

Wenzel's theory^[82] deals with the wetting of rough and chemically homogeneous solid surfaces (which implies complete penetration of a liquid into the surface grooves) as shown in **Figure 2.1a**. The correlation between the surface roughness, Young's CA, and the apparent CA of the wetted surface is given by:

$$\cos\theta^w = r\cos\theta^y \quad \text{Eq. 2.1}$$

Where θ^w is the apparent CA, θ^y is the Young's CA, and r is the surface roughness factor which is defined as:

$$r = \frac{\text{actual surface}}{\text{geometric surface}} \quad \text{Eq. 2.2}$$

Since the roughness factor (r) is always higher than 1, the apparent CA on a rough surface is smaller when the CA of a liquid is $< 90^\circ$ on a smooth surface, while for a real surface $CA > 90^\circ$, the angle on a rough surface will be larger due roughness effects.

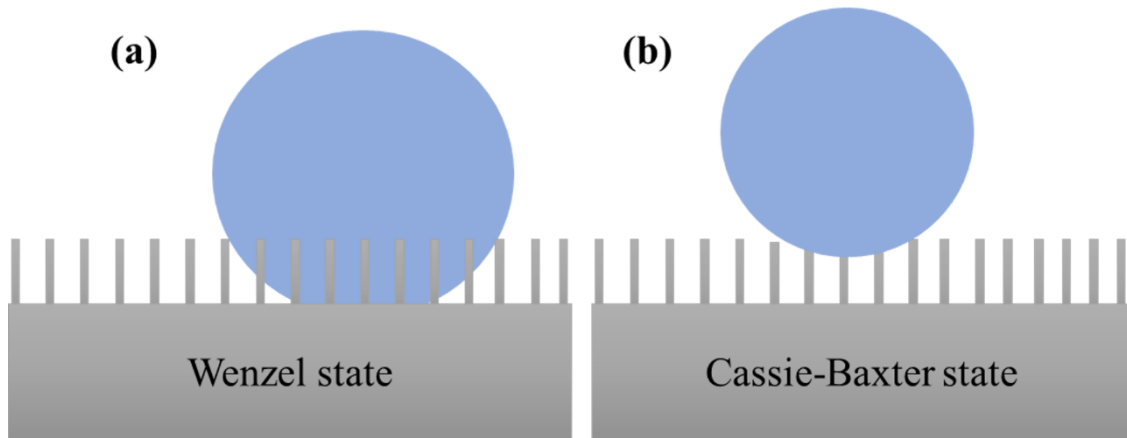


Figure 2.1. schematic diagrams of a liquid droplet on (a) Wenzel and (b) Cassie-Baxter states in air

Hence, three important conclusions are drawn from Wenzel's theory:

- I. A homogeneous smooth hydrophilic surface ($\theta^Y < 90^\circ$) will be more hydrophilic when wetted: $\theta^W < \theta^Y$ given that $r > 1$.
- II. For the same reason, a homogeneous hydrophobic flat surface ($\theta^Y > 90^\circ$) is more hydrophobic if it is grooved: $\theta^W > \theta^Y$
- III. The Wenzel angle in Eq. 2.1 is independent of the drop geometry and the external field.

However, Wenzel's model does not account for the fact that rough surfaces can alter the equilibrium positions of the interfacial tension of a liquid to partially penetrate the roughness grooves. This was first investigated by Cassie and Baxter^[96]

2.2.2. Cassie-Baxter's Model

The Cassie-Baxter theory assumes that air pockets are trapped beneath the liquid, resulting in a chemically heterogeneous surface (a surface of a composite material made up of different chemical compositions and uneven throughout the surface)^[96]. Defining the apparent CA in the Cassie-Baxter model^[97] as θ^c can be linked to the chemical heterogeneity of a rough surface according to:

$$\cos\theta^c = f_s \cos\theta^s + f_v \cos\theta^v \quad \text{Eq. 2.3}$$

where f_s and f_v are the fractional surface area of the solid and vapor on the surface, θ^c and θ^s are the Cassie and the solid surface CA and θ^v is the CA of the vapor phase, respectively.

The trapped air pockets form a CA of 180° ($\theta^v = 180^\circ$) and $\cos(180) = -1$, also $f_s + f_v = 1$, and $\theta^s = \theta^Y$ then Eq. 2.3 becomes

$$\cos \theta^c = -1 + f_s (\cos \theta^y + 1) \quad \text{Eq. 2.4}$$

Equation 2.4 is often referred to as the basis of the Cassie-Baxter model [96]. The Cassie-Baxter equation applies not only to chemically heterogeneous surfaces but also to porous homogeneous surfaces where the presence of air makes the system heterogeneous. In this configuration, a liquid does not fully wet the solid surface but instead is suspended on the rough surface, as depicted in **Figure 2.1b**.

2.3. Effect of Shape and Geometry of Surface Features on Surface Wettability

The wettability of a surface can be tuned by manipulating the shape, the size, and the geometry of surface features. Studies have demonstrated the significant impact these factors can have on the wettability of a surface. McCarthy et al. [98] utilized a photolithographic technique to create hydrophobic surfaces with posts of different shapes and sizes on a flat Si surface. They found that square-shaped posts with dimensions of 2-32 μm exhibited a superhydrophobic behavior, while larger posts with dimensions of 64 μm and 128 μm did not. Huang et al. [99] compared the wetting characteristics of PDMS surfaces patterned with "microlens-array-like" and "microbowl-array-like" structures and they found that microlens-array-like structures exhibited strong pinning of water droplets in comparison to the microbowl-array-like ones. Furthermore, Choi et al. [50] showed that the pinning behavior of water on superhydrophobic surfaces could be controlled by manipulating the surface morphologies of Si nanowire arrays, with clumped nanowires exhibiting a superhydrophobic state with low sticking behavior compared to straight nanowires. A recent study by Aktas et al. [100] demonstrates the impact of porosity and surface structures (a combination of both micro- and nanostructures) on the superhydrophobicity. They demonstrated that highly porous 3D structures at first exhibited superhydrophilic behavior due to the high capillary force [101] but after applying a thin layer of polytetrafluoroethylene (PTFE) such structures became superhydrophobic with advancing and receding CAs of 167° and 164°, respectively. These studies demonstrate the significant impact of the shape, the size, and the geometry of surface features on the wettability.

2.4. Effect of Surface Chemistry on Wettability

2.4.1. Surface Energy

The surface energy of a material is a crucial aspect that can affect its behavior and properties. It is determined by the strength of the bonds between the atoms or molecules at the surface. Materials with strong intermolecular forces, such as covalent bonds, have higher surface energies than those with weaker forces, such as van der Waals interactions. This means that it takes more energy to create a new surface area in a material with strong bonds. The surface energy can be used to determine the wetting behavior of a liquid on a solid surface. Researchers have explored the relationship between surface chemistry and surface energy to understand how liquids interact with solid surfaces [102–106]. Young's equation is a widely used model that describes the thermodynamic equilibrium state of an interface, taking into account the boundary condition at the liquid-gas interface and the local contact angle [107]. For solid-liquid-gas systems, the interfacial free energy is given by:

$$\cos \theta^y = \frac{\gamma_{sv} - \gamma_{sl}}{\gamma} \quad \text{Eq. 2.5}$$

where θ^y is the Young's CA ($0^\circ \leq \theta \leq 180^\circ$) γ_{sv} and γ_{sl} are the solid-vapor and solid-liquid interfacial tensions, respectively, and γ is the surface tension of the liquid (**Figure 2.2**).

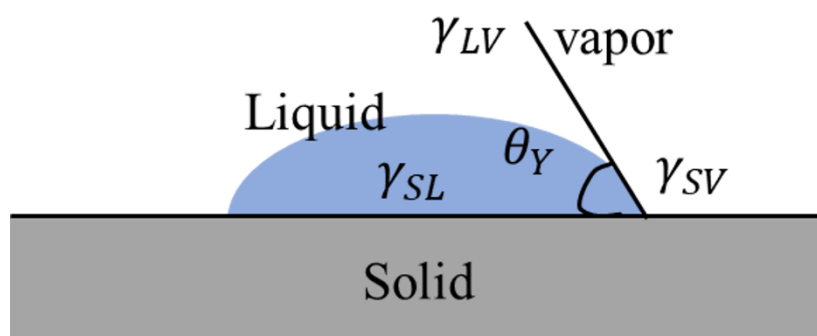


Figure 2.2. Schematic of a liquid drop showing the quantities in the Young equation

The Young's equation is a theoretical model that assumes a perfect solid surface - one that is rigid, flat, inert, chemically homogeneous, smooth, and nonporous. However, in reality, it can be challenging to find a surface that meets all of these criteria. This is because the energy at the interface between solids and liquids is affected by the polar and dispersive components of the surface energies of each solid and liquid^[104]. The relationship between the surface chemistry and the surface energy is one of the mostly studied theme and various research groups explore the effect of different sample preparation methods and surface functional groups on the surface energy. For example, Vidal et al. ^[108] investigated the surface free energy of amorphous and crystalline silica and found that the physicochemical properties and especially heterogeneity in wettability depend heavily on the sample preparation methods. Another study by Zeng et al. ^[109] focused on the effect of nanoscale surface structures and chemical composition differences on hydrophobic interactions. Using bubble probe atomic force microscopy, the researchers found that surfaces with similar hydrophobicity can have different hydrophobic interactions, and surfaces with different hydrophobicity can possess a range of hydrophobic interactions. The authors attributed these differences to the functional groups on the surfaces, specifically self-assembled monolayer functional groups, such as alkanethiol species with different tail groups like hydrophobic methyl or hydrophilic carboxyl, amino, or hydroxyl groups.

2.4.2. Effect of Functional Groups (Surface Chemical State) on Wettability

In general, functional groups define the physical and chemical properties of molecules. Functional groups are sets of connected atoms or groups of atoms that are classified as electron-withdrawing (-I) or electron-donating (+I) groups relative to the hydrogen^[110]. Numerous functional groups exist with distinct chemical properties^[111]. Depending on the applications, the properties of functional groups can be altered either by changing their position within the molecule or by changing their proximity to other functional groups. Therefore, altering the surface chemistry (functional group) can be used to tune the wetting of a solid surface. The influence of functional groups on the surface wettability has been widely explored^[112-117]. For example, Lee et al. evaluated the interfacial wettability of fluoropolymers and pointed out that CF_2 functional groups provide an increased number of attractive dispersive contacts per unit area on the surface when compared to CF_3 groups (leading to enhanced non-wettability of the former surfaces^[118]). Zhou et al. studied the effect of oxygen-containing functional groups on the surface wettability of coal dust with various metamorphic degrees^[119]. Their study estimated the atomic concentration ratio of surface oxygen to carbon using X-Ray Photoelectron Spectroscopy (XPS) to reveal the effect of oxygen content on wetting. Their elemental analysis showed that as the degree of metamorphism increases, the carbon content in coal samples increases, but the oxygen content decreases. The data was further correlated with water CA analysis and concluded that oxygenated polar group content affects the wettability of coal dust ^[119]. Therefore, functional group chemistry is an indispensable tool in controlling the surface wettability of materials.

2.5. Surface Modification

Surface modification is a widely used approach to enhance the properties of materials for various applications. It involves altering the surface of a material to improve its functionality and make it suitable for specific tasks. These modifications can be achieved through chemical, ionic, or light-based processes, which add functional groups to the surface to improve its energy and wetting properties^[120]. Additionally, the surface topography and the roughness can be modified through mechanical or chemical processes, which create micro- and nanoscale roughness on the material surface, to attain anti-wetting and anti-fouling properties^[121]. Surface modification methods can be categorized into mechanical^[122] and chemical processes^[123]. Mechanical methods such as micromachining, polishing, grinding, and surface blasting are commonly used to modify the morphology, the topography, and the roughness of solid surfaces. The choice of the proper technique depends on the intended application and desired surface functionality^[124]. For example, while increasing the surface roughness can improve the adhesion the decrease in roughness facilitates the removal of the surface contamination^[125]. However, it is important to note that after the mechanical surface modification step a chemical treatment can also be needed to get desired properties (chemical resistance, biocompatibility, etc.)^[126].

2.5.1. Wet Chemical Surface Modification Methods

The wet chemical surface modification methods involve the use of various chemical solutions and techniques to alter the surface properties. One of the most used wet chemical surface modification methods is the chemical etching. This method involves the use of chemical solutions to remove material selectively from the surface of a substrate, resulting in a modified surface with different properties^[50]. For example, the chemical etching can be used to create micro- and nanoscale patterns on a surface, which can be used in applications such as microelectronics and biotechnology^[127–131]. Another common wet chemical surface modification method is the chemical functionalization. This method involves the introduction of chemical groups onto the surface of a substrate, resulting in a modified surface with new chemical properties. These functional groups can be chemical groups such as carboxyl, amino, or hydroxyl groups, which can alter the material properties. The functionalization process can be achieved through various methods, including physical adsorption and self-assembling monolayer approaches^[132]. Self-assembled monolayers (SAMs) are thin layers of molecules that spontaneously organize themselves in a highly ordered and dense manner on a substrate surface. They are formed by the directed adsorption of molecules from a solution or vapor phase onto a substrate, resulting in a highly ordered, two-dimensional arrangement of the molecules. Examples of SAMs include alkyl phosphonic acid, alkanethiols, silanes, etc. These molecules can create hydrophobic or chemically functional surfaces that can be used in various applications such as oil-water separation, biotechnology, and electronic devices^[127–131]. In addition to chemical etching and functionalization, other wet chemical surface modification methods include electroplating, electroless plating, and sol-gel processing^[123,133].

2.5.2. Dry Surface Modification Methods

As alternative to wet chemical techniques dry surface modification methods are also preferred for altering the surface properties of materials. These techniques can be listed as ultraviolet-visible and laser-assisted treatments^[134], flame^[135], corona discharge^[136], plasma treatment^[137], lithography^[138], physical vapor deposition^[139] and chemical vapor deposition^[139]. The main advantage of dry surface modification methods is the ability of surface modification without the risk of introducing any contaminant. Additionally, dry surface modification methods are often faster and more efficient than wet chemical methods, making them a cost-effective alternative. In the following section, some of these dry surface modification methods (sputtering and chemical vapor deposition) and especially their use to change or create new material properties will be discussed.

2.5.2.1. Sputtering

Sputtering is a physical vapor deposition (PVD) technique used to deposit thin films of material onto a substrate. It involves bombarding a target material with a high-energy beam of ions (typically argon ions), which causes the target material to sputter and release atoms that then condense on the substrate, typically a few nanometers to microns thick^[140]. The process is performed in a vacuum chamber, and the substrate is positioned close to the target material. The sputtering process can be described as a three-step process:

- i. the ionization of the inert gas, typically argon in the sputtering chamber by applying a high voltage
- ii. the bombardment of the target material by the ions, which results in the physical removal of atoms from the target surface
- iii. the transport of the sputtered atoms to the substrate surface, where they condense and form a thin film

Sputtering is a versatile technique that can be used to deposit a wide range of materials, including metals, ceramics, alloys, insulators, and semiconductors. There are several types of sputtering techniques, each with its own limitations. These include direct current (DC) sputtering, radio frequency (RF) sputtering, magnetron sputtering, Pulsed DC sputtering, reactive magnetron sputtering, and ion-assisted sputtering^[141]. Within the scope of this research work, the focus is given to the reactive magnetron sputtering method.

2.5.2.2. Reactive Magnetron Sputtering

In reactive magnetron sputtering method basically a magnetron source in combination with a reactive gas is used to deposit a thin film of a specific material^[139]. In this process, a target material under vacuum is bombarded with ions from the magnetron source. At the same time, a reactive gas, such as oxygen or nitrogen, is introduced into the chamber. The ions from the target material and the reactive gas react to form a film on the substrate. As illustrated in **Figure 2.3**, the magnetron sputtering head comprises several key components, including a negatively charged target, a grounded cap serving as a counter electrode, inlets for gas and cooling supply, and permanent magnets positioned at the backside of the target. The process is conducted under vacuum conditions to achieve a sufficient mean-free path for the sputtered target atoms, which results in a steady flux of target material towards the substrate. The working principle of a magnetron is based on the interaction between a magnetic field and an electric field. When the target is bombarded by ions generated from a stable plasma or glow discharge of an inert gas, typically argon (Ar^+). The target is maintained at a negative potential, typically a few hundred volts, which causes the Ar^+ to accelerate towards the target material. This plasma is confined to the target material by the magnetic field, and the electrons in the plasma are accelerated toward the target material by the electric field^[142]. When these accelerated electrons collide with the target material, they sputter atoms and are then deposited on a substrate placed a few centimeters from the target material.

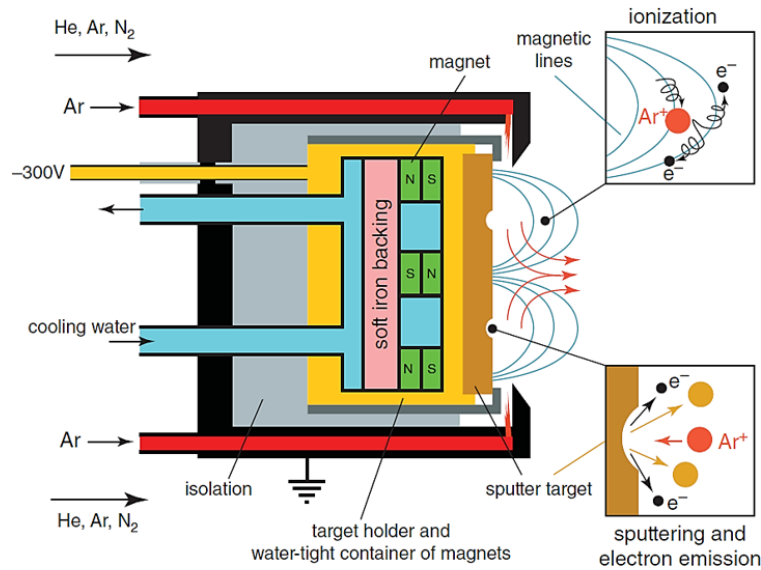


Figure 2.3. A schematic of the components of a magnetron sputtering head. A cylindrical magnetic field is used. Charge generation and surface erosion are maximum in the region where the magnetic field is parallel to the surface, as indicated by the two insets, and electron capture occurs through the magnetic field (Adopted from ^[143])

When the magnetron sputtering system is in operation, it must be cooled to prevent diffusion in the target, which could lead to changes in the elemental composition in the surface region, especially when using composite sputtering targets. Therefore, in sputter deposition, the sputtering targets play a vital role in determining the purity and the properties of the material to be modified or produced during the sputtering process. Commonly, there are commercially available metal and polymeric targets depending on the need and application, one can select from noble metal targets such as Gold (Au), silver (Ag) with high purity of 99.99 %, and many transition metals^[144]. Generally, magnetron sputtering allows the precise control over the composition of the deposited material and the ability to create desired properties in the final product. However, reactive sputtering processes require more careful control than metal sputtering, as the target surface can react strongly and cause target poisoning.

2.5.3. Chemical Vapor Deposition

Chemical Vapor Deposition (CVD) is an effective tool for deposition of thin films on substrates through a chemical reaction of gaseous precursors. These precursors are typically in the form of gases or vapors that are introduced into a reactor, where they react to form the desired film on the substrate^[145]. This technology is employed heavily to produce high-quality semiconductor and dielectric thin films for various applications including microelectronics, optoelectronics, biosensors, and energy conversion devices^[136,145–147].

A typical conventional CVD method uses thermal energy to activate chemical reactions. This involves three steps: the precursor injection, the thermal decomposition, and the film growth. In the precursor injection step, the reactive gases (usually in the form of a gas or a liquid) are introduced into the reaction chamber. These gases are then heated to a high temperature, usually in the range of 800–1100 °C, to initiate the thermal decomposition step^[148]. In this step, the gases undergo a chemical reaction, typically in the presence of a catalyst, to form the desired film on the substrate. Finally, in the film growth step, the newly formed film continues to grow on the substrate until the desired thickness is achieved. Depending on the energy source, there are different variants of CVD techniques, such as plasma-enhanced CVD (PECVD)^[149] and photo-assisted CVD (PACVD)^[150], that use plasma and light to

activate chemical reactions, respectively. Other variants include metalorganic CVD (MOCVD) using metalorganic as the precursor^[151], Flame assisted vapor deposition (FAVD) using a flame source to initiate the chemical reaction^[152], and initiated chemical vapor deposition (iCVD) employing both initiator and monomer to instigate chemical reactions^[147]. In this research work, iCVD is discussed in detail (in relation to the experimental work carried out in Chapter 4).

2.5.3.1. Initiated Chemical Vapor Deposition

iCVD is an effective tool for synthesizing chain-growth polymers (radical polymerization)^[147]. This method involves introducing a thermal initiator and monomer(s) into a growth reactor. In the iCVD process, a thermal initiator is introduced concurrently with the monomer(s) into the growth reactor. Then, the resistively heated filament wires placed just a few centimeters above the growth surface are used to decompose the initiator selectively, resulting in the reaction of the initiator fragments with monomers adsorbed on the cooled substrate. This leads to the growth of film on the substrate at a thickness starting from a few nanometers to micrometers. The iCVD method is compatible with vinyl monomers, including acrylates, methacrylates, and styrenes. These monomers have desirable pendant functional groups, such as epoxy, amine, or carboxylic acid moieties (essential for fabricating films that are responsive to changes in humidity, temperature, or pH^[153]). Most iCVD vinyl polymers are electrical insulators but using monomers with acetylenic bonds can extend the use of iCVD to the preparation of conjugated semiconducting polymers^[147,154].

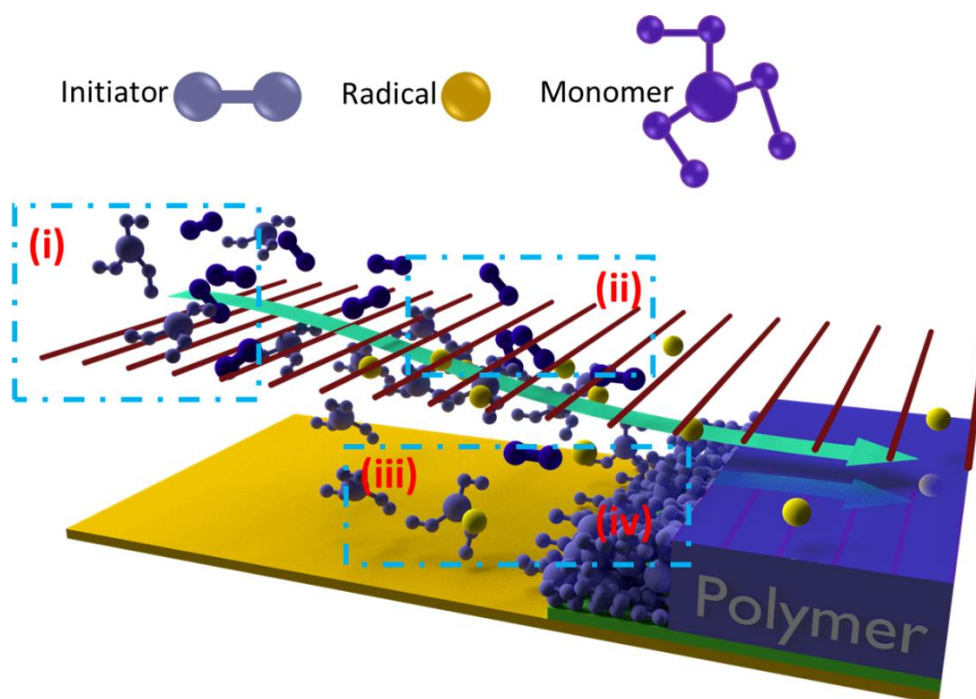


Figure 2.4 Schematical representation of mechanisms within a typical iCVD process (i) precursor vapor delivery (ii) monomer adsorption (iii) breakdown of initiator by the heated filament and (iv) polymerization and film growth (Sketched by Salih Veziroglu).

Typical processes in iCVD can be summarized in the following steps as shown in **Figure 2.4**:

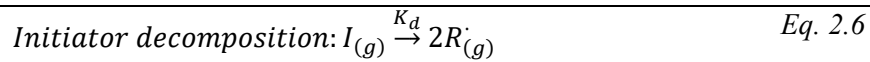
- i. vapor delivery of the monomer (or co-monomers) and the corresponding initiator into the reactor
- ii. adsorption of the monomer vapor unto the cooled substrate surface

- iii. activation of the initiator by an array of resistively heated filament wires placed slightly above the substrate.
- iv. polymerization at the substrate surface to form a film

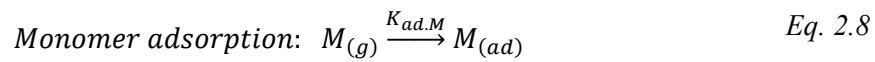
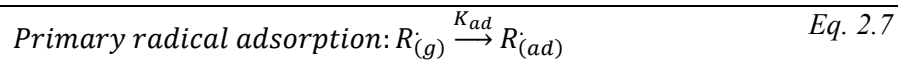
The polymerization process begins with the initiation step, in which an activated initiator reacts with an adsorbed monomer molecule. This is followed by the propagation step, in which more adsorbed monomer units are added to the growing polymer chain. The process ends with the termination step, in which the active polymer chain tails are capped. The vinyl bond is where iCVD polymerization occurs, and the polymer chain grows over time as more monomer is adsorbed.

Lau et al. [156] proposed a surface-driven radical polymerization mechanism to explain the rate behavior observed in experiments. This mechanism takes gas-phase reactions, the transfer of reactions from the gas phase to the surface, and surface reactions into account. The kinetics of this mechanism is represented in equations 2.6-2.13:

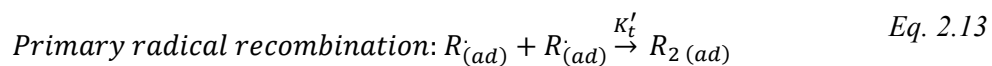
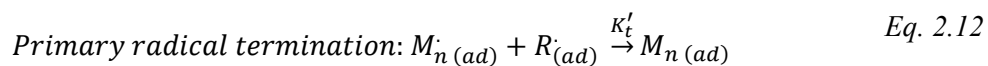
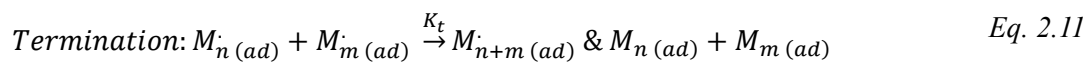
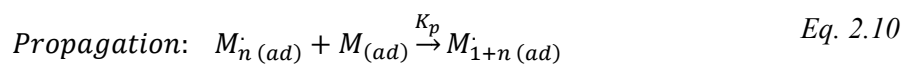
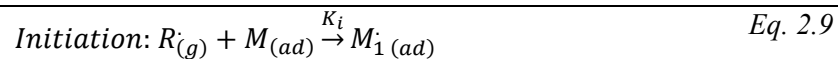
Gas-phase reactions



Gas to surface processes



Surface reactions



By adjusting the deposition parameters (including process pressure, monomer partial pressure, filament temperature, and substrate temperature) the properties of the polymer film can be influenced. Therefore, the alteration of these parameters can lead to changes in the film characteristics.

2.5.4. An Alternative Surface Modification Method: Photocatalytic Surface Patterning

The photocatalytic surface patterning and/or structuring can be applied for surface modification of photocatalytic materials due to its simplicity, cost-effectiveness, and non-contact nature^[157]. Creating patterns on solid surfaces that control chemical affinity, such as hydrophilicity, is essential for developing various devices and functional materials. Especially the creation of superhydrophobic and superhydrophilic patterns is particularly useful in sensor technologies^[158], lab-on-a-chip applications^[159], oil-water separation, and liquid flow control^[160]. Hideo et al.^[161] used the photocatalytic lithography method to create a superhydrophobic/superhydrophilic patterns on gold surfaces. First, they roughened the gold surface and modified it with perfluorodecanethiol to make it superhydrophobic. Then they used a TiO₂-coated glass-based photomask and a polyimide film to selectively expose the surface to a Hg-Xe lamp, resulting in a patterned surface exhibiting a strong wettability contrast. Similarly, Tatsuma et al.^[162] used diazonium salts and the visible light to pattern (photocatalytically) a cellulose surface. Recently, Veziroglu et al.^[163] applied the photocatalytic deposition technique using a polymeric mask to pattern the TiO₂ surface with hierarchical Au needle clusters (HAuNCs), as shown in Figure 2.5.

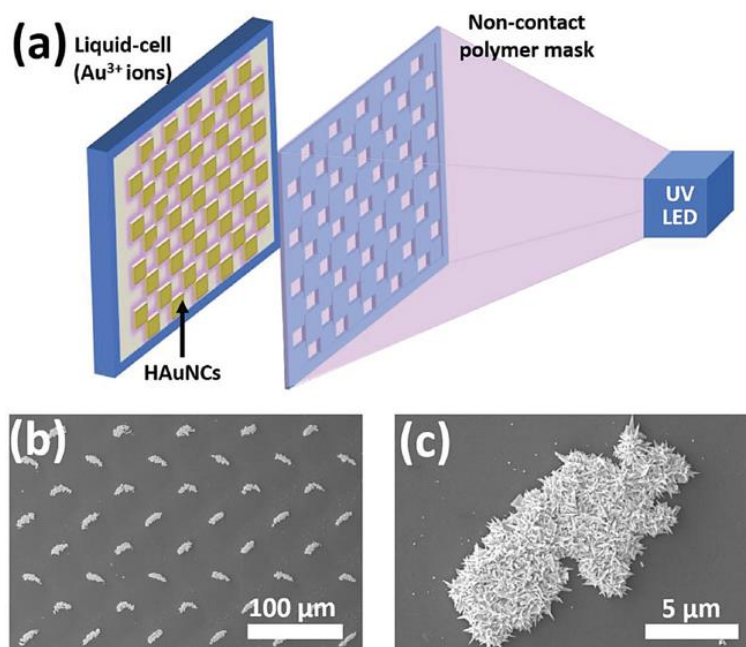


Figure 2.5. a) Schematic of photocatalytic patterning of TiO₂ thin film with HAuNCs using a non-contact polymer mask. SEM images of b) periodic HAuNC arrays and c) a single HAuNC (Adopted from ^[163])

2.6. Pollutants Separation Based on Wettability

The growing problem, “oil pollution”, triggered the research for developing new materials especially with unique wettability properties. Such materials ideally should be robust, cheap, environmentally friendly, and recyclable/reusable. To design such materials, it is important to understand the type of the oil to be separated, the mechanism of the separation, and the environmental conditions. Oil-water mixtures are typically examined in two groups: stratified and emulsified oil-water (including oil-in-water and water-in-oil emulsions) mixtures^[47]. Stratified oil-water mixtures contain large, dispersed droplets (>20 μm) that can exhibit phase separation easily over time due to the thermodynamical instability^[164]. In such mixtures, the denser phase settles while the lighter phase floats. On the other

hand, emulsified oil-water mixtures are thermodynamically stable colloidal dispersions composed of micro-/nanoscale droplets of a dispersed phase within a continuous phase^[165]. These droplets are usually stable due to the robust oil-water interfacial film components and adsorbed surfactants. **Figure 2.6** illustrates the composition of oil-water emulsions.

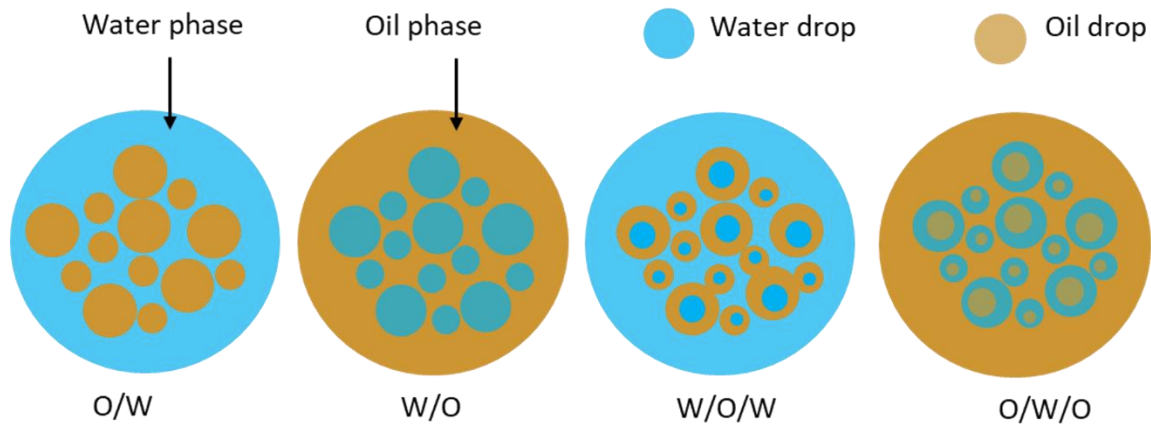


Figure 2.6. Schematic illustration emulsion types (Adopted from^[166])

2.6.1. Mechanisms of Oil-Water Separation Based on Surface Wettability

Oil-water separation using surface wettability properties relies on the principle of the interfacial tension and the intrinsic properties of the liquids including density, viscosity, and surface tension^[82]. Basically, the interfacial tension between the oil and the water is relatively high, thus makes it difficult to mix them^[167]. Therefore, the surface wettability properties of materials play a crucial role in separating oil and water. As illustrated in **Figure 2.7a**, a hydrophobic material has a low surface energy, which means that the surface does not interact well with water molecules, resulting in a high CA between the liquid and the surface^[46]. When the oil and the water are placed on a hydrophobic surface, the oil molecules will preferentially spread out on the surface, forming a thin film, while the water molecules will remain in the bulk liquid phase, separating the two liquids. On the other hand, a hydrophilic material has a high surface energy, which means that the surface interacts well with water molecules, resulting in a low contact angle between the liquid and the surface (see **Figure 2.7b**). When the oil and the water are placed on a hydrophilic surface, the water molecules will preferentially spread out on the surface, forming a thin film, while the oil molecules will remain in the bulk liquid phase, resulting in a separation of the two liquids^[168]. In addition to the interfacial tension, the separation process also relies on the properties of the liquids (such as density, viscosity, and surface tension). The density of oil is typically lower than that of water, which means that oil will float on top of the water^[169]. Also, the viscosity of the oil is typically higher than that of water, meaning that oil will be less mobile than water and will tend to form a separate layer on top of the water. Similarly, the surface tension of oil is typically lower than that of water, which means that oil will spread out more readily on a surface than water.

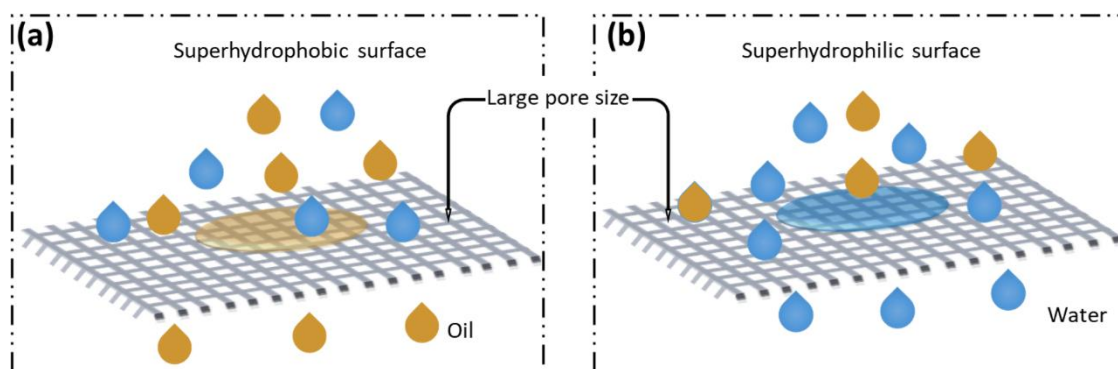


Figure 2.7. Design strategies and the mechanism of separation of oil/water mixtures(adopted from^[46]).

Materials exhibiting opposite affinities in terms of wetting for the oil and the water are the most promising materials for an effective selective oil-water separation. For instance, hydrophobic-oleophilic materials and/or hydrophilic-oleophobic material combinations are preferred for the oil-water separation applications.^[170,171] Materials for the oil-water separation can be categorized into two types (based on the methods used for oil-water separation): (i) filtering materials and (ii) absorption materials. Filtering materials are used for the selective separation of the oil from the water or the water from the oil, allowing a homogeneous single-phase passage of the oil or the water while preventing the other from passing through^[172]. On the other hand, absorbents are materials that can selectively absorb the oil or the water on their surface and in their internal voids but repel the other phase when exposed to an oil-water mixture. The use of the above methods for the oil-water separation has been studied extensively^[93,173–177]. However, the reusability and recyclability of such remain as a challenge.

2.7. Photocatalytic Decomposition and Clean-up of Organic Pollutants

In this section, a brief overview of photocatalysis including its mechanism, the use of metal oxide semiconductor as photocatalyst, the preparation of photocatalytic films, and the photodegradation process will be given. The application of photocatalysis in self-cleaning and cleaning oil contaminants on surfaces and the strategies for monitoring the photocatalytic decomposition will be discussed, too.

2.7.1. Photocatalysis

Basically, the photocatalysis uses the light energy to alter the rate of a chemical reaction in the presence of a photocatalyst. A photocatalyst is a material that can accelerate chemical reactions by absorbing light without being consumed in the process. In photocatalysis, the photocatalytic reactions are classified into two main groups based on the occurrence of the physical state of the reactants.

- i. Homogeneous photocatalysis: Both the semiconductor and reactants are in the same phase, i.e., gas, solid, or liquid^[178]
- ii. Heterogeneous photocatalysis: Semiconductor and reactants are in different phases^[179]

Heterogeneous photocatalysis is generally considered to be superior to homogeneous photocatalysis due to the stability and the ease of separation and recycling of the photocatalysts. Among the various heterogeneous photocatalysts, semiconductor catalysts such as TiO₂, ZnO, Fe₂O₃, CdS, GaP, and ZnS have been found to be highly efficient in degrading even the most recalcitrant organic compounds^[64,65,180–182]. TiO₂ is the most widely studied semiconductor photocatalysts due to its durability, low cost, low toxicity, superhydrophilicity, and remarkable chemical and photochemical stability^[183].

2.7.2. Fundamental Principle of Photocatalytic Reactions

When a photocatalyst, such as TiO_2 , absorbs the light (with an energy level that is equal to or greater than its bandgap energy) it forms a photoexcited state and generates an electron-hole pair^[184]. The separation of charges from this pair results in positively charged holes in the valence band and negatively charged electrons in the conduction band (Figure 2.8a)^[184].

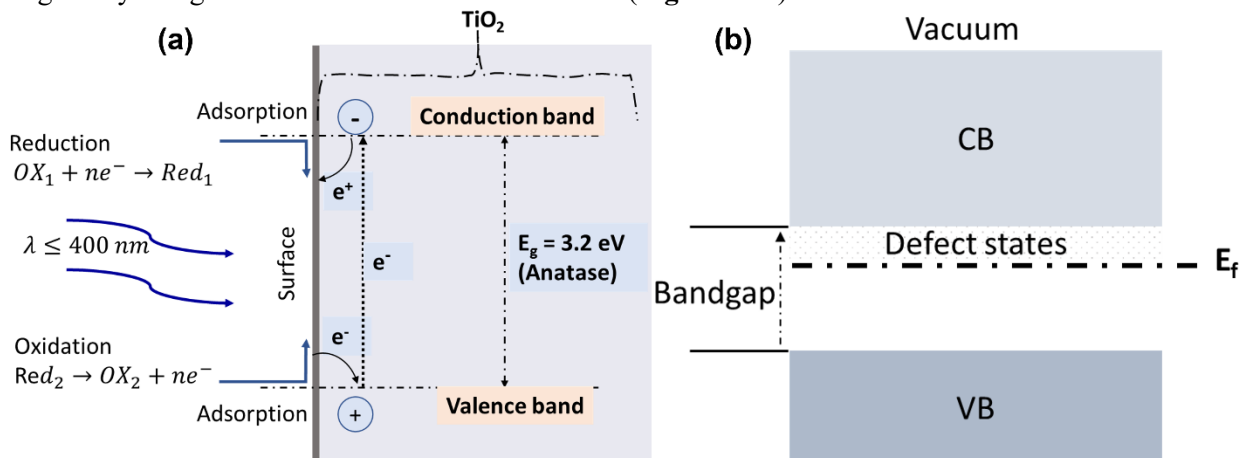


Figure 2.8. Electron energy band diagram of TiO_2 showing (a) electron energy E plotted upwards as a function of the distance from the surface to the bulk of the solid (b) electronic structure with defect states (adopted from^[184] ^[183])

The photocatalytic activity of a semiconductor is influenced by the ability of the material to transfer electrons and holes to adsorbed compounds, which can then be oxidized or reduced. However, these charge carriers can also recombine, and this may inhibit any chemical/catalytic reaction.^[185] The effectiveness of the photocatalysis is often linked to the wavelength of the light source and the energy of the bandgap of the corresponding semiconductor. For example, for the activation of TiO_2 (with a bandgap energy of 3.20 eV) a light source operating at a wavelength of 350-400 nm^[183] is needed. The unique feature of the photocatalysis is that it offers both oxidation and reduction reactions on the same surface. Therefore, the positions of the conduction and valence bands of the semiconductor and the redox levels of the substrate govern the behavior of the excited electrons and holes.

2.7.3. Metal Oxide Photocatalysts

Metal oxides, such as TiO_2 , ZnO , WO_3 , and Fe_2O_3 , have important technological applications in environmental remediation and electronics due to their ability to generate charge carriers (electrons and holes) when exposed to specific amounts of energy, known as the bandgap energy^[186]. TiO_2 is the most commonly used photocatalyst due to its non-toxicity, stability, resistance to photo-corrosion, water insolubility, hydrophilicity, and low cost. However, TiO_2 is only active under UV light due to its large bandgap. Consequently, several other metal oxides have been tested as possible alternatives. ZnO is also a commonly studied n-type semiconductor, with a bandgap of 3.37 eV^[187]. However, its band gap is typically larger than expected due to its ionic character. On the other hand, WO_3 is another n-type semiconductor with a bandgap of 2.4 – 2.8 eV (that is capable of absorbing visible light) making it a suitable candidate for the photocatalytic degradation of organic pollutants under solar radiation, but its conversion efficiency under visible light illumination is questionable^[188]. Similarly, $\alpha\text{-Fe}_2\text{O}_3$ (hematite) is an n-type semiconductor material with a bandgap of around 2.1 eV (lies in the visible region of the solar spectrum) and stable in most aqueous solutions at $\text{pH} > 3$ ^[189]. Additionally, several other metal oxides for instance CeO_2 , V_2O_5 , Ta_2O_5 , Bi_2O_3 , NiO , ZrO_2 , Ga_2O_3 , CuO , and Cu_2O have been investigated for photocatalytic applications^[190]. These metal oxides are of great importance in

environmental remediation and electronics due to their photocatalytic properties, which can be utilized to degrade pollutants and other substances.

2.7.4. Titanium (IV) Oxide as Photocatalyst

TiO₂ is a naturally occurring compound that exists in three distinct phases: rutile, anatase, and brookite. These phases are all composed of TiO₆ octahedra, but they have different structural distortions^[191]. The properties of TiO₂ are heavily influenced by the characteristics of the Ti-O bonds within it^[192]. Among the phases, rutile is the most stable, while anatase and brookite are considered metastable phases^[183]. However, at high temperatures, these metastable phases will transform into the rutile phase. Due to the unique properties of each TiO₂ phase, they are widely studied for various solar energy conversion applications such as photocatalytic H₂O splitting, industrial wastewater treatment, and biomass conversion^[183]. The main drawback of TiO₂ as a photocatalyst is its large band gap; the band gaps of bulk anatase and rutile materials are 3.20 and 3.02 eV (corresponding to 384 nm and 410 nm), respectively, meaning that TiO₂ can only absorb 4% of the solar spectrum^[62].

2.7.4.1. Electronic Structures of TiO₂

TiO₂ can be defined as an electrical insulator at some level due to its large bandgap, which is composed of conduction bands (CB) and valence bands (VB) made up of Ti 3d and O 2p states, respectively^[193]. However, all crystalline TiO₂ phases have point defects, such as oxygen vacancy, interstitial titanium ions (Ti³⁺), and substituted ions, that affect the catalytic properties of a material as well as the mass transport and the electrical conduction^[183]. The presence of point defects in TiO₂ introduces new electronic states, referred to as defect states, within its bandgap as illustrated in **Figure 2.8b**. The energy position of these defect states within the bandgap is influenced by both the phase and surface structure of TiO₂. For instance, defect states in rutile-TiO₂(110) have been observed to occur at energies approximately 0.8 to 1.0 electron volts below the conduction band edge, while those in anatase-TiO₂(101) are positioned at roughly 0.4 to 1.1 electron volts below the conduction band edge^[194,195].

2.7.4.2. Formation of Oxygen Vacancies in TiO₂

Oxygen vacancies, which occur when there is a change in the position of oxygen atoms within a crystal lattice, are a common type of anionic defect found in oxide materials. These defects can occur in bulk materials, as well as on the surface or the subsurface of nanomaterials^[196]. The presence of oxygen vacancies in semiconductor oxides like TiO₂ and ZnO has been shown to affect their electronic and optical properties^[197,198]. **Figure 2.9** illustrated the theoretical representation of oxygen vacancies in TiO₂ with unpaired electrons or Ti³⁺ centers, which can produce a donor level in the electronic structure of TiO₂ and influence the process of recombination of photogenerated charge carriers^[199]. Experimental observation also revealed that oxygen vacancies affect the surface reactivity and the adsorption of water molecules on TiO₂^[200]. Furthermore, the concentration of oxygen vacancies plays a critical role on photocatalytic performance. Recent studies have shown that precise control of oxygen vacancy concentrations within the crystal lattice can effectively decrease the rate of recombination of photo-excited electron-hole pairs^[185,201]. This process can reduce the band gap energy, thereby broadening the absorption spectrum into the visible region as a result of the improved charge separation process^[185,201]. In summary, oxygen vacancy defects, when introduced in a controlled manner and at optimal concentrations, can enhance the photocatalytic properties of semiconductor oxides by promoting an efficient charge separation and as well as increasing the absorption of visible light.

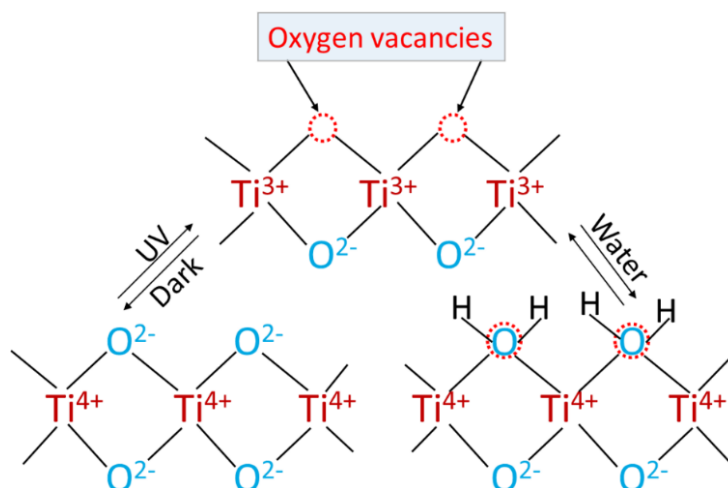


Figure 2.9. Schematic illustration of electron reduction process of Ti^{4+} to Ti^{3+} and creation of oxygen vacancies^[201]

2.7.5. Photocatalytic Thin Films

Thin films have become an integral part of many scientific and technological applications commonly used to improve the physical and chemical properties of materials^[202]. The thin film can be defined as “two-dimensional layers” of a solid material with thicknesses ranging from fractions of a nanometer to several microns^[203]. There are various methods for preparation of thin films, which can be broadly classified into bottom-up and top-down approaches^[204]. Among the various types of thin films, photocatalytic thin films have gained a significant attention due to their potential use in a wide range of applications, such as energy conversion, water-splitting, environmental remediation, self-cleaning, antibacterial/antiviral, and biomedical applications^[205–209]. The most widely studied photocatalysts are TiO_2 and ZnO ,^[186] and various techniques have been developed for the fabrication of these thin films at a commercial scale^[204]. TiO_2 thin films have been particularly well-explored due to their photocatalytic activities and suitability for water treatment and other environmental remediation applications^[192]. However, low surface area-to-volume ratios of thin films impede their chemical reactivity, making it difficult to use them in most photocatalytic applications. Therefore, it is crucial to control the surface morphology, the electronic structure, the crystal size, the thickness of photocatalytic thin films to retain an optimal photocatalytic performance^[210]. One of the most effective ways to enhance the photocatalytic performance of TiO_2 thin films is the modifying their surface with metallic such as Au and Ag nanoparticles (NPs). These metallic NPs can improve the photocatalytic efficiency through the localized surface plasmon resonance (LSPR) effect, which results in an enhanced plasmon resonance and red-shift^[210]. Additionally, metallic NPs can enhance the photocatalytic performance through a non-plasmonic mechanism by functioning as electron sink centers^[207] that enhance the charge separation.

2.7.6. Photocatalytic Decomposition of Pollutants

Photocatalytic decomposition is a promising technology for breaking down pollutants into harmless substances. This process involves the use of photocatalytic materials to decompose pollutants in gas-solid and liquid-solid systems^[190]. The reactions occur at the interface between the photocatalyst and pollutants. Although various photocatalytic materials have been studied for the effective photodecomposition of various pollutants, TiO_2 arguably remains the strongest contender because of its ability to mineralize organic pollutants^[211]. In the following section, the mechanism of photocatalytic reactions at liquid (organic pollutants in wastewater)- TiO_2 interface will be discussed.

2.7.6.1. Mechanism of Photocatalytic Degradation of Organic Pollutants in Wastewater

In **Figure 2.10** the mechanism of the photocatalytic degradation (using TiO_2) of organic pollutants in wastewater is illustrated. The mechanism of the photocatalytic degradation is based on the generation of electron-hole pairs (which are created when the photocatalyst (TiO_2) absorbs light energy). The electrons are excited to a higher energy state, and they become free to participate in chemical reactions as shown in eq.2.14^[184].

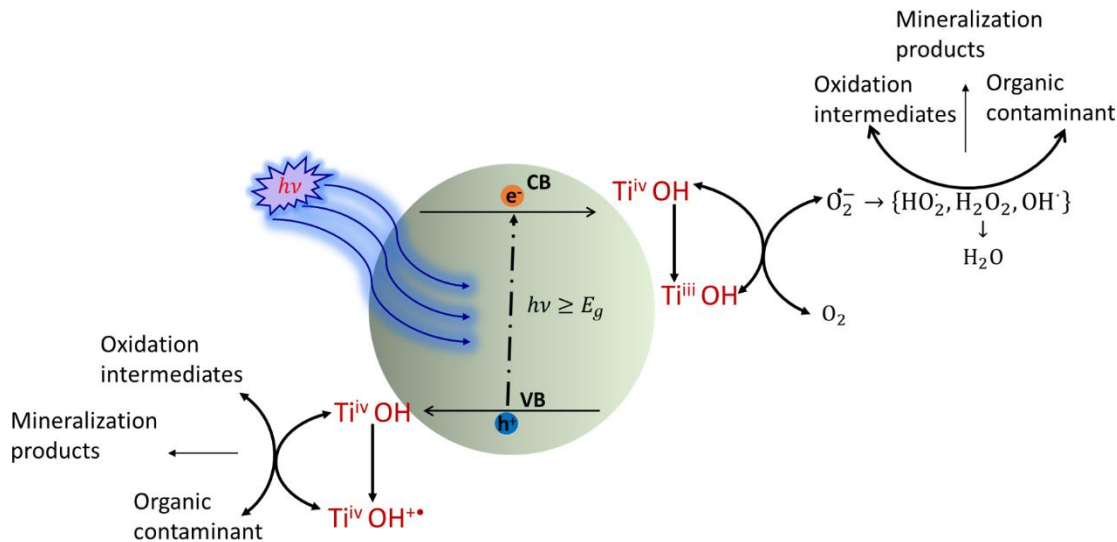
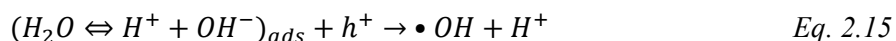


Figure 2.10. Schematic representation of the photocatalytic degradation mechanism^[212]

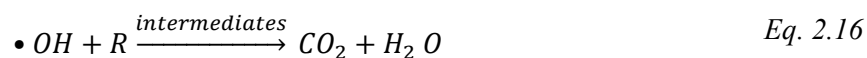
The holes are electron deficiencies in the valence band, and they react with the H_2O molecules to generate hydroxyl radicals ($\bullet\text{OH}$) (Eq.2.15)^[213]. The hydroxyl radicals are transitory species with strong oxidizing potential for decomposing and mineralizing organic molecules into CO_2 , H_2O and inorganic ions because of their electrophilic nature (electron acceptor)^[214](Eq.2.16). On the other hand, the generated e^- at the conduction band interact with the dissolved O_2 to form a superoxide radical ($\bullet\text{O}_2^-$) (Eq.2.17). Continued reaction can produce hydrogen peroxide, leading to the formation of $\bullet\text{OH}$. Therefore, the presence of dissolved oxygen is very crucial during the photocatalytic decomposition since it can reduce the recombination rate in TiO_2 (e^-/h^+) by maintaining the electroneutrality of the TiO_2 ^[215]. So, for the optimum photocatalytic decomposition of organic pollutants, it is important that the reduction process of oxygen and the oxidation of pollutants occur at the same time to avoid the buildup of electrons in the conduction band and therefore reducing the recombination rate of electron-hole pair.



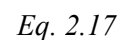
Neutralization of OH^- group into OH by the hole

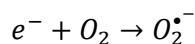


Oxidation of the organic pollutants via successive attack by $\bullet\text{OH}$ radicals



Formation of superoxide radical anion





Typically, the hydroxyl radical ($\bullet\text{OH}$) and the superoxide radical anions ($\text{O}_2^{\bullet -}$) are known to be the primary oxidizing species in the photocatalytic oxidation processes.

2.8. Self- Cleaning Surfaces

A self-cleaning surface has the ability to remove various contaminants, such as dirt, harmful substances, and microbes, through various means. These surfaces are inspired by natural materials like lotus leaves, gecko feet, and water striders^{9,10,159}. The development and understanding of self-cleaning materials have gained a significant attention due to their wide range of potential applications, including fabrics, window glasses, roof tiles, car mirrors, and solar panels^[201]. Self-cleaning surfaces can be broadly categorized into three types: superhydrophobic surfaces, superhydrophilic surfaces, and photocatalytic surfaces. These categories are discussed in the following section.

2.8.1. Self-Cleaning Superhydrophobic Surfaces

Superhydrophobic surfaces are known for their self-cleaning properties, which are attributed to the removal of dirt by the impact or rolling of water droplets. This is due to the low surface energy layer and external forces present on these surfaces^[216]. These surfaces typically have a water CA exceeding 150° , making them ideal for self-cleaning applications. Additionally, superhydrophobic surfaces have a low CA hysteresis, which allows the rolling of water droplets over the surface, thereby collecting dirt and other contaminants^[83]. As shown in **Figure 2.11a**, the rolling motion of droplets over the surface is often accompanied by the adsorption of surface-contaminants at the water-air interface, thereby cleaning the surface. The most widely accepted mechanism for superhydrophobic self-cleaning surfaces is the lotus effect^[83], which is attributed to the micropapillae and the epicuticular wax on the surface of a lotus leaf. These structures have low surface energy and high surface roughness, creating a small CA with low CA hysteresis, making the surface superhydrophobic^[217]. In literature different mechanisms have been proposed for the superhydrophobic self-cleaning^[218], but the Lotus effect is the most accepted and practiced one. The self-cleaning mechanism of the superhydrophobic surfaces relies on the minuscule CA of water droplets with the surface. The attachment and the detachment forces of contaminants also play a significant role in the self-cleaning process^[109]. It is important to note that while superhydrophobic surfaces are effective in removing water-based contaminants, they may not be as effective in removing other types of contaminants, such as oils. In these cases, different surface properties, such as superhydrophilicity, may be required.

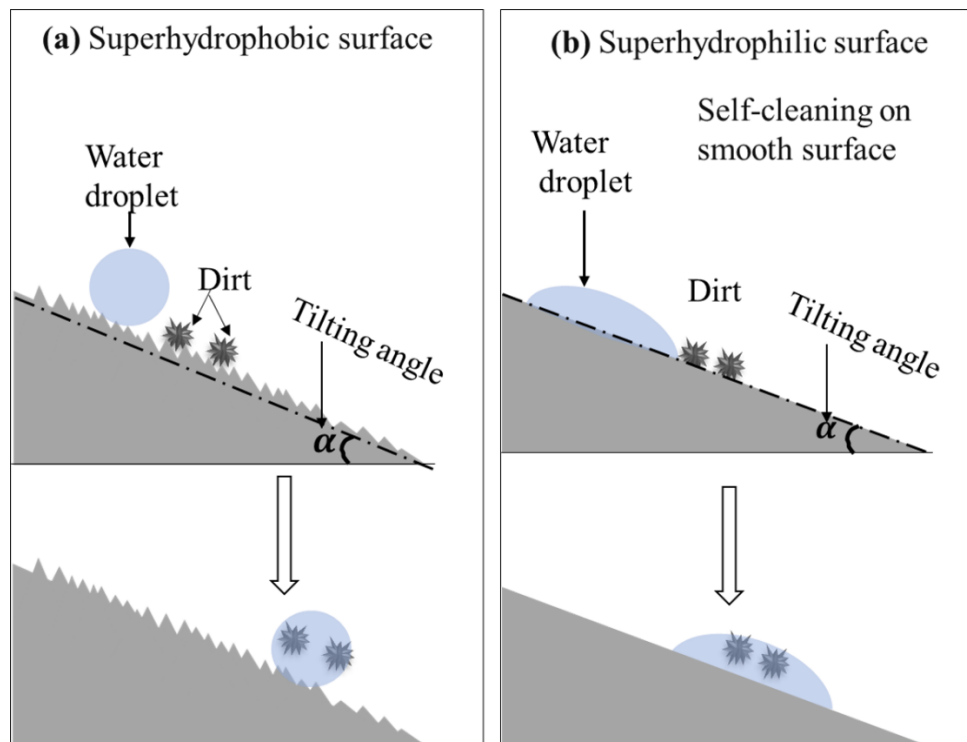


Figure 2.11. Schematic representation of the self-cleaning process on (a) a roughened superhydrophobic and (b) a smoothed superhydrophilic surface (Adopted from ^[219]).

2.8.2. Self-Cleaning Superhydrophilic Surfaces

Superhydrophilic surfaces have the ability to clean themselves by utilizing the flow of water droplets on the surface. Unlike superhydrophobic surfaces, which repel water, superhydrophilic surfaces have an extremely low water CA, causing droplets to spread out and form a film on the surface^[59]. As depicted in **Figure 2.11b**, the flowing film carries the dirt and the debris away from the surface. The effectiveness of this self-cleaning mechanism depends on how quickly the liquid film flows off the surface without forming a bulging front or sticking to the contact lines. In nature, certain living organisms, such as fish, snails, and frogs, have adapted this method on their skin to prevent any contamination from oil while swimming in a mixture of oil and water^[218,220]. By studying the self-cleaning properties of some of these organisms, it is possible to create a superhydrophilic surface that effectively removes the dirt and other contaminants. However, sometimes, these types of surfaces may not be able to tackle organic contaminants such as oil, so a different cleaning method, such as photocatalytic cleaning, may be necessary.

2.8.3. Photocatalytic Self-Cleaning Surfaces

Semiconductor oxide thin films, particularly TiO_2 , have gained significant attention in recent research due to their self-cleaning properties under UV irradiation^[221]. The use of TiO_2 in self-cleaning applications is based on its photocatalytic and photoinduced hydrophilic properties, as well as its transparency in the visible region of the electromagnetic spectrum^[61]. Various mechanisms have been proposed to explain the photoinduced hydrophilicity of TiO_2 surfaces, but they all involve the following three basic assumptions:

- i. the formation of surface defects and water dissociation
- ii. the formation of surface hydroxyl groups
- iii. the photo-oxidation of hydrocarbon layers or carbonaceous species

Under UV irradiation, the TiO₂ surface generates surface oxygen vacancies at the bridging sites, which increases the affinity for hydroxyl ions and forms hydrophilic domains^[222]. However, it is important to note that storing hydrophilic TiO₂ in a dark medium can reverse the wettability. The reconstruction of absorbed -OH groups with oxygen mainly causes the conversion from hydrophilic to hydrophobic states^[223]. Additionally, the influence of relative humidity and the amount of oxygen also play a significant role in the hydrophilic properties of TiO₂^[62].

2.8.4. Photocatalytic Thin Films for Clean-up of Oil-like Organic Molecules

TiO₂ is a promising semiconductor material for the decomposition and clean-up of oily wastewater. Its unique optical, electronic, and catalytic properties make it a highly attractive material for this purpose^[183]. For such applications mostly TiO₂ is used in the form of NPs due to their high surface area-to-volume ratio and photoactive sites^[224]. However, the use of TiO₂ NPs as a slurry in water can be costly and the removal of such NPs will possess a severe problem. Thus, the use of TiO₂ in thin film form can be more suitable for the treatment of oily-wastewater and other environmental applications^[190]. Despite their advantages, TiO₂ thin films have a lower surface area than TiO₂ NPs, which can hinder their efficiency in decomposing organic pollutants. To overcome this limitation, various approaches have been proposed to enhance the surface area of TiO₂ thin films and improve their photocatalytic performance. One of these approaches is to combine the TiO₂ thin films with other semiconductor materials, such as cerium oxide (CeO₂). For example, a study by Veziroglu et al.^[207] utilized a reactive sputtering process to create a CeO₂-TiO₂ hybrid structures, which showed superior photocatalytic activity for the clean-up of oleic acid under UV irradiation. The enhancement in the photocatalytic activity was attributed to the formation of fine CeO₂ nanoclusters at the TiO₂ interface, which suppressed the recombination of electron-hole pairs. Another common approach is to dope TiO₂ thin films with nitrogen (N). Hsu et al.^[225] synthesized nitrogen-doped TiO₂ nanotube (N-TNT) thin films using ZnO nanorods as templates. The authors found that the such N-TNT films had superior photocatalytic activity for the degradation of toluene and 1-hexadecene under visible light irradiation. Additionally, the use of polytetrafluoroethylene (PTFE) TiO₂ nanocomposite films have been proposed as a promising approach for the clean-up of oil-like organic molecules. A study by Kamegawa et al.^[226] showed that PTFE-TiO₂ nanocomposite films have the potential for the environmental remediation of oil pollutants. In addition to the photocatalytic activity of the catalyst, the effectiveness of the photocatalytic clean-up of oil contamination depends on the quantity of catalyst, the oil concentration, and/or the thickness of the oil film on the surface, pH of the media, temperature, and as well as the wavelength, and intensity of the light source^[214].

2.9. Detection of Organic Pollutants

Industry generates a large number of effluents that are frequently released into the environment without a proper treatment. These effluents contain a mixture of organic pollutants such as chlorobenzenes, polychlorobiphenyls, polychlorodibenzofurans, polycyclic aromatic hydrocarbons, pesticides, poly-fluoroalkyl, and plastic compounds^[227]. These pollutants can be found in air, water, soil, and food, and they pose a severe threat to the environment and human health due to their toxic effects, ranging from chronic to acute toxicity^[228]. To monitor the presence of these pollutants in the environment, especially in water and the food chain, there is a need for analytical tools that can detect them at trace levels with a high sensitivity and a precise specificity. There are various conventional techniques, such as gas chromatography, liquid chromatography, mass spectrometry, Fourier transform infrared spectroscopy, atomic absorption spectrophotometry, ultraviolet-visible spectroscopy (UV-Vis), Raman spectroscopy, infrared (IR) spectroscopy, high-performance liquid chromatography (HPLC), and gas chromatography-mass spectrometry (GC-MS), which can be used to detect these pollutants^[72,229]. Each

of these methods has its own advantages and limitations, and the choice of method depends on the specific requirements of the analysis. However, the need for the sample preparation, the technical expertise in handling the devices, and the high acquisition and operating costs have made it difficult to use these techniques for remote monitoring applications.

To address these challenges, chemical sensors based on optical spectroscopic techniques have emerged as a solution^[230]. Optical chemical sensing has shown the most potential in meeting the sensitivity and selectivity requirements. Techniques such as fluorescence, absorption, reflection, refractive index, colorimetry, surface plasmon resonance, and surface-enhanced Raman scattering (SERS) study the optical variation of target organic pollutants from concentration to composition analysis^[72,73]. In recent years, SERS has gained significant attention as the method of choice for detecting organic pollutants in water. Unlike infrared absorption spectroscopy, SERS does not interfere with the vibrational spectrum of water, and the sample preparation method is simple and inexpensive^[231]. The following section provides a brief overview of Raman scattering and the SERS mechanism for detecting organic pollutants in water.

2.9.1. Raman Scattering

Light-matter interactions (in gas, solid, and liquid forms) generally result in two types of scattering: elastic and inelastic, as illustrated in **Figure 2.12**. Elastic scattering, also known as Rayleigh scattering^[232], occurs when the scattered photons have the same energy (frequency and wavelength) as the incident photons but in a different direction. On the other hand, inelastic scattering, called Raman scattering, occurs when the energy of the scattered photons differs from that of the incident photons.

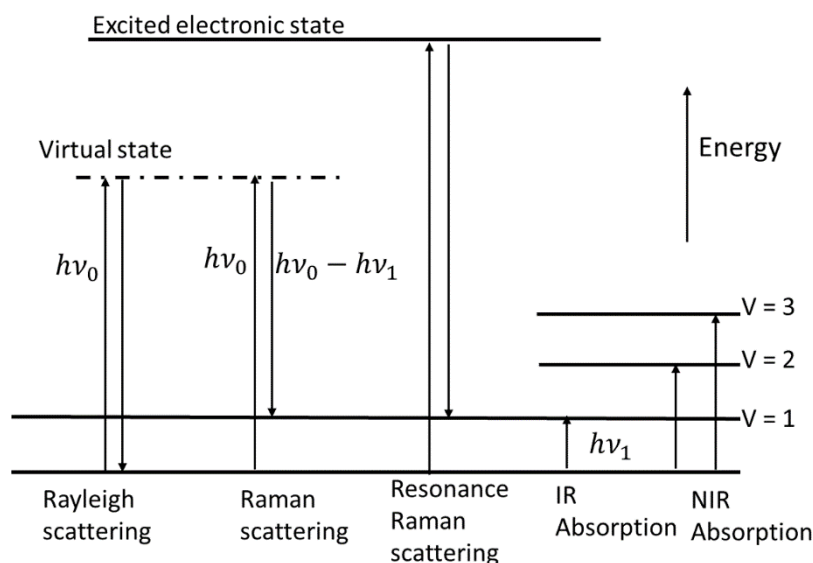


Figure 2.012. Spectroscopic transitions showing different modes of vibrational spectroscopy. ν_0 indicates the laser frequency, while ν is the vibrational quantum number. The virtual state is a short-lived distortion of the electron distribution by the electric field (Adopted from ^[233]).

This phenomenon was discovered by Raman and Krishna in 1928^[234], and the resulting spectroscopic analysis technique is known as Raman spectroscopy. Raman spectroscopy is a highly selective technique that can probe the vibrational energy levels of molecules and distinguish between closely related molecules^[233]. In Raman scattering, the scattered photon has lower energy by an amount equal to a vibrational transition. However, if the molecule is in an excited vibrational state when an incident photon is scattered, the scattered photon can gain energy, resulting in anti-Stokes Raman scattering. The Stokes and anti-Stokes Raman peaks are symmetrical around the Rayleigh peak, but their intensities

differ, especially for low vibrational energies. Infrared (IR) absorption, also known as Fourier transform infrared (FTIR) or mid-IR absorption, also depends on molecular vibrations, as seen in **Figure 2.12**. Although Raman spectroscopy indirectly probes vibrational transitions through light scattering, the Raman shift has the same energy range as the FTIR absorption, and the same energies are often observed. Although the selection rules for Raman scattering and FTIR differ, the chemical information obtained is similar. IR absorption is a more probable event than Raman scattering, with over 90% of incident photons absorbed over a 1 cm path length^[231]. On the other hand, Raman scattering occurs in only about 1 in 10^{10} incident photons^[233]. This weak signal has historically limited the use of Raman spectroscopy for chemical analysis, but it was significantly improved by Fleischmann et al.^[235], who reported an enhancement of the Raman signal by pyridine adsorbed on a silver electrode. The signal amplification mechanism was initially thought to be due to fractal effects (an increase in effective surface area due to roughness), but Moskovits later linked it to localized surface plasmons in nanostructured metals^[236].

2.9.2. Mechanism of SERS

The underlying mechanisms of SERS have been a subject of debate among scientists, but the two most widely accepted explanations are the Electromagnetic Mechanism (EM) and Chemical Mechanism (CM). These were proposed after the initial discovery of SERS on a silver electrode with a rough surface.^[235,237]

2.9.2.1. Electromagnetic Mechanism of SERS

The role of surface plasmons in Surface Enhanced Raman Scattering (SERS) has been well established^[74]. The enhancement of the electromagnetic (EM) field in SERS is linked with the surface plasmon resonance (SPR) induced by metallic nanostructured^[238]. When the light at a particular frequency strikes plasmon-active structures/particles which are much smaller than the wavelength of the incident light, localized surface plasmons are excited. The plasma frequency of the induced vibration, which is the result of the restoring force between the electrons and nuclei, is determined by the inherent properties of the structure/particle, such as its size, shape, and morphology^[239]. As shown in **Figure 2.13a**, localized surface plasmon resonance (LSPR) occurs when the light frequency matches the oscillating frequency of the electrons, resulting in an enhanced electric field near the particle surface^[240].

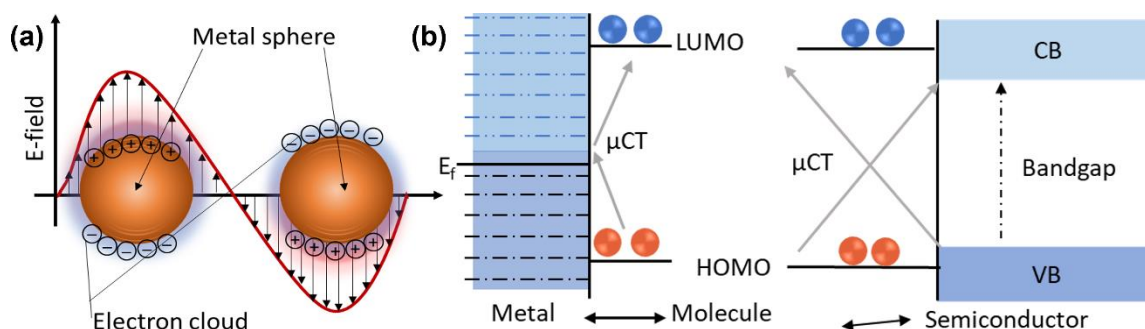


Figure 2.13. Electromagnetic and chemical mechanisms for SERS Enhancement. (a) electromagnetic enhancement in SERS based on plasmonic nanospheres and (b) comparison of the charge-transfer transitions in a metal-molecule system and a semiconductor-molecule system (Adopted from ^[241])

In theory, the bulk plasmon resonance (ω_p) is a function of the free carrier density (N) of the substrate and the effective mass (m^*) of the carriers, which could be either electrons or holes.

$$\omega_p = \left(\frac{4\pi N e^2}{\epsilon_\infty m^*} \right)^{1/2} \quad \text{Eq. 2.58}$$

Usually, N is large (10^{22} - 10^{23} cm^{-3}) in metals, whereas it ranges from 10^{16} to 10^{21} cm^{-3} for doped semiconductors^[242]. In essence, the location of the bulk plasmon resonance is influenced by the properties of the particle and the characteristics of the substrate. Therefore, the concentration of the electromagnetic field between nanoparticles, particularly in structures near the percolation threshold, can amplify the active local incident field on the Raman analyte^[243]. This leads to the re-emitted Raman scattering, typically with an enhancement factor greater than 10^{10} ^[244].

The concept of LSPR enhanced field has been explained using the principles of harmonic oscillator^[245]. In this principle, the light is assumed to be an external driving force for plasmon oscillations near particles, and the resonant elastic light scattering on a metallic NP can increase the local field relative to the incident field. This enhanced electric field is the electromagnetic basis for SERS in plasmonic substrates and involves two consecutive steps: the first step is the local field enhancement near the plasmonic NPs at the resonant incidence frequency (ω_0), and the second step is the enhancement of the Raman scattered light when the Raman frequency overlaps with the plasmon resonance (ω_R)^[246]. When the frequencies of the incident laser light and Stokes Raman scattering in the probe molecule are similar,

the enhancement gains for the two steps are comparable. Therefore, the magnitude of the signal intensity gain is approximately proportional to the fourth power of the field amplitude, as expressed by the equation^[247]:

$$I_M = \frac{[E_{loc}(\omega_0)]^2 [E_{loc}(\omega_R)]^2}{[E_0(\omega_0)]^2 [E_0(\omega_R)]^2} \approx \frac{[E_{loc}(\omega_R)]^4}{[E_0(\omega_0)]^4} \quad \text{Eq. 2.20}$$

Although, this enhancement does not depend on the analyte properties but on the electric field strength in plasmonic metals, which can be tuned by changing the nanostructure morphology, dielectric functions, and plasmonic coupling. In this way, hot-spots can be created between neighboring metallic NPs.

2.9.2.2. Chemical Mechanism of SERS

The chemical enhancement mechanism (CM) of SERS is a complex phenomenon that involves the interaction of the analyte molecules with the substrate surface. Despite ongoing debates among scientists, several models have been proposed to explain CM, including the Charge Transfer (CT) process, polarizability modulation, Fermi level modification, adatoms, bias-voltage enhanced Raman in molecular junctions, and the resonant or resonance-like Raman process^[248-254]. Among these models, the CT resonance between molecular electronic levels and the Fermi level or band edges of the substrate, as well as the creation of a substrate-molecule complex, have been widely studied to better understand CM enhancement^[238,255]. When an analyte molecule is in close proximity to a semiconductor substrate, electrons in the valence band of the substrate are excited to the conduction band or a hot state. This results in the transfer of electrons to the lowest unoccupied molecular orbital (LUMO) level of the molecule, which enhances the molecular polarizability and releases the absorbed energy (see **Figure 2.13b**)^[256]. Thus, this increases the vibrational energy of the molecule and results in the emission of Stokes photons with an enhanced Raman scattering cross-section. The reverse process occurs when electrons in the highest occupied molecular orbital (HOMO) level of the molecule are photoexcited to the LUMO level and transferred back to the initial state. The typical CM enhancement factor is less than 10^3 ^[257], but recent reports have shown that the Raman signal from probe molecules on Au-TiO₂ or/and Ag NP-TiO₂ substrates can be significantly enhanced when the substrate is pre-irradiated with

UV light for a given time^[258]. This new phenomenon, known as Photo-induced Enhanced Raman Spectroscopy (PIERS), is capable of detecting even a single molecule.

2.9.3. Mechanism of PIERS

The mechanism of the PIERS signal in SERS is still a topic of debate among researchers. A few models have been proposed based on the system being studied. Parkin's group proposed that the PIERS enhancement is due to the surface oxygen vacancy states in noble metal-semiconductor metal oxide substrates, which are created by UV irradiation and increase with longer exposure time^[258]. This creates electron donor states and allows the transfer of electrons into the energy levels of metal NPs, leading to enhanced Raman scattering^[258–260] as illustrated in **Figure 2.14**.

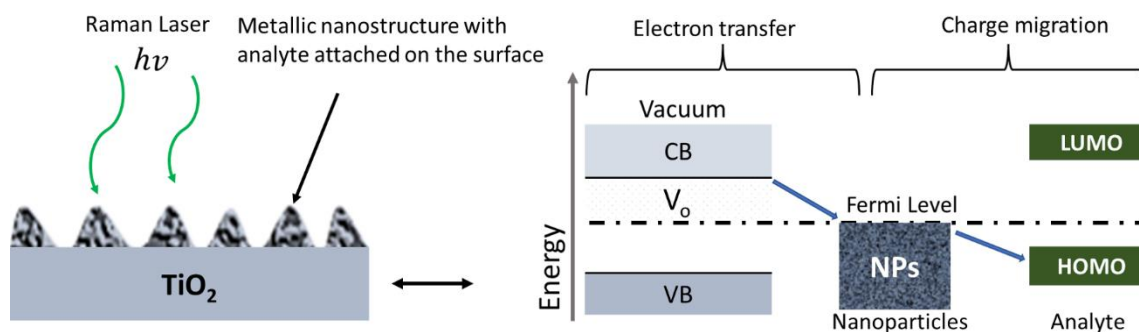


Figure 2.14 Mechanism of PIERS illustrating electron transfer from TiO₂ to NPs and electromagnetic amplification and charge transfer interaction of NPs with the analyte (Adopted from ^[261]).

Hybridizing plasmon-active metals with semiconductor metal oxides enhances the electromagnetic field effect and extend the carrier lifetime, which increases photocatalytic activity^[258,260]. For some semiconductors, such as organic semiconductors^[262] and lithium niobate^[263], the formation of oxygen vacancies is difficult. In these cases, the PIERS enhancement effect can arise from the charge separation and the migration. When the semiconductor is irradiated with a proper light source (at a wavelength matching the band gap), electrons are excited from the valence band to the conduction band and then they can migrate to the energy level of plasmon-active metallic NPs, creating an electric field around the NPs and enhancing the Raman scattering signal. In a recent study, Lidgi-Gigui and colleagues proposed a new PIERS mechanism based on the formation of oxygen vacancies in the depletion region during UV irradiation of Au NPs embedded in TiO₂^[200]. This process leads to width narrowing in the TiO₂ depletion zone and the transfer of electrons from the Ti³⁺ defect site to the Au NPs. Therefore, for PIERS, one can argue that both CM dominated by CT processes and EM can occur simultaneously or sequentially, but this still requires a detailed investigation. In summary, the PIERS mechanism involves a complex interplay of UV light activation, electron transfer, and charge transfer interactions that collectively contribute to the enhanced sensing capabilities of the substrate, which appear to be governed by various factors such as the substrate and the irradiation wavelength, intensity, time and analyte properties.

2.9.3.1. Substrate Effect

The choice of an appropriate substrate is important issue for the performance of PIERS. The substrates are not limited to hybrid noble metallic NPs-Metal-oxide semiconductors but can also include transition metal dichalcogenides^[264], niobates^[262], organic semiconductors^[263], heterostructure metal oxide semiconductors^[260], and insulators^[258]. Substrates are usually designed with a high surface area and easy charge transfer pathway to increase PIERS effects. The substrates can be classified into three groups: hybrid noble metal-TiO₂ (e.g., Au@TiO₂ thin film^[258], Ag@TiO₂ NPs^[265]), metal-supported Si/SiO₂

(e.g., Ag@Si^[263], Au, and Ag@SiO₂ thin film^[262]), and metal-supported ZnO (e.g., Ag and Au@ZnO nanowires^[259]). Other substrates include Ag and Au@diphenylalanine peptide nanotubes^[263], Au@WO₃ film^[266], Au@WS₂ nanosheet^[264], and Ag@LiNbO₃ thin film^[262]. The choice of the substrate determines the contribution of the CM and EM under photo-irradiation.

2.9.3.2. Irradiation Effect

The energy of the incident photons is a crucial factor in determining the outcomes of PIERS measurements, as it influences the excitation of valence electrons and the creation of oxygen vacancies in the semiconductor substrate. The incident photons must have an energy that is equal to or greater than the band gap energy of the substrate for effective excitation to occur. Conversely, if the photon energy is lower than the band gap energy or if the substrate is non-photoactive, the Raman signal may not change even under illumination. It is imperative to regulate the intensity of the light source, particularly for substrates with high photocatalytic activity, to prevent photobleaching of the analytes^[260]. The duration of substrate exposure to the light source also impacts the PIERS signal. However, the exposure time seems to be a material dependent property. For highly photocatalytic substrates, such as Ag-TiO₂, have been shown to have a critical exposure time beyond which the signal decreases^[260]. Therefore, the relationship between the irradiation time and the Raman signal heavily depends on intrinsic properties of the substrate.

2.9.3.3. Relaxation Effect

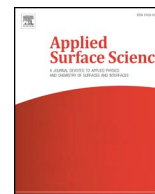
The PIERS relaxation effect refers to a gradual decrease in Raman signal intensity over time following the initial excitation of the substrate. The rate of this decrease can vary among different substrates, with most having a relaxation time of less than an hour. However, some, such as Ag@LiNbO₃ and Au NPs embedded in TiO₂, have been found to have longer relaxation times^[200,262]. This difference may be due to the varying half-life of photoexcited carriers in different substrates, as most metal oxides have a half-life in the picosecond to microsecond range^[267]. The PIERS relaxation effect is not uniform across samples, even those with similar compositions, as it appears to depend on preparation method, chemical properties, and the type of the substrate used. These factors can impact the probability of charge recombination, which affects the half-life of photoexcited carriers.

CHAPTER THREE

This chapter explains a two-step approach for the preparation of hierarchical Au needle clusters (HAuNCs) on highly active TiO₂ thin film. Herein, a systematic study presents tuning the wettability of TiO₂ thin films by the photocatalytic deposition of 3D flower- and hedgehog-like HAuNCs and self-assembled monolayers. In addition, the photocatalytic patterning approach was explored to induce a wettability contrast on the surface (superhydrophobic and superhydrophilic regions).

This chapter is a reprint from the following publication:

J. Shondo, S. Veziroglu, D. Stefan, Y. K. Mishra, T. Strunskus, F. Faupel, O. C. Aktas, *Appl Surf Sci* 2020, 147795.



Tuning wettability of TiO₂ thin film by photocatalytic deposition of 3D flower- and hedgehog-like Au nano- and microstructures



Josiah Shondo^{a,1}, Salih Veziroglu^{a,1}, Dominik Stefan^a, Yogendra Kumar Mishra^b, Thomas Strunskus^a, Franz Faupel^{a,*}, Oral Cenk Aktas^{a,c,*}

^a Chair for Multicomponent Materials, Institute for Materials Science, Faculty of Engineering, Kiel University, Kaiserstr. 2, 24143 Kiel, Germany

^b Mads Clausen Institute, NanoSYD, University of Southern Denmark, Alsion 2, 6400 Sønderborg, Denmark

^c Department of Metallurgical and Materials Engineering, Faculty of Engineering, METU - Middle East Technical University, Çankaya, 06800 Ankara, Turkey

ARTICLE INFO

Keywords:

Photocatalysis
TiO₂
Thin film
Nano- and microstructure
Superhydrophobic
Superhydrophilic

ABSTRACT

We propose a two-steps photocatalytic deposition method to synthesize hierarchical Au nano- and microstructures on TiO₂ surface. While the first deposition leads to the formation of flower-like Au microstructures on a highly active TiO₂ thin film, needle-like sharp Au nanostructures are grown on the former Au microstructures after the second deposition. TiO₂ surface decorated with hierarchical Au structures exhibits a superhydrophilic state with a contact angle (CA) below 5°. After the modification of Au-TiO₂ surface by octadecyl-phosphonic acid (ODP)-self-assembly monolayer (SAM), an extreme water-repellency (with CA > 163°) is achieved which retains its stability even after multiple low-high temperature cycles. The spatially controlled photocatalytic decomposition of OPD-SAM on TiO₂ thin film allows a superhydrophilic-superhydrophobic patterning which may open lot of application avenues in microfluidics, oil-water separation including in water harvesting technologies.

1. Introduction

Superhydrophobic surfaces with water contact angles (CAs) larger than 150° are still in high focus because of their significant technological scopes in self-cleaning surfaces, water treatment, anti-icing surfaces, microfluidics and as well as in advanced medical applications such as anti-thrombosis surfaces for cardiac-implants and devices [1–3]. In some high-end technologies including cell growth, the spotting of biomolecules, fluid microchips and microreactors hydrophobic-hydrophilic patterning of surfaces is strongly needed rather than just attaining only a fully not-wetting state throughout the whole surface [4–6]. In such applications, achieving an extreme wettability contrast with superhydrophobic-superhydrophilic patterns is very much desired and is actually an important and necessary criterion.

Titanium (IV) oxide (TiO₂) is known to exhibit a strong hydrophilic character especially in its photo-excited state, which is referred as photoinduced superhydrophilicity (PSH) [7,8]. Although various diverse mechanisms have been proposed, basically the photogeneration of electron/hole pairs and their migration to the surface play the major role for attaining a strong hydrophilicity. Kume et al. claimed that photocatalytic oxidative removal of organic contaminants by UV light is

the main mechanism behind the PSH on TiO₂ surfaces [9]. Zubkov et al. reported a very detailed and a systematic study which proves the effect of oxidative removal of hydrocarbons on hydrophilicity of TiO₂ surfaces [10]. On the other hand, Wang et al. reported that the dissociative adsorption of water at TiO₂ surface defects by UV light, rather than the oxidative removal of organics, is the main driving force for hydrophilicity [11]. Upon UV irradiation photogenerated electrons and holes are trapped by the surface and O₂⁻ ions present in the medium, leading to formation of Ti³⁺ (by reduction of Ti⁴⁺ sites) and oxygen vacancies (ejection of oxygen atoms), respectively. Oxygen vacancies are thought to accommodate higher amount of hydroxyl groups and this enhances the absorption of water molecules. Following a systematic study, Sakai et al. proposed that the hydrophilic conversion rate depends on the capability of the surface to enable hydroxyl group formation [12].

Actually, this hydrophilic nature of TiO₂ enhances its photocatalytic self-cleaning performance surfaces in outdoor and indoor applications such as self-cleaning windows and walls and as well as anti-fogging mirrors and glasses [13]. TiO₂ self-cleaning mechanism is totally different than that of well-established Lotus leaf effect [14]. The self-cleaning in TiO₂ is basically provided by well spreading of the water on the surface (due to the hydrophilicity) and the subsequent

* Corresponding authors at: Chair for Multicomponent Materials, Institute for Materials Science, Faculty of Engineering, Kiel University, Kaiserstr. 2, 24143 Kiel, Germany (O.C. Aktas).

E-mail addresses: ff@tf.uni-kiel.de (F. Faupel), oca@tf.uni-kiel.de (O.C. Aktas).

¹ Both authors contributed equally.

<https://doi.org/10.1016/j.apsusc.2020.147795>

Received 29 May 2020; Received in revised form 27 July 2020; Accepted 3 September 2020

Available online 07 September 2020

0169-4332/ © 2020 Elsevier B.V. All rights reserved.

photocatalytic decomposition of organic residues. In contrast, in a Lotus leaf, the hydrophobicity of the surface retards getting dirty rather than an active catalytic clean-up [15]. Interestingly, the TiO₂ surfaces can be hydrophobic too by either inducing a special morphology or surface modification by a hydrophobic self-assembled monolayer (SAM) [16,17]. In case of surface topography induced hydrophobicity, the best performance is generally achieved in dark conditions since the light triggers a gradual transition from hydrophobicity into hydrophilicity [18]. The second approach, conformal coating of a rough TiO₂ surface with a low surface energy layer, leads to a rather more stable non-wetting state.

Utilization of octadecyl-phosphonic acid (ODP) as a conformal coating, enables the switchable wettability on TiO₂ thin films, from a hydrophilic state to a hydrophobic state [19]. By modifying the sputter deposited TiO₂ thin film with ODP, Maeda et al. reported a contact angle (CA) of 130° [20]. However, they also reported that depending on the applied light intensity and the photocatalytic performance of underlying TiO₂ layer ODP layer can be photocatalytically decomposed, and the wettability can be switched from the hydrophobic to the hydrophilic state.

Hydrophobicity of ODP-TiO₂ highly depends on the surface roughness and the morphology of the TiO₂ layer. Lai et al. achieved an extreme non-wetting state on TiO₂ by combining electrochemical structuring (anodization) and ODP-SAM modification [21]. They reported that one dimensional (1D) tubular TiO₂ nano- and microstructures lead to a high CA. However, the utilization of the electrochemical anodization approach in their process is unfortunately limited to only metallic titanium substrates. In general, such electrochemical deposition of TiO₂ leads to the formation of a fully amorphous layer which lacks any photocatalytic activity. Alternatively, various dry etching processes such as CF₄ plasma etching have been proposed to structure TiO₂ thin films. In this context, Zhang et al. fabricated anisotropic nanostructures on TiO₂ surface by CF₄ etching and following ODP-SAM modification they observed CAs that exceeded 150° [19]. On the other hand, such energetic etching processes are known to severely damage as well as lead to lot of undesired contaminants. The dry etching may lead to various detrimental effects including residue layers, impurities and hydrogen permeation layers, and bonding damage layers [22].

Recently, we reported a novel method which allows patterning of TiO₂ by sea urchin-like metallic Au structures with sharp needles using photocatalytic reduction of Au³⁺ ions in an appropriate solvent [23]. This enables controlling the size and the geometry of deposited Au structures by simply altering the UV light intensity and irradiation time. Subsequently it was also found that the dielectric constant and the pH of the medium drastically influence the morphology of structures during the process which can range from globular rounded to almost ultra-sharp needle-like structures [24]. Basically, the method is not limited to only Au and it allows patterning of TiO₂ with various types of other metallic ions [25].

Herein, we combine the photocatalytic patterning of highly active TiO₂ thin film with ODP-SAM modification to achieve a superhydrophobic surface. A two-step photocatalytic patterning method is proposed to form hierarchical Au nano- and microstructures on columnar TiO₂ thin film in order to tune the wettability through a wide range (superhydrophilic-superhydrophobic). Robustness of the prepared surface has been tested by heating the sample to 250 °C and cooling it down to -20 °C. By selective exposure to UV light through a mask the prepared surface allows photocatalytic superhydrophobic-superhydrophilic patterning.

2. Materials and methods

2.1. Preparing of TiO₂ thin films

The TiO₂ thin film was deposited by reactive pulsed DC magnetron sputtering from a two-inch Ti target in a custom-built vacuum

deposition chamber [26,27]. Quartz glass and silicon wafer pieces were used as substrates. By combining a rotary pump (Agilent Technologies, SH-110) and a turbo molecular pump (Pfeiffer Vacuum, HiPace 400), a base pressure of 10⁻⁵ Pa was achieved prior to the deposition. Before the deposition, the target (Ti-Goodfellow, 99.99% with a 50 mm diameter) was cleaned in a pure Ar plasma for 15 min followed by a conditioning phase of 5 min with both Ar and O₂ flow. The deposition was conducted at a magnetron output power of 90 W while keeping Ar: O₂ ratio as 250 sccm: 10 sccm by using two separate mass flow controllers (MKS Multi-Gas-Controller 647C). For achieving a homogenous film, the sample holder was rotated during deposition. Following the deposition process the samples were heat treated for 1 h at 650 °C in an oven (Nabertherm, LE 4/11/R6) and subsequently air quenched.

2.2. Photo-deposition of Au clusters on TiO₂ thin films

Au clusters were grown on the TiO₂ thin films by a modified photo-deposition method as reported previously [23,24]. The starting materials, gold chloride (HAuCl₄) and non-ionic surfactant (Triton X-100) were purchased from Alfa Aesar. First prepared TiO₂ thin films were dipped into a quartz cuvette filled with 6.5 mL of an aqueous AuCl₄ (0.8 × 10⁻³ M-Alfa Aesar) solution and 50 µL of Triton X-100. Then, the cuvette was exposed to low-intensity UV light (4.5 mW/cm², UV lamp operated at λ = 365 nm). The exposure time was altered systematically from 30 min to 240 min. After UV illumination, samples were rinsed with deionized water and dried with air to remove any residual solution.

2.3. Preparation of self-assembled monolayer (SAM)

First, octadecylphosphonic acid (Carl Roth GmbH) was dissolved in n-hexane/2-propanol (Carl Roth GmbH) in a 100/0.4 (v/v) solvent mixture at a concentration of 500 µM [19]. Then, the prepared solution was ultrasonicated for 30 min, filtered and stored until use. Au deposited TiO₂ samples were separately immersed in 5 mL of ODP solution for 48 h. Afterwards samples were removed from the solution and washed carefully with isopropyl alcohol and dried with nitrogen. The whole process is schematically presented in Fig. 1.

2.4. Characterization

The surface morphology and structure of prepared samples were investigated by scanning electron microscopy (SEM, Supra55VP-Carl Zeiss). The surface chemistry of samples was analyzed by X-ray photoelectron spectroscopy (XPS, Omicron NanoTechnology GmbH, Al anode, 240 W). CasaXPS software (2.3.13PR1.0) was used to perform quantitative analyses and detailed peak investigation. All the binding energies (BE) were calibrated with reference to the Au 4f line at 84.0 eV of gold on the sample surface. Contact angle (CA) measurements were performed using a semi-automated CA meter (OCA 30, Dataphysics). For static CA measurements, 10 µL of water droplets were used and advancing/receding CAs were videotaped and measured by the addition and subtraction of water to/from droplets sitting on the sample surface.

3. Results and discussions

Before the photocatalytic deposition of Au structures, we showed that sputter deposited TiO₂ film exhibits anatase phase, which is known as the most active TiO₂ phase as shown in Table S1a. Prepared TiO₂ film is composed of nanocrack networks (Fig. S1b) which lead to higher surface area (promoting photocatalytic activity) as we previously presented elsewhere [26,27]. The SEM analysis (following the photocatalytic deposition of Au) depicts the growth and morphology of the deposited Au structures on TiO₂ thin film (Fig. 2) in which a clear difference between typical morphologies achieved by one-step

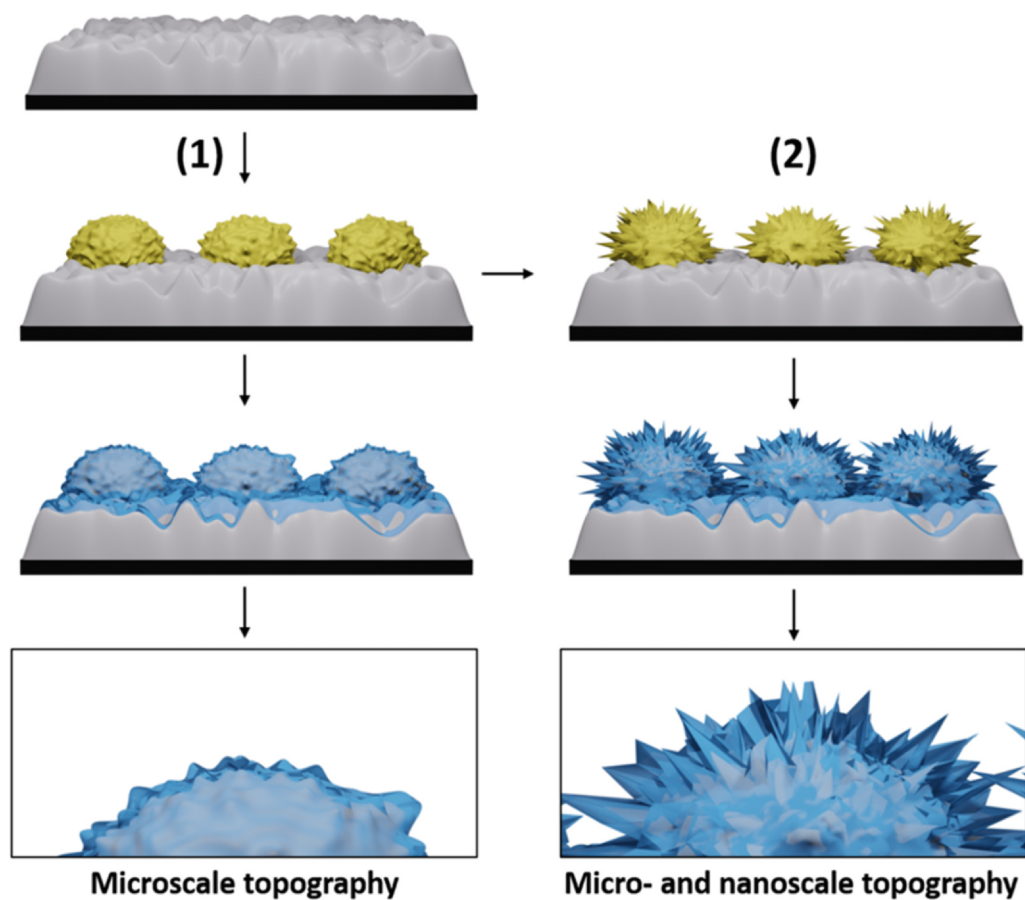


Fig. 1. Schematic representation of photocatalytic Au structuring on TiO₂ thin film: (1) First photocatalytic deposition in HAuCl₄/Triton X-100 mixture forms flower-like Au microstructures and (2) Second photocatalytic deposition in HAuCl₄ forms needle-like sharp Au nanostructures on former flower-like structures. Both types of structures are modified by ODP-SAM (represented by the blue color). (For interpretation of the references to color in this figure legend, the reader is referred to the web version of this article.)

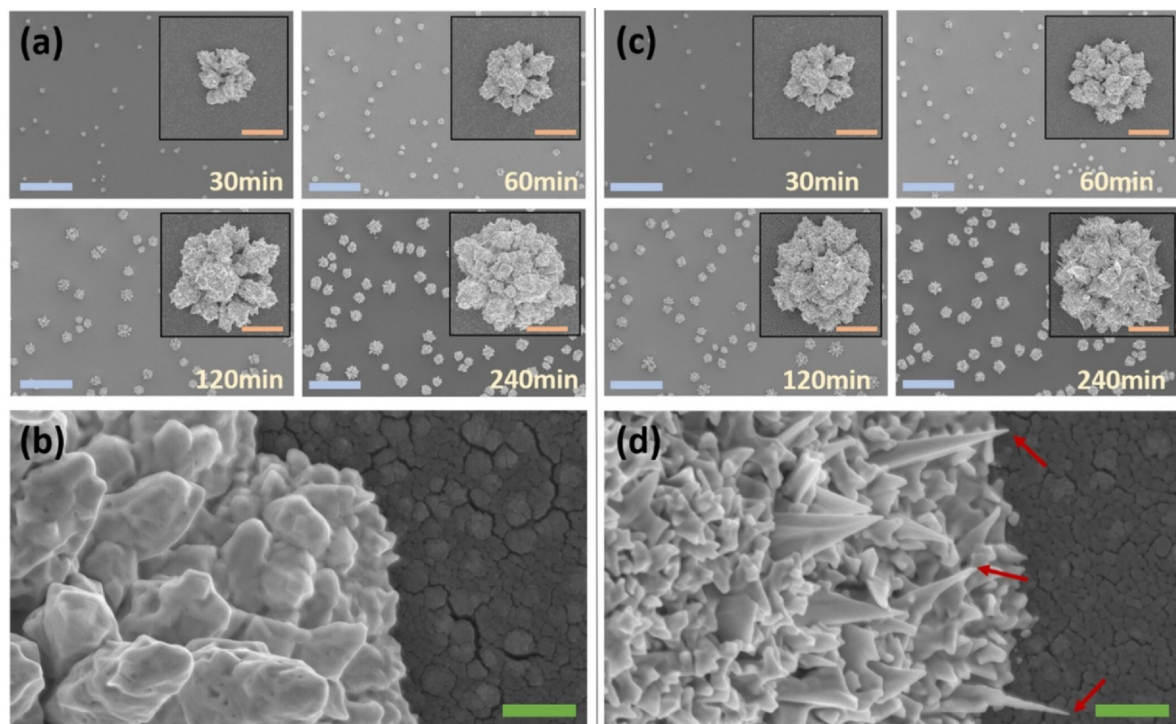


Fig. 2. SEM images of Au structures prepared via one-step photocatalytic deposition: (a) at different deposition periods and (b) single Au cluster at higher magnification. SEM images of Au structures prepared via two-steps photocatalytic deposition: (c) at different deposition periods and (d) single Au cluster at higher magnification. (Blue, orange, and green scale bars represent 50 μm , 3 μm , and 400 nm, respectively.)

deposition and two-steps deposition is visible. In one-step deposition process, a non-ionic surfactant (50 μL TritonX-100) was added to HAuCl_4 solution to control the nucleation of Au clusters and their stabilization on the TiO_2 surface (Fig. 2a). Triton X-100 is a well-known effective stabilizing agent for synthesis of Au and similar metallic nanostructures [28].

It has been shown that the use of HAuCl_4 without any surfactant led to the formation of sharp needle-like structures with a low nucleation rate [23]. In our recent study we have shown that dielectric constant and as well as the acidity of the solvent govern the morphology of photo-deposited Au structures [24]. Here by adding non-ionic surfactant to HAuCl_4 we achieved a higher nucleation rate which is crucial to form densely distributed Au structures on TiO_2 . Afterwards we conducted a second photo deposition step by dipping the Au decorated TiO_2 substrate into HAuCl_4 solution without adding Triton X-100. As it is seen in Fig. 2b sharp needle like structures (indicated by red arrows) were grown on former globular Au structures, which reminds of a hedgehog morphology. It is very likely that Au^{3+} ions were selectively deposited on metallic Au structures rather than forming clusters directly on the TiO_2 surface [23,24,29]. Once a metallic cluster has been deposited at the surface of a semiconductor, it serves as an electron sink and upon UV irradiation electron-hole pairs separate at the metal-semiconductor interface and electrons accumulating in the metal cause further metal reduction and selective growth at the deposition site [30]. This is most likely the mechanism involved in the transformation process of flower-like Au structures into sea-urchin like hierarchical Au structures after second photocatalytic deposition.

The surface analysis results of ODP-SAM modified 240-Au- TiO_2 obtained by XPS are shown in Fig. 3. The wide-scan XPS spectrum confirmed the presence of Ti, O, Au, P and C on the sample surface (Fig. 3a). The Au $4f_{7/2}$ line of the Au on the surface was used for charge

correction and set to 84.0 eV, the value for bulk gold. Note, that all substrate line can be shifted by the interaction with ODP adsorbate, but also the ODP adsorbate lines have been found to depend on the actual substrate [28]. Thus, using the Au $4f_{7/2}$ line appeared to be the most rational choice. Thus the Au $4f_{7/2}$ and Au $4f_{5/2}$ doublet appears at 84.0 eV and 87.7 eV [31] as shown in Fig. S2a. The Ti 2p doublet with the Ti $2p_{3/2}$ (459.2 eV) and Ti $2p_{1/2}$ (465.0 eV) lines arising from spin orbit-splitting shows the binding energy typical for TiO_2 (Fig. S2b) [24]. This is the same binding energy as we have observed previously for the bare Au/ TiO_2 system [24]. The slight shift to higher binding energy observed for the Ti $2p_{3/2}$ line compared to a more commonly observed value for TiO_2 (458.8 eV) could indicate the absence of Ti^{3+} defect states that can be induced by the adsorbate [25,29]. The O 1s spectrum exhibits an asymmetric shape with a broader base stretching in the direction of higher binding energies. It was fitted with four main peaks which may correspond to the lattice oxygen (530.7 eV), the P-O-Ti oxygen at 531.4 eV, the phosphate oxygen (532.8 eV) and hydroxyl oxygen (533.5 eV) as shown in Fig. 3b [32,33]. This result is consistent with the typical strong covalent bonding of the ODP to the TiO_2 [33]. The C 1s line is deconvoluted into three components including C-C (285.2 eV) of the ODP backbone, C-O-P (286.8 eV) of the ODP headgroup, and C=O (287.6 eV) revealing the presence of a small fraction of oxidized carbon atoms as shown in Fig. 3c [34-36].

In contrast to a typical P 2p spectrum, we observed a broad P 2p peak with a relatively low signal-to-noise ratio. P $2p_{3/2}$ and P $2p_{1/2}$ doublet was fitted with a fixed energy difference of 0.9 eV and a ratio of 2:1 [33,37]. We resolved P 2p spectrum into two doublets as shown in (Fig. 3d) because it could not be fitted with just one doublet. The main components P $2p_{3/2}$ and P $2p_{1/2}$ at 133.3 eV and 134.2 eV can be attributed to the head groups of the ODP adsorbed on TiO_2 [33]. The assignment for the second doublet with P $2p_{3/2}$ and P $2p_{1/2}$ at 134.7 eV

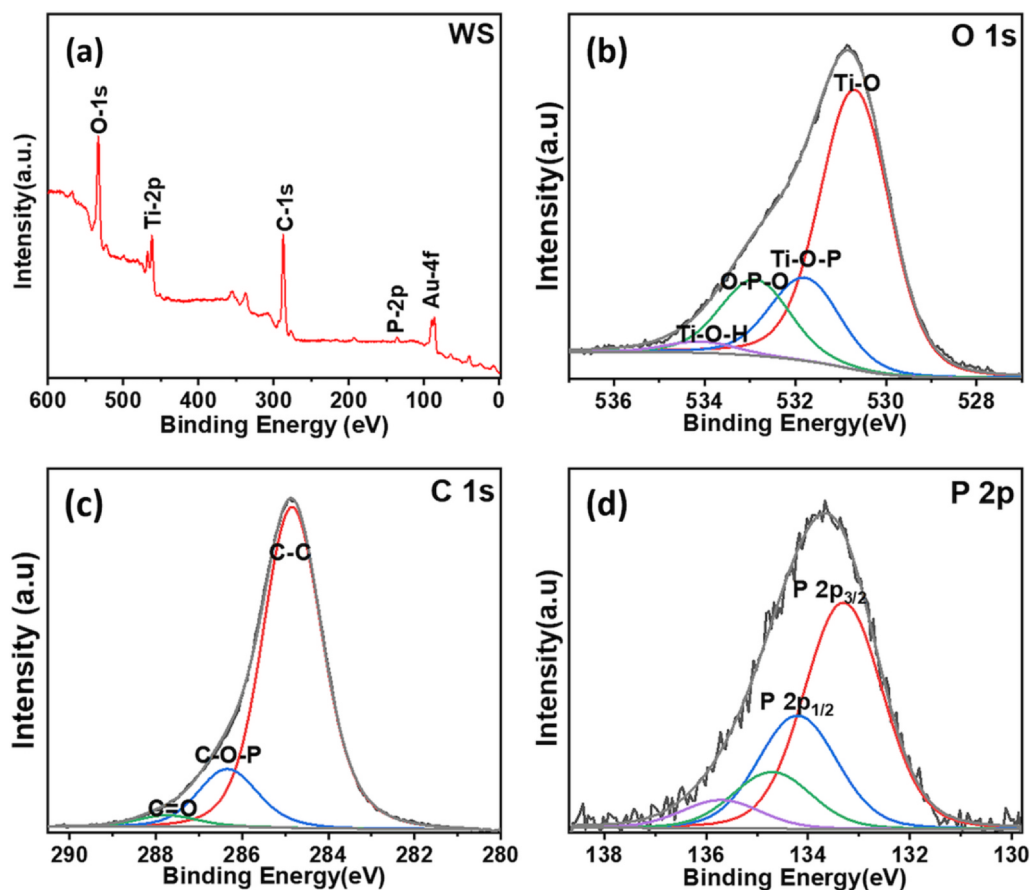


Fig. 3. (a) Wide scan and high-resolution XPS spectra of (b) O 1s, (c) C 1s, and (d) P 2p.

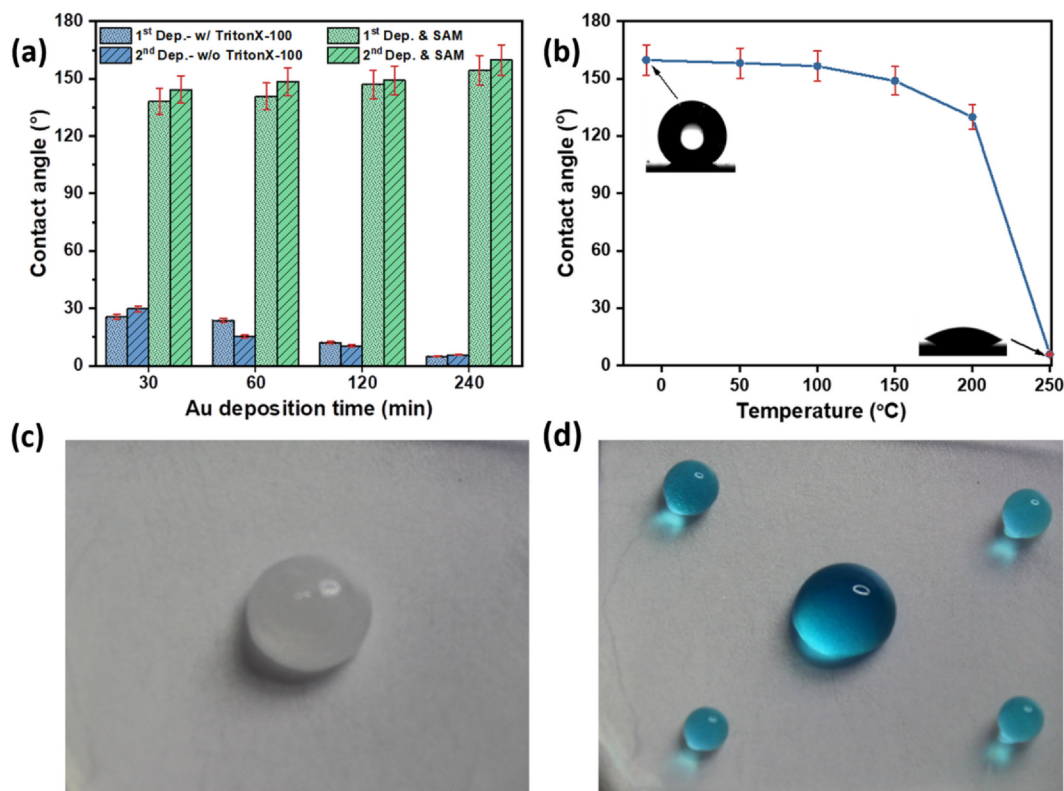


Fig. 4. (a) Water CA analysis of prepared samples (w/: with and w/o: without) (b) Stability analysis of CA against temperature, (c) Anti-icing effect of the prepared surface and (d) Stability of non-wetting state after freezing/de-freezing cycle of ODP-SAM modified 240-Au-TiO₂.

and 135.6 eV is not so clear. It may be assigned to ODP at another adsorption site, perhaps near or on the Au nanostructures or to physisorbed ODP [36].

XPS quantitative analysis revealed an atomic ratio (C:P) of 22.8, which is slightly above the theoretical value (C:P = 18). A slightly higher value is expected, because in the quantitative analysis homogeneous distribution of the atoms has been assumed, and thus attenuation of the phosphorous atoms by the long carbon tail has been neglected. But also, a small amount of additional adsorbed carbon cannot be excluded which may arise as the consequence of exposing samples to the atmosphere.

The XPS results are consistent with previous observations that TiO₂ with oxygen vacancies is known to improve the oxo-titanium cluster formation with phosphonate anionic moiety thereby promoting a strong covalent bond between the metal oxide and the ODP-SAM [38]. Such an interaction of PO₃⁻ ions on the 240-Au-TiO₂ surface might enhance the bonding of C–O–P–O with an outward hydrocarbon tail (octadecyl).

TiO₂ is known to exhibit an intrinsic hydrophilicity such that the water CA on a smooth TiO₂ layer is 72–74°. As shown in Fig. 4a, prepared Au-TiO₂ surfaces showed significantly lower CAs as expected. While a CA of 30° was achieved after 30 min Au deposition (30-Au-TiO₂), we observed a CA below 5° following a longer deposition period (240-Au-TiO₂). Nanoscale features of needle-like sharp Au structures seem to foster the wetting. Briefly, inducing secondary topography (needle-like sharp structures induced by the 2nd photocatalytic deposition) led to lower CAs in all cases. After ODP-SAM modification, we observed a clear transition from hydrophilic to hydrophobic state. While 240-Au-TiO₂ surface, which composed of globular Au structures (after 1st photocatalytic deposition cycle), showed a CA of 147°, adding the needle-like sharp structures (after 2nd photocatalytic deposition cycle) on these former structures led to a significant increase in CA (> 163°). We tested the stability of ODP-SAM modified 240-Au-TiO₂ surface against the temperature by gradually heating it to 250 °C (Fig. 4b). The prepared sample kept its superhydrophobic state till

150 °C and after 250 °C there is sharp decrease in the water CA which may indicate the decomposition of ODP-SAM. This is in agreement with the XPS analysis conducted before and after heating the sample to 150 °C for 30 min. In XPS spectra no significant change in the binding energies of C-1s, O-1s and P-2p was observed (Fig. S3).

It is known that in addition to their extraordinary water-repellency, superhydrophobic surfaces are also used to reduce the accumulation of the snow and the ice and to even completely prevent the formation of ice on solid surfaces. At first, we attached 50 µL water droplet on the prepared surface and put the sample in freezer (-20 °C) for 2 h. We observed that droplet kept its globular form after freezing (Fig. 4c); this prevents the adhesion on the surface and makes it easy to remove (anti-freezing effect). Afterwards the prepared sample was fully coated with water (dipping into a Petri dish) and then put into a freezer. After two hours the sample was taken out and the thin ice layer was removed manually. We observed that the sample still exhibited a clear non-wetting state as shown in Fig. 4d. This procedure was repeated for 3 cycles and we did not observe any significant change in CA (Video S1).

In order to create superhydrophilic-superhydrophobic patterns on ODP-SAM modified 240-Au-TiO₂, we remove the ODP-SAM partially from the surface by photocatalytic decomposition [6]. First, we prepared a simple mask in the form of the official logo of Technical Faculty, Kiel University, which is basically made of t and f letters. Then through this mask we exposed ODP-SAM modified 240-Au-TiO₂ surface to the UV light (at a wavelength of 365 nm and a fluence of 4.5 mW/cm²) for 20 min, as shown in Fig. 5a. The UV source was held directly over the patterned mask at an angle of ~90°. The distance between the UV light source and the sample was kept around 20 mm. The mask was not directly placed on the sample rather it was held slightly above the sample surface with alligator clip to avoid any distortion on the surface. After removing the mask superhydrophilic patterns (t and f letters) were achieved on a superhydrophobic surface as shown in Fig. 5b and Video S2. As one sees that the surface (e.g. at the four corners) which was not exposed to UV light exhibited a clear non-wetting state. This gives rise

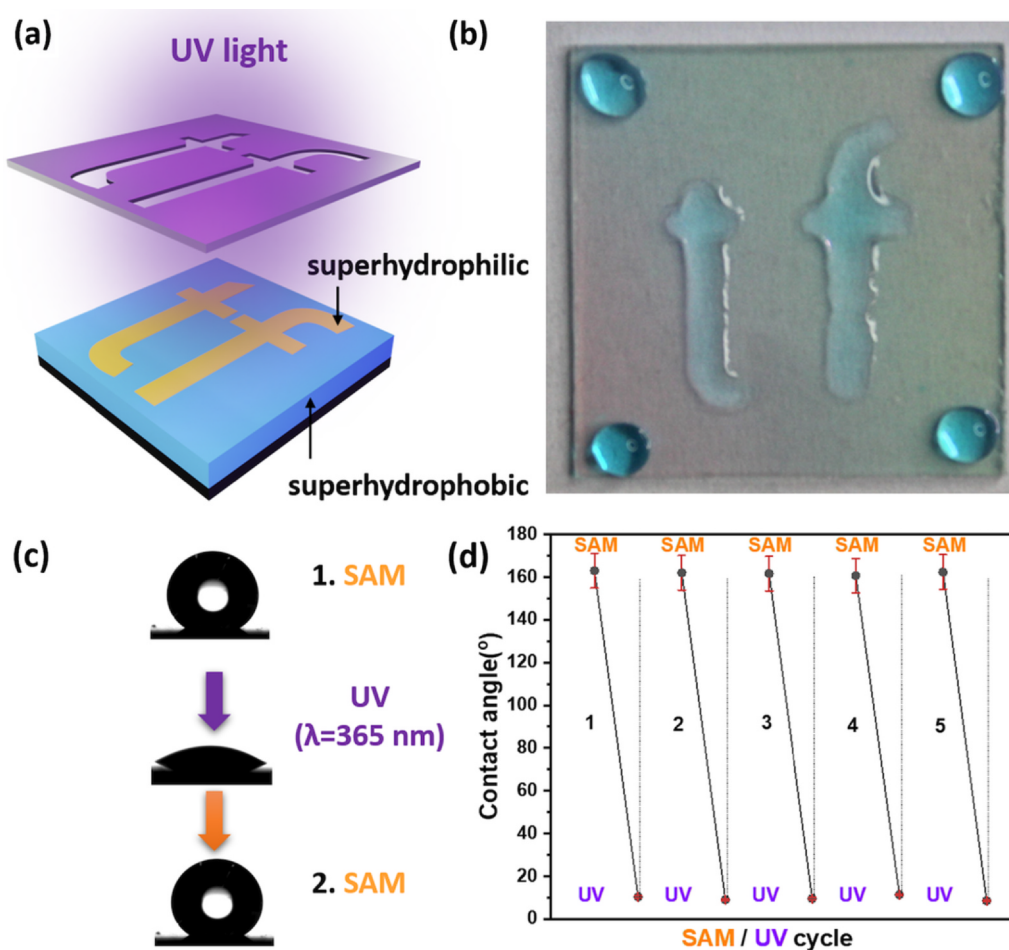


Fig. 5. (a) Schematic representation of superhydrophilic-superhydrophobic patterning by UV light through the mask, (b) Superhydrophilic-superhydrophobic patterning on 240-Au-TiO₂ (*t* and *f* letters), (c) Water CA images showing superhydrophobic-superhydrophilic conversion by ODP-SAM modification and UV illumination and (d) Repeated superhydrophobic-superhydrophilic conversion cycles by alternating ODP-SAM modification and UV illumination.

to a high wetting contrast to areas exposed to UV light. Such superhydrophilic-superhydrophobic patterns can be applied in microfluidics, oil-water separation and probably water harvesting.

Under UV irradiation, the Au decorated TiO₂ surface can degrade the ODP-SAM as a result of its high photocatalytic activity. Fig. 5c shows the change of the water CA of an ODP-SAM modified 240-Au-TiO₂ surface during UV illumination. This indicates an exciting UV-responsive wettability control on superhydrophobic ODP-SAM modified Au-TiO₂ surface. We observed that by dipping the ODP-SAM modified 240-Au-TiO₂ surface after exposing to UV into the ODP solution led to the recovery of the superhydrophobic state as a result of re-chemisorption of the ODP monolayer. The UV treatment-chemisorption cycle was repeated 5 times and we did not observe a significant change in water CA shown in Fig. 5d. This cyclic proven reproducibility allows multiple-step superhydrophilic-superhydrophobic patterning (for complicated structures) and on/off type water-repellency.

4. Conclusion

In conclusion, we demonstrated to fabricate hierarchical Au structures by a two-step photocatalytic reduction of Au³⁺ ions on TiO₂ film. While the first photocatalytic deposition in a mixture of HAuCl₄ and non-ionic surfactant led to the formation of flower-like Au microstructures on TiO₂, second photocatalytic deposition within a highly acidic HAuCl₄ solution triggered the growth of needle-like sharp Au nanostructures selectively on former Au microstructures. Such a dual-scale topography on TiO₂ enhanced the hydrophilicity significantly. We

tuned superhydrophobic state of the same surface to superhydrophilic state by modifying it with ODP-SAM. Prepared surface stays stable under extreme temperature conditions and therefore it can be applied for harsh outdoor applications including anti-icing. In addition, photocatalytic nature of Au-TiO₂ layer allows superhydrophilic -superhydrophobic patterning, which may find applications in cell growth technologies, spotting of biomolecules, fluid microchips and micro-reactors.

CRediT authorship contribution statement

Josiah Shondo: Methodology, Formal analysis, Investigation, Writing - original draft. **Salih Veziroglu:** Formal analysis, Investigation, Visualization, Writing - original draft. **Dominik Stefan:** Data curation. **Yogendra Kumar Mishra:** Validation. **Thomas Strunskus:** Validation. **Franz Faupel:** Conceptualization, Supervision, Writing - review & editing. **Oral Cenk Aktas:** Conceptualization, Supervision, Writing - original draft, Writing - review & editing.

Declaration of Competing Interest

The authors declare that they have no known competing financial interests or personal relationships that could have appeared to influence the work reported in this paper.

Acknowledgements

J. Shondo thanks DAAD (Deutscher Akademischer Austauschdienst) and PTFD (Petroleum Technology Development Fund) for funding for his doctoral studies. Authors thank to NanoBMT Co. Ltd. for assisting surface wetting analysis.

Appendix A. Supplementary material

Supplementary data to this article can be found online at <https://doi.org/10.1016/j.apsusc.2020.147795>.

References

- [1] A.A. Ali, A. Haidar, O. Polonskyi, F. Faupel, H. Abdul-Khaliq, M. Veith, O.C. Aktas, Extreme tuning of wetting on 1D nanostructures: from a superhydrophilic to a perfect hydrophobic surface, *Nanoscale* 9 (2017) 14814–14819.
- [2] M. Zhang, C. Wang, S. Wang, J. Li, Fabrication of superhydrophobic cotton textiles for water-oil separation based on drop-coating route, *Carbohydr. Polym.* 97 (2013) 59–64.
- [3] A. Haidar, A.A. Ali, S. Veziroglu, J. Fiutowski, H. Eichler, I. Müller, K. Kiefer, F. Faupel, M. Bischoff, M. Veith, O.C. Aktas, H. Abdul-Khaliq, PTfEP-Al₂O₃ hybrid nanowires reducing thrombosis and biofouling, *Nanoscale Adv.* 1 (2019) 4659–4664.
- [4] J.-L. Liu, X.-Q. Feng, G. Wang, S.-W. Yu, Mechanisms of superhydrophobicity on hydrophilic substrates, *J. Phys.: Condens. Matter* 19 (2007) 356002.
- [5] A. Ghosh, R. Ganguly, T.M. Schutzius, C.M. Megaridis, Wettability patterning for high-rate pumpless fluid transport on open non-planar microfluidic platforms, *Lab Chip* 14 (2014) 1538–1550.
- [6] D. Zahner, J. Abagat, F. Svec, J.M.J. Fréchet, P.A. Levkin, A facile approach to superhydrophilic-superhydrophobic patterns in porous polymer films, *Adv. Mater.* 23 (2011) 3030–3034.
- [7] M. Takeuchi, K. Sakamoto, G. Martra, S. Coluccia, M. Anpo, Mechanism of photo-induced superhydrophilicity on the TiO₂ photocatalyst surface, *J. Phys. Chem. B* 109 (2005) 15422–15428.
- [8] A. Mills, M. Crow, A study of factors that change the wettability of titania films, *Int. J. Photoenergy* 2008 (2008) 1–6.
- [9] S. Kume T. Nozu Difficult stainable glass product application J. P. Patent Office Sho 63-100042 1988.
- [10] T. Zubkov, D. Stahl, T.L. Thompson, D. Panayotov, O. Diwald, J.T. Yates, Ultraviolet light-induced hydrophilicity effect on TiO₂ (110)(1 × 1). Dominant role of the photooxidation of adsorbed hydrocarbons causing wetting by water droplets, *J. Phys. Chem. B* 109 (2005) 15454–15462.
- [11] R. Wang, K. Hashimoto, A. Fujishima, M. Chikuni, E. Kojima, A. Kitamura, M. Shimohigoshi, T. Watanabe, Light-induced amphiphilic surfaces, *Nature* 388 (1997) 431–432.
- [12] N. Sakai, A. Fujishima, T. Watanabe, K. Hashimoto, Quantitative evaluation of the photoinduced hydrophilic conversion properties of TiO₂ thin film surfaces by the reciprocal of contact angle, *J. Phys. Chem. B* 107 (2003) 1028–1035.
- [13] S. Veziroglu, K. Röder, O. Gronenberg, A. Vahl, O. Polonskyi, T. Strunskus, H.-G. Rubahn, L. Kienle, J. Adam, J. Fiutowski, F. Faupel, O.C. Aktas, Cauliflower-like CeO₂-TiO₂ hybrid nanostructures with extreme photocatalytic and self-cleaning properties, *Nanoscale* 11 (2019) 9840–9844.
- [14] S. Nishimoto, B. Bhushan, Bioinspired self-cleaning surfaces with superhydrophobicity superoleophobicity and superhydrophilicity, *RSC Adv.* 3 (2013) 671–690.
- [15] J. Schneider, M. Matsuoka, M. Takeuchi, J. Zhang, Y. Horiuchi, M. Anpo, D.W. Bahnemann, Understanding TiO₂ photocatalysis: mechanisms and materials, *Chem. Rev.* 114 (2014) 9919–9986.
- [16] X. Feng, J. Zhai, L. Jiang, The fabrication and switchable superhydrophobicity of TiO₂ nanorod films, *Angew. Chem.* 117 (2005) 5245–5248.
- [17] X. Zhang, H. Kono, Z. Liu, S. Nishimoto, D.A. Tryk, T. Murakami, H. Sakai, M. Abe, A. Fujishima, A transparent and photo-patternable superhydrophobic film, *Chem. Commun.* (2007) 4949–4951.
- [18] X. Kong, Y. Hu, X. Wang, W. Pan, Effect of surface morphology on wettability conversion, *J. Adv. Ceram.* 5 (2016) 284–290.
- [19] X. Zhang, M. Jin, Z. Liu, D.A. Tryk, S. Nishimoto, T. Murakami, A. Fujishima, Superhydrophobic TiO₂ surfaces: Preparation photocatalytic wettability conversion and superhydrophobic-superhydrophilic patterning, *J. Phys. Chem. C* 111 (2007) 14521–14529.
- [20] H. Maeda, T. Kobayashi, S. Konishi, Patterning of wettability using the photocatalytic decomposition of hydrophobic self-assembled monolayer on the TiO₂ 2 pattern Jpn, *J. Appl. Phys.* 56 (2017) 06GN09.
- [21] Y. Lai, C. Lin, H. Wang, J. Huang, H. Zhuang, L. Sun, Superhydrophilic-superhydrophobic micropattern on TiO₂ nanotube films by photocatalytic lithography, *Electrochem. Commun.* 10 (2008) 387–391.
- [22] S.J. Fonash, ChemInform abstract: an overview of dry etching damage and contamination effects, *ChemInform.* 22 (2010).
- [23] S. Veziroglu, M.Z. Ghorri, M. Kamp, L. Kienle, H.G. Rubahn, T. Strunskus, J. Fiutowski, J. Adam, F. Faupel, O.C. Aktas, Photocatalytic growth of hierarchical Au needle clusters on highly active TiO₂ thin film, *Adv. Mater. Interfaces* 5 (2018) 1800465.
- [24] S. Veziroglu, A.-L. Obermann, M. Ullrich, M. Hussain, M. Kamp, L. Kienle, T. Leißner, H.-G. Rubahn, O. Polonskyi, T. Strunskus, J. Fiutowski, M. Es-Souni, J. Adam, F. Faupel, O.C. Aktas, Photodeposition of Au nanoclusters for enhanced photocatalytic dye degradation over TiO₂ thin film, *ACS Appl. Mater. Interfaces* 12 (2020) 14983–14992.
- [25] S. Veziroglu, M.Z. Ghorri, A.L. Obermann, K. Röder, O. Polonskyi, T. Strunskus, F. Faupel, O.C. Aktas, Ag nanoparticles decorated TiO₂ thin films with enhanced photocatalytic activity, *Phys. Status Solidi Appl. Mater. Sci.* 216 (2019) 1–6.
- [26] M.Z. Ghorri, S. Veziroglu, B. Henkel, A. Vahl, O. Polonskyi, T. Strunskus, F. Faupel, O.C. Aktas, A comparative study of photocatalysis on highly active columnar TiO₂ nanostructures in-air and in-solution, *Sol. Energy Mater. Sol. Cells* 178 (2018) 170–178.
- [27] A. Vahl, S. Veziroglu, B. Henkel, T. Strunskus, O. Polonskyi, O.C. Aktas, F. Faupel, Pathways to tailor photocatalytic performance of TiO₂ thin films deposited by reactive magnetron sputtering, *Materials (Basel)* 12 (2019) 2840.
- [28] T. Ahmad, I.A. Wani, J. Ahmed, O.A. Al-Hartomy, Effect of gold ion concentration on size and properties of gold nanoparticles in TritonX-100 based inverse micro-emulsions, *Appl. Nanosci.* 4 (2014) 491–498.
- [29] J. Kim, Conformal Titanil phosphate surface passivation for enhancing photocatalytic activity, *Appl. Sci.* 8 (2018) 1402.
- [30] J.F.S. Fernando, M.P. Shortell, C.J. Noble, J.R. Harmer, E.A. Jaatinen, E.R. Waclawik, Controlling Au photodeposition on large ZnO nanoparticles, *ACS Appl. Mater. Interfaces* 8 (2016) 14271–14283.
- [31] A. Zwijnenburg, A. Goossens, W.G. Sloof, M.W.J. Crajé, A.M. Van, L.J. der Kraan, M. De Jongh, J.A. Makkee, Mouljin XPS and Mössbauer characterization of Au/TiO₂ propene epoxidation catalysts, *J. Phys. Chem. B* 106 (2002) 9853–9862.
- [32] M.C. Biesinger, L.W.M. Lau, A.R. Gerson, R.S.C. Smart, Resolving surface chemical states in XPS analysis of first row transition metals oxides and hydroxides: Sc Ti V Cu and Zn, *Appl. Surf. Sci.* 257 (2010) 887–898.
- [33] D.M. Spori, N.V. Venkataraman, S.G.P. Tosatti, F. Durmaz, N.D. Spencer, S. Zürcher, Influence of alkyl chain length on phosphate self-assembled monolayers, *Langmuir* (2007).
- [34] N.S. McIntyre, H.Y. Nie, A.P. Grosvenor, R.D. Davidson, D. Briggs, XPS studies of octadecylphosphonic acid (OPA) monolayer interactions with some metal and mineral surfaces, *Surf. Interface Anal.* 37 (2005) 749–754.
- [35] G. Tizazu, A.M. Adawi, G.J. Leggett, D.G. Lidzey, Photopatterning etching and derivatization of self-assembled monolayers of phosphonic acids on the native oxide of titanium, *Langmuir* 25 (2009) 10746–10753.
- [36] M. Textor, L. Ruiz, R. Hofer, A. Rossi, K. Feldman, G. Hähner, N.D. Spencer, Structural chemistry of self-assembled monolayers of octadecylphosphoric acid on tantalum oxide surfaces, *Langmuir* 16 (2000) 3257–3271.
- [37] M. Pramanik, V. Malgras, J. Lin, S.M. Alshehri, T. Ahamad, J.H. Kim, Y. Yamauchi, Electrochemical property of mesoporous crystalline iron phosphonate anode in lithium rechargeable battery, *J. Nanosci. Nanotechnol.* 16 (2016) 9180–9185.
- [38] W. Hua, P. Kar, P. Roy, L. Bu, L. Shoute, P. Kumar, K. Shankar, Resistance of superhydrophobic surface-functionalized TiO₂ nanotubes to corrosion and intense cavitation, *Nanomaterials* 8 (2018) 783.

Supplementary Information

Tuning wettability of TiO₂ thin film by photocatalytic deposition of 3D flower-and hedgehog-like Au nano- and microstructures

Josiah Shondo,^{a†} Salih Veziroglu,^{a†} Dominik Stefan,^a Yogendra Kumar Mishra,^b Thomas Strunskus,^a
Franz Faupel,^{a*} and Oral Cenk Aktas,^{a,c*}

^a Chair for Multicomponent Materials, Institute of Materials Science, Faculty of Engineering, Kiel University, Kaiserstr. 2, 24143 Kiel, Germany

^b Mads Clausen Institute, NanoSYD, University of Southern Denmark, Alision 2, 6400 Sønderborg, Denmark

^c Department of Metallurgical and Materials Engineering, Faculty of Engineering, METU - Middle East Technical University, Çankaya, 06800 Ankara, Turkey

†Both authors contributed equally.

*Corresponding authors: ff@tf.uni-kiel.de, oca@tf.uni-kiel.de

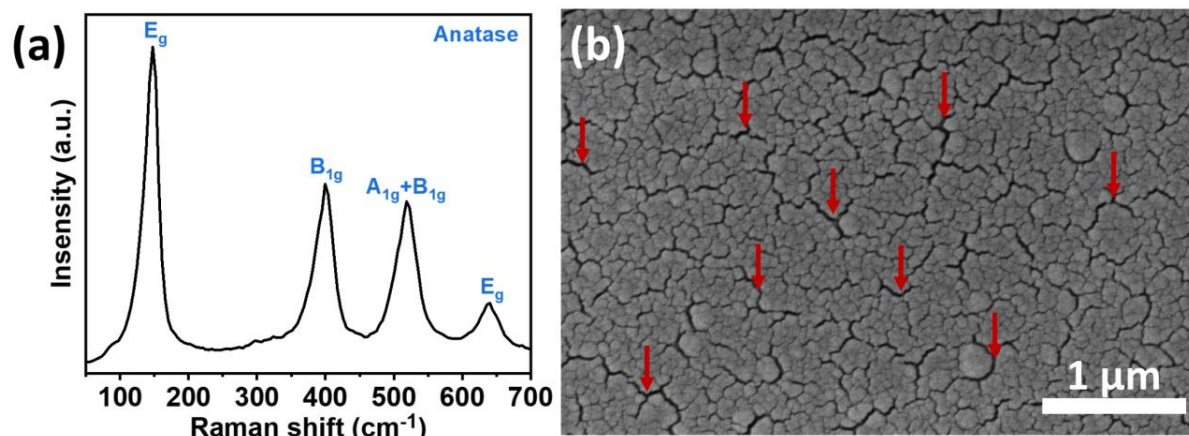


Figure S1. (a) Raman spectra of TiO₂ thin films (which matches with ref. [1,2]) and (b) SEM image of TiO₂ thin film showing its morphology and nanocrack formation. (Red arrows represent the nanocrack formation on the TiO₂ thin film surface).

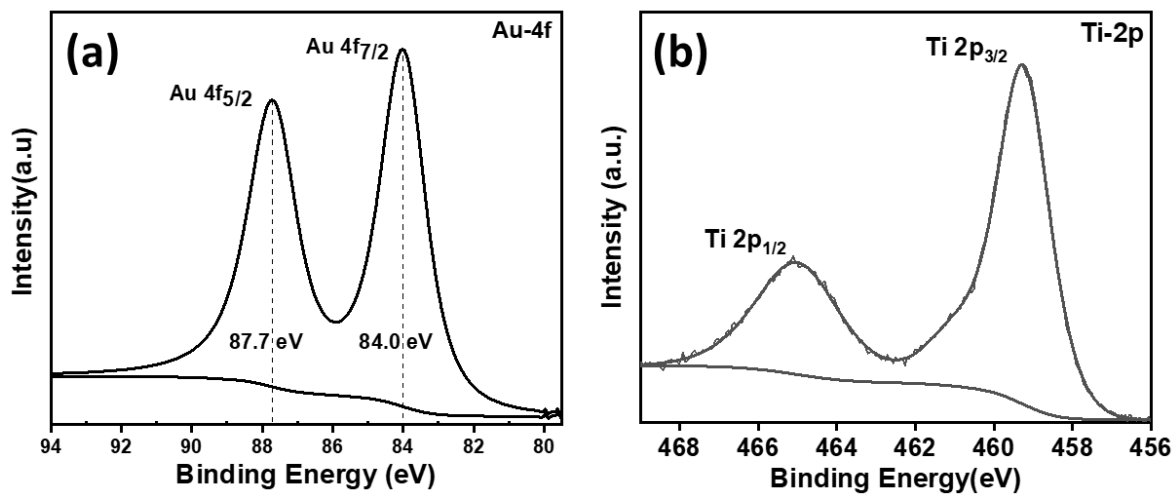


Figure S2. The high-resolution XPS spectra of (a) Au-4f and (b) Ti-2p.

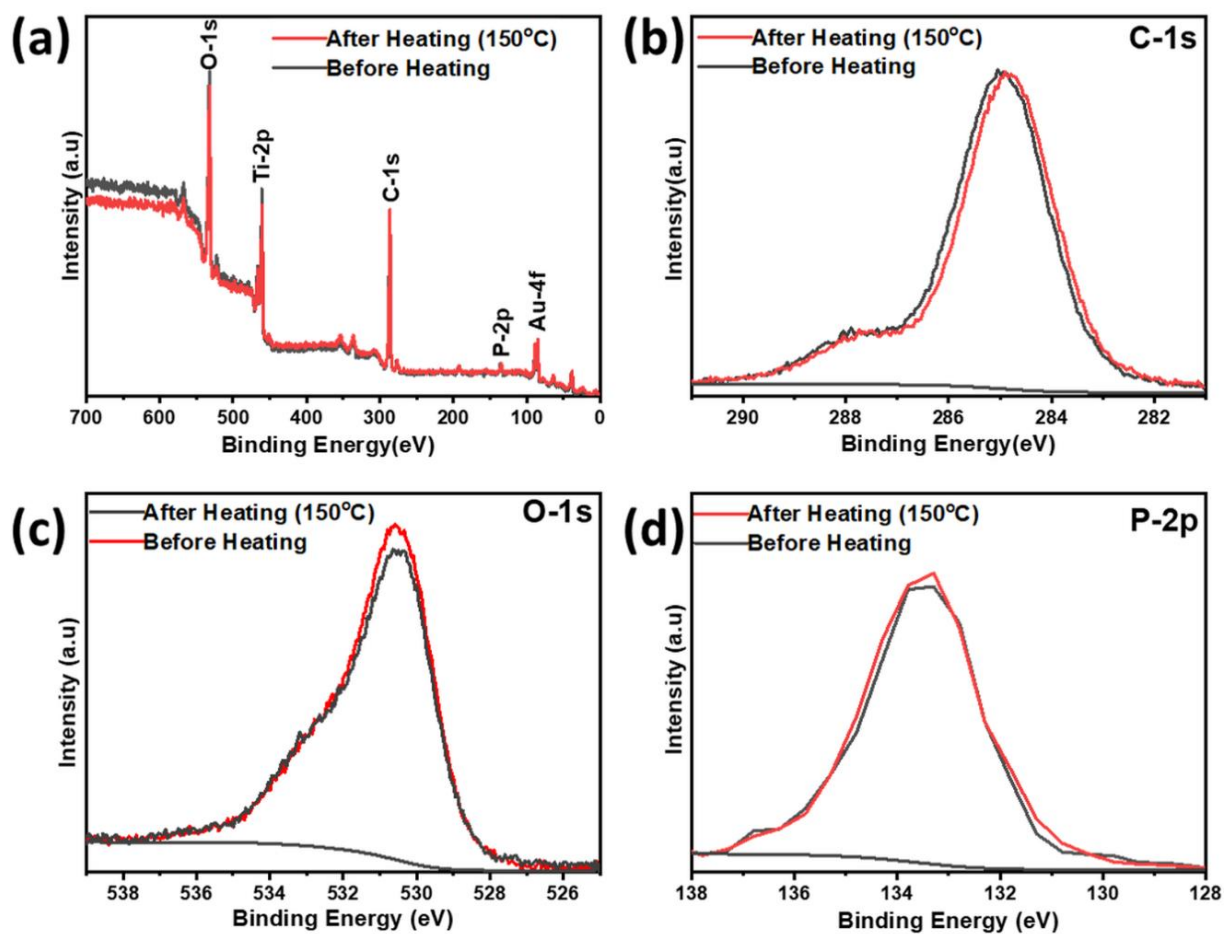


Figure S3. (a) Wide scan and high-resolution XPS spectra of (b) C-1s (c) O-1s and (d) P-2p.

References

- [1] S. Veziroglu, M.Z. Ghori, M. Kamp, L. Kienle, H.G. Rubahn, T. Strunskus, J. Fiutowski, J. Adam, F. Faupel, O.C. Aktas, Photocatalytic Growth of Hierarchical Au Needle Clusters on Highly Active TiO₂ Thin Film, *Adv. Mater. Interfaces*. 5 (2018) 1800465.
- [2] M.Z. Ghori, S. Veziroglu, B. Henkel, A. Vahl, O. Polonskyi, T. Strunskus, F. Faupel, O.C. Aktas, A comparative study of photocatalysis on highly active columnar TiO₂ nanostructures in-air and in-solution, *Sol. Energy Mater. Sol. Cells*. 178 (2018) 170–178.

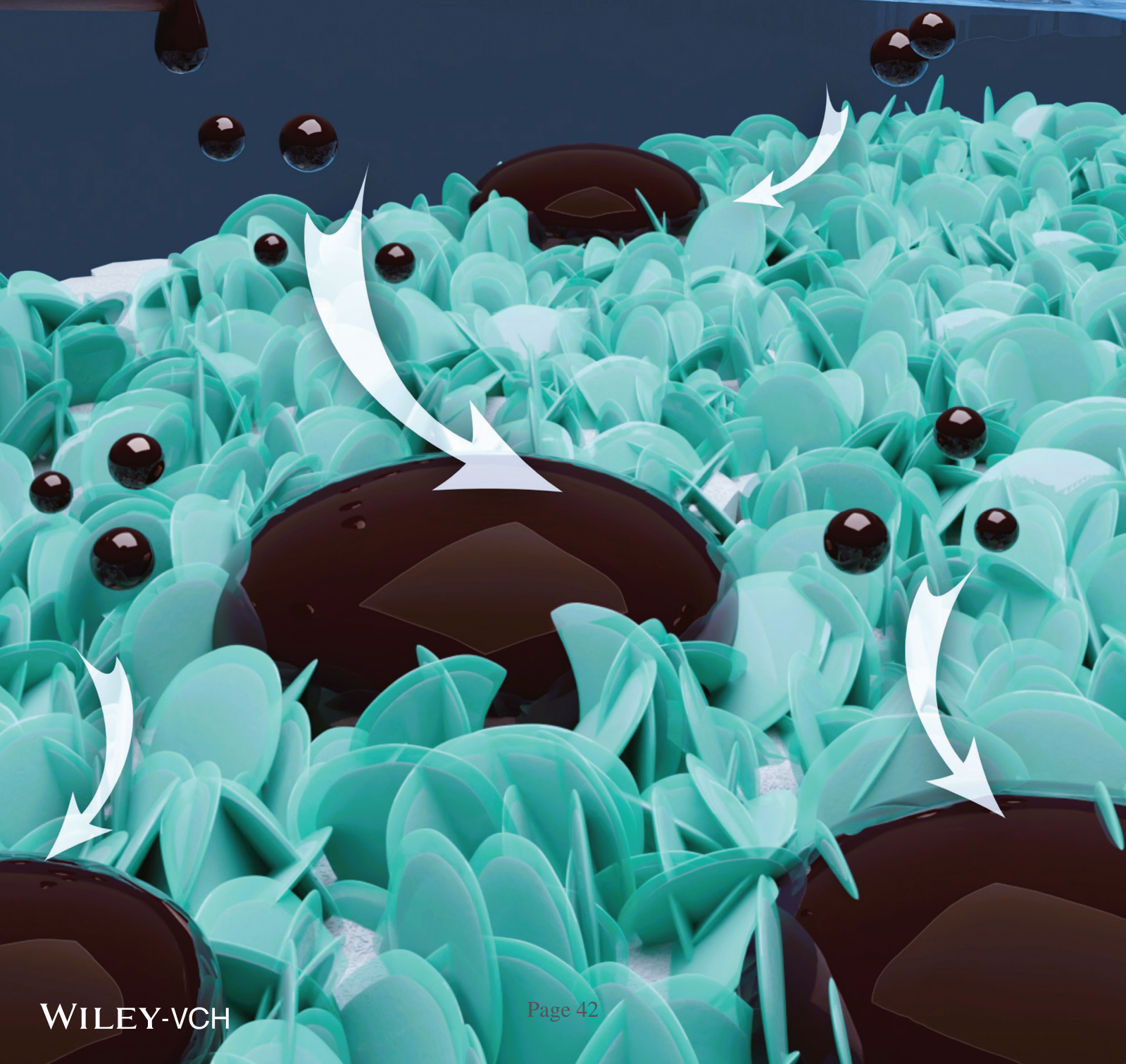
CHAPTER FOUR

This chapter presents the selective adsorption and the photocatalytic oil clean-up by the TiO₂ thin film decorated with poly(1,3,5-trimethyl-1,3,5-trivinyl cyclotrisiloxane) (p-V₃D₃) modified flowerlike Ag nanoplates. A novel “three-in-one (3-in-1)” surface, which is composed of (i) a highly photocatalytic layer, (ii) micro- and nanostructures, and (iii) a low surface energy layer, is introduced. First, the TiO₂ photocatalytic layer is prepared by magnetron sputtering. Then flowerlike Ag nanoplates are photocatalytically deposited on the sputtered TiO₂ layer. Last a thin layer of p-V₃D₃ is over-coated.

This chapter is a reprint from the following publication:

J. Shondo, S. Veziroglu, T. Tjardts, J. Fiutowski, S. Schröder, Y. K. Mishra, T. Strunskus, H. G. Rubahn, F. Faupel, O. C. Aktas, *Adv Mater Interfaces* 2022, 9, DOI 10.1002/admi.202102126.

ADVANCED MATERIALS INTERFACES



Selective Adsorption and Photocatalytic Clean-Up of Oil by TiO₂ Thin Film Decorated with p-V₃D₃ Modified Flowerlike Ag Nanoplates

Josiah Shondo, Salih Veziroglu, Tim Tjardts, Jacek Fiutowski, Stefan Schröder, Yogendra Kumar Mishra, Thomas Strunskus, Horst-Günther Rubahn, Franz Faupel, and Oral Cenk Aktas*

Various methods are developed and used to treat oil-contaminated water, including mechanical separation, chemical treatment, biological treatment, membrane filtration, and sorption. Oil clean-up via selective sorption of the oil by an engineered surface is the most accepted technique due to its high removal efficiency and low cost. Here, a multifunctional surface providing highly selective oil sorption and clean-up capability via the photocatalytic decomposition is proposed. This novel surface is named as the “three-in-one (3-in-1) surface” since it is composed of 1) a highly photocatalytic layer, 2) micro- and nanostructures, and 3) a low surface energy layer. First, the TiO₂ photocatalytic layer is prepared by magnetron sputtering. Then flowerlike Ag nanoplates are photocatalytically deposited on the sputtered TiO₂ layer. Afterward, a low surface energy layer, poly-1,3,5-trivinyl-1,3,5-trimethylcyclotrisiloxane (p-V₃D₃), is over-coated on Ag/TiO₂ surface by initiated chemical vapor deposition (iCVD) while retaining the topographical features of the surface (micro- and nanoscale surface structures). The p-V₃D₃/Ag/TiO₂ surface demonstrates a high selective adsorption to oil whereas simultaneously it shows extreme repellency to water. The p-V₃D₃/Ag/TiO₂ surface can also be photocatalytically cleaned up and this may find applications in various technology fields including water treatment, microfluidics, self-cleaning, and water harvesting.

1. Introduction

Increasing demand for petrochemical, mining, pharmaceutical, textile, metal processing, and food industries increases also the risk of water wasting by oil and oil-originated pollutants.^[1] Moreover, oil spill incidents during oil exploration and extraction, refining, and transportation form a high threat for water contamination.^[2,3] Various methods have been developed and used to treat oil-contaminated water including mechanical separation, chemical treatment, biological treatment, membrane filtration, and sorption.^[4–6] Among all these methods, oil clean-up via the sorption of the oil by an engineered surface is the most preferred method thanks to its ease of application, high removal efficiency, low cost, and as well as eco-friendly nature.^[7] An ideal sorbent material for oil clean-up should exhibit both high hydrophobicity and oleophilicity.^[8] Different types of materials possessing such a dual wettability nature (exhibiting both hydrophobicity and oleophilicity) has been proposed for the selective adsorption

J. Shondo, S. Veziroglu, T. Tjardts, S. Schröder, T. Strunskus, F. Faupel, O. C. Aktas
Chair for Multicomponent Materials
Institute of Materials Science
Faculty of Engineering
Kiel University
Kaiserstr. 2, 24143 Kiel, Germany
E-mail: oca@tf.uni-kiel.de

J. Fiutowski, Y. K. Mishra, H.-G. Rubahn
Mads Clausen Institute
NanoSYD
University of Southern Denmark
Alsion 2, Sønderborg 6400, Denmark
O. C. Aktas
Additive Manufacturing Excellence Centre – URTEMM
Kahramankazan, Ankara 06980, Turkey

 The ORCID identification number(s) for the author(s) of this article can be found under <https://doi.org/10.1002/admi.202102126>.

© 2022 The Authors. Advanced Materials Interfaces published by Wiley-VCH GmbH. This is an open access article under the terms of the Creative Commons Attribution License, which permits use, distribution and reproduction in any medium, provided the original work is properly cited.

DOI: 10.1002/admi.202102126

of the oil,^[9] on the other hand after adsorbing a certain amount of the oil, the surface of such materials are saturated and their oil removal capacity significantly goes down.^[10,11] Therefore, an ideal material surface should also exhibit recoverability of the adsorbed oil in addition to hydrophobicity and oleophilicity for the efficient oil clean-up. In recent years, using materials that show preferential wetting and nonwetting characteristics, have gained tremendous interest in developing oil clean-up technologies.^[12]

In this current work, we propose a novel surface that exhibits highly selective oil adsorption and clean-up capability via the photocatalytic decomposition of the adsorbed oil. We developed so-called three-in-one (3-in-1) surface composed of 1) a highly photocatalytic layer, 2) micro- and nanostructures, and 3) a low surface energy layer. The photocatalytic layer was prepared by the magnetron sputtering of TiO₂ and then Ag structures were photocatalytically deposited onto this active layer to achieve stable micro- and nanoscale topographic features. Afterward, a low surface energy layer (poly-1,3,5-trivinyl-1,3,5-trimethylcyclotrisiloxane, p-V₃D₃), was deposited onto the Ag/TiO₂ surface by the initiated chemical vapor deposition (iCVD). The iCVD technique allows a well-controlled film thickness (down to 5–10 nm) promoting the retention of the surface topography (morphology of flowerlike Ag nanoplates and columnar TiO₂ structures), which is necessary to achieve superhydrophobic state. Photocatalytic p-V₃D₃/Ag/TiO₂ surface demonstrates a high adsorption selectivity toward oil whereas simultaneously it shows an extreme repellency to water. Adsorbed oil can be decomposed photocatalytically under UV light and then p-V₃D₃/Ag/TiO₂ surface can be reused for oil–water separation. Due to its siloxane backbone, the p-V₃D₃ layer seems to exhibit high stability to UV irradiation and atomic oxygen exposure. The proposed 3-in-1 surface concept may

find applications in oil-water separation, microfluidics,^[13] self-cleaning, and water harvesting^[12] technologies.

2. Results and Discussion

The preparation of p-V₃D₃/Ag/TiO₂ and PTFE/Ag/TiO₂ (used as a control substrate for comparison) surfaces follows three steps approach: i) preparation of TiO₂ thin film, ii) photocatalytic deposition of flowerlike Ag nanoplates, and iii) deposition of polymer layers via iCVD as schematically shown in **Figure 1**.

To investigate the surface morphology of the photocatalytically deposited flowerlike Ag nanoplates, helium ion microscope (HIM) was utilized as presented in **Figure 2**. Previously, we showed that Ag⁺ ions were reduced to stable and globular Ag nanostructures on TiO₂ thin films under UV illumination (4.5 mW cm² UV lamp operating at $\lambda = 365$ nm).^[14] We demonstrated that the formation of such Ag nanostructures was mainly governed by photoexcited charge carriers generated in TiO₂ during photocatalytic reactions. However, in this work, we used trisodium citrate (Na₃C₆H₅O₇) as the reducing agent and we observed a quite different morphology in comparison to those which we reported previously.^[14] Therefore, the growth mechanism of Ag nanoplates should be different. We assume that the first photoexcited charge carriers generated by TiO₂ induced the photooxidation of the citrate (C₆H₅O₇) and this leads to the decarboxylation to organic radicals. Then, these radicals seem to be chemisorbed onto Ag⁺ ions via the electron transfer and finally, Ag⁺ ions are reduced to immobilized stable metallic Ag structures on the TiO₂ surface.^[15] It seems that the arrangement of interconnected Ag nanoplates results in the formation of flowerlike Ag structures as shown in **Figure 2a,b**. The elemental mapping of silver (Ag), titanium (Ti), and oxygen (O) by scanning electron microscopy–energy

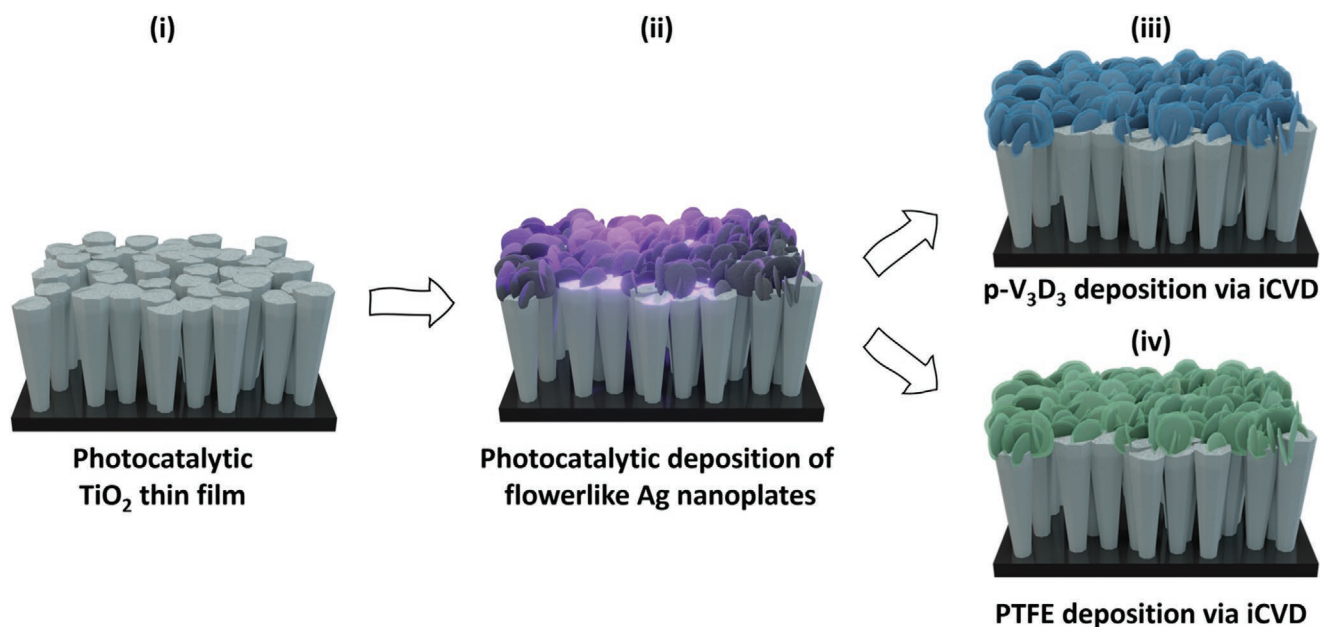


Figure 1. i) Sputter-deposited TiO₂ thin film, ii) photocatalytic deposition of flowerlike Ag nanoplates on TiO₂ thin film, iii) p-V₃D₃ deposition on Ag/TiO₂ via iCVD, and iv) PTFE (as control substrate) deposition on Ag/TiO₂ via iCVD.

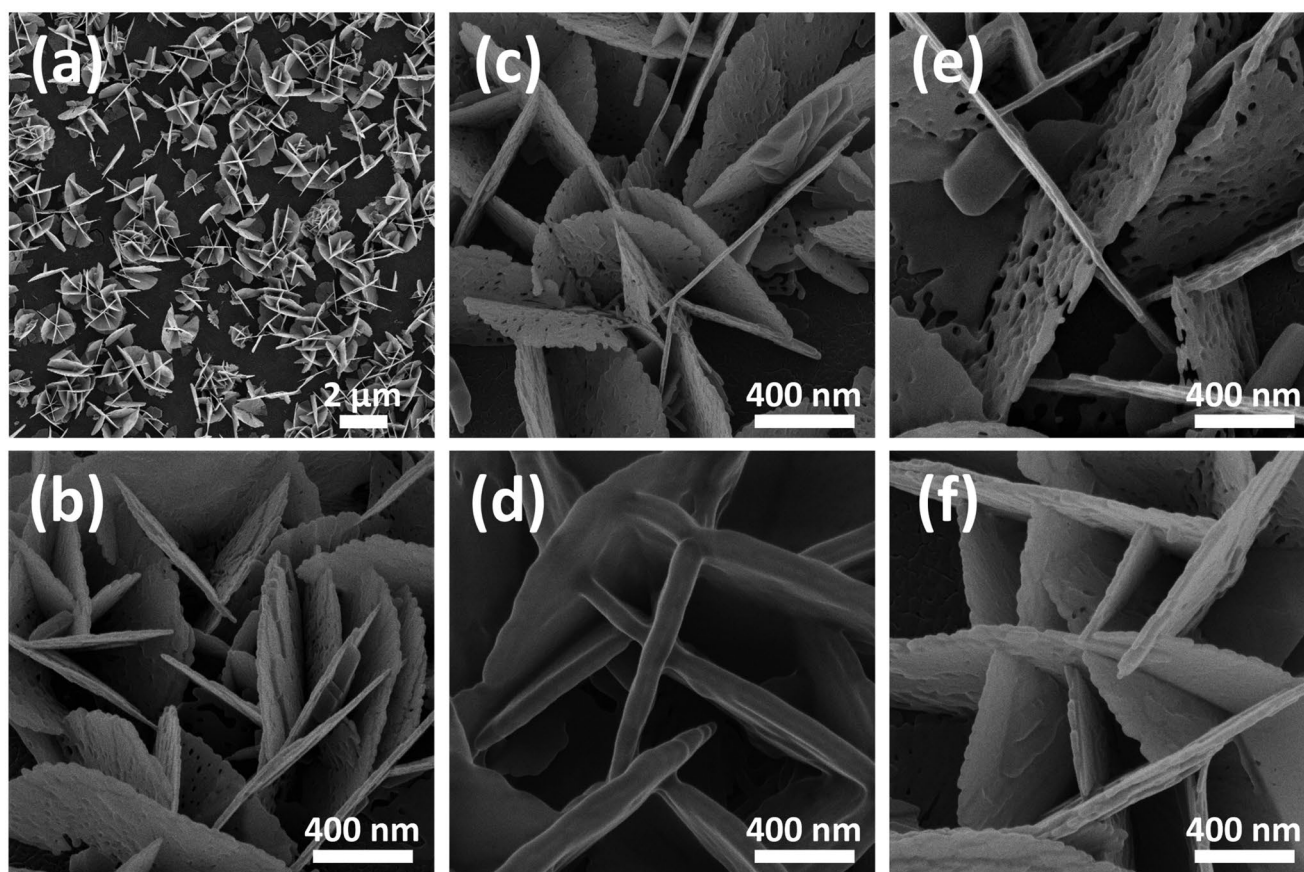


Figure 2. HIM images of photocatalytically deposited flowerlike Ag nanoplates on TiO_2 a) at low and b) at high magnification. HIM images of photocatalytically deposited flowerlike Ag on TiO_2 after over-coating with a c) 25 nm $\text{p-V}_3\text{D}_3$ layer and d) 100 nm $\text{p-V}_3\text{D}_3$ layer, e) 25 nm PTFE layer, and f) 100 nm PTFE layer.

dispersive spectroscopy (SEM-EDS) demonstrates the presence of TiO_2 decorated with flowerlike Ag nanoplates shown in Figure S1 of the Supporting Information (the additional silicon (Si) mapping results from the Si-wafer substrate).

The X-ray diffraction (XRD) analysis revealed the preferential orientation of flowerlike Ag nanoplates in (111) direction as shown in Figure S2 of the Supporting Information. Various studies proposed different mechanisms for the growth of Ag structures in nanoplate form. Especially in the case of photochemical synthesis routes, it is believed that dipole plasmon excitation may induce an ultrafast charge separation on Ag nanostructures surface and this triggers the face-selective reduction of Ag^+ ions and anisotropic crystal growth.^[16] Moreover, during photocatalytic reactions, H_2O_2 may counterattack the reduction of Ag^+ by $\text{C}_6\text{H}_5\text{O}_7^-$. This may lead to the formation of Ag seeds with (111) twin planes and stacking faults. It is known that such seeds are more stable against oxidative etching, and they grow at the expense of less stable nanoparticles with smaller sizes and/or other shapes (they dissolve in O_2 rich medium and serve as the Ag^+ source for the nanoplate growth).^[17]

Figure 2c,d presents HIM images of 25 and 100 nm thick $\text{p-V}_3\text{D}_3$ over-coated Ag/TiO_2 , respectively. Similarly, Figure 2e,f shows PTFE over-coated Ag/TiO_2 (with the thickness of 25 and 100 nm, respectively). HIM images showed no significant

change in the morphology of Ag structures before and after the deposition of the polymer layers. This confirms that iCVD leads to a highly conformal coating. Since it was not possible to distinguish deposited polymer layers on Ag/TiO_2 surface via HIM analysis, the presence of $\text{p-V}_3\text{D}_3$ and PTFE layers were revealed by X-ray photoelectron spectroscopy (XPS) analysis. Wide-scan XPS spectrum survey shows C 1s, F 1s, O 1s, Ag 3d, and Ti 2p peaks as presented in Figure 3a,b for $\text{p-V}_3\text{D}_3$ and PTFE over-coated Ag/TiO_2 , respectively. In the XPS spectrum of $\text{p-V}_3\text{D}_3$ over-coated samples, as expected we observed the Si 2p peak, which is a clear indication of the silicon backbone of $\text{p-V}_3\text{D}_3$ (a high-resolution spectrum is given in Figure 3c).

In comparison to XPS spectra of 25 nm thick polymer layers over-coated Ag/TiO_2 surfaces, we observed a decrease in intensities of Ag 3d and Ti 2p peaks for 100 nm thick polymer layers over-coated Ag/TiO_2 surfaces, which is a clear consequence of the increase in over-coated polymer thickness.^[18] In addition, we observed a slight difference between morphologies of 100 nm thick $\text{p-V}_3\text{D}_3$ and PTFE layers. While the 100 nm thick $\text{p-V}_3\text{D}_3$ layer exhibited a high conformality, we observed some protrusion type inhomogeneities at the 100 nm thick PTFE layer, which may be due to the lack of the good adhesion between PTFE films and Ag nanoplates (Figure 2f). The $\text{p-V}_3\text{D}_3$ layer seems to have better adhesion affinity to the Ag/TiO_2 surface which may be due to the Si–O backbone of $\text{p-V}_3\text{D}_3$.^[19,20]

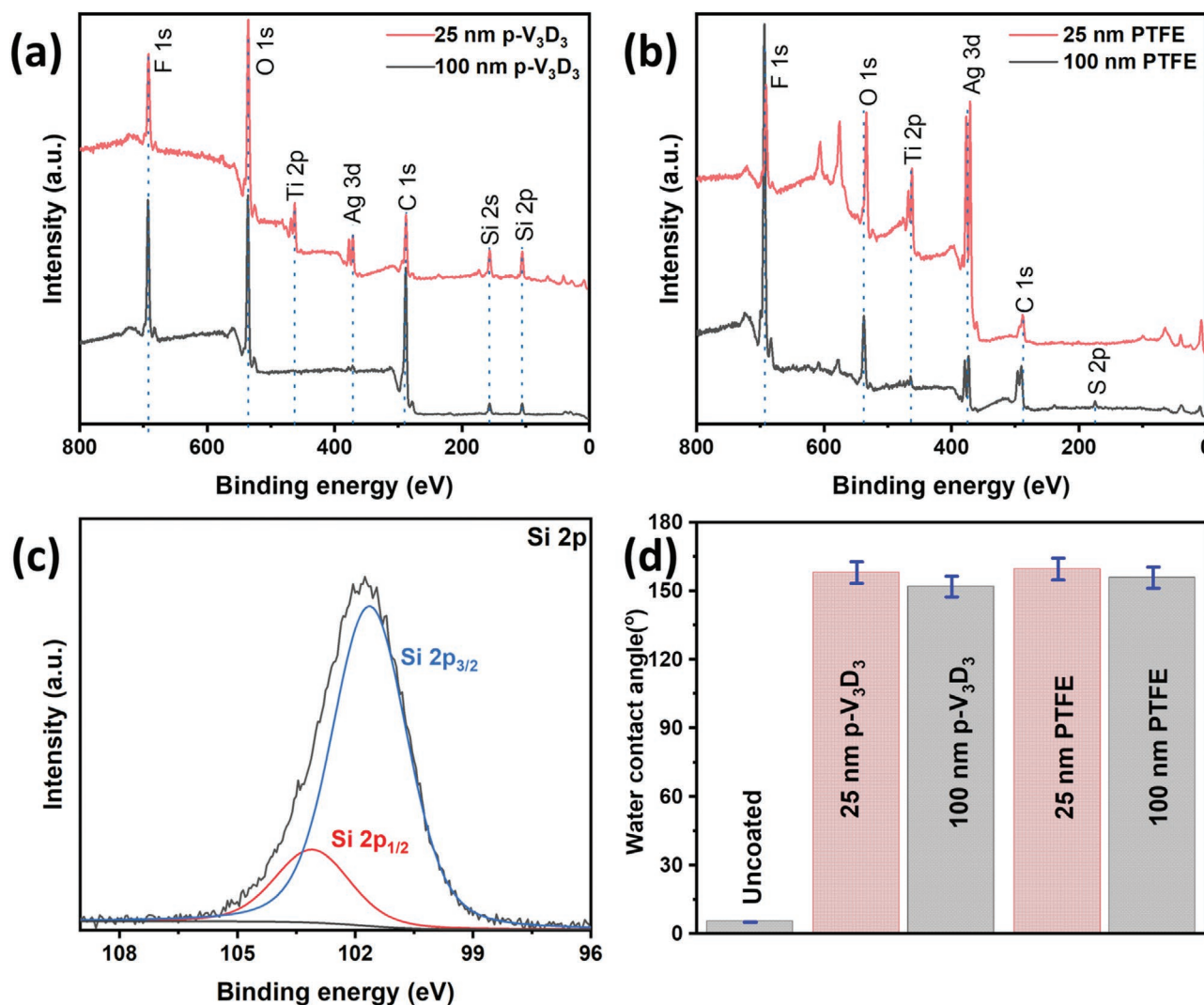


Figure 3. a) XPS spectra of 25 nm and 100 nm thick p-V₃D₃ over-coated Ag/TiO₂ surfaces, b) XPS spectra of 25 and 100 nm thick PTFE over-coated Ag/TiO₂ surfaces, c) high-resolution Si 2p XPS spectrum of 25 nm thick p-V₃D₃ over-coated Ag/TiO₂ surface, and d) water contact angle (WCA) analysis of p-V₃D₃ and PTFE coated samples at respective thicknesses (static, advancing, receding, and sliding WCAs are given in Table S1, Supporting Information).

Using a semiautomated goniometer, we investigated the effects of Ag/TiO₂ surface features and polymer layers (p-V₃D₃ and PTFE) on the wettability. As shown in various studies including ours, TiO₂ exhibits a hydrophilic nature and under the UV light a superhydrophilic state can be achieved.^[21–23] In Figure 3d one can see that the TiO₂ layer showed a water contact angle (WCA) around 5° after photocatalytic deposition of the Ag structures. Indeed, this is in agreement with Wenzel's rule which states that an intrinsically hydrophilic material will become more hydrophilic by increasing the surface roughness and/or introducing hierarchical roughness.^[24–27] To further confirm the surface roughness, which plays an important role in enhancing the wettability properties of flowerlike Ag nanoplates on TiO₂, the surface topography of the prepared samples was analyzed by atomic force microscopy (AFM) as shown in Figure S3 of the Supporting Information. The average surface roughness (Ra) and root mean square roughness (rms) were

measured as 704.4 (± 24.6) nm and 744.8 (± 26.1) nm for Ag/TiO₂ and 18.9 (± 1.1) nm and 23.8 (± 1.3) nm for bare TiO₂, respectively; which clearly indicates a significant change in surface roughness after photocatalytic deposition of flower like Ag nanoplates.^[28] After the deposition of p-V₃D₃ and PTFE layers, we observed a transition from the superhydrophilic state to a superhydrophobic state. Although all iCVD modified samples exhibited a superhydrophobic state (WCA > 150°) regardless of the type and thickness of the deposited layers, the highest WCA of 163° was observed in the case of the 25 nm p-V₃D₃ over-coated Ag/TiO₂ surfaces. Furthermore, we observed that iCVD modified surfaces were not only superhydrophobic but also, showed superoleophilic properties with an oil contact angle (OCA) below 6° (Figure S4, Supporting Information).

To further reveal the superhydrophobic and superoleophilic behavior of the p-V₃D₃/ Ag/TiO₂ sample, we recorded the interaction of water and oil droplets with the surface with

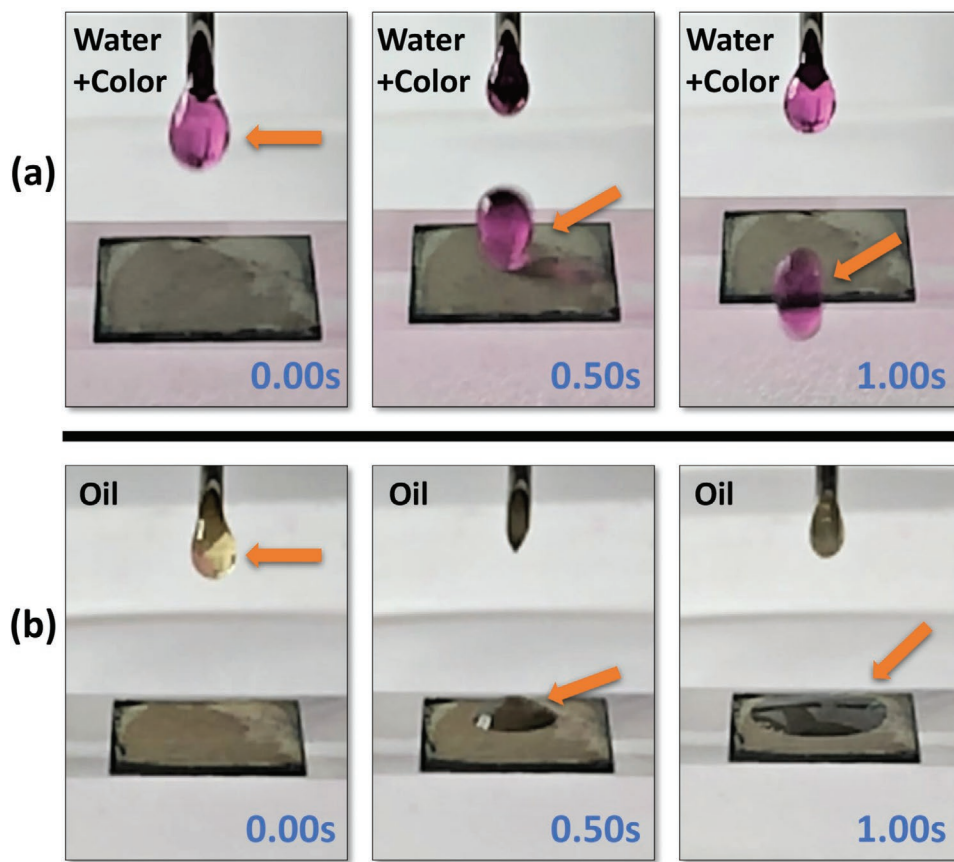


Figure 4. a) Bouncing of the water droplet (colored with pinkish dye) on $p\text{-V}_3\text{D}_3/\text{Ag}/\text{TiO}_2$ surface and b) spreading of the oil droplet on $p\text{-V}_3\text{D}_3/\text{Ag}/\text{TiO}_2$ surface (orange arrows represent the position of the droplets).

a high-speed camera (Videos S1 and S2, Supporting Information). By tilting the base plane of the semiautomated contact angle goniometer with help of a precise micromanipulator, we measured a sliding angle of $6^\circ\text{--}8^\circ$ which indicates high water repellence. For instance, as soon as the water droplet impacted the $p\text{-V}_3\text{D}_3/\text{Ag}/\text{TiO}_2$ surface it bounced and completely left the surface as shown in **Figure 4a**. We did not observe any residual from water droplets (colored with E127 Eritrosina dye, E127 eritrosina granular B20g supplies by Fast colors LLP). When the same volume of an oil droplet contacted with $p\text{-V}_3\text{D}_3/\text{Ag}/\text{TiO}_2$ surface, the droplet spread out rather than bouncing on the surface (as observed in the case of the water droplet) as shown in **Figure 4b**.

In addition, to demonstrate the oil adsorption properties of $p\text{-V}_3\text{D}_3/\text{Ag}/\text{TiO}_2$ surface first, we prepared an oil contaminated water model by drop-casting a limited amount of motor-oil into water. Afterward, the $p\text{-V}_3\text{D}_3/\text{Ag}/\text{TiO}_2$ sample was immersed into the prepared oil–water mixture as shown in **Figure 5** and Video S8 (Supporting Information). By moving the $\text{V}_3\text{D}_3/\text{Ag}/\text{TiO}_2$ sample back-and-forth in oil–water mixture, the oil droplets were captured. The selective capturing of oil droplets clearly indicates an oleophilic state of the surface in addition to its superhydrophobicity.

The dual nature, superhydrophobicity and superoleophilicity, of $p\text{-V}_3\text{D}_3/\text{Ag}/\text{TiO}_2$ surface forms a good basis for an effective oil–water separation. On the other hand, the cumulative oil

adsorbate by the time may hinder the oil–water separation performance in the long term. The adsorbed oil needs to be eliminated from the surface to achieve a sustainable oil–water separation. To investigate the photocatalytic clean-up capability of the prepared $p\text{-V}_3\text{D}_3/\text{Ag}/\text{TiO}_2$ surface a motor-oil droplet with a volume of $5\ \mu\text{L}$ was spread out on $p\text{-V}_3\text{D}_3/\text{Ag}/\text{TiO}_2$ surface to induce an artificial contamination. Just after spreading out of the oil droplet on $p\text{-V}_3\text{D}_3/\text{Ag}/\text{TiO}_2$ surface, the corresponding WCA dropped to 90° . This is a clear indication of surface contamination since the same surface exhibited a superhydrophobic state (with a WCA of 162.8°) before spreading of the oil droplet. Then $p\text{-V}_3\text{D}_3/\text{Ag}/\text{TiO}_2$ surface was exposed to UV light (with the intensity of $5.85\ \text{mW cm}^{-2}$ operating at $\lambda = 365\ \text{nm}$) and the change in WCA was monitored at defined time frames. By the time a gradual recovery of the hydrophobicity was observed as shown in **Figure 6a**. A similar recovery was also observed for the oil-contaminated PTFE/ Ag/TiO_2 surface (used as a comparison) as shown in **Figure 6b**.

Previously, we showed that the photocatalytic activity of TiO_2 thin films can be enhanced by the incorporation of Ag nanostructures on the TiO_2 surface.^[14] Basically, this occurs by inhibiting the recombination of photoexcited charge carriers (electron–hole (e^-/h^+)) due to the electron affinity of Ag nanostructures.^[29] Therefore, in case of TiO_2 layer decorated with flowerlike Ag nanoplates photoexcited charges might be easily transferred from the semiconductor (e.g. TiO_2) to the matching

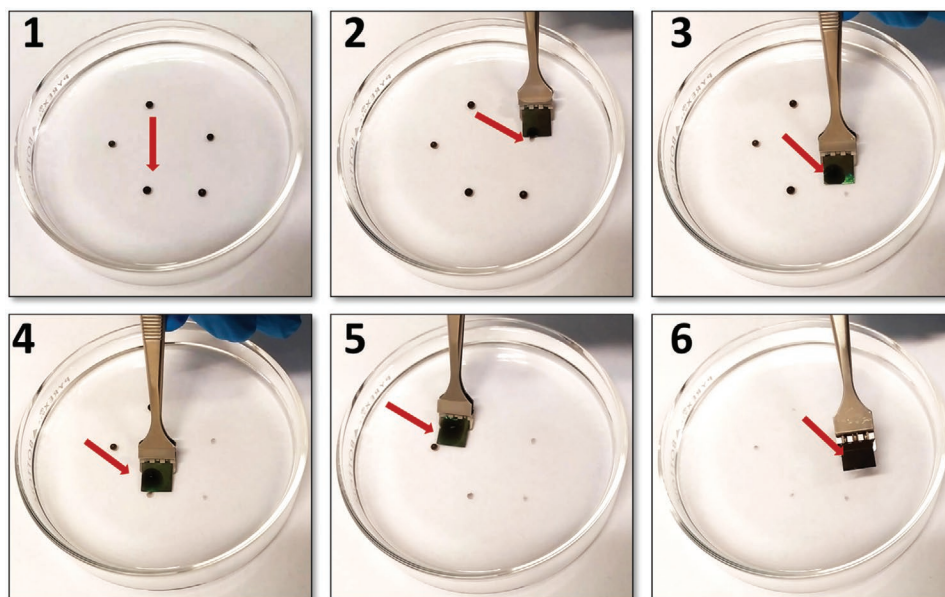


Figure 5. Selective capturing of oil droplets from motor oil–water mixture by $p\text{-V}_3\text{D}_3/\text{Ag}/\text{TiO}_2$ surface (1) motor oil droplets in water and (2–6) selective adsorption of motor oil droplets on $p\text{-V}_3\text{D}_3/\text{Ag}/\text{TiO}_2$ from water.

energy level of metallic structures (e.g. Ag nanoplates).^[30,31] On the other hand, in case of $p\text{-V}_3\text{D}_3/\text{Ag}/\text{TiO}_2$ and $\text{PTFE}/\text{Ag}/\text{TiO}_2$ the top-polymer layer acts as the dielectric layer (especially $p\text{-V}_3\text{D}_3$ is known to have a large bandgap of 8.25 eV),^[32] which makes the charge transfer and separation mechanism more complicated. Kamegawa et al. showed that the composite layer composed of TiO_2 and PTFE exhibited a strong photocatalytic activity and authors claimed that PTFE promotes the charge separation.^[33] Similarly, Ibhaddon et al. showed that SiO_2 particles deposited onto TiO_2 induced an efficient separation of electron–hole pairs and this increased the photocatalytic activity of TiO_2 .^[34] Moreover, Mahesh Reddy et al. reported a similar mechanism for the strong photocatalytic activity of polyurethane-modified TiO_2 .^[35] By comparing our result with these findings, we resolve that the ultrathin nature of PTFE and $p\text{-V}_3\text{D}_3$ polymer layers seem to allow the electron transfer to the surface from Ag/TiO_2 layer beneath. This allows the photodegradation of adsorbed oil (e.g. hexadecane) on the surface and renders the superhydrophobic state.^[36] In addition to its effect on the charge-separation, the top-layer covering Ag/TiO_2 seems to promote the photocatalytic performance by increasing the overall optical absorption as shown by measuring their UV–vis spectra (Figure S5a, Supporting Information). The optical spectrum of bare TiO_2 shows a clear cut-off wavelength at 352 nm corresponding to a bandgap of 3.52 eV (Figure S5b, Supporting Information), which is in agreement with reported bandgap values for sputter deposited TiO_2 (e.g. anatase) thin films.^[37–39] On the other hand, we observed a significant shift of the optical spectrum to higher wavelengths (with a new value of the cut-off wavelength film remains high) after over coating Ag/TiO_2 surface with polymer top-layer. It is difficult to reveal the bandgap of $p\text{-V}_3\text{D}_3/\text{Ag}/\text{TiO}_2$ by simply Tauc plot since flower-like Ag nanoplates are composed of hierarchical plasmonic. In addition, the presence of a nonhomogenous optical medium, $p\text{-V}_3\text{D}_3/\text{Ag}/\text{TiO}_2$ (cross-sectional look at the presence of Ag

structures) and $p\text{-V}_3\text{D}_3/\text{TiO}_2$ (cross-sectional look at absence of Ag structures) makes it a complicated optical system. Nevertheless $p\text{-V}_3\text{D}_3/\text{Ag}/\text{TiO}_2$ exhibited much higher optical absorption in comparison to bare TiO_2 , which may clearly contribute to the overall photocatalytic performance.

For further evaluation of the photocatalytic clean-up performance of $p\text{-V}_3\text{D}_3/\text{Ag}/\text{TiO}_2$, the 100 nm thick $p\text{-V}_3\text{D}_3$ coated sample surface was contaminated by oleic acid (volume: 10 μL) and then exposed to UV light for 3 h while visually monitoring the surface as shown schematically in Figure 6c. After exposing the sample to UV light for 1 h, we could notice a gradual decrease in the volume of oleic acid on the surface and after 3 h barely any residual from oleic acid could be seen on the surface (Figure 6d). A quick check with the goniometer showed that the surface kept its superhydrophobic state with water WCA > 154°. On the other hand, the TiO_2 thin film surface was also contaminated with oleic acid and exposed to UV light for 10 h. XPS investigation showed a gradual decrease in peak intensity and concentration % of C 1s while those increase in case of both Ti 2p and O 1s (Figure S6 and Table S2, Supporting Information).^[40] Here, high stability of the $p\text{-V}_3\text{D}_3$ coating might arise due to the presence of the Si–O bond (which can also promote a strong adhesion of the polymer layer to the Ag/TiO_2 surface).^[19] This clearly shows that a $p\text{-V}_3\text{D}_3$ layer is more suitable than the conventional PTFE coating for oil–water separation and photocatalytic clean-up application. Moreover, such a $p\text{-V}_3\text{D}_3$ layer (100 nm) has a high potential to replace PTFE also due to its eco-friendly nature.

Ag/TiO_2 shows high photocatalytic activity for clean-up of the oil contamination. Conversely, one should think that photocatalytic reactions may lead to the degradation of the polymer layers used as the top-coat. For instance, as shown in Figure 6a we observed a decrease in WCA on the 25 nm thick $p\text{-V}_3\text{D}_3$ over-coated Ag/TiO_2 after 5 h, which indicates a possible photocatalytic decomposition of the $p\text{-V}_3\text{D}_3$ layer. The XPS

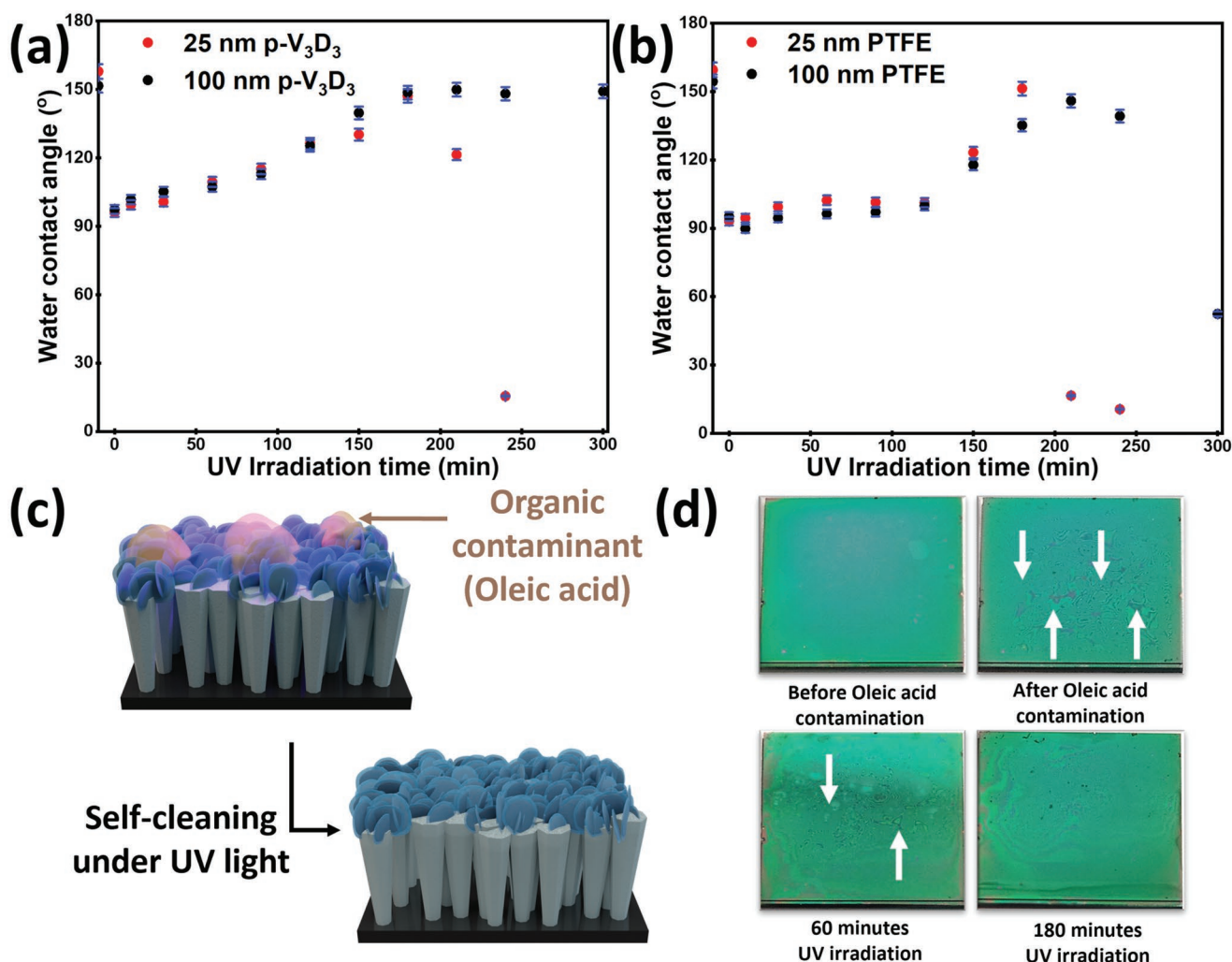


Figure 6. Change in water contact angle (WCA) by the contamination of the sample surface by hexadecane oil and the photocatalytic clean-up under UV light irradiation for a) p-V₃D₃ and b) PTFE-coated samples. c) Schematic of the photodegradation process and d) photocatalytic clean-up of oleic acid residue on the sample surface under UV light irradiation.

analysis revealed that p-V₃D₃ layer alone without the active Ag/TiO₂ layer does not show any self-decomposition under UV irradiation as shown in Figure S7 of the Supporting Information.

In comparison, the 25 nm p-V₃D₃ layer showed a much higher UV stability than the 25 nm PTFE layer as shown in Figure 6b. As expected, the stability of deposited polymer layers against exposure to UV light and photocatalytic self-degradation reactions was improved with the increasing thickness of the deposited polymer top-layer. Figure 6a shows that the 100 nm thick layers showed high WCAs after 300 min of UV irradiation, which indicates high stability of the layers against UV light and as well as photocatalytic reactions (self-degradation). So, one needs to think about a compromise between enhancing the stability of the deposited layers and retention of surface topography (which is essential for attaining high WCAs) while choosing a proper thickness.

The robustness of the p-V₃D₃ coated surface (100 nm) was further tested against the chemical shielding effect^[41] in both acidic (3 M H₂SO₄ and 3 M HCl, Sigma-Aldrich, Germany) and

alkaline (3 M NaOH and 3 M KOH, Sigma-Aldrich, Germany) medium (Videos S3–S6, Supporting Information). There were no visible reactions after 2 min (commonly waiting for 1 min) of immersion in both acids and bases. Most interestingly, the WCA of the surface showed no significant changes (Table S3, Supporting Information) after chemical stability tests. We further tested robustness of the surface under a pressurized water jet. After a continuous flow of the pressurized water on the surface for an hour, the surface still retained its superhydrophobicity (Figure S8 and Video S7, Supporting Information).

The change in surface chemistry of p-V₃D₃/Ag/TiO₂ after photocatalytic reaction induced by the exposure to UV light was further investigated with XPS (Figures S9 and S10, Supporting Information). The XPS analysis showed a slight decrease in surface atomic concentrations of C 1s and F 1s after exposure to UV light (Table S4, Supporting Information). The oxygen (O) to carbon (C) ratio was observed to steadily increase with UV irradiation due to oxygen-containing species on the surface (at a binding energy of 532.8 eV, which is assigned to typical oxygen

functional groups as carbonyl and siloxane).^[42] This shows that both UV irradiation and as well as photocatalytic reactions affect the overall stability of polymer top-layer, thus the hydrophobicity. By comparing the change in the intensity of F1s peak after exposure to UV light (Figure S11, Supporting Information), it is obvious that the 25 nm PTFE layer exhibited much lower stability than the 25 nm p-V₃D₃ layer. Siloxane backbone seems to endorse the stability of p-V₃D₃, and this promotes the reusability of p-V₃D₃/Ag/TiO₂ for oil–water separation after the photocatalytic clean-up. The 3-in-1 surface, p-V₃D₃/Ag/TiO₂, may be used in various oil–water separation and self-cleaning applications.

3. Conclusion

In summary, we prepared a stable superhydrophobic and photocatalytically active surface by the 3-in-1 approach which combines 1) photocatalytic thin film, 2) micro- and nanostructuring via photocatalytic deposition, and 3) low surface energy coating via iCVD. Our results show that not only p-V₃D₃ coating, but also the unique surface topography composed of flowerlike Ag nanoplates and columnar TiO₂ structures promoted the superhydrophobicity of the surface. iCVD led to a highly conformal p-V₃D₃ coating retaining the surface topography on TiO₂, which is crucial to achieve an extreme non-wetting regime. Additionally, due to its siloxane backbone, the p-V₃D₃ layer exhibited high stability against the UV irradiation and atomic oxygen exposure (photodegradation). The superhydrophobic (WCA > 160°) and photocatalytically active p-V₃D₃/Ag/TiO₂ surface shows high selectivity to oil adsorption, which may lead to several functional applications in oil–water separation, microfluidics, self-cleaning, and water harvesting technologies.

4. Experimental Section

Preparation of TiO₂ Thin Film: TiO₂ thin film with a thickness of 500 nm was deposited by DC magnetron sputtering from 2 in. titanium (Ti) target in a custom-built vacuum deposition chamber.^[43,44] Silicon wafer pieces (10 mm × 10 mm) were used as substrates. Before the deposition of TiO₂ thin film, a base pressure of 10⁻⁵ Pa was achieved by using a fused rotary (Agilent Technologies, SH-110) in combination with a turbo molecular pump (Pfeiffer Vacuum, HiPace 400). Initially, the Ti target (Goodfellow, 99.99% with a 50 mm diameter) was cleaned in a pure Ar plasma for 10 min followed by a conditioning phase of 5 min with both argon (Ar) and oxygen (O₂) flow. The deposition was conducted (for 90 min) at a magnetron output power of 90 W while keeping the gas flow ratio of Ar (process gas):O₂ (reactive gas) at 250:5 by using two separate mass flow controllers (MKS Multi-Gas-Controller 647C). To achieve a homogenous TiO₂ film, the sample holder was rotated during the deposition. Following the deposition process, the samples were heat-treated for 1 h at 650 °C in an oven (Nabertherm, LE 4/11/R6) and subsequently air quenched to induce a nanocracks network (leading to high surface area) in the TiO₂ columnar structures, as described before.^[45]

Photocatalytic Deposition of Flowerlike Ag Nanoplates on TiO₂ Thin Films: Aqueous solutions of silver nitrate (AgNO₃, Sigma-Aldrich, Germany) and trisodium citrate (Na₃C₆H₅O₇, Sigma-Aldrich, Germany) were prepared separately at concentrations of 0.003 m and 0.3 m, respectively. Then the freshly prepared TiO₂ thin film samples were dipped into a quartz cuvette filled with 6.5 mL of AgNO₃ solution, 200 μL Na₃C₆H₅O₇ solution, and 50 μL of Triton-X100 (Carl-Roth,

Germany). Additionally, tetramethylammonium hydroxide and nitric acid (HNO₃ Sigma-Aldrich, Germany) were used to adjust the pH (Tester kit pH 5, supplied by Carl Roth GmbH+Co.KG) value of the solution to 2.2. Afterward, samples were exposed to low-intensity (4.5 mW cm⁻²) UV irradiation (using UV LED StellarNet EPP2000C-SR-50 with SL5-DH light source, operating at a wavelength of 365 nm) through the quartz cuvette for 10 min. Subsequently, the samples were rinsed with deionized water to remove excess solution left on the surface and air-dried at room temperature.

Deposition of Polymer Layer by iCVD: p-V₃D₃ layer was deposited on prepared Ag/TiO₂ samples in a custom-built iCVD reactor system operated in a constant flow mode, as described before.^[27,46,47] First the reactor was evacuated for at least 3 h before introducing the monomer (1,3,5-trivinyl-1,3,5-trimethylcyclotrisiloxane, V₃D₃-ABCR, Germany) and the initiator perfluorobutanesulfonyl fluoride (PFBSF, 95% Fluorochem, UK). The reactor pressure was set to 50 Pa and controlled by a downstream butterfly valve (VAT Series 615), coupled to a capacitance manometer (MKS Baratron), that is connected to the reactor. V₃D₃ monomer was heated in a custom-made jar to 60 °C and delivered through a precise metering valve (Swagelok, Germany) to the reactor. The PFBSF initiator gas flow was feed into the reactor via a leak valve. Then the flow of the initiator and the monomer were calibrated. Flow rates were set to 0.2 and 0.1 sccm for V₃D₃ and PFBSF, respectively. By keeping calibrated flow constant Nichrome (Ni/Cr: 80/20, Goodfellow GmbH) filaments were resistively heated at a filament power of 38.3 W and the sample stage was kept at 30 °C using water cycling through a thermostat (Huber CC-K6). For 25 nm thickness and 100 nm thickness, the deposition time was adjusted to 7 and 28 min, respectively.

A similar procedure was applied to the deposition of the PTFE layer on Ag/TiO₂ (as control substrate). Here, the PFBSF monomer and the initiator hexafluoropropylene oxide (97%, Fluorochem, UK) were mixed at a ratio of 0.2. The filament power of 35.5 W was applied during the deposition to the Nichrome filament array. During the deposition, the sample stage was cooled to 20 °C by the water circulating thermostat. The process pressure inside the reactor was set to 50 Pa controlled by the downstream butterfly valve. To achieve 25 nm thickness and 100 nm thickness, the deposition time was adjusted to 7.5 and 29.5 min, respectively.

Characterization: The surface morphology and the structure of the prepared samples were characterized by helium ion microscope (HIM, Orion NanoFab-Carl Zeiss) and scanning electron microscope (SEM, Supra55VP-Carl Zeiss) integrated energy - dispersive (EDS, Ultim Max 65-Oxford) detector. The surface roughness of the bare TiO₂ and TiO₂ decorated with flowerlike Ag nanoplates was determined using an AFM operating at oscillating cantilever (AC) mode (WITec Alpha 300 RA). The Ra and rms were quantified using an open access software Gwyddion 2.59. The surface chemistry of the samples was analyzed by XPS (Omicron Nano-Technology GmbH, Al anode, 240 W). CasaXPS software (2.3.13PR1.0) was used to perform quantitative analyses and detailed peak investigation. All binding energies (BE) were calibrated with reference to the Ag 3d line at 368.3 eV of silver on the sample surface. WCA measurements were performed using a semiautomated contact angle goniometer (OCA 30, Dataphysics). For static WCA measurements water droplets with a volume of 10 μL were used, and advancing/receding angles were recorded by the addition and subtraction of water gradually as explained by Tadmor.^[48] The XRD measurement of prepared samples was carried out using a 9 kW rotating Cu anode X-ray source (λ ≈ 1.54 Å) in a Grazing incidence XRD setup with omega (ω) of 0.7 at a scanning rate of 2° min⁻¹ with high-quality semiconductor detector that supports 0D, 1D or 2D X-ray diffraction measurement (Rigaku SmartLab), operating at the voltage of 45kV and a current of 200mA.

Supporting Information

Supporting Information is available from the Wiley Online Library or from the author.

Acknowledgements

J.S. and S.V. contributed equally to this work. J.S. wishes to thank DAAD (Deutscher Akademischer Austauschdienst) and PTFD (Petroleum Technology Development Fund) for providing funding for his doctoral studies. The authors thank NanoBMT Co. Ltd. for wetting analysis of prepared surfaces.

Open access funding enabled and organized by Projekt DEAL.

Conflict of Interest

The authors declare no conflict of interest.

Data Availability Statement

The data that support the findings of this study are available in the supplementary material of this article.

Keywords

flowerlike nanoplates, initiated chemical vapor deposition, oil clean-up, photocatalytic layer, selective oil adsorption

Received: October 30, 2021

Revised: January 25, 2022

Published online: March 2, 2022

- [1] M. I. Ramirez, A. P. Arevalo, S. Sotomayor, N. Bailon-Moscoco, *Environ. Pollut.* **2017**, 231, 415.
- [2] A. B. Nordvik, J. L. Simmons, K. R. Biting, A. Lewis, T. Strøm-Kristiansen, *Spill Sci. Technol. Bull.* **1996**, 3, 107.
- [3] Z. Chu, Y. Feng, S. Seeger, *Angew. Chem., Int. Ed.* **2015**, 54, 2328.
- [4] G. Deschamps, H. Caruel, M. E. Borredon, C. Bonnin, C. Vignoles, *Environ. Sci. Technol.* **2003**, 37, 1013.
- [5] R. J. Archer, B. Becher-Nienhaus, G. J. Dunderdale, A. Hozumi, *Adv. Funct. Mater.* **2020**, 30, 1907772.
- [6] L. Yan, X. Yang, Y. Zhao, Y. Wu, R. Motilhaetsi Moutloali, B. B. Mamba, P. Sorokin, L. Shao, *Sep. Purif. Technol.* **2022**, 285, 120383.
- [7] J. Ge, H. Y. Zhao, H. W. Zhu, J. Huang, L. A. Shi, S. H. Yu, *Adv. Mater.* **2016**, 28, 10459.
- [8] X. Feng, L. Jiang, *Adv. Mater.* **2006**, 18, 3063.
- [9] H.-M. Choi, J. P. Moreau, *Microsc. Res. Tech.* **1993**, 25, 447.
- [10] M. Paven, L. Mammen, D. Vollmer, *RSC Smart Mater.* **2016**, 20, 209.
- [11] B. Tansel, M. Lee, *J. Environ. Manage.* **2019**, 247, 363.
- [12] J. Wu, F. Xu, S. Li, P. Ma, X. Zhang, Q. Liu, R. Fu, D. Wu, *Adv. Mater.* **2019**, 31, 1802922.
- [13] M. Pumera, *Chem. Commun.* **2011**, 47, 5671.
- [14] S. Veziroglu, M. Z. Ghori, A. Obermann, K. Röder, O. Polonskyi, T. Strunskus, F. Faupel, O. C. Aktas, *Phys. Status Solidi* **2019**, 216, 1800898.
- [15] G. P. Lee, Y. Shi, E. Lavoie, T. Daeneke, P. Reineck, U. B. Cappel, D. M. Huang, U. Bach, *ACS Nano* **2013**, 7, 5911.
- [16] H. Yu, Q. Zhang, H. Liu, M. Dahl, J. B. Joo, N. Li, L. Wang, Y. Yin, *ACS Nano* **2014**, 8, 10252.
- [17] R. W. Berriman, R. H. Herz, *Nature* **1957**, 180, 293.
- [18] S. Tougaard, *Microsc. Microanal.* **2005**, 11, 2005.
- [19] G. Aresta, J. Palmans, M. C. M. van de Sanden, M. Creatore, *J. Vac. Sci. Technol., A* **2012**, 30, 041503.
- [20] S. Schröder, O. Polonskyi, T. Strunskus, F. Faupel, *Mater. Today* **2020**, 37, 35.
- [21] T. Watanabe, A. Nakajima, R. Wang, M. Minabe, S. Koizumi, A. Fujishima, K. Hashimoto, *Thin Solid Films* **1999**, 351, 260.
- [22] O. Carp, C. L. Huisman, A. Reller, *Prog. Solid State Chem.* **2004**, 32, 33.
- [23] J. Shondo, S. Veziroglu, D. Stefan, Y. K. Mishra, T. Strunskus, F. Faupel, O. C. Aktas, *Appl. Surf. Sci.* **2021**, 537, 147795.
- [24] D. Soto, A. Ugur, T. A. Farnham, K. K. Gleason, K. K. Varanasi, *Adv. Funct. Mater.* **2018**, 28, 1707355.
- [25] M. A. Gondal, M. S. Sadullah, M. A. Dastageer, G. H. McKinley, D. Panchanathan, K. K. Varanasi, *ACS Appl. Mater. Interfaces* **2014**, 6, 13422.
- [26] M. J. Kreder, J. Alvarenga, P. Kim, J. Aizenberg, *Nat. Rev. Mater.* **2016**, 1, 15003.
- [27] O. C. Aktas, S. Schröder, S. Veziroglu, M. Z. Ghori, A. Haidar, O. Polonskyi, T. Strunskus, K. Gleason, F. Faupel, *Adv. Mater. Interfaces* **2019**, 6, 1801967.
- [28] N. Atthi, W. Sripumkhai, P. Pattamang, O. Thongsook, R. Meananeatra, P. Saengdee, N. Ranron, K. Pankong, W. Uahchinkul, S. Radomyos, A. Srihapat, J. Supadech, N. Klunngien, W. Jeamsaksiri, *Jpn. J. Appl. Phys.* **2021**, 60, SCCJ01.
- [29] D. S. Kilin, O. V. Prezhdo, Y. Xia, *Chem. Phys. Lett.* **2008**, 458, 113.
- [30] T. Zubkov, D. Stahl, T. L. Thompson, D. Panayotov, O. Diwald, J. T. Yates, T. Zubkov, D. Stahl, T. L. Thompson, D. Panayotov, O. Diwald, J. T. Yates, *J. Phys. Chem. B* **2005**, 109, 15454.
- [31] Q. Ruan, T. Miao, H. Wang, J. Tang, *J. Am. Chem. Soc.* **2020**, 142, 2795.
- [32] H. Moon, H. Seong, W. C. Shin, W. T. Park, M. Kim, S. Lee, J. H. Bong, Y. Y. Noh, B. J. Cho, S. Yoo, S. G. Im, *Nat. Mater.* **2015**, 14, 628.
- [33] T. Kamegawa, K. Irikawa, H. Yamashita, *Sci. Rep.* **2017**, 7, 13628.
- [34] A. O. Ibadon, G. M. Greenway, Y. Yue, *Catal. Commun.* **2008**, 9, 153.
- [35] K. P. O. Mahesh, D.-H. Kuo, B.-R. Huang, M. Ujihara, T. Imae, *Appl. Catal. A Gen.* **2014**, 475, 235.
- [36] S. Cho, W. Choi, *J. Photochem. Photobiol., A* **2001**, 143, 221.
- [37] V. Senthikumar, M. Jayachandran, C. Sanjeeviraja, *Thin Solid Films* **2010**, 519, 991.
- [38] H. Fakhouri, J. Pulpytel, W. Smith, A. Zolfaghari, H. R. Mortaheb, F. Meshkini, R. Jafari, E. Sutter, F. Arefi-Khonsari, *Appl. Catal., B* **2014**, 144, 12.
- [39] J. Tauc, R. Grigorovici, A. Vancu, *Phys. Status Solidi* **1966**, 15, 627.
- [40] C. Adomnitez, S. Tascu, D. Luca, M. Dobromir, M. Girtan, D. Mardare, *Bull. Mater. Sci.* **2015**, 38, 1259.
- [41] S. Pan, A. K. Kota, J. M. Mabry, A. Tuteja, *J. Am. Chem. Soc.* **2013**, 135, 578.
- [42] G. B. D. Briggs, *J. Chem. Educ.* **1993**, 70, A25.
- [43] S. Veziroglu, A.-L. Obermann, M. Ullrich, M. Hussain, M. Kamp, L. Kienle, T. Leifner, H.-G. Rubahn, O. Polonskyi, T. Strunskus, J. Fiutowski, M. Es-Souni, J. Adam, F. Faupel, O. C. Aktas, *ACS Appl. Mater. Interfaces* **2020**, 12, 14983.
- [44] M. Z. Ghori, S. Veziroglu, B. Henkel, A. Vahl, O. Polonskyi, T. Strunskus, F. Faupel, O. C. Aktas, *Sol. Energy Mater. Sol. Cells* **2018**, 178, 170.
- [45] A. Vahl, S. Veziroglu, B. Henkel, T. Strunskus, O. Polonskyi, O. C. Aktas, F. Faupel, *Materials* **2019**, 12, 2840.
- [46] S. Schröder, T. Strunskus, S. Rehders, K. K. Gleason, F. Faupel, *Sci. Rep.* **2019**, 9, 2237.
- [47] S. Schröder, A. M. Hinz, T. Strunskus, F. Faupel, *J. Phys. Chem. A* **2021**, 125, 1661.
- [48] R. Tadmor, *Langmuir* **2004**, 20, 7659.

Supporting Information

for *Adv. Mater. Interfaces*, DOI: 10.1002/admi.202102126

Selective Adsorption and Photocatalytic Clean-Up of Oil by TiO₂ Thin Film Decorated with p-V₃D₃ Modified Flowerlike Ag Nanoplates

*Josiah Shondo, Salih Veziroglu, Tim Tjardts, Jacek Fiutowski, Stefan Schröder, Yogendra Kumar Mishra, Thomas Strunskus, Horst-Günther Rubahn, Franz Faupel, and Oral Cenk Aktas**

Supporting Information

Selective Adsorption and Photocatalytic Clean-up of Oil by TiO₂ Thin Film Decorated with p-V₃D₃ Modified Flowerlike Ag Nanoplates

Josiah Shondo, Salih Veziroglu, Tim Tjardts, Jacek Fiutowski, Stefan Schröder, Yogendra Kumar Mishra, Thomas Strunskus, Horst-Günther Rubahn, Franz Faupel, * and Oral Cenk Aktas *

Josiah Shondo, Dr. Salih Veziroglu, Tim Tjardt, Dr. Stefan Schröder, Dr. Thomas Strunskus, Prof. Dr. Franz Faupel*

Chair for Multicomponent Materials, Institute of Materials Science, Faculty of Engineering, Kiel University, Kaiserstr. 2, 24143 Kiel, Germany.

Dr. Jacek Fiutowski, Prof. Dr. Yogendra Kumar Mishra, Prof. Dr. Horst-Günther Rubahn

Mads Clausen Institute, NanoSYD, University of Southern Denmark, Alsion 2, 6400 Sønderborg, Denmark.

Prof. Dr. Oral Cenk Aktas *

Chair for Multicomponent Materials, Institute of Materials Science, Faculty of Engineering, Kiel University, Kaiserstr. 2, 24143 Kiel, Germany.

Additive Manufacturing Excellence Centre - URTEMM, Kahramankazan, 06980 Ankara, Turkey.

* *Corresponding authors: ff@tf.uni-kiel.de, oca@tf.uni-kiel.de*

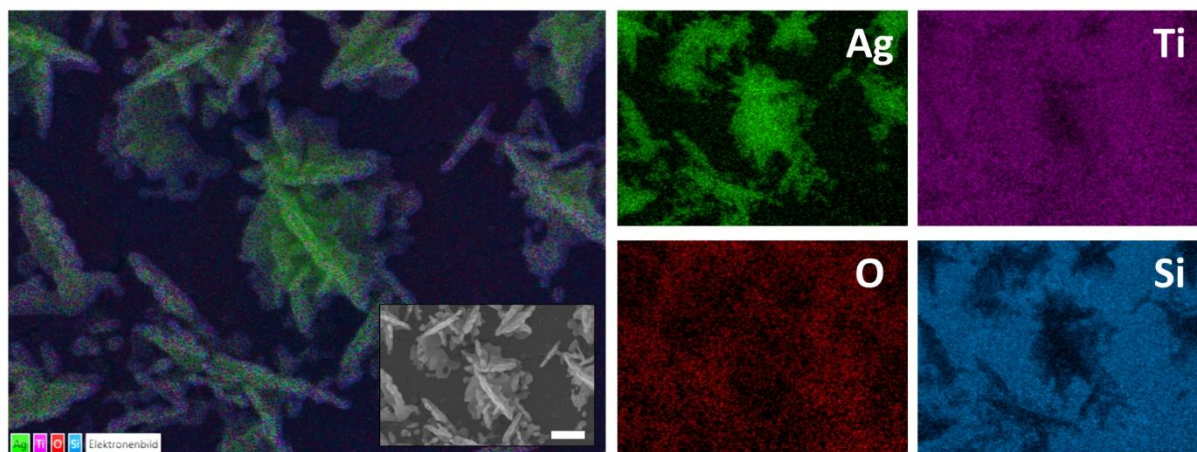


Figure S1. EDS elemental mapping of Ag, Ti, O and Si (from substrate) on the sample (Ag-TiO₂) surface (The corresponding SEM image is given in the inset. Scale bar: 500nm).

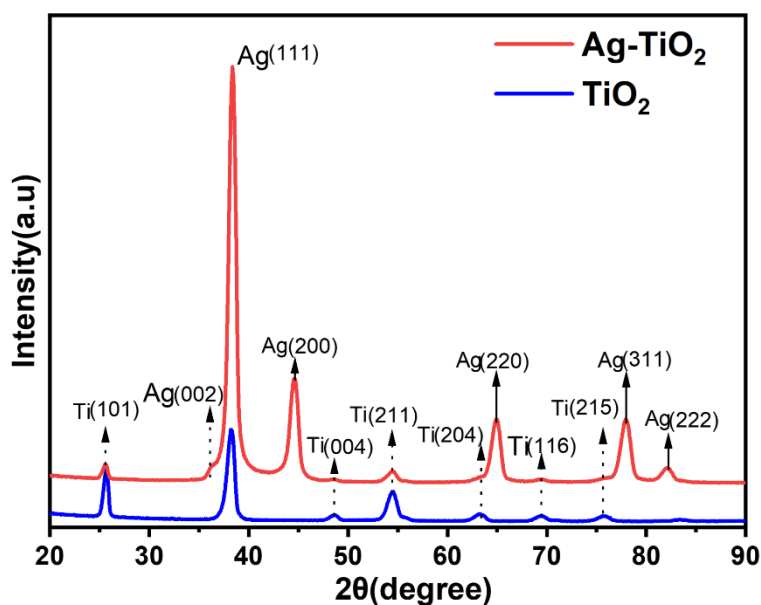


Figure S2: Grazing incidence X-ray diffractogram (GIXRD) pattern of TiO₂ thin film (Blue) and flowerlike Ag nanoplates on TiO₂ (Red).

Table S1: Static, advancing, receding, and sliding water contact angles of p-V₃D₃ and PTFE over-coated Ag/TiO₂ at respective thicknesses.

Coated polymer	Film thickness (nm)	Static WCA (deg)	Advancing WCA (deg)	Receding WCA (deg)	Sliding WCA (deg)
p-V ₃ D ₃	25	162.8	166.1	152.4	<10.0
p-V ₃ D ₃	100	155.9	165.5	152.1	<10.0
PTFE	25	163.7	167.2	153.5	<10.0
PTFE	100	157.8	165.8	152.7	<10.0

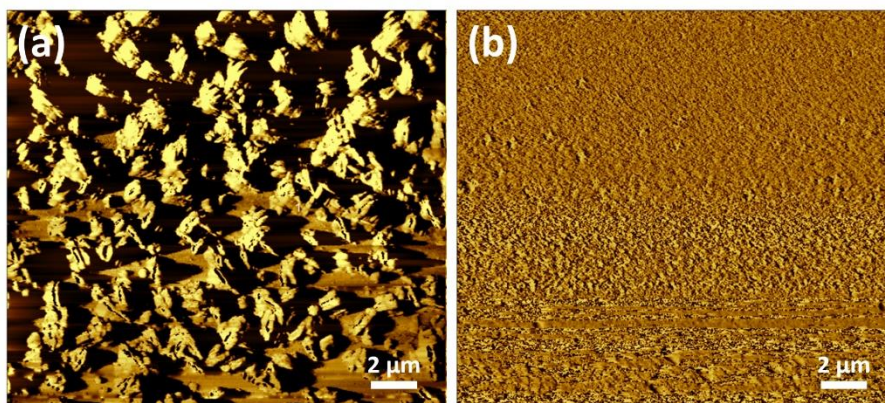


Figure S3: AFM images of surface topography of (a) TiO₂ thin film decorated with flowerlike Ag nanoplates and (b) bare TiO₂ thin film.

Contact angle: **5.8°**



Figure S4. Contact angle image of the oil droplet on p-V₃D₃/Ag/TiO₂ surface.

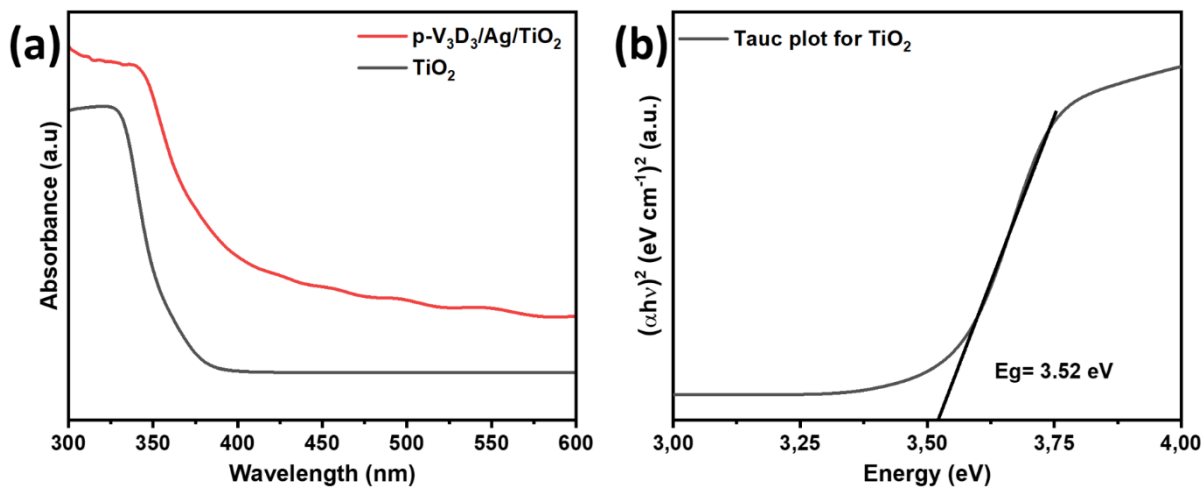


Figure S5. (a) UV-Vis absorbance spectra of TiO₂ and p-V₃D₃-Ag/TiO₂ and (b) the corresponding Tauc plot for the bandgap calculation of TiO₂.

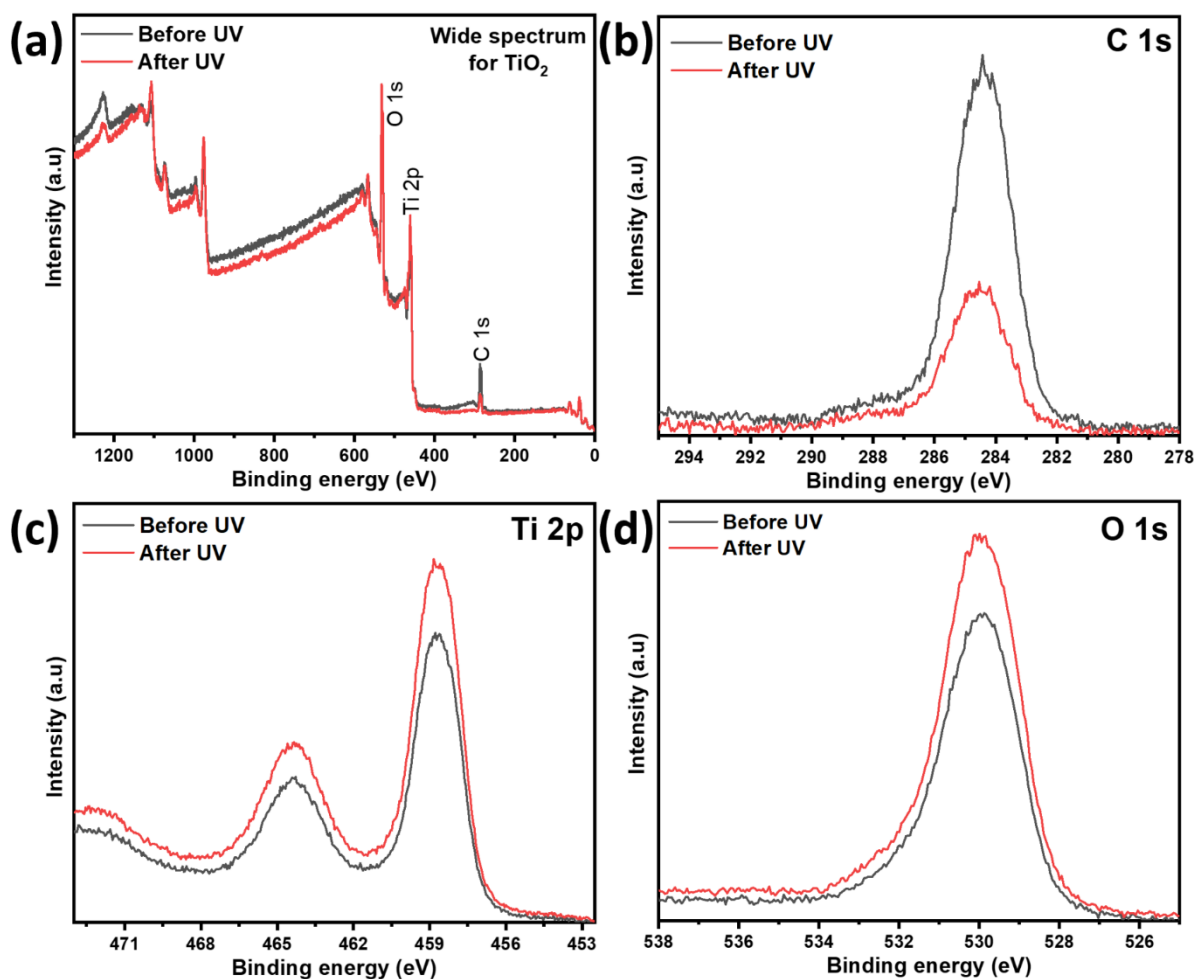


Figure S6: XPS spectra of TiO₂ contaminated with oleic acid (a) wide spectrum, (b) C 1s, (c) Ti 2p, and (d) O 1s.

Table S2: Relative atomic concentration (%) distribution on TiO₂ contaminated with oleic acid.

Element line	% Atomic concentration before UV irradiation	Peak intensity	% Atomic concentration after UV irradiation	Peak Intensity
C 1s	40.8	3000.0	19.8	1507.6
O 1s	43.6	1260.6	59.2	1507.2
Ti 2p	15.6	860.2	21.0	1050.0

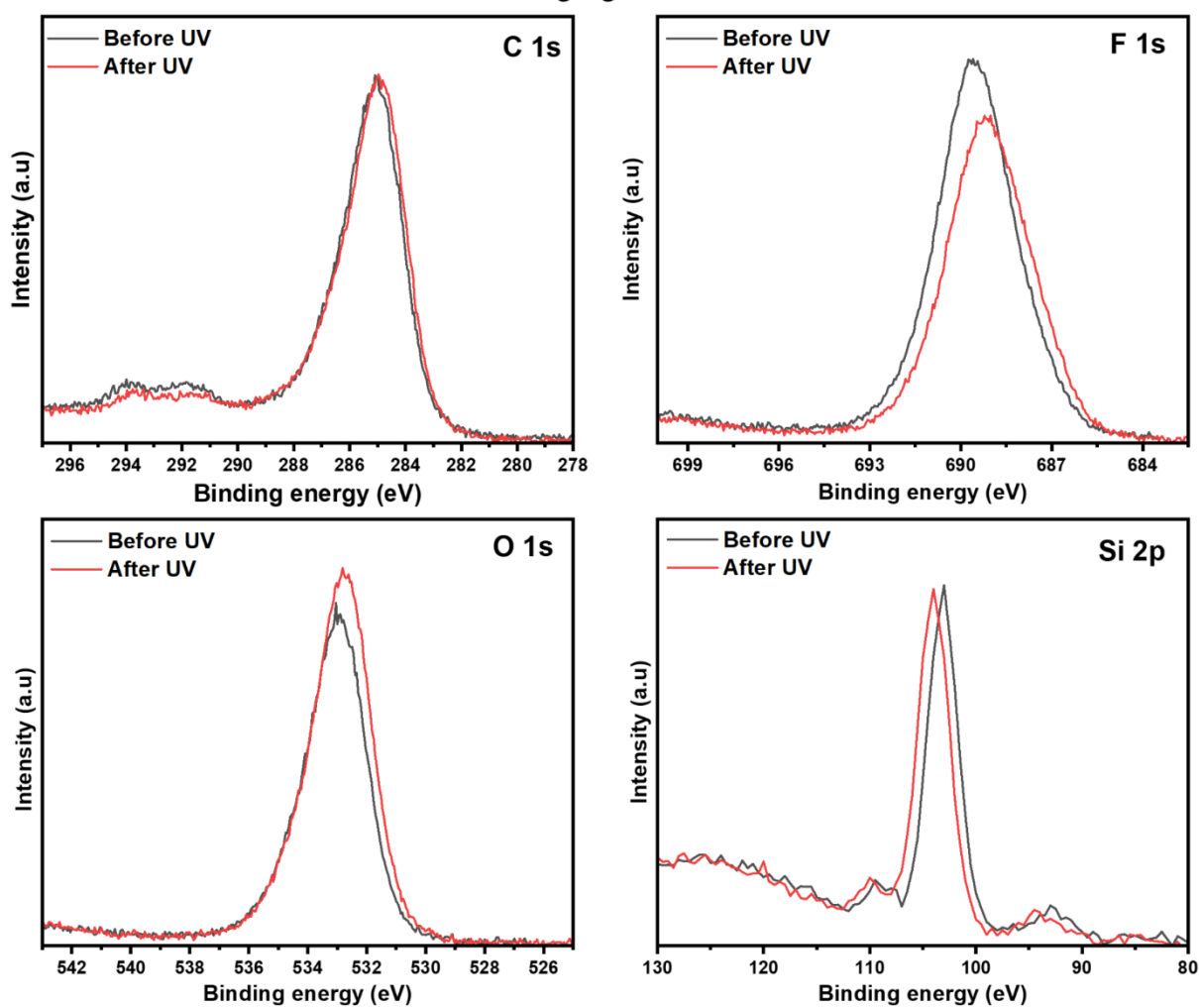
p-V₃D₃ Layer

Figure S7. Curve-fitted as-measured C 1s, F 1s, O 1s, and Si 2p XPS core-level spectra for p-V₃D₃ before and after UV irradiation.

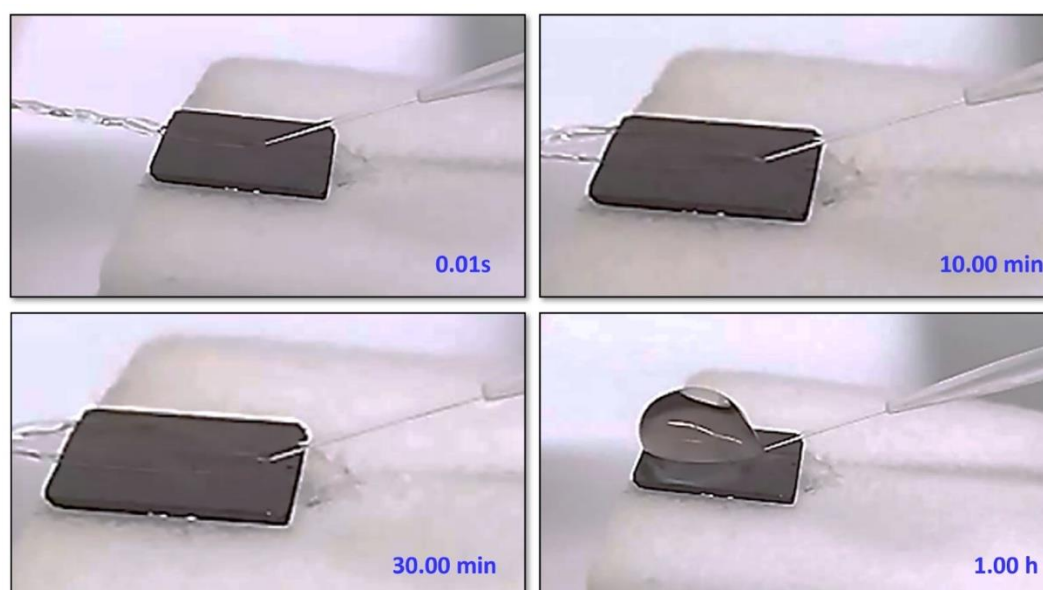


Figure S8: Jets of pressurized water bouncing on the surface of pV₃D₃ over-coated Ag-TiO₂ surface.

Table S3: Chemical robustness testing of p-V₃D₃ over-coated Ag/TiO₂ surface.

Chemical /Concentration	Wetting Angle Before dipping test	Wetting Angle After dipping test
3M KOH	153.0°±3	151.8°±3
3M NaOH	151.8°±3	150.5°±3
3M H ₂ SO ₄	150.5°±3	151.0°±3
3M HCl	151.0°±3	149.8°±3

25 nm p-V₃D₃ on Ag-TiO₂

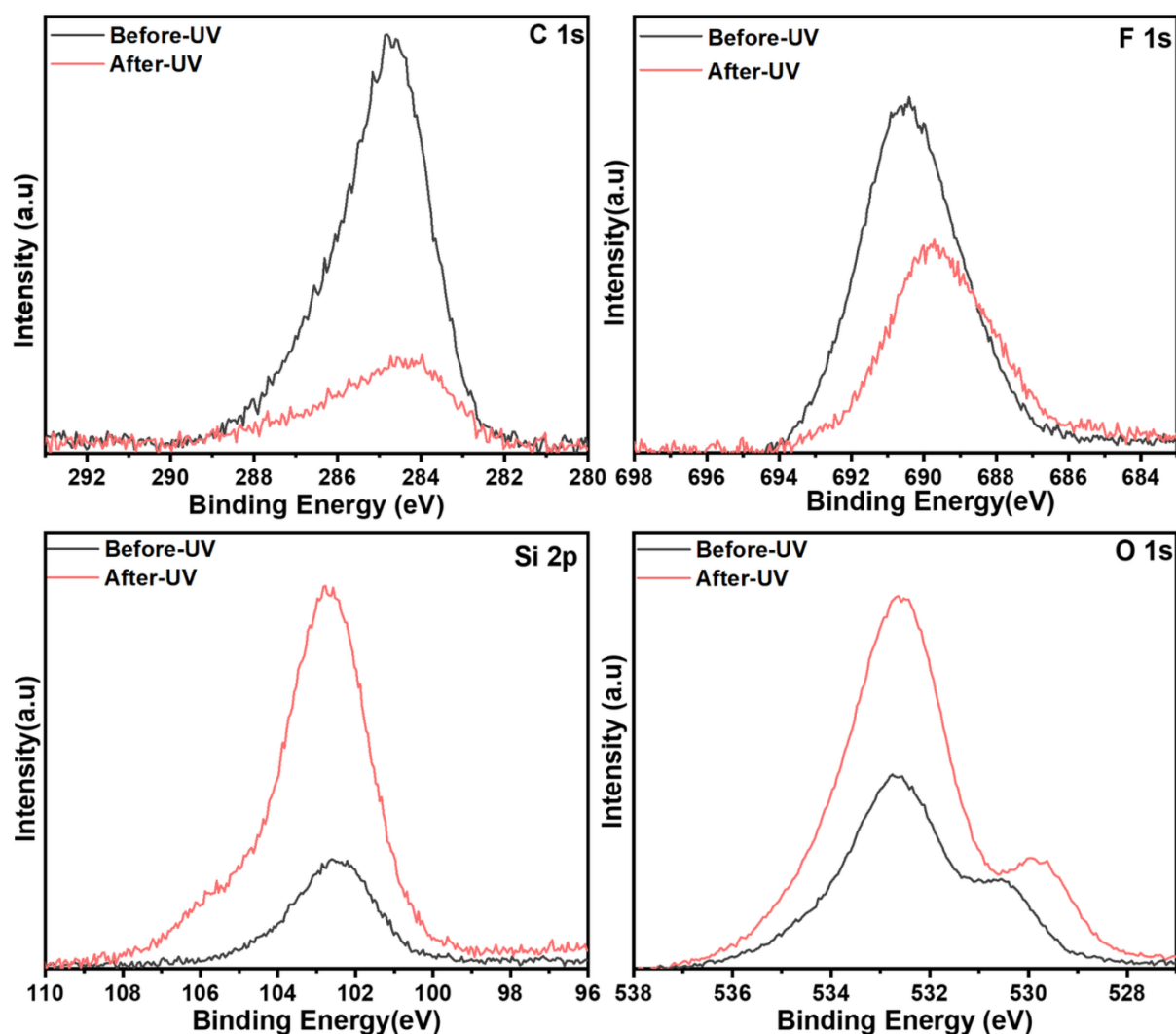


Figure S9: High resolution XPS spectra of hexadecane oil contaminated 25 nm p-V₃D₃ over-coated Ag/TiO₂ showing (a) C 1s, (b) F 1s, (c) Si 2p, and (d) O 1s, respectively before and after UV irradiation.

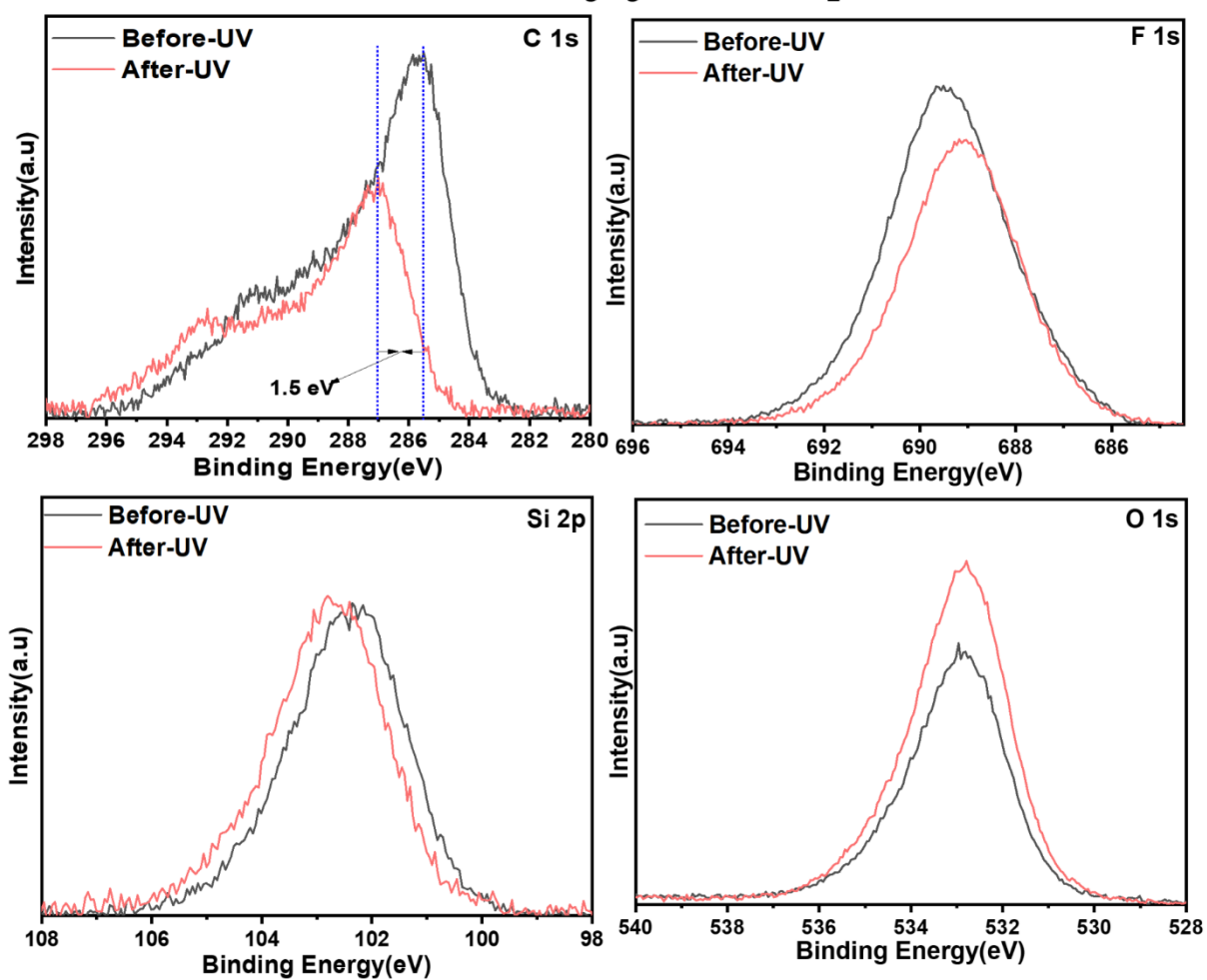
100 nm p-V₃D₃ on Ag-TiO₂

Figure S10: High resolution XPS of hexadecane oil contaminated 100 nm p-V₃D₃ over-coated Ag/TiO₂ showing (a) C 1s, (b) F 1s, (c) Si 2p, and (d) O 1s, respectively before and after UV irradiation.

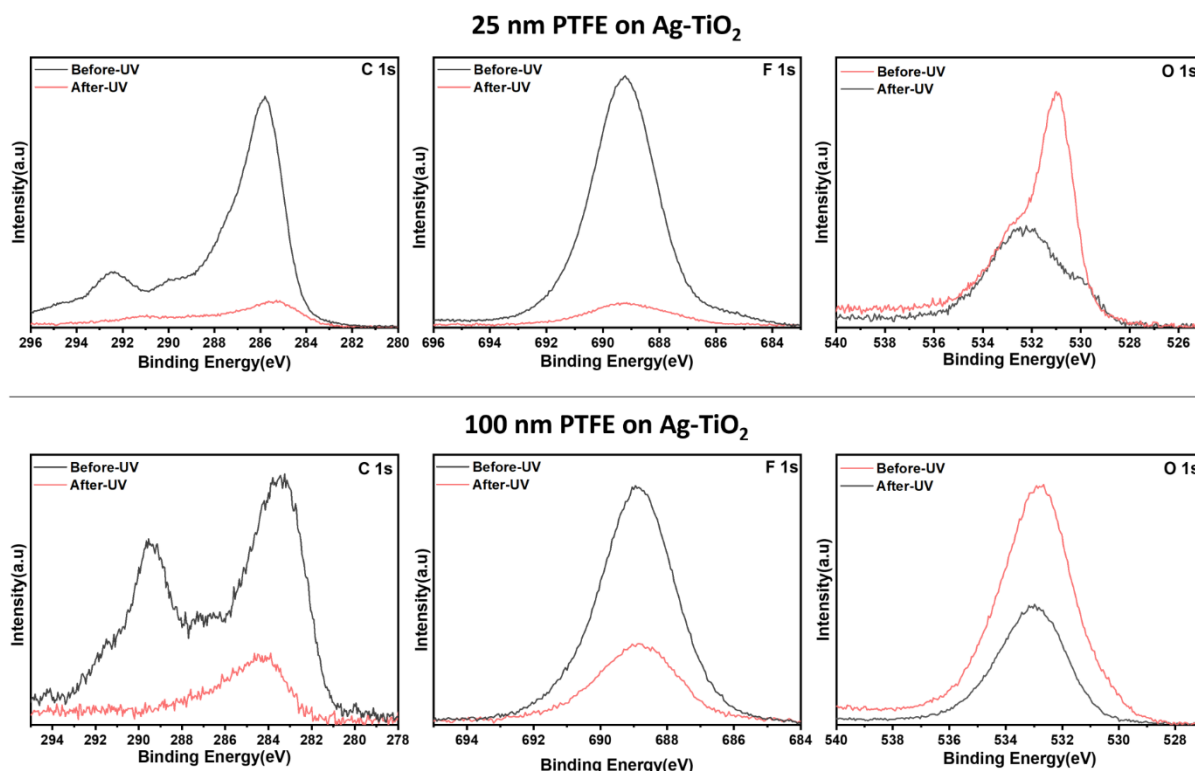


Figure S11: High resolution XPS spectra showing C 1s, F 1s, and O 1s on hexadecane contaminated 25 nm and 100 nm PTFE over-coated Ag/TiO₂ before and after UV irradiation.

Table S4: Elemental atomic concentration (%) analysis on p-V₃D₃/Ag/TiO₂ before and after UV irradiation.

Elemental composition	Before UV irradiation 25 nm	After UV irradiation 25 nm	Before UV irradiation 100 nm	After UV irradiation 100 nm
O 1s	20.54	62.53	20.15	35.48
C 1s	45.26	7.32	46.16	34.33
F 1s	17.22	1.29	19.20	11.97
Si 2p	13.82	24.06	14.44	13.42
Ag 3d	1.84	2.50	0.05	1.36
Ti 2p	1.32	2.30	-	3.44

Captions for Supplementary Videos

Video S1: Bouncing of the water droplet (colored with pinkish dye) on p-V₃D₃/Ag/TiO₂ surface

Video S2: Spreading of the oil droplet on p-V₃D₃/Ag/TiO₂ surface

Video S3: Chemical robustness testing of p-V₃D₃/Ag/TiO₂ surface in 3M KOH

Video S4: Chemical robustness testing of p-V₃D₃/Ag/TiO₂ surface in 3M H₂SO₄

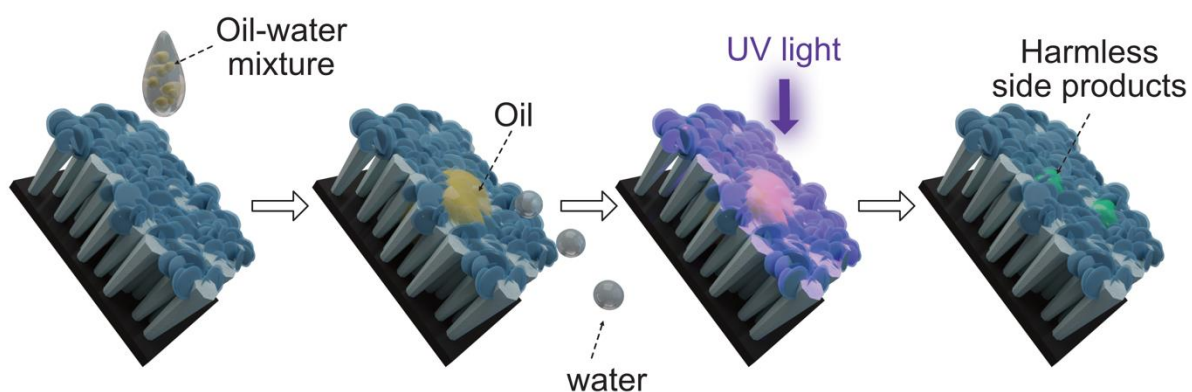
Video S5: Chemical robustness testing of p-V₃D₃/Ag/TiO₂ surface in 3M HCl

Video S6: Chemical robustness testing of p-V₃D₃/Ag/TiO₂ surface in 3M NaOH

Video S7: Bouncing off water jet from superhydrophobic surface

Video S8: Selective oil adsorbance on p-V₃D₃/Ag/TiO₂ surface

Graphical Abstract



CHAPTER FIVE

This chapter explains nanoscale synergetic effects on Ag–TiO₂ hybrid substrate for photoinduced enhanced Raman spectroscopy (PIERS) with ultra-sensitivity and reusability. 4N-in-1 hybrid substrate concept (nanocolumnar structures, nanocrack network, nanoscale mixed oxide phases, and nanometallic structures) for ultra-sensitive and reliable photo-induced-enhanced Raman spectroscopy (PIERS) and photocatalytic clean-up of analytes.

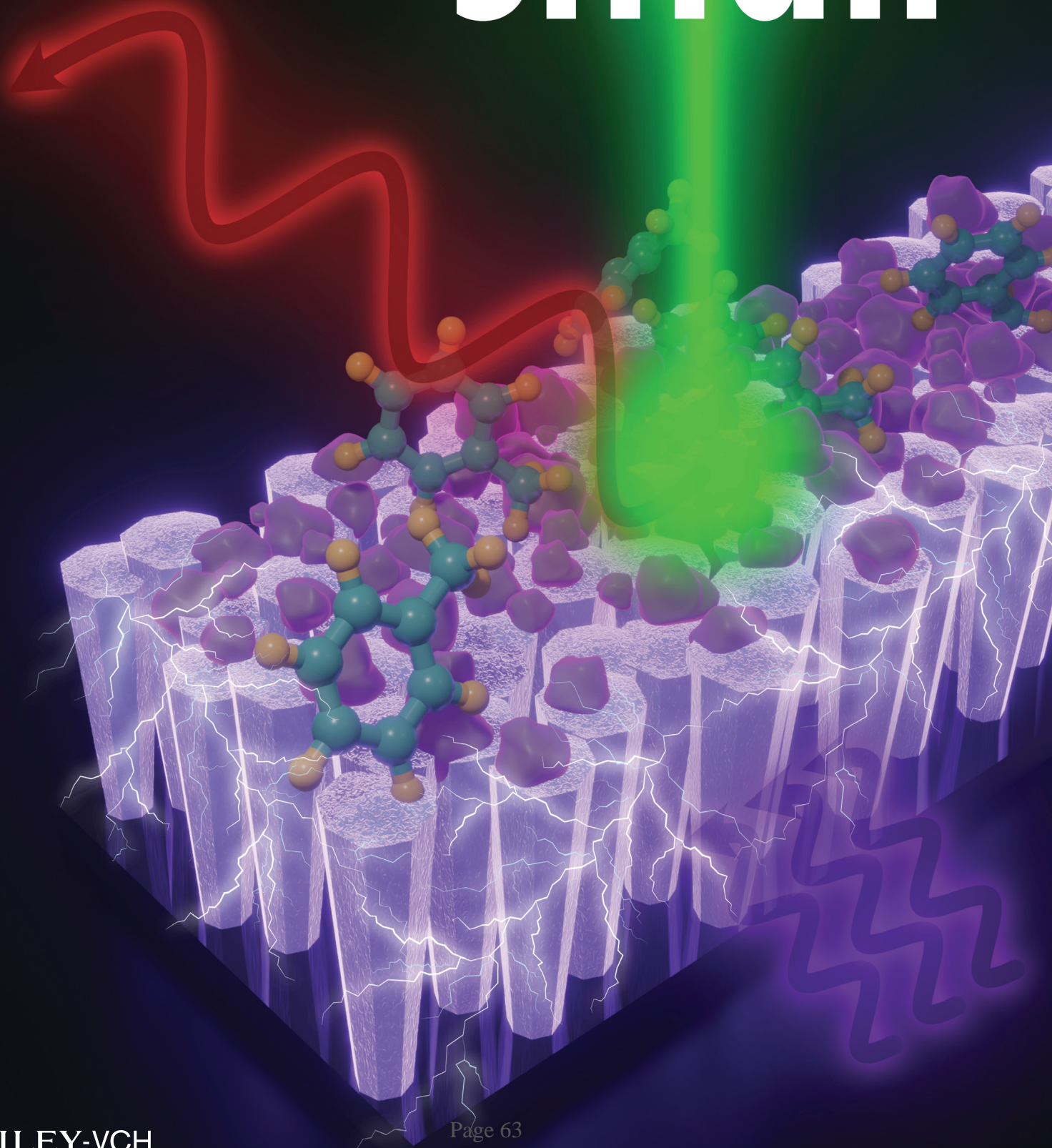
This chapter is a reprint from the following publication:

J. Shondo, S. Veziroglu, T. Tjardts, T. bin Sarwar, Y. K. Mishra, F. Faupel, O. C. Aktas, *Small* 2022, 18, DOI 10.1002/sml.202203861.

Vol. 18 • No. 50 • December 15 • 2022

www.small-journal.com

NANO • MICRO small



Nanoscale Synergetic Effects on Ag–TiO₂ Hybrid Substrate for Photoinduced Enhanced Raman Spectroscopy (PIERS) with Ultra-Sensitivity and Reusability

Josiah Shondo, Salih Veziroglu, Tim Tjardts, Tamim Bin Sarwar, Yogendra Kumar Mishra, Franz Faupel,* and Oral Cenk Aktas*

Here, a 4N-in-1 hybrid substrate concept (nanocolumnar structures, nano-crack network, nanoscale mixed oxide phases, and nanometallic structures) for ultra-sensitive and reliable photo-induced-enhanced Raman spectroscopy (PIERS), is proposed. The use of the 4N-in-1 hybrid substrate leads to an ≈50-fold enhancement over the normal surface-enhanced Raman spectroscopy, which is recorded as the highest PIERS enhancement to date. In addition to an improved Raman signal, the 4N-in-1 hybrid substrate provides a high detection sensitivity which may be attributed to the activation possibility at extremely low UV irradiation dosage and prolonged relaxation time (long measurement time). Moreover, the 4N-in-1 hybrid substrate exhibits a superior photocatalytic degradation performance of analytes, allowing its reuse at least 18 times without any loss of PIERS activity. The use of the 4N-in-1 concept can be adapted to biomedicine, forensic, and security fields easily.

and biomolecules,^[1] monitoring the environmental pollution and toxicity,^[2] identification of narcotics and explosives, and detection of chemical and biological hazards within the forensic context^[3,4] due to its ease of use and integration, chemical-specific detection capability, nondestructiveness, and label-free mode of operation.^[5] In comparison to ordinary Raman spectroscopy, SERS provides a superior Raman intensity with an enhancement factor (EF) of several orders of magnitude, thanks to both the electromagnetic mechanism (EM) and chemical mechanism (CM) involved at the substrate surface.^[6] EM arises basically from the localized surface plasmon resonance (LSPR) and CM results from the

chemical interactions (charge transfer and charge resonance) between the analyte molecules and the substrate surface.^[7] EM is accepted as the primary SERS mechanism by providing an EF of 10⁷–10¹² through plasmonic metallic nanostructures, while CM leads to an EF of 10–10³ and it acts as the secondary mechanism for SERS.^[8,9]

The substrate plays the most critical role in the performance of SERS-based analytic techniques. The shape, orientation, and interspacing of plasmonic nanostructures on the SERS substrate greatly affect the SERS intensity and sensitivity since all these play a role on the interaction of light with the surface.^[10,11] It has been shown that periodic metallic nanostructures provide more reproducible, uniform, and high-density hotspots on the substrate surface.^[12] Although various advanced bottom-up and top-down fabrication methods and material combinations (1D, 2D, and 3D nanomaterials) have been demonstrated to prepare SERS active substrates, it is still challenging to achieve substrates with uniformly distributed hotspots and to maintain their stability against the analytes, solvents, and aging by the time.^[13,14] In addition, time-consuming fabrication methods as well as single use nature of SERS substrates cause a high operational cost.

Apart from intense research going on the development of SERS substrates with high EFs and low-cost fabrication methods to produce such substrates, Parkin et al. reported totally a different approach which yields a significant enhancement of the Raman signal of analyte molecules on a metal–semiconductor hybrid substrate through preirradiating it by ultraviolet (UV) light (which is termed as photo-induced enhanced Raman

1. Introduction


Surface-enhanced Raman spectroscopy (SERS) has become a widely used analytical technique for the detection of biocides

J. Shondo, S. Veziroglu, T. Tjardts, T. B. Sarwar, F. Faupel, O. C. Aktas
Chair for Multicomponent Materials
Institute of Materials Science
Faculty of Engineering
Kiel University
Kaiserstr. 2 24143, Kiel, Germany
E-mail: ff@tf.uni-kiel.de; oca@tf.uni-kiel.de

S. Veziroglu, F. Faupel
Kiel Nano, Surface and Interface Science KiNSIS
Kiel University
Christian Albrechts-Platz 4 24118, Kiel, Germany

Y. K. Mishra
Mads Clausen Institute
NanoSYD
University of Southern Denmark
Alsion 2, Sønderborg 6400, Denmark

O. C. Aktas
Additive Manufacturing Excellence Centre – URTEMM
Kahramankazan, Ankara 06980, Turkey

 The ORCID identification number(s) for the author(s) of this article can be found under <https://doi.org/10.1002/smll.202203861>.

© 2022 The Authors. Small published by Wiley-VCH GmbH. This is an open access article under the terms of the Creative Commons Attribution-NonCommercial-NoDerivs License, which permits use and distribution in any medium, provided the original work is properly cited, the use is non-commercial and no modifications or adaptations are made.

DOI: 10.1002/smll.202203861

spectroscopy—PIERS).^[15] Basically, the preirradiation with UV light generates oxygen vacancies (V_O) (through catalytic reactions with adsorbed O_2 and H_2O), and the V_O density increases with the irradiation time.^[15–17] Various studies showed that the metal–oxide semiconductor interface can locate and stabilize V_O . Basically, V_O leads to the enhancement of the Raman signal through facilitating the charge transfer between the photoirradiated oxide semiconductor film (decorated with metallic nanostructures) and analyte molecules via metallic nanostructures deposited on the surface (a semiconductor composed of V_O exhibits a valence state below the conduction band and this facilitates the charge transfer from V_O to the metallic nanostructures and then to the analyte molecule).^[16] Li et al. showed that on a Ag– TiO_2 hybrid surface photogenerated electrons in TiO_2 and the hot electrons injected (LSPR) from Ag nanostructures simultaneously promote the photocatalytic reactions and charge transfer to analyte molecules.^[18] Therefore in metal–semiconductor hybrid substrates, the increase in the electron density (photogenerated) as well as the plasmonic nature of metallic nanostructures (LSPR) enhance the Raman scattering of analyte molecules.^[19]

Following the pioneering work of Parkin's research group, various substrates including sole semiconductors and their combination with metallic nanostructures, have been studied to reveal their applicability as PIERS substrates.^[15] The ultrafast recombination time ranging from picoseconds to microseconds hinders the use of semiconductors solely as PIERS substrate.^[17] Semiconductors and even insulators decorated with metallic nanostructures have been shown as alternative PIERS substrates, but a large bandgap limits the PIERS performance since incident photon energy becomes insufficient to create adequate amount of oxygen vacancies.^[20]

Combining metallic nanostructures with semiconductors such as TiO_2 and ZnO, has been shown to trigger the formation of V_O with high density and stability.^[12,21] Irradiation wavelength and duration also play an important role in the V_O formation.^[22] The energy of the incident photons must be at least equal or even larger than the bandgap energy of the semiconductor substrate to induce V_O formation. V_O act as additional valence states below the conduction band edge of the semiconductor, and this facilitates the charge migration from the semiconductor to the metallic nanostructures.^[23] Here, V_O is proportional to the irradiation time and the intensity, but very high irradiation dosages (irradiation intensity and/or time) can lead to vacancy healing and photo-induced bleaching of the analyte molecule, which decrease overall Raman detection performance.^[24]

The performance of PIERS substrate also depends on the relaxation time; the intensity of the Raman signals decays gradually to the original level after the removal of light irradiation due to the recombination of electrons and holes.^[17] Obviously, a longer relaxation time allows for efficient collection of Raman signals and reproducible measurements. Parkin et al. achieved an EF of 34.79 after exposing TiO_2 surface decorated with Au nanostructures to UV light for extremely a long time interval (exceeding 240 min).^[15] Zhang et al. reached EF of 27.8 by preirradiating Ag– TiO_2 surface with a mercury lamp operating at extremely high power (300 W) for 1–3 h.^[25] In both cases, high EF was achieved by applying an extremely high irradiation

dosage, but this increases the risk of photo-induced (UV driven photochemical reactions) and/or photocatalytic (catalytic reactions induced by photogenerated electrons) bleaching of analytes.^[26] On the other hand, if the photocatalytic bleaching of analyte molecules can be controlled, this may allow the reusability of PIERS substrates. But for such an approach, the metal–semiconductor hybrid substrate should be highly photocatalytically active to facilitate the generation of oxygen vacancies at extremely low UV irradiation dosage (otherwise, the use of high intensity irradiation will be needed, which is detrimental for organic analytes). Additionally, at such a low irradiation dosage, the relaxation time should still be long enough to conduct multiple measurements. Such a PIERS substrate can be simply cleaned up by increasing the UV irradiation slightly. For reusability of the PIERS substrate, one should also ensure the stability in terms of PIERS signal (position, intensity, and sensitivity) after several measurement cycles (analyte loading, measurement, and cleaning) and ideally, stability should be proven by employing different types of analytes for consecutive cycles.^[27]

In the current study, we report on a significant enhancement of PIERS signal for Ag– TiO_2 hybrid substrate at extremely low UV irradiation dosage (with an irradiation intensity of 4.5 mW cm^{-2} and irradiation period of 8 min). We term this novel hybrid substrate, which leads to the enhancement of PIERS signal by a factor of around 50, as “4N-in-1 PIERS substrate.” In addition to the long relaxation time exceeding 240 min, the 4N-in-1 PIERS substrate exhibited an excellent reusability without any loss of PIERS activity after 18 cycles.

2. Results and Discussion

2.1. 4N-in-1 Hybrid Substrate and Characterization

Here 4N refers to i) nanocolumnar structures, ii) nanocrack network, iii) nanoscale mixed oxide phases, and iv) nanometallic structures (as depicted schematically in **Figure 1a**. Reactive sputtering and subsequently conducted heat treatment (heating and air quenching) led to the formation of columnar nanostructures and dense network of nanocracks, respectively. A critical temperature has been revealed to maximize the crack generation and promote the coexistence of rutile and anatase phases (which foster charge transfer and migration due to slight differences in their band gaps.^[28] High photocatalytic nature of mentioned TiO_2 film allows the controlled deposition of metallic Ag nanostructures under low-intensity UV irradiation, which prevents any agglomeration and excessive growth.

The 4N-in-1 hybrid substrate was prepared by a two-step process. First, TiO_2 thin film with a thickness of 500 nm (composed of columnar nanostructures and nanocrack networks as shown in Figures 1b and 1c (Figure S1, Supporting Information), respectively) was prepared by reactive DC magnetron sputtering under relatively high oxygen partial pressure as reported earlier.^[29,30] As we showed previously, subsequent heat treatment just after the sputtering led to the formation of networks of dense nanocracks and mixed rutile and anatase phases (Figure 1d and Figure S2, Supporting Information). We have shown that our sputter deposited TiO_2 layer outperforms

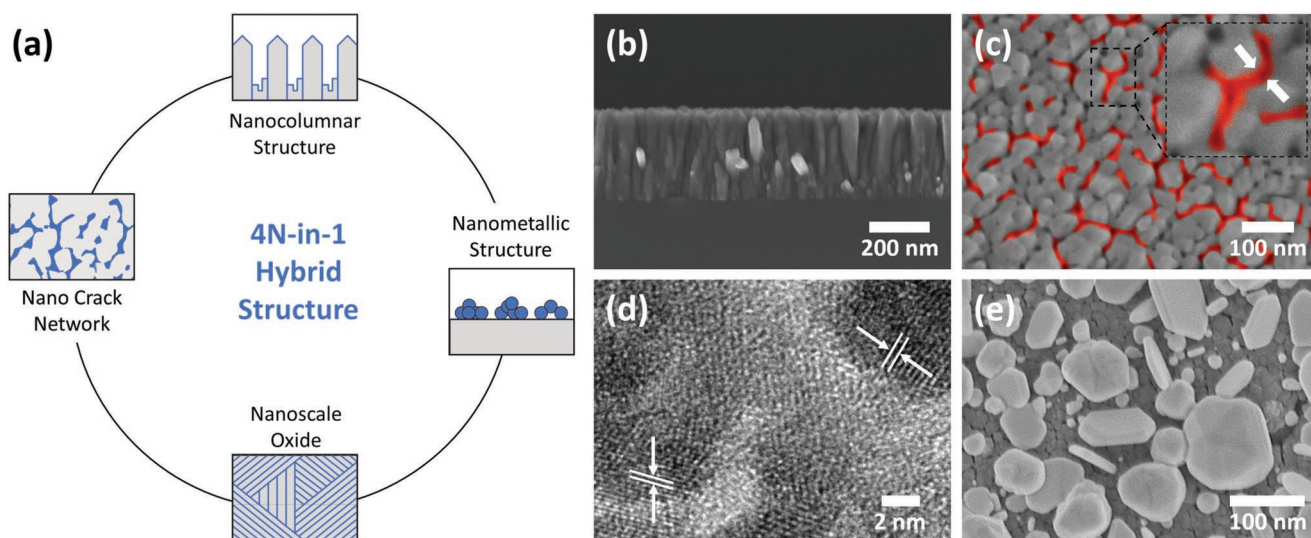


Figure 1. a) Schematic depicting 4N-in-1 PIERS substrate concept, b) cross-sectional SEM image of TiO_2 nanocolumnar structures, c) SEM image of nanocracks networks on TiO_2 thin film; (arrows indicate a crack size of 30–35 nm), d) HR-TEM images of mixed TiO_2 phases (Anatase + Rutile phases are revealed by corresponding lattice spacings), and e) SEM images of TiO_2 thin film decorated with Ag nanostructures (corresponding surface coverage is $\approx 44.9\%$) via photocatalytic deposition.

well-known P25 TiO_2 nanoparticles, which are highly crystalline and have a high surface area of $35\text{--}65\text{ m}^2\text{ g}^{-1}$ (as accepted as the golden standard to evaluate the photocatalytic activity of materials), by a factor of 29.5%.^[29] As a second step, Ag nanostructures were reduced (from an aqueous solution of AgNO_3) preferentially on TiO_2 thin film surface via the photocatalytic deposition process developed earlier.^[31] Following the irradiation of TiO_2 thin film surface with UV light operating at a wavelength of 365 nm and a power of 4.5 mW cm^{-2} for 20 min, photogenerated electrons reduced Ag^+ ions to stable Ag^0 (metallic silver) on the TiO_2 thin film surface. The prepared 4N-in-1 hybrid surface morphology is visualized by scanning electron microscopy (SEM) analysis as shown in Figure 1e. One can alter the surface coverage of Ag% on the TiO_2 thin film surface simply by increasing the photocatalytic deposition time as shown in Figure S3, Supporting Information. The possibility of using low UV irradiation (thanks to the high photocatalytic activity of TiO_2 thin film) seems to be effective in hindering the growth within the solution and uncontrolled agglomeration of Ag particles on TiO_2 surface. We conducted X-ray photoelectron spectroscopy (XPS) to determine the surface chemistry of the prepared 4N-in-1 hybrid substrates with different Ag% surface coverage. For all samples, we observed that Ag 3d spectra consists of two peaks corresponding to Ag $3d_{3/2}$ and Ag $3d_{5/2}$ with a binding energy difference of $\approx 6.0\text{ eV}$, which clearly proves the formation of stable metallic Ag (Figure S4, Supporting Information).^[32] In Figure S4, Supporting Information, one can see that Ti 2p spectra are composed of two prominent characteristic peaks known as Ti $2p_{1/2}$ and Ti $2p_{3/2}$, respectively.^[31] The distance between these two peaks is $\approx 5.6\text{ eV}$ in case of bare TiO_2 , which can be attributed to the Ti^{4+} state indicating the formation of stable TiO_2 .^[33,34] On the other hand, it can be clearly seen from high-resolution XPS spectra of Ti 2p (Figure S4, Supporting Information), that increasing Ag content on the surface causes a positive shift of the two-distinct Ti 2p peaks. Pei et al.

reported a positive shift in Ti 2p which may be attributed to defective Ti^{3+} structure.^[35] In principle, V_O transfer their extra two electrons to the adjacent two Ti^{4+} atoms to form Ti^{3+} .^[36,37] Here the increase in the amount of V_O with the increase in Ag% on the surface can be explained by the growth of Ag– TiO_2 interface.^[38]

Furthermore, the O 1s spectrum originated from adsorbed oxygen, hydroxyl groups, and lattice oxygen are also shown in Figure S4, Supporting Information.^[39] This clearly shows that increasing of Ag content on TiO_2 surface promotes the adsorption of higher amounts of oxygen and hydroxyl groups which certainly also plays a role in the formation and stabilization of V_O .^[40] On the other hand, we did not see any oxidation on Ag particles since satellite peaks at 366 eV (Figure S4, Supporting Information). This also explains that the increase in adsorbed oxygen amount (O 1s spectra) should be related to the change in the state of Ti^{4+} (increase in the amount of V_O and transformation of Ti^{4+} state to Ti^{3+}).

2.2. PIERS Analysis and Mechanism

To demonstrate the PIERS performance of the 4N-in-1 hybrid substrate, we conducted two consecutive SERS measurements with and without applying a UV pre-irradiation step. For PIERS, we exposed the 4N-in-1 hybrid substrate to the UV-LED light source operating at a wavelength of 365 nm for 8 min. Afterward, $10\text{ }\mu\text{L}$ of ethanolic solution of Rhodamine 6G analyte ($\text{R6G} \approx 10^{-7}\text{ M}$) was drop-casted on 4N-in-1 hybrid substrate, and the sample was dried in the dark for 10 min. Similarly, we loaded the same analyte on another 4N-in-1 hybrid substrate and allowed it to dry in the dark for also 10 min. The intensity difference of PIERS and SERS spectra recorded at an integration time of 5 s (using a laser source operating at a wavelength of 532 nm and an intensity of $15\text{ }\mu\text{W}$) is shown in Figure 2a;

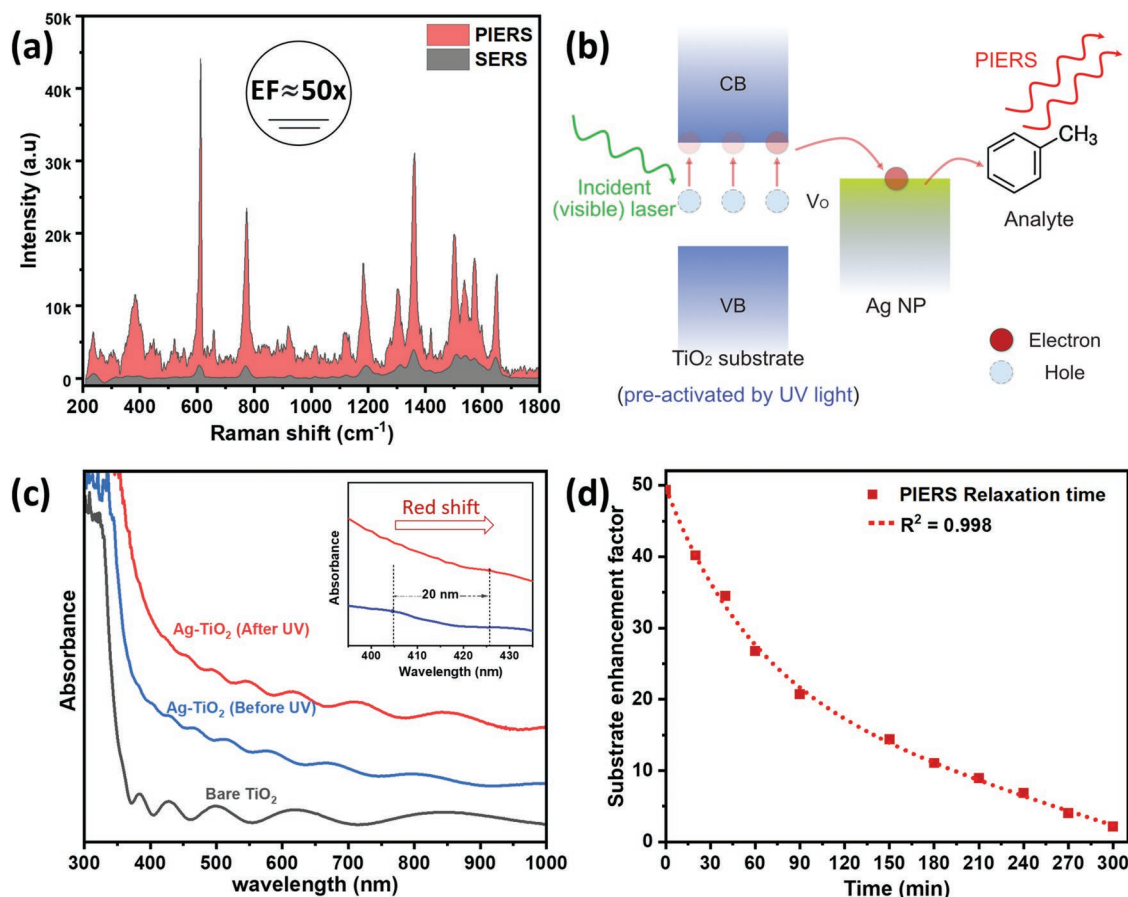


Figure 2. a) Comparison of PIERS and SERS performance of 4N-in-1 hybrid substrate for the detection of trace amount of RG6 analyte ($\approx 10^{-7}$ molar), b) PIERS mechanism for 4N-in-1 hybrid substrate, c) comparison of UV-vis absorbance spectra of 4N-in-1 hybrid substrate before and after UV irradiation (inset shows the red-shift), and d) relaxation curve (decay of the PIERS signal) after removing UV irradiation.

there is a significant enhancement in terms of Raman signal intensity through UV irradiation. The Raman intensity of the peak located at 611 cm^{-1} increases from 894 to 44 098 cps, which is around 50-fold (depending on the distribution density of Ag nanostructures, slight differences can be seen in enhancement in Raman signals recorded from different position on 4N-in-1 PIERS substrate as shown in Figure S5, Supporting Information). Our systematic study showed that EF is proportional to preirradiation time (Figure S6, Supporting Information) but we achieved the highest EF (which corresponds to the highest photoinduced charge generation) between 5 and 10 min. In general, the rate of a photocatalytic reaction is proportional to the irradiation flux (high irradiation flux generates high number of photo-induced electrical charges). On the other hand, above a certain value (estimated to be $\approx 25\text{ mW cm}^{-2}$) the reaction rate reaches a saturation;^[41] similarly we observed that longer irradiation period ($>10\text{ min}$) does not lead to further enhancement in Raman signal (Figure S6, Supporting Information).

Similar like commercial SERS substrates, 4N-in-1 hybrid substrate also exhibits a significant enhancement in Raman signal without any preirradiation by UV (which can be referred as classical SERS enhancement). However, after UV preirradiation 4N-in-1 hybrid substrate (in PIERS mode) exhibits a superior detection capability (R6G prepared at $\approx 10^{-7}\text{ M}$) in comparison

to commercial SERS substrates (Figure S7, Supporting Information). Detection limit of 4N-in-1 hybrid structure can be extended to very low concentrations around 10^{-14} M as demonstrated at Figure S8, Supporting Information.

While in classical SERS, Raman signal enhancement is mainly determined by the LSPR of metallic nanostructures on the surface, in PIERS, an additional enhancement comes from the UV induced charge migration from the semiconductor substrate to the metallic nanostructures as schematically depicted in Figure 2b. Various studies showed that the metal-oxide interface can locate and stabilize V_O .^[16,42] Here, the production of V_O permits enhancing the Raman signal of chemical molecules through charge transfer processes between the photo-irradiated TiO_2 film and analyte molecules via metallic Ag nanostructures.^[16] High-resolution XPS spectra of Ti 2p (at Figure S4, Supporting Information) shows that increasing Ag content on the surface causes a positive shift of two-distinct Ti 2p peaks, which may indicate indirectly the presence of V_O .^[35] The increase in the amount of V_O with the increase in Ag% on the surface can be explained by the growth of Ag-TiO₂ interface. Figure S9, Supporting Information, shows initial increasing of the surface coverage ($\approx 6.3\%$) has significant effect on the PIERS enhancement which may be correlated with the formation and as well as the stabilization of V_O . However,

further increase in Ag surface coverage (>44.9%) enhances the reflection therefore reduces the absorption of the light by TiO₂^[26] and this seems to hinder further PIERS enhancement (Figure S9, Supporting Information).

To further reveal the mechanism of PIERS effects, we measured absorption spectra of 4N-in-1 hybrid substrate before and after the UV irradiation. We observed an apparent increase in the overall absorption and a clear red-shift of LSPR band from 405 to 425 nm after the UV irradiation (Figure 2c). Here red-shift in the 4N-in-1 hybrid substrate can be attributed to the increased electron density on Ag nanostructures covering TiO₂.^[40] Therefore definitely hot electrons play also a major role for achieving high EFs in PIERS. We believe that there is a synergistic effect of the i) plasmonic nature of Ag nanostructures (hot electrons), ii) Schottky barrier at the Ag–TiO₂ interface, and iii) V_O stabilization at the Ag–TiO₂ interface.

Since PIERS leads to diverse EFs for different analytes and even for different Raman bands for the same analytes, one needs to take this into account to conduct reliable comparison between different measurements (Table S1, Supporting Information). For instance, while Parkin et al. showed an EF of 2.76 (PIERS to SERS signal ratio at a peak position of 610 cm⁻¹) for rhodamine 6G, we achieved an EF of 49.58 by using the same analyte prepared at identical molarity.^[15] The decay of PIERS intensity to its original state lasted longer than 240 min, as shown in Figure 2d, which clearly indicates a very slow vacancy healing in air. Such a long relaxation time is ideal to get reproducible and highly sensitive measurements (4N-in-1 hybrid substrate exhibited around four to five times longer relaxation time in comparison to reported values to the date.^[15,21,43] Here extremely high EF difference between ours and those reported so far can be attributed to high photocatalytic activity of 4N-in-1 hybrid substrate.

In addition to the PIERS effect, the proposed 4N-in-1 hybrid substrate can decompose organic molecules by applying UV-irradiation (either by using high intensity UV light or conducting a prolonged UV-irradiation time). 4N-in-1 hybrid substrate shows superior decomposition performance of analyte

compared to commercial SERS substrate due to its highly active photocatalytic nature (Figure S10, Supporting Information). Therefore, by simply exposing the analyte deposited 4N-in-1 hybrid substrate to UV light source (operating at 365 nm) just after collecting Raman spectra, we decomposed the analyte fully, and this allows the reuse of the 4N-in-1 hybrid substrate.

2.3. Reusability for PIERS Analysis

To demonstrate the reusability of the proposed hybrid substrate first, after the UV preirradiation we contaminated the surface by drop casting 10 μL of dilute (molarity ≈10⁻⁷ M) R6G solution. Then we collected the Raman signal from the surface, and finally, we exposed the substrate to a high intensity (10 mW cm⁻²) UV light to clean up the surface totally (clean-up time depends on the amount of the analyte adsorbed on the surface as shown in Figure S11, Supporting Information). The UV preirradiation can be termed as the activation step, and other consecutive steps such as loading of the analyte, collecting the Raman spectra and the photocatalytic decomposition of analyte (this can be given as a single cycle as shown schematically in Figure 3a). We showed the self-cleaning process by the UV irradiation and reversible Raman activity in Figure 3b. PIERS activity could be restored after the simple UV cleaning step, and the same substrate could be reused at least 18 times without any loss of PIERS activity, which clearly indicates an excellent reusability. Even after some cycles, we observed that the PIERS signal exceeded its original value, which can be easily explained by consecutively repeated UV irradiation (cumulative activation) for every cycle. When we compare the reusability of 4N-in-1 hybrid surface with those proposed by Parkin et al. and Zhang et al. (surfaces fail after five and 15 times use, respectively) it is clearly seen that our hybrid substrate exhibits extremely high stability after multiple measurements.^[15,21] Therefore, our hybrid surface may act as reliable (see comparison Table S1, Supporting Information) PIERS platform for multiple detection.

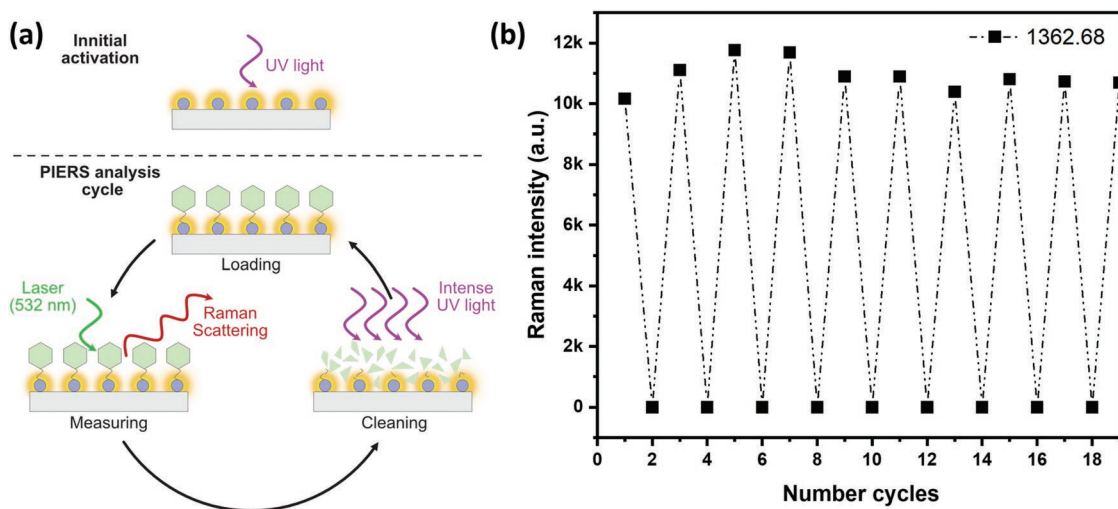


Figure 3. a) Schematic depiction of initial PIERS activation and PIERS analysis cycle, and b) reusability of 4N-in-1 hybrid substrate for multiple PIERS analysis.

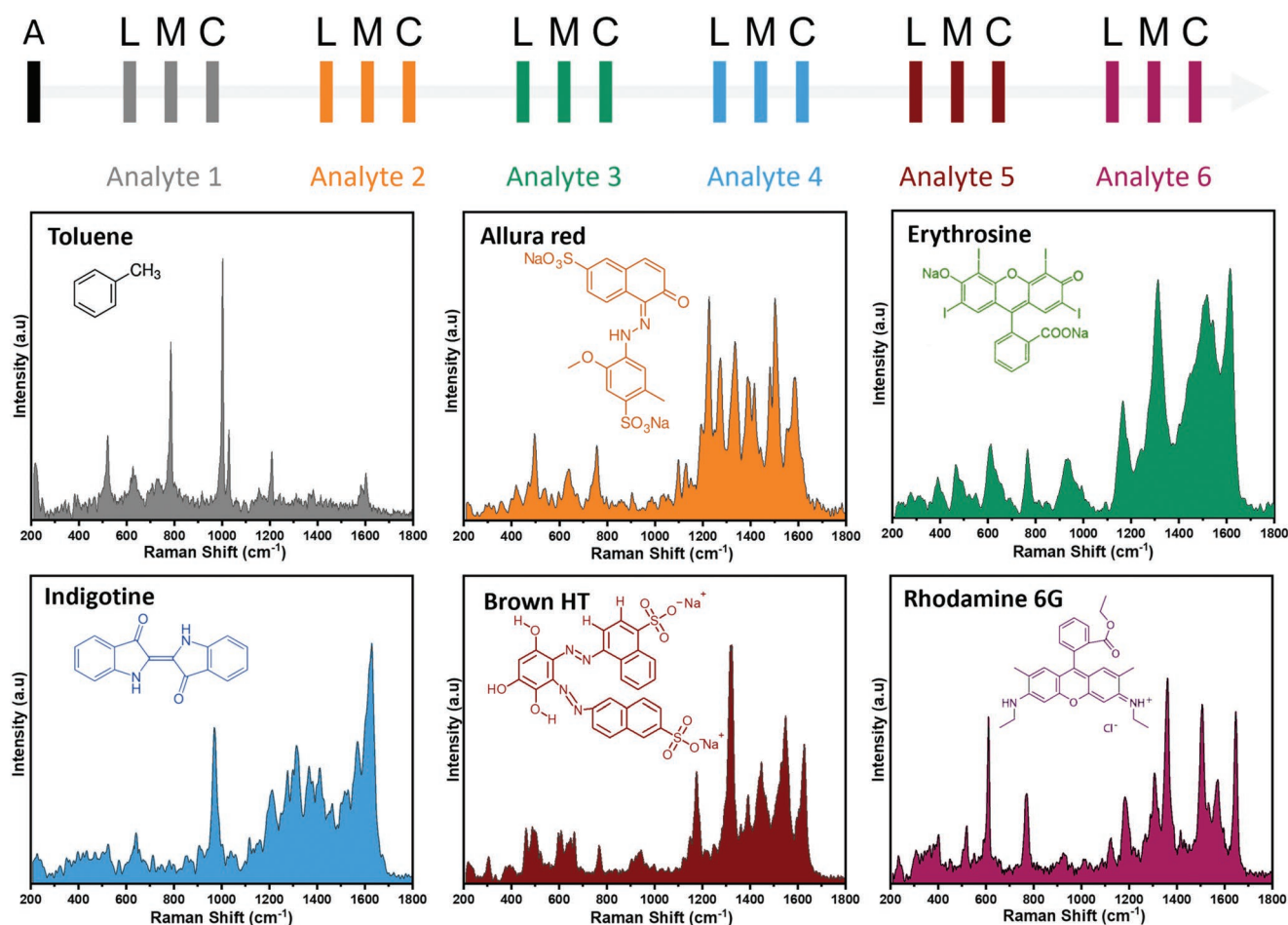


Figure 4. Illustration of PIERS initial activation and consecutive six PIERS analysis cycles for six different analytes with corresponding PIERS spectra (Toluene, Allura red, Erythrosine, Indigo tine, Brown HT, and Rhodamine 6G). (A: PIERS Activation, L: PIERS Analyte Loading, M: PIERS Measurement, and C: PIERS Cleaning)

To further demonstrate the reusability of 4N-in-1 hybrid substrate for multiple PIERS analysis, the same substrate was subjected to six consecutive loading-measurement-clean up cycles (following initial activation step) and for every cycle, a new type of analyte (first cycle: Toluene, second cycle: Allura red, third cycle: Erythrosine, fourth cycle: Indigotine, fifth cycle: Brown HT, and sixth cycle: Rhodamine 6G) was loaded. As presented in **Figure 4**, we were able to detect all characteristics peaks for each analyte without loss of any analyte signal and position (as shown in detail in Table S2, Supporting Information). This proves that the 4N-in-1 hybrid substrate can preserve its specificity and reusability after the photocatalytic clean-up.

2.4. Vapor Phase PIERS Analysis

To reveal how the sensitivity was improved by our PIERS approach in comparison to normal SERS, we compared the detection capabilities of both methods to monitor the surface contamination induced also by a vapor phase analyte. In a typical experiment, 10 μL of vinyl chloride ($\approx 10 \text{ ng mL}^{-1}$) was diluted in a methanol solution. The UV preirradiated

substrate was held at 5 cm above the prepared solution, as schematically illustrated in **Figure 5a**. Afterward, the PIERS signal was acquired, and similarly, the SERS signal was recorded without the UV preirradiation step for comparison. As shown in **Figure 5b**, 4N-in-1 hybrid substrate exhibited a PIERS signal which is 20 times higher than that recorded by SERS (all characteristic peaks of vinyl chloride recorded by PIERS and SERS are given in Table S3, Supporting Information).

In conclusion, we proposed an ultrasensitive and reliable PIERS active substrate termed as “4N-in-1 PIERS substrate” based on Ag-TiO₂ hybrid structures. Upon UV irradiation, we achieved a PIERS enhancement up to 50 times in comparison to normal SERS intensity. In addition to improved Raman signal, 4N-in-1 hybrid substrate provided a high detection sensitivity which may be attributed to the activation possibility with an extremely low incident photon energy and prolonged relaxation time. Moreover, 4N-in-1 hybrid substrate showed a superior photocatalytic degradation performance of analytes, allowing its reuse at least for 18 cycles without any loss of PIERS activity. Our 4N-in-1 hybrid substrate concept can be combined with any type of Raman spectroscopy by simply integrating a UV light

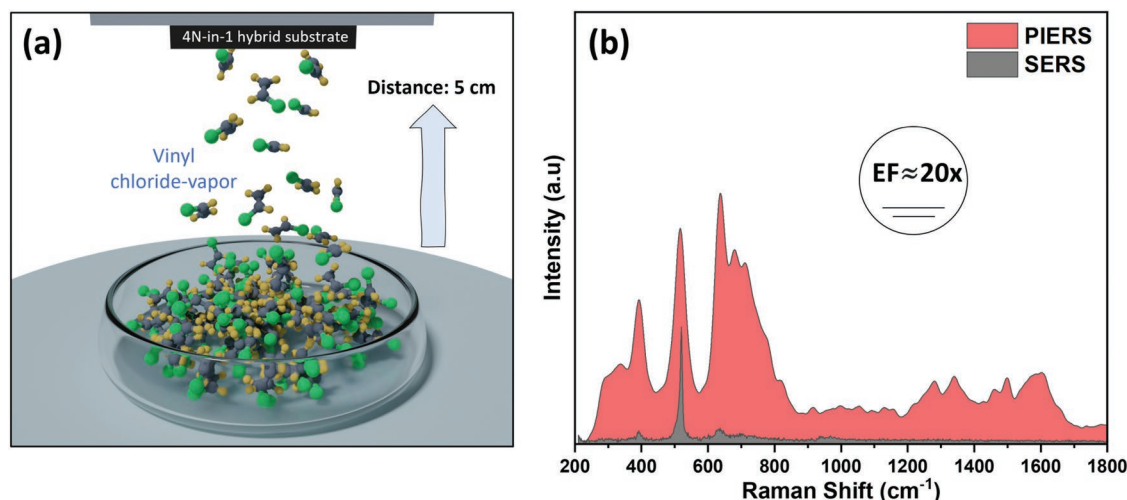


Figure 5. a) Schematic illustration of the detection of vapor phase analyte and b) a comparative analysis of vapor phase analyte by PIERS and SERS.

source, and this may trigger new applications for biomedicine, forensic, and security fields (a possible case is shown in Figure S12, Supporting Information)

3. Experimental Section

Materials and Methods: Silver nitrate (99.999%), rhodamine 6 g (99.8%), methyl alcohol (99.99%), ethyl alcohol (99.8%), 1-methyl-4-nitrobenzene (99%), vinyl chloride solution (2000 $\mu\text{g mL}^{-1}$ in methanol), and methylbenzene (anhydrous 99.8%), were obtained from Sigma-Aldrich, Germany. Allura red, Erythrosine, Brown HT, and Indigotin were obtained from FastColours LLP, UK.

Preparation of TiO_2 Thin film: The deposition of 500 nm thick TiO_2 thin film was carried out using direct current magnetron sputtering from a titanium (Ti) target in a custom-built vacuum deposition chamber as previously reported.^[30,44,45] Silicon wafer pieces (10 mm \times 10 mm) were used as substrate. Before the deposition of TiO_2 thin film, the chamber was conditioned to reach a base pressure of 10^{-5} Pa using a rotary pump (Agilent Technologies, SH-110) in combination with a molecular turbopump (Pfeiffer Vacuum, HiPace 400). First, the Ti target (Goodfellow, 99.99% of 50 mm diameter) was cleaned in a pure Ar plasma for 10 min. Afterward, the deposition was carried out (for 65 min) under a gas mixture of Ar and O_2 (at a ratio of 250:5 maintained by using two separate mass flow controllers-MKS Multi-Gas-Controller 647C) and at a magnetron output power of 120 W. A homogeneous TiO_2 film was achieved by rotating an automated sample holder during the deposition. Afterward, the prepared thin films were annealed for an hour at 650 $^\circ\text{C}$ in an oven (Nabertherm, LE 4/11/R6) and subsequently air quenched to induce a nano-cracks network (leading to high surface area), as was reported previously.^[29]

Photocatalytic Deposition of Ag Nanostructures on TiO_2 Thin Film: In a typical experiment, 6.5 mL of silver nitrate ($[\text{AgNO}_3] = 1 \times 10^{-3}$ M) was filled in methanol, a UV-transparent quartz cuvette as was described in detail previously.^[45] Afterward, prepared TiO_2 thin film samples were dipped into the quartz cuvette and exposed to low-intensity (operating at a wavelength of 365 nm and a power of 4.5 mW cm^{-2}) UV light (UV LED StellarNet EPP2000C-SR-50) for 20 min. Then, samples were rinsed with deionized water to remove excess solution and left to dry at room temperature.

Scanning Electron Microscopy (SEM): The surface morphology of prepared samples was analyzed with SEM (Supra55VP-Carl Zeiss) at an accelerating voltage of 3 kV (with 3 mm working distance).

X-ray Photoelectron Spectroscopy (XPS): XPS (using Omicron Nano-Technology GmbH, Al anode, 240 W) was employed to determine the chemical state on the surface. CasaXPS software (2.3.13PR1.0) was used for quantitative analysis and detailed peak investigation. All binding energies (BE) were referenced according to the C 1s line at 285 eV (originates from adventitious carbon on the sample surface).

UV-Vis Measurement: For UV-vis analysis, 500 nm thick TiO_2 film was deposited on quartz pieces (10 mm \times 10 mm), and these samples were annealed at 650 $^\circ\text{C}$ for an hour. Then, prepared samples were fixed onto a custom-designed optical holder for UV-vis analysis. UV-vis spectra were collected within the 200–1000 nm wavelength range at a scanning rate of 2 nm s^{-1} using a spectrophotometer (PerkinElmer LAMBDA-900, Made in Germany). The quartz glass spectrum was used for the baseline correction.

Raman Measurement: Raman Spectroscopy analysis was conducted using a commercially available confocal Raman microscope (WITec alpha300 RA, Ulm, Germany) equipped with an Nd: YAG 532 nm laser source. Intensity calibration was performed using a silicon wafer via the most significant silicon mode at 520 cm^{-1} . All SERS and PIERS spectra were acquired using 1200 g mm^{-1} BLZ 300NM grating at the excitation source power of 15 μW .

To acquire the Raman signal of the individual analytes, a fixed volume of 10 μL of analyte was drop-cast onto the Ag decorated TiO_2 and allowed to dry in air for 10 min. Typically, SERS spectra were acquired without UV preirradiation step. On the other hand, in PIERS data acquisition, 10 μL of the analyte was deposited on the UV preirradiated samples and allowed to dry in air for 10 min and kept in the dark.

Supporting Information

Supporting Information is available from the Wiley Online Library or from the author.

Acknowledgements

J.S. and S.V. contributed equally to this work. J.S. thanks the Petroleum Technology Development Fund (PTDF) and the Deutscher Akademischer Austauschdienst (DAAD) for providing funding for his doctoral studies. This work is financially supported by the Deutsche Forschungsgemeinschaft (DFG, German Research Foundation)- project number 448935424 i.e., project FA234/35-1. The authors thank NanoBMT Co. Ltd. for preparing of some analytes.

Conflict of Interest

The authors declare no conflict of interest.

Data Availability Statement

The data that support the findings of this study are available in the supplementary material of this article.

Keywords

hybrid structures, photocatalysis, reusability, surface-enhanced Raman spectroscopy, ultra-sensitivity

Received: June 22, 2022

Revised: August 26, 2022

Published online:

- [1] A. J. M. Fleischmann, P. J. Hendra Mcquillan, *Chem. Phys. Lett.* **1974**, 26, 163.
- [2] J. Langer, D. J. de Aberasturi, J. Aizpurua, R. A. Alvarez-Puebla, B. Augu e, J. J. Baumberg, G. C. Bazan, S. E. J. Bell, A. Boisen, A. G. Brolo, J. Choo, D. Cialla-May, V. Deckert, L. Fabris, K. Faulds, F. J. Garc a de Abajo, R. Goodacre, D. Graham, A. J. Haes, C. L. Haynes, C. Huck, T. Itoh, M. K all, J. Kneipp, N. A. Kotov, H. Kuang, E. C. Le Ru, H. K. Lee, J. F. Li, X. Y. Ling, et al., *ACS Nano* **2020**, 14, 28.
- [3] C. Andreou, M. R. Hoonejani, M. R. Barmi, M. Moskovits, C. D. Meinhart, *ACS Nano* **2013**, 7, 7157.
- [4] H. Dies, J. Raveendran, C. Escobedo, A. Docoslis, *Sens. Actuators B Chem.* **2018**, 257, 382.
- [5] T. K. Naqvi, A. Bajpai, M. S. S. Bharati, M. M. Kulkarni, A. M. Siddiqui, V. R. Soma, P. K. Dwivedi, *J. Hazard. Mater.* **2021**, 407, 124353.
- [6] Y. S. Yamamoto, Y. Ozaki, T. Itoh, *J. Photochem. Photobiol. C* **2014**, 21, 81.
- [7] K. A. Willets, R. P. Van Duyne, *Annu. Rev. Phys. Chem.* **2007**, 58, 267.
- [8] L. Guerrini, D. Graham, *Chem. Soc. Rev.* **2012**, 41, 7085.
- [9] B. N. J. Persson, K. Zhao, Z. Zhang, *Phys. Rev. Lett.* **2006**, 96, 207401.
- [10] R. Pilot, R. Signorini, C. Durante, L. Orian, M. Bhamidipati, L. Fabris, *Biosensors* **2019**, 9, 57.
- [11] S. Gullace, V. Montes-Garc a, V. Mart n, D. Larios, V. Girelli Conso-laro, F. Obelleiro, G. Calogero, S. Casalini, P. Samor , *Small* **2021**, 17, 2100755.
- [12] A. Fularz, S. Almohammed, J. H. Rice, *ACS Appl. Nano Mater.* **2020**, 3, 1666.
- [13] J. Chen, H. Su, X. You, J. Gao, W. M. Lau, D. Zhang, *Mater. Res. Bull.* **2014**, 49, 560.
- [14] S. Zhao, H. Wang, L. Niu, W. Xiong, Y. Chen, M. Zeng, S. Yuan, L. Fu, *Small* **2021**, 17, 2103442.
- [15] S. Ben-Jaber, W. J. Peveler, R. Quesada-Cabrera, E. Cort es, C. Sotelo-Vazquez, N. Abdul-Karim, S. A. Maier, I. P. Parkin, *Nat. Commun.* **2016**, 7, 12189.
- [16] G. Barbillon, *Materials* **2021**, 14, 4423.
- [17] D. Glass, E. Cort es, S. Ben-Jaber, T. Brick, W. J. Peveler, C. S. Blackman, C. R. Howle, R. Quesada-Cabrera, I. P. Parkin, S. A. Maier, *Adv. Sci.* **2019**, 6, 1901841.
- [18] L. Li, L. Song, L. Zhu, Z. Yan, X. Cao, *Catal. Sci. Technol.* **2018**, 8, 1277.
- [19] T. Bora, in *Noble and Precious Metals - Properties, Nanoscale Effects and Applications* (Eds: M. S. Seehra, A. D. Bristow), IntechOpen, London **2018**, pp. 118–129.
- [20] S. Cong, Y. Yuan, Z. Chen, J. Hou, M. Yang, Y. Su, Y. Zhang, L. Li, Q. Li, F. Geng, Z. Zhao, *Nat. Commun.* **2015**, 6, 7800.
- [21] M. Zhang, H. Sun, X. Chen, J. Yang, L. Shi, T. Chen, Z. Bao, J. Liu, Y. Wu, *ACS Sens.* **2019**, 4, 1670.
- [22] J. Zhao, Z. Wang, J. Lan, I. Khan, X. Ye, *Nanoscale* **2021**, 13, 8707.
- [23] R. Kavitha, S. G. Kumar, *Chem. Pap.* **2020**, 74, 717.
- [24] H. Yamashita, M. Harada, J. Misaka, M. Takeuchi, K. Ikeue, M. Anpo, *J. Photochem. Photobiol. A Chem.* **2002**, 148, 257.
- [25] M. Zhang, H. Sun, X. Chen, J. Yang, T. Chen, Z. Bao, J. Liu, Y. Wu, *ACS Sens.* **2019**, 4, 1670.
- [26] S. Veziroglu, A.-L. Obermann, M. Ullrich, M. Hussain, M. Kamp, L. Kienle, T. Leif ner, H.-G. Rubahn, O. Polonskyi, T. Strunskus, J. Fiutowski, M. Es-Souni, J. Adam, F. Faupel, O. C. Aktas, *ACS Appl. Mater. Interfaces* **2020**, 12, 14983.
- [27] X. Jiang, X. Sun, D. Yin, X. Li, M. Yang, X. Han, L. Yang, B. Zhao, *Phys. Chem. Chem. Phys.* **2017**, 19, 11212.
- [28] B. Henkel, T. Neubert, S. Zabel, C. Lamprecht, C. Selhuber-Unkel, K. R atzke, T. Strunskus, M. Verg hl, F. Faupel, *Appl. Catal. B* **2016**, 180, 362.
- [29] M. Z. Ghorri, S. Veziroglu, B. Henkel, A. Vahl, O. Polonskyi, T. Strunskus, F. Faupel, O. C. Aktas, *Sol. Energy Mater. Sol. Cells* **2018**, 178, 170.
- [30] A. Vahl, S. Veziroglu, B. Henkel, T. Strunskus, O. Polonskyi, O. C. Aktas, F. Faupel, *Materials* **2019**, 12, 2840.
- [31] S. Veziroglu, M. Z. Ghorri, A. Obermann, K. R oder, O. Polonskyi, T. Strunskus, F. Faupel, O. C. Aktas, *Phys. Status Solidi* **2019**, 216, 1800898.
- [32] A. M. Ferraria, A. P. Carapeto, A. Maria, **2012**, 86, 1988.
- [33] Z. Cheng, S. Zhao, Z. Han, Y. Zhang, X. Zhao, L. Kang, *CrystEng-Comm* **2016**, 18, 8756.
- [34] S. Zhao, Z. Cheng, L. Kang, M. Li, Z. Gao, *RSC Adv.* **2017**, 7, 50064.
- [35] D. N. Pei, L. Gong, A. Y. Zhang, X. Zhang, J. J. Chen, Y. Mu, H. Q. Yu, *Nat. Commun.* **2015**, 6, 2.
- [36] Y. Xu, S. Wu, P. Wan, J. Sun, Z. D. Hood, *RSC Adv.* **2017**, 7, 32461.
- [37] M. Batzill, E. H. Morales, U. Diebold, *Chem. Phys.* **2007**, 339, 36.
- [38] Y. Wang, M. Zhang, S. Lv, X. Li, D. Wang, C. Song, *ACS Omega* **2020**, 5, 13994.
- [39] D. Briggs, in *Handbook of Adhesion*, 2nd ed. (Ed: D. E. Packham), Wiley, New York **2005**, pp. 621–622.
- [40] L. Yang, W. Wang, H. Jiang, Q. Zhang, H. Shan, M. Zhang, K. Zhu, J. Lv, G. He, Z. Sun, *Sens. Actuators B Chem.* **2017**, 242, 932.
- [41] J.-M. Herrmann, *Catal. Today* **1999**, 53, 115.
- [42] T. Zhou, K. Ioannidou, F. J. Ulm, M. Z. Bazant, R. J. M. Pellenq, *Proc. Natl. Acad. Sci. U. S. A.* **2019**, 166, 10652.
- [43] K. Abid, N. H. Belkhir, S. B. Jaber, R. Zribi, M. G. Donato, G. Di Marco, P. G. Gucciardi, G. Neri, R. Ma lej, *J. Phys. Chem. C* **2020**, 124, 20350.
- [44] J. Shondo, S. Veziroglu, D. Stefan, Y. K. Mishra, T. Strunskus, F. Faupel, O. C. Aktas, *Appl. Surf. Sci.* **2020**, 537, 147795.
- [45] S. Veziroglu, M. Z. Ghorri, M. Kamp, L. Kienle, H. G. Rubahn, T. Strunskus, J. Fiutowski, J. Adam, F. Faupel, O. C. Aktas, *Adv. Mater. Interfaces* **2018**, 5, 1800465.

Supporting Information

for *Small*, DOI: 10.1002/smll.202203861

Nanoscale Synergetic Effects on Ag–TiO₂ Hybrid Substrate for Photoinduced Enhanced Raman Spectroscopy (PIERS) with Ultra-Sensitivity and Reusability

Josiah Shondo, Salih Veziroglu, Tim Tjardts, Tamim Bin Sarwar, Yogendra Kumar Mishra, Franz Faupel, and Oral Cenk Aktas**

SUPPLEMENTARY INFORMATION

Nanoscale Synergetic Effects on Ag-TiO₂ Hybrid Substrate for Photoinduced Enhanced Raman Spectroscopy (PIERS) with Ultra-sensitivity and Reusability

Josiah Shondo,^{a,†} Salih Veziroglu,^{a,b,†} Tim Tjardts,^a Tamim Sarwar,^a Yogendra Kumar Mishra,^c Franz Faupel,^{a,b*} and Oral Cenk Aktas^{a,d*}

^aChair for Multicomponent Materials, Institute of Materials Science, Faculty of Engineering, Kiel University, Kaiserstr. 2, 24143 Kiel, Germany

^bKiel Nano, Surface and Interface Science KiNSIS, Kiel University, Christian Albrechts-Platz 4, 24118 Kiel, Germany

^cMads Clausen Institute, NanoSYD, University of Southern Denmark, Alsion 2, Sønderborg 6400, Denmark

^dAdditive Manufacturing Excellence Centre – URTEMM, Kahramankazan, Ankara 06980, Turkey

* Corresponding authors: ff@tf.uni-kiel.de, oca@tf.uni-kiel.de

† These authors contributed equally.

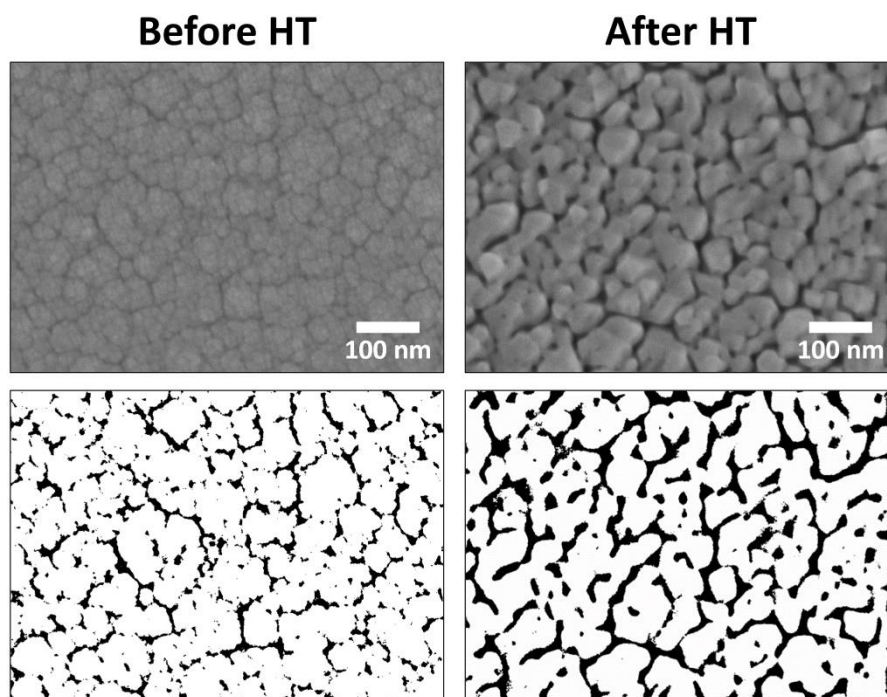


Figure S1: SEM images for nano-crack networks in TiO_2 at before and after heat treatment (HT) with corresponding binary images for calculation of crack network.

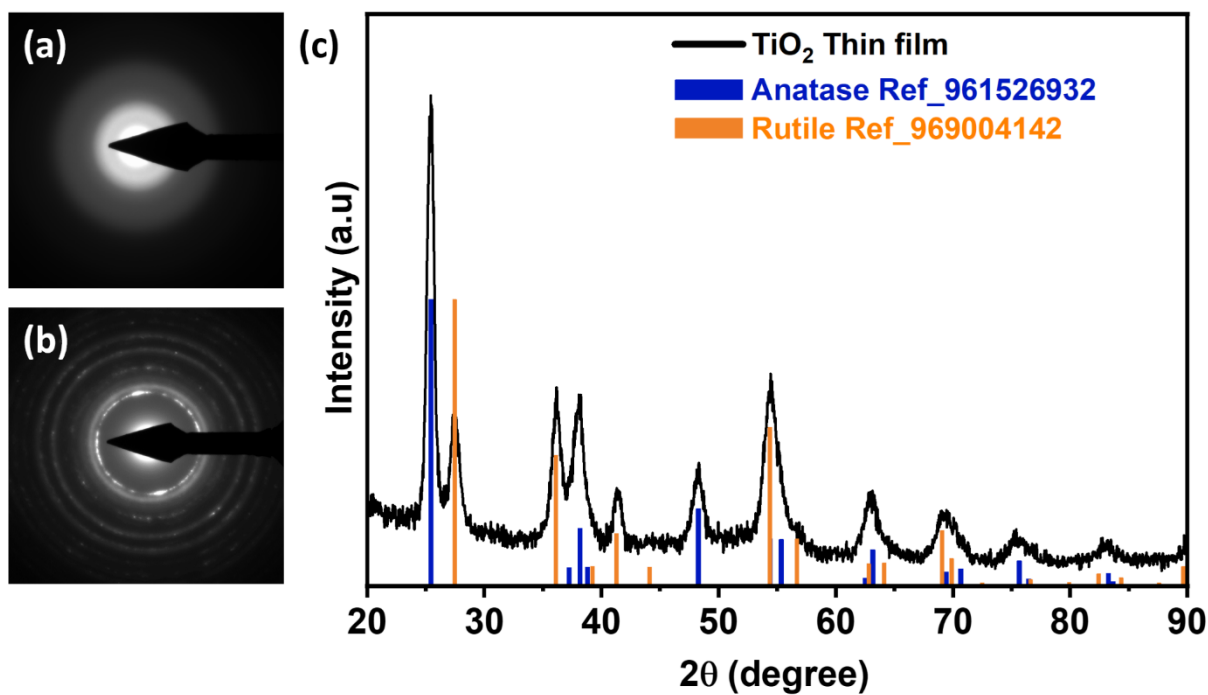


Figure S2: Selected area electron diffraction (SAED) pattern of TiO_2 thin film (a) before and (b) after heat treatment. (c) Grazing incidence X-ray diffraction (GIRXD) pattern of TiO_2 thin film.

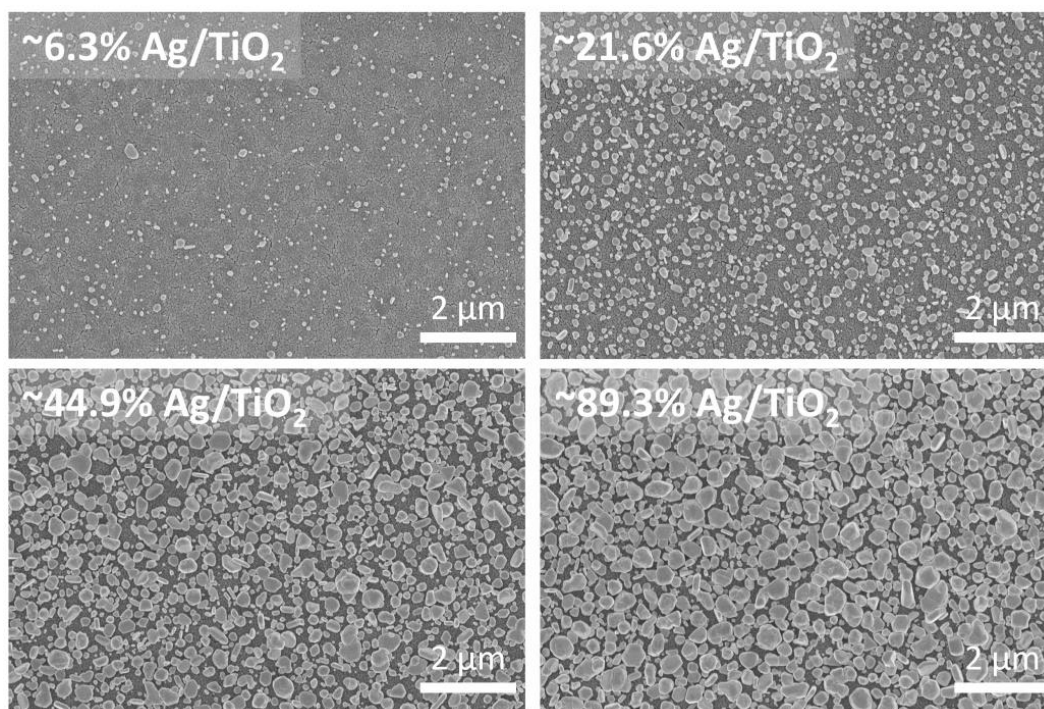


Figure S3. SEM images of 4N-in-1 hybrid substrates with various surface coverage of Ag %.

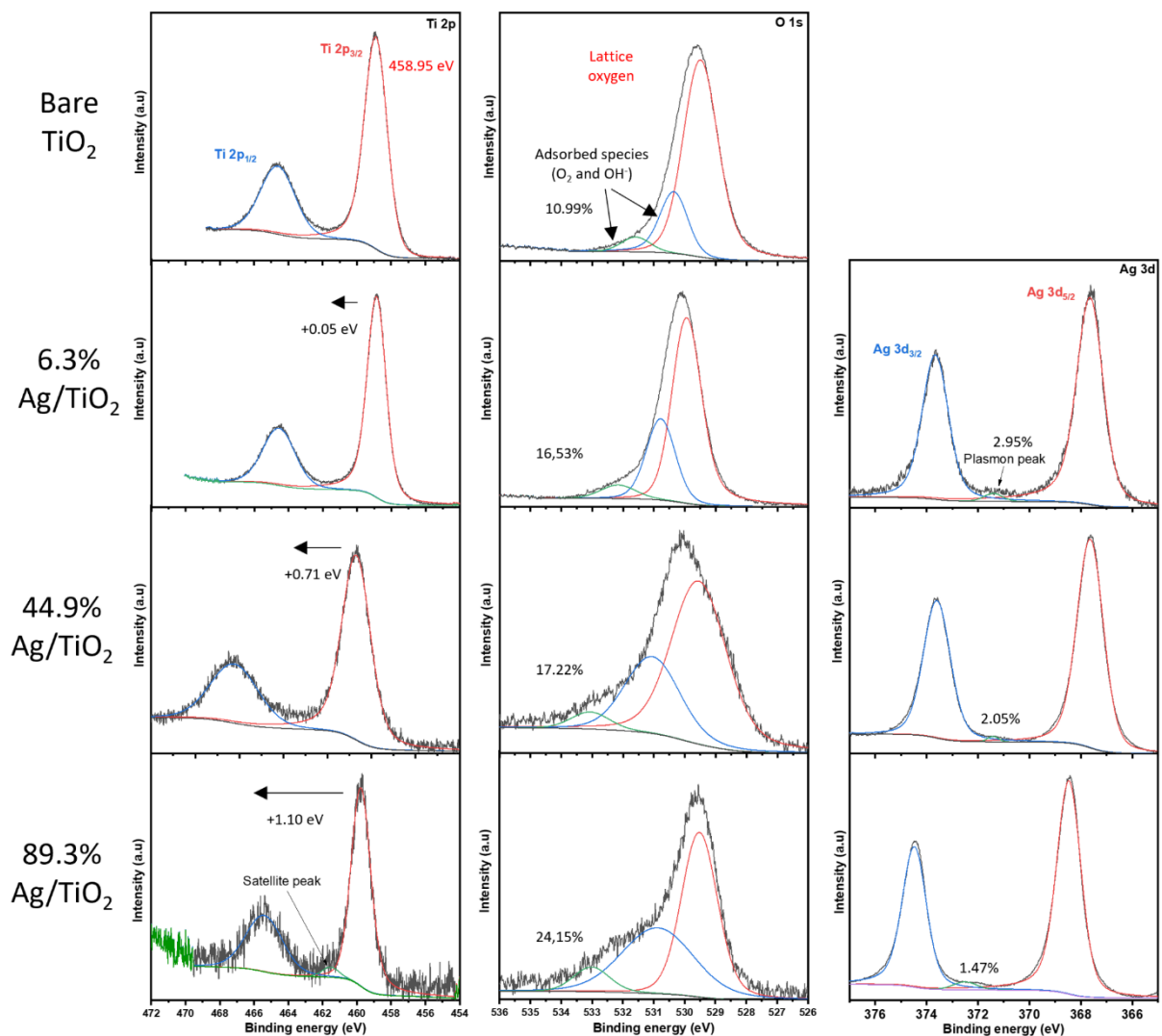


Figure S4. High-resolution XPS spectra of Ti, O, and Ag elements on bare TiO₂ and 4N-in-1 hybrid substrates (Ag/TiO₂) with various surface coverage of Ag %.

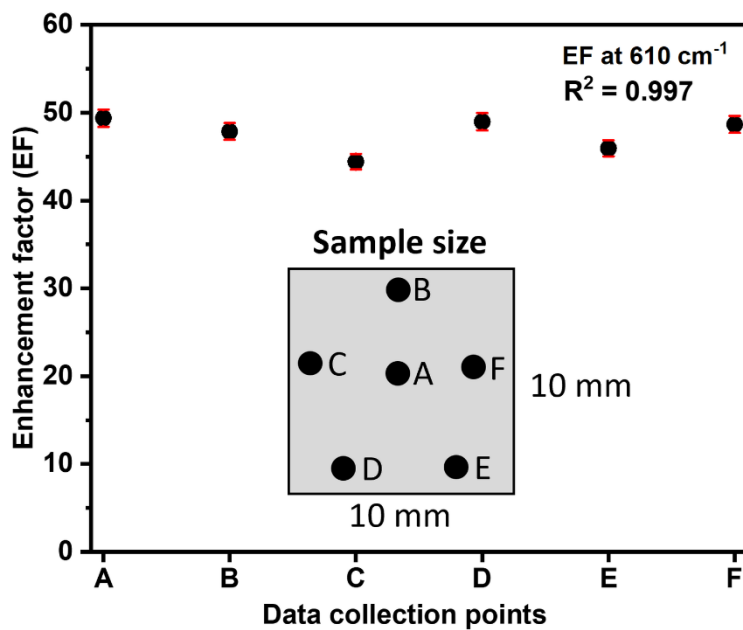


Figure S5. Spectral enhancement factor (EF) of PIERS over SERS (peak at 630 cm⁻¹) for R6G (ca. 10⁻⁷ molar) with corresponding data collection points.

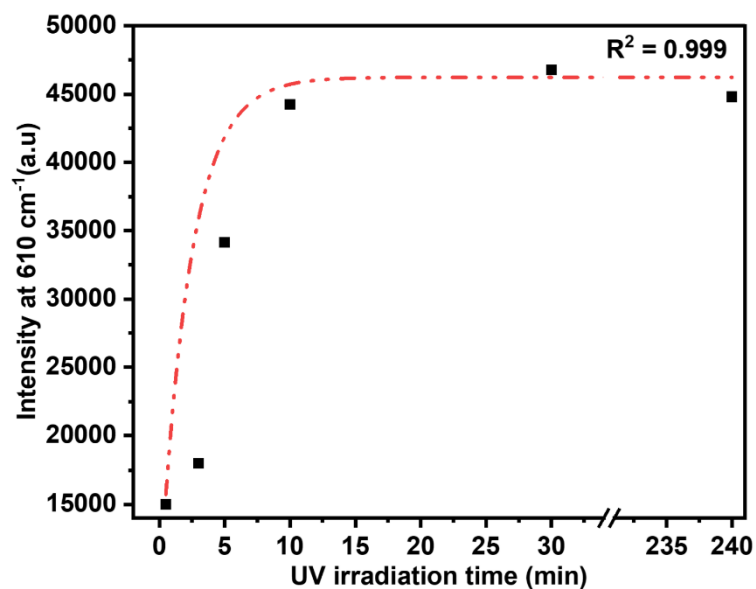


Figure S6: Measured Raman band intensities, where peak position is at 610 cm⁻¹ for R6G (ca. 10⁻⁷ M) under various UV pre-irradiation times.

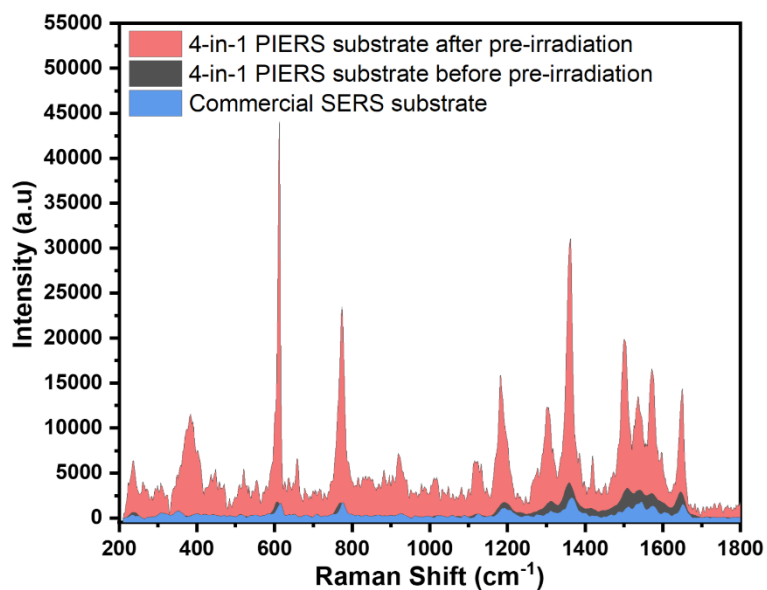


Figure S7. Comparison of PIERS and SERS performance of 4N-in-1 hybrid and commercial SERS substrate for detection of trace amount of R6G analyte at 10^{-7} M concentration.

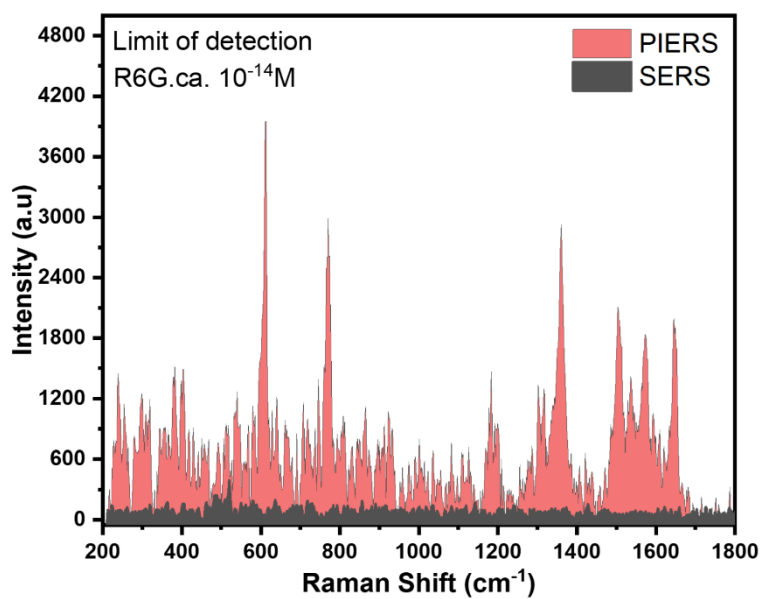


Figure S8. PIERS and Raman spectra of R6G at extremely low concentration (ca: 10^{-14} M).

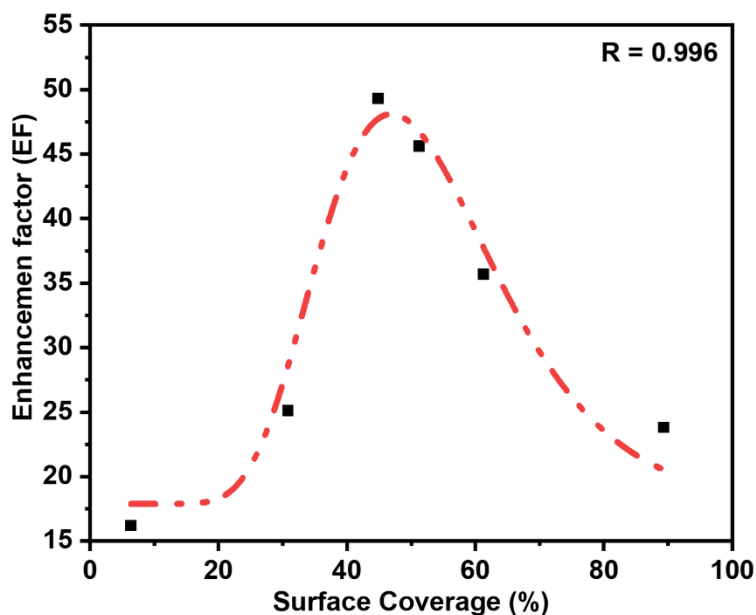


Figure S9. Average of total spectral enhancement factor (EF) of PIERS over SERS (peak at 610 cm^{-1}) for R6G (ca. 10^{-7} molar) with a corresponding surface coverage of Ag %.

Table S1. Comparison of different PIERS substrates on some operation/analysis conditions and corresponding enhancement factors (PIERS/SERS) for different analytes.

Substrate	Reactant / Concentration	Enhancement Factor	Pre-irradiation time	Pre-irradiation wavelength and intensity	Decaying Time	Degradation Time	Ref.
4N-in1 hybrid substrate	Rhodamine 6G (10^{-7} M)	49.38	8 min	365 nm – 4.5 mWcm ⁻²	300 min	8 min (10 mWcm ⁻²)	Current study
AuNPs on TiO ₂ (rutile)	Rhodamine 6G (10^{-7} M)	2.76	180 min	254 nm – 2x 8 W bulbs (at a distance of 13 cm)	60 min	240 min	Ben-Jaber et al.
Ag NPs on TiO ₂ nanosheets (anatase and rutile)	Rhodamine 6G (5×10^{-6} M)	14.9	24 min	UPV mercury lamp - 100 W (at a distance of 8 cm)	40 min	60-180 min (300 W mercury lamp)	Zhang et al.
	Thiram (10^{-5} M)	27.8					
Ag NPs on TiO ₂ thin film (anatase)	Adenosine triphosphate (ATP) (10^{-10} M)	3	30 min	365 nm - 2 X 6 W bulbs (with a distance of 10 cm)	60 min	NA	Man et al.
TiO ₂ -Ag nanopore arrays	Crystal violet (10^{-7} M)	8	21	300 W mercury lamp light source (at a distance of 8 cm)	30	210	Zhang et al.

Refs:

- Ben-Jaber et al., Nature Communication, 2016, 7, 12189.
- Zhang et al, ACS Sensor 2019, 4, 1670.
- Man et al., Biosensors and Bioelectronics 2020, 147, 111742.
- Zhang et al., ChemNanoMat 2019, 5, 55.

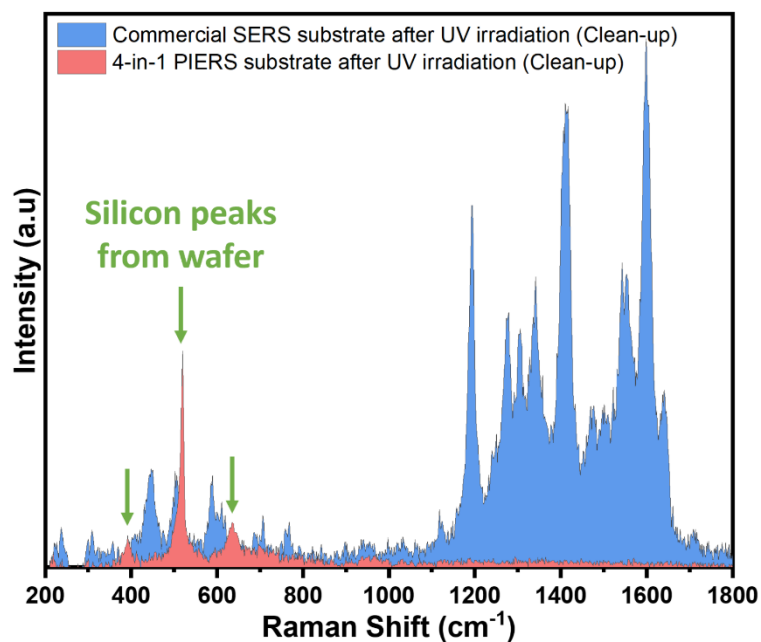


Figure S10. Comparison of clean-up performance of 4N-in-1 hybrid and commercial SERS substrates after UV illumination (λ :365 nm and 10 mW/cm²) for 8 minutes.

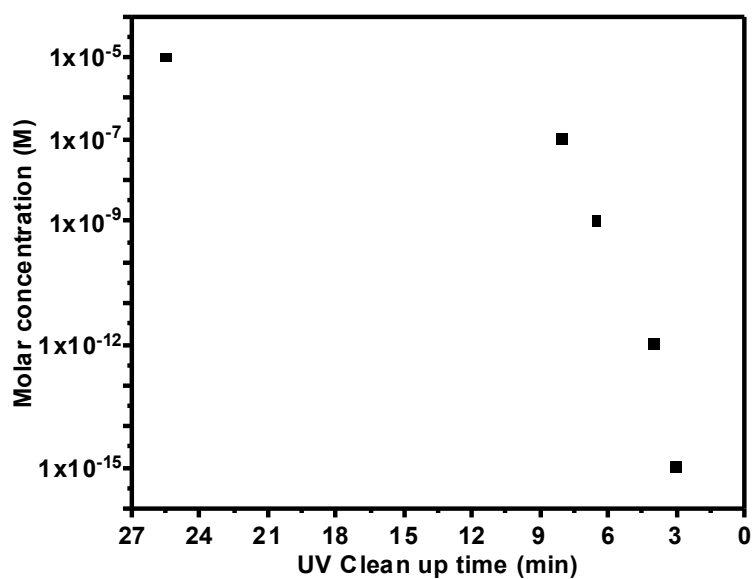
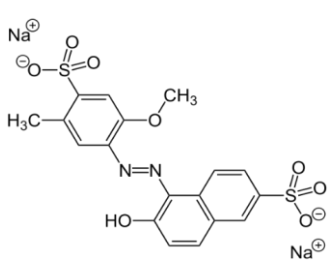
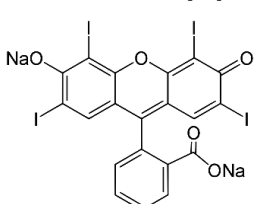
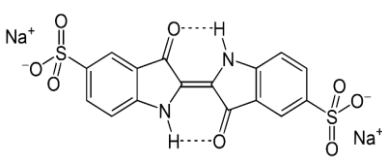


Figure S11: Demonstration the fast clean-up process of the 4N-in-1 hybrid substrate for various concentrations of R6G with corresponding UV illumination time.

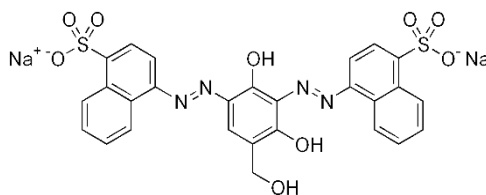
Table S2: Showing Raman bands and their corresponding assigned functional groups.

Chemicals	Raman Peak positions (cm ⁻¹)	Functional group	Chemical structures	Ref.
Allura Red	495.55 (m)	C-S stretching		[1-3]
	641.67 (w)	C-S stretching		
	756.23 (m)	C-N vibration		
	903.18 (w)	C-C stretching in the benzene ring		
	987.75 (w)	C=C aromatic ring chain vibrations		
	1097.18 (w)	SO ₃ In-phase stretching vibration		
	1128.41 (vs)	NH ₂ rocking vibration		
	1226.72 (s)	SO ₂ symmetrical stretching vibration		
	1273.58 (s)	C-O-C stretch		
	1334.39 (s)	(O) CH ₃ In-plane bending vibration		
	1385.85 (s)	Aryl CH ₃ In-plane bending vibration		
1415.85 (s)	C-N=N stretching vibration			
1501.58 (vs)	Aromatic Semicircle stretching vibration			
1581.11 (s)	C=C aromatic ring chain stretch			
Erythrosine	415.11 (w)	C-I deformation		[4,5]
	541.26 (m)	C-I stretch		
	667.06 (m)	C-I stretch		
	832.93 (m)	C=C aromatic ring chain vibrations		
	933.36 (m)	C-O-C asymmetric stretching		
	1075.06 (m)	Aryl-I stretching vibration.		
	1215.86 (vs)	CH-I stretch		
	1321.91 (s)			
	1410.56 (vs)	C-C=O bend		
1508.53 (vs)	C=O stretch			
Indigotine	525.29 (w)	C=O bending vibration		[6,7]
	641.67 (w)	C-S stretching		
	711.78 (w)	C-S ring in-plane bending		
	969.04 (s)	SO ₂ Anti-symmetric stretch		

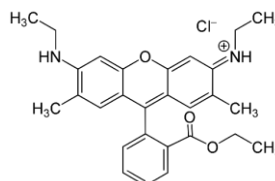
1117.40 (w)	C=O stretching
1212.24 (m)	C=C aromatic ring chain vibrations
1277.17 (m)	CH In-plane rock
1314.77 (m)	NH-C=C-NH rock
1366.38 (m)	NH-C=C-NH rock
1412.32 (m)	C-C-C stretch— Benzene ring
1464.97 (m)	C-C-C stretch-- Benzene ring
1515.48 (m)	C=C stretch
1569.06 (m)	C=C stretch
1630.66 (vs)	C=O in phase stretch

Brown HT

487.57 (m)	SO ₃ - Rocking; C–H out-of-plane; OH deformation	[8]
608.34 (m)	C–N=N bend + C–C str.	
665.11 (m)	C–S stretching (S=O sulfoxides) out-of-plane	
767.78 (m)	SO ₃ - bending	
944.65 (m)	SO ₃ - Stretching symmetric	
1175.91 (s)	phenyl ring bonding at azo group bending	
1248.38 (w)	phenols O–H deformation vibration	
1323.70 (vs)	–C–N=N–C– stretch	
1392.92 (m)	sodium 1-naphthalenesulfonate (C ₁₀ H ₇ NaO ₃ S)	
1447.46 (s)	N=N stretching of trans-aromatic azo	
1550.10 (vs)	Longitudinal vibration of the naphthene	
1629.06 (s)	C=C stretch penta-substituted benzenes	

**Rhodamine 6G**

610.86 (vs)	C–C aromatic ring chain stretch	[9–12]
770.10 (m)	C–H out-of-plane bending	
924.20 (w)	C–O–C	
1008.45 (w)	C–CH ₃ in-plane rocking mode	
1124.81 (m)	C–O–C asymmetric stretching	
1183.21 (m)	C–H in-plane bending	

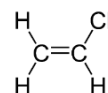


1305.74 (m)	C-N stretch
1360.91 (vs)	C=N stretch
1506.52 (vs)	C=C aromatic ring chain stretch
1572.17 (m)	C-C aromatic ring chain stretch
1645.71 (vs)	C=O aromatic ring chain stretch

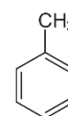
[13,14]

Vinylchloride

395.99 (m)	C-Cl rocking
518.07 (s)	C-Cl rocking
636.32 (vs)	C-Cl rocking
679.23 (vs)	C-Cl twisting
1280.69 (w)	CH rocking
1343.16 (w)	CH ₂ deformation
1499.57 (w)	CH ₂ asym
1603.05 (w)	C=C stretching vibration

**Toluene**

520.06 (m)	C-H rocking vibrations in the benzene ring
626.54 (w)	C-H rocking vibrations in the benzene ring
785.47 (s)	CH out of plane deformation
1002.82 (vs)	phenyl bending
1028.91 (m)	phenyl bending
1206.8 (m)	Aryl CH ₃
1604.76 (w)	Ring quadrant stretching



[15,16]

W= weak signal bands, m= medium signal bands, s= strong signal bands and vs= very strong signal bands

Table S3: Raman resonances of Vinylchloride and their enhancement factors

SERS Vinylchloride		PIERS Vinylchloride		PIERS/SERS
PEAK position	Intensity	PEAK position	Intensity	
398.01	62.12	396.00	981.98	15.80
514.10	383.17	516.09	1496.30	3.90
630.45	91.70	638.28	1738.36	18.95
907.23	30.20	912.89	276.15	9.14

1457.74	24.56	1457.48	378.94	15.48
1603.05	23.47	1606.47	491.93	20.95

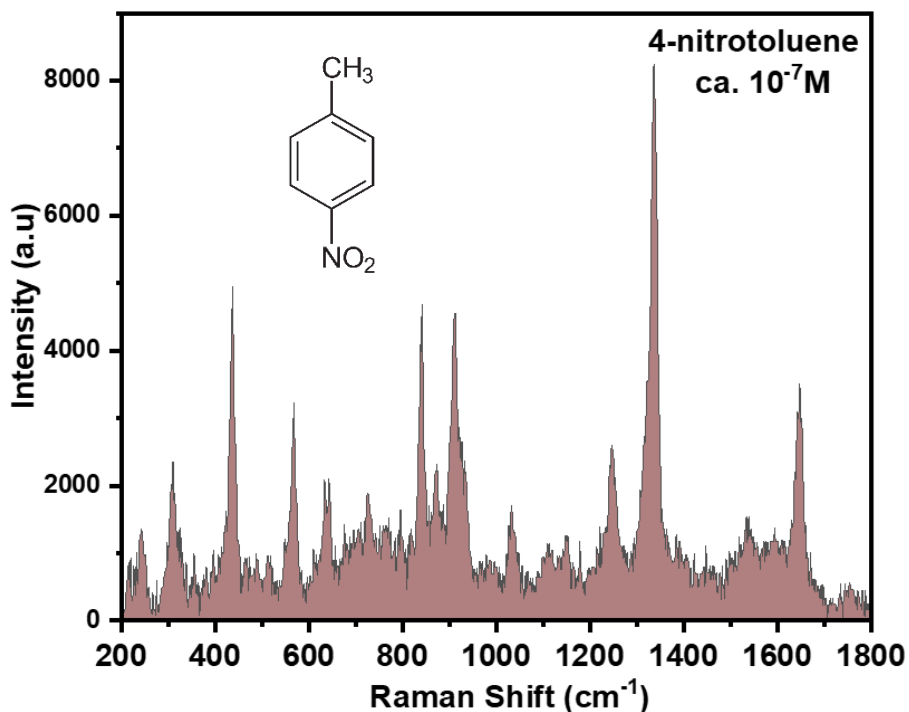


Figure S12. PIERS performance of 4N-in-1 hybrid substrate for the detection of trace amount of 4-nitrotoluene (ca. 10^{-7} molar).

Reference

- [1] Y. Ou, X. Wang, K. Lai, Y. Huang, B. Rasco, Y. Fan, *J. Agric. Food Chem* **2018**, *66*, 2954.
- [2] K. Rovina, S. Siddiquee, S. M. Shaarani, *Front. Microbiol* **2016**, *7*, 1.
- [3] A. K. Ávila-martínez, J. H. Roque-ruiz, J. Torres-pérez, *Environ. Technol. Innov.* **2020**, *18*, 100760.
- [4] V. A. Narayanan, D. L. Stokes, N. A. Stump, G. M. Begun, & T. Vo-dinh, *Polycycl. Aromat. Compd.* **1993**, *3*, 137.
- [5] E. Pinilla-Peñalver, M. J. Villaseñor, A. M. Contento, Á. Ríos, *Microchem. J.* **2020**, *157*, 104937.
- [6] G. D. Smith, V. J. Chen, A. Holden, M. H. Keefe, S. G. Lieb, *Herit. Sci.* **2019**, *7*, 1.
- [7] D. A. Long, *J. Raman Spectrosc.* **2004**, *35*, 905.
- [8] M. Leulescu, I. P. I. Rotaru, A. Moanta, N. Cioatera, M. Popescu, E. Morintale, M. C. Vărut, Petre, *J. Therm Anal Calorim.* **2019**, *136*, 1249.
- [9] C. Silver, P. Hildebrandt, M. Stockburger, **1984**, 5935.
- [10] C. Dong, Z. Yan, J. Kokx, D. B. Chrisey, C. Z. Dinu, *Appl. Surf. Sci.* **2012**, *258*, 9218.
- [11] K. H. Lee, H. Jang, Y. S. Kim, C. H. Lee, S. H. Cho, M. Kim, H. Son, K. Bin Bae, D. Van

Dao, Y. S. Jung, I. H. Lee, *Adv. Sci.* **2021**, *8*, 1.

[12] M. Zhang, H. Sun, X. Chen, J. Yang, L. Shi, T. Chen, Z. Bao, J. Liu, Y. Wu, *ACS Sensors* **2019**, *4*, 1670.

[13] C. W. Gullikson and J. Rud Nielsen, *J. Mol. Spectrosc.* **1957**, *1*, 158.

[14] M. Dorobantu Bodoc, L. Prat, C. Xuereb, C. Gourdon, T. Lasuye, *Chem. Eng. Technol.* **2012**, *35*, 705.

[15] J.k. Wilmshurst and, H. J. Bernstein, *Can. J. Chem.* **1957**, *35*, 911.

[16] J. Kapitán, L. Hecht, P. Bouř, *Phys. Chem. Chem. Phys.* **2008**, *10*, 1003.

CHAPTER SIX

6. Conclusion and Outlook

6.1. Conclusion

The environmental pollution, particularly oil-water pollution, and its remediation stay as crucial problem for the whole world. Various technologies (such as mechanical treatment, chemical treatment, membrane technology, and photocatalytic decomposition) have been demonstrated and these are currently being pursued to address the oil-water pollution problem. This thesis focused on the separation of oil-based pollutants through providing a wettability contrast (between the water and the oil). First, the effect of the surface topography and the surface chemistry on wettability has been reviewed. Afterwards various surface functionalization and modification methods used to tune the wettability have been discussed. The use and effectiveness of such methods to improve/control the wettability and to attain an effective oil-water separation is also explained in detail.

This thesis also discussed the photocatalytic decomposition of organic pollutants as an alternative method to tackle the oil pollution. This method of remediation relies on the use of metal oxides, particularly the TiO_2 thin film, which has been shown to be effective in breaking down and mineralizing various organic pollutants. In addition, the thesis presented the use of such a highly active TiO_2 surface for monitoring and detection of organic pollutants (as SERS and PIERS substrates).

In Publication 1, a novel method ‘the fabrication of hierarchical Au nanostructures on TiO_2 film by a two-step photocatalytic reduction process’ was introduced. While the first photocatalytic deposition in a mixture of HAuCl_4 and non-ionic surfactant led to the formation of flower-like Au microstructures on TiO_2 , second photocatalytic deposition within a highly acidic HAuCl_4 solution triggered the growth of needle-like sharp Au nanostructures selectively on former Au microstructures. Such a dual scale topography on TiO_2 enhanced the hydrophilicity significantly. After the surface modification (ODP-SAM) such hydrophilic nanostructures exhibited superhydrophobicity. Prepared surface stays stable under extreme temperature conditions and therefore it can be applied for harsh outdoor uses including self-cleaning and anti-icing applications. In addition, the photocatalytic nature of Au- TiO_2 hybrid layer allows superhydrophilic-superhydrophobic patterning (selective photocatalytic deposition of Au micro- and nanostructures), which may find applications in cell growth technologies, spotting of biomolecules, fluid microchips and microreactors.

In Publication 2, the ‘3-in-1’ concept, which leads to a superhydrophobic and photocatalytically surface, was introduced. This concept combines (i) photocatalytic thin film (TiO_2), (ii) micro- and nanostructuring (Ag nanoplates), and (iii) low surface energy coating (V_3D_3) via iCVD. Not only p- V_3D_3 coating, but also the unique surface topography composed of flowerlike Ag nanoplates and columnar TiO_2 structures seems to promote the superhydrophobicity of the prepared surface. iCVD led to a highly conformal p- V_3D_3 coating retaining the surface topography on TiO_2 , which is crucial to achieve an extreme non-wetting regime. Additionally, due to its siloxane backbone, the p- V_3D_3 layer exhibited high stability against the UV irradiation and atomic oxygen exposure (photodegradation). The superhydrophobic (water CA > 160°) and photocatalytically active p- $\text{V}_3\text{D}_3/\text{Ag}/\text{TiO}_2$ surface shows high selectivity to the oil adsorption, which may

lead to several functional applications in oil–water separation, microfluidics, self-cleaning, and water harvesting technologies.

In Publication 3, 4N-in-1 hybrid substrate concept (nanocolumnar structures, nano crack network, nanoscale mixed oxide phases, and nanometallic structures) was introduced. Basically, 4N-in-1 hybrid substrate (AgTiO_2) acts an ultrasensitive and reliable PIERS active platform. Upon UV irradiation, a PIERS enhancement up to 50 times (in comparison to conventional SERS intensity) was achieved. In addition to improved Raman signal, 4N-in-1 hybrid substrate provides a high detection sensitivity which may be attributed to the activation capability at an extremely low incident photon energy and prolonged relaxation time. Moreover, 4N-in-1 hybrid substrate exhibits a superior photocatalytic degradation performance, allowing its reuse at least for 18 cycles without any loss of PIERS activity. 4N-in-1 hybrid substrate concept can be combined with any type of Raman spectroscopy (by simply integrating a UV light source), and this may trigger new applications for biomedicine, forensic, and security field.

6.2. Outlook

Despite the advancements in the field of oil and water pollution remediation, several challenges still exist. One of the major challenges is the lack of the durability and the stability of superwetting/non-wetting materials (most of such materials are easily damaged by mechanical forces and harsh environments). Additionally, the cost of such materials is still so high to realize their use in large amounts. Improving antifouling and recycling properties of such materials is also crucial to prolong their service life.

Most organic pollutants studied in laboratories are pure compounds, which is vastly different from the multi-component oily wastewater produced by industrial processes. Such multi-component contaminants (especially high-viscosity oil-water mixtures) may easily damage the surface textures and wettability properties of materials used for oil-water separation. Additionally, the reusability of such materials for oil-water separation remains a challenge.

In recent developments, the use of photocatalytic materials for water pollutant detection and clean-up offers promising solutions to some of the problems highlighted above by enabling light-stimulated surface detection and cleaning of organic pollutants. However, there are still several challenges that need to be addressed especially the optical sensors use for pollutants detection and degradation. For example, in the PIERS technique, the prolongation of the substrate relaxation time after UV activation is very important for multiple measurements, and this requires the suppression of the charge recombination. For effective organic pollutant detection and analysis parameters (such as light intensity, laser power, and probe molecule concentration) need to be optimized. Then standard protocols should be developed for improved performance and selectivity in analysis.

List of Figures

Figure 2.1. schematic diagrams of a liquid droplet on (a) Wenzel and (b) Cassie-Baxter states in air	8
Figure 2.2. Schematic of a liquid drop showing the quantities in the Young equation	9
Figure 2.3. A schematic of the components of a magnetron sputtering head. A cylindrical magnetic field is used. Charge generation and surface erosion are maximum in the region where the magnetic field is parallel to the surface, as indicated by the two insets, and electron capture occurs through the magnetic field	12
Figure 2.4 Schematical representation of mechanisms within a typical iCVD process (i) precursor vapor delivery (ii) monomer adsorption (iii) breakdown of initiator by the heated filament and (iv) polymerization and film growth.....	13
Figure 2.5. a) Schematic of photocatalytic patterning of TiO ₂ thin film with HAuNCs using a non-contact polymer mask. SEM images of b) periodic HAuNC arrays and c) a single HAuNC	15
Figure 2.6. Schematic illustration emulsion types	16
Figure 2.7. Design strategies and the mechanism of separation of oil/water mixtures.	17
Figure 2.8. Electron energy band diagram of TiO ₂ showing (a) electron energy E plotted upwards as a function of the distance from the surface to the bulk of the solid (b) electronic structure with defect states.....	18
Figure 2.9. Schematic illustration of electron reduction process of Ti ⁴⁺ to Ti ³⁺ and creation of oxygen vacancies	20
Figure 2.10. Schematic representation of the photocatalytic degradation mechanism ^[215]	21
Figure 2.11. Schematic representation of the self-cleaning process on (a) a roughened superhydrophobic and (b) a smoothed superhydrophilic surface.	23
Figure 2.012. Spectroscopic transitions showing different modes of vibrational spectroscopy. ν_0 indicates the laser frequency, while ν is the vibrational quantum number. The virtual state is a short-lived distortion of the electron distribution by the electric field.	25
Figure 2.13. Electromagnetic and chemical mechanisms for SERS Enhancement. (a) electromagnetic enhancement in SERS based on plasmonic nanospheres and (b) comparison of the charge-transfer transitions in a metal-molecule system and a semiconductor-molecule system.....	26
Figure 2.14 Mechanism of PIERS illustrating electron transfer from TiO ₂ to NPs and electromagnetic amplification and charge transfer interaction of NPs with the analyte.....	28

Declaration of Authorship / Co-authorship

I, Josiah N. Shondo, state here the nature of my involvement to the work in the following publications that are part of this cumulative dissertation. The own contribution is determined on the basis of the following factors: Conceptualization of the investigation (C), Methodology (M), data collection (D), interpretation of the data (I), and writing of the manuscript (W).

Publication 1:

J. Shondo, S. Veziroglu, D. Stefan, Y. K. Mishra, T. Strunskus, F. Faupel, O. C. Aktas, Tuning wettability of TiO₂ thin film by photocatalytic deposition of 3D flower- and hedgehog-like Au nano- and microstructures. *Appl Surf Sci* 2021, 537, 147795.

Contribution:

C	M	D	I	W
Medium	High	High	High	Medium

Publication 2:

J. Shondo, S. Veziroglu, T. Tjardts, J. Fiutowski, S. Schröder, Y. K. Mishra, T. Strunskus, H. G. Rubahn, F. Faupel, O. C. Aktas, Selective Adsorption and Photocatalytic Clean-Up of Oil by TiO₂ Thin Film Decorated with p-V₃D₃ Modified Flowerlike Ag Nanoplates. *Adv Mater Interfaces* 2022, 9, DOI 10.1002/admi.202102126.

Contribution:

C	M	D	I	W
High	High	High	Medium	High

Publication 3:

J. Shondo, S. Veziroglu, T. Tjardts, T. bin Sarwar, Y. K. Mishra, F. Faupel, O. C. Aktas. Nanoscale Synergetic Effects on Ag–TiO₂ Hybrid Substrate for Photoinduced Enhanced Raman Spectroscopy (PIERS) with Ultra-Sensitivity and Reusability. *Small* 2022, 18, DOI 10.1002/sml.202203861.

Contribution:

C	M	D	I	W
Medium	High	High	High	Medium

Kiel date:

M.Sc. Josiah N. Shondo

Prof. Dr. Franz Faupel

REFERENCES

- [1] L. Yong, *United Nations Industrial Development Organization* **2020**, 192.
- [2] A. P. Galvani, C. T. Bauch, M. Anand, B. H. Singer, S. A. Levin, *Proc Natl Acad Sci U S A* **2016**, *113*, 14502.
- [3] J. Lelieveld, K. Klingmüller, A. Pozzer, R. T. Burnett, A. Haines, V. Ramanathan, *Proc Natl Acad Sci U S A* **2019**, *116*, 7192.
- [4] M. Kampa, E. Castanas, *Environmental Pollution* **2008**, *151*, 362.
- [5] E. Silva, A. Marco, J. da Graça, H. Pérez, E. Abella, J. Patino-Martinez, S. Martins, C. Almeida, *J Photochem Photobiol B* **2017**, *173*, 240.
- [6] Moore Charles, “plastic pollution ,” can be found under <https://www.britannica.com/science/plastic-pollution>, **2022**.
- [7] T. Münzel, F. P. Schmidt, S. Steven, J. Herzog, A. Daiber, M. Sørensen, *J Am Coll Cardiol* **2018**, *71*, 688.
- [8] J. Briffa, E. Sinagra, R. Blundell, *Heliyon* **2020**, *6*, e04691.
- [9] R. M. Harrison, *Pollution: Causes , Effects and Control*, **2014**.
- [10] J. V. Macías-Zamora, *Waste* **2011**, 265.
- [11] Audrey Hepburn, “Water is life, and clean water means...,” can be found under https://www.brainyquote.com/quotes/audrey_hepburn_700248, **n.d.**
- [12] Peter Burek, Satoh Yusuke, Fischer Günther, Mohammed Taher Kahil, Scherzer Angelika, Tramberend Sylvia, Wib Luzma Fabiola Nava, Wada Yoshihide, Stephanie Eisner, Martina Flörke, Naota Hanasaki, Piotr Magnuszewski, Bill Cosgrove, David Wiberg, *International Institute for Applied Systems Analysis* **2016**, 1.
- [13] 2019 UNESCO World Water Assessment Program, *WWAP (UNESCO World Water Assessment Program). 2019. The United Nations World Water Development Report 2019: Leaving No One Behind . Paris, UNESCO., 2019*.
- [14] A. Boretti, L. Rosa, *NPJ Clean Water* **2019**, *2*, DOI 10.1038/s41545-019-0039-9.
- [15] BJ Cisneros, **2011**.
- [16] B. Petrie, R. Barden, B. Kasprzyk-Hordern, *Water Res* **2015**, *72*, 3.
- [17] M. I. Ramirez, A. P. Arevalo, S. Sotomayor, N. Bailon-Moscoco, *Environmental Pollution* **2017**, *231*, 415.
- [18] A. B. Nordvik, J. L. Simmons, K. R. Bitting, A. Lewis, T. Strøm-Kristiansen, *Spill Science and Technology Bulletin* **1996**, *3*, 107.
- [19] A. C. Bejarano, J. Michel, *Environmental Pollution* **2016**, *218*, 709.
- [20] O. I. L. Pollution, *Drydock* **1981**, *2*, 67.
- [21] ITOPF, **2020**.
- [22] H. -M Choi, J. P. Moreau, *Microsc Res Tech* **1993**, *25*, 447.
- [23] L. Shao, X. Q. Cheng, Y. Jiao, Z. Sun, X. Yang, Z. Cheng, Q. Bai, Y. Zhang, K. Wang, *ACS Nano* **2021**, *15*, 3500.
- [24] X. Ruan, T. Xu, D. Chen, Z. Ruan, H. Hu, **2020**, DOI 10.1039/c9ra08018j.
- [25] ITOPF, “Containment & Recovery - ITOPF,” can be found under <https://www.itopf.org/knowledge-resources/documents-guides/response-techniques/containment-recovery/>, **n.d.**
- [26] J. Idris, U. Teknologi, J. Idris, **2014**.
- [27] M. O. Adebajo, R. L. Frost, J. T. Klopogge, O. Carmody, S. Kokot, *Journal of Porous Materials* **2003**, *10*, 159.

- [28] J. Ge, H. Y. Zhao, H. W. Zhu, J. Huang, L. A. Shi, S. H. Yu, *Advanced Materials* **2016**, 28, 10459.
- [29] Nancy E. Kinner and Doug Helton., *The Future of Dispersant Use in Oil Spill Response*, **2012**.
- [30] ECOLAB, “Oily Waste Water | Nalco Water,” can be found under <https://www.ecolab.com/nalco-water/offering/oily-wastewater>, **n.d.**
- [31] K. Toyota, N. A. McNabb, D. D. Spyropoulos, T. Iguchi, S. Kohno, *Journal of Applied Toxicology* **2017**, 37, 201.
- [32] B. Tansel, M. Lee, *J Environ Manage* **2019**, 247, 363.
- [33] R. M. Atlas, T. C. Hazen, *Environ Sci Technol* **2011**, 45, 6709.
- [34] T. C. Hazen, R. C. Prince, N. Mahmoudi, *Environ Sci Technol* **2016**, 50, 2121.
- [35] N. Das, P. Chandran, *Biotechnol Res Int* **2011**, 2011, 1.
- [36] N. E. Kimes, A. V. Callaghan, J. M. Suflita, P. J. Morris, *Front Microbiol* **2014**, 5, 1.
- [37] L. An, C. Bai, Y. Bai, B. Zhang, Y. Yu, Y. Hu, *High Perform Polym* **2020**, 32, 73.
- [38] W. N. S Hoffmann, *Chem. Eng. Technol.* **2001**, 24, 22.
- [39] L. Xu, Y. He, X. Feng, F. Dai, N. Yang, Y. Zhao, L. Chen, *J Memb Sci* **2018**, 563, 43.
- [40] S. Zhang, G. Jiang, S. Gao, H. Jin, Y. Zhu, F. Zhang, J. Jin, *ACS Nano* **2018**, 12, 795.
- [41] J. A. Howarter, J. P. Youngblood, *J Colloid Interface Sci* **2009**, 329, 127.
- [42] T. C. Arnot, R. W. Field, A. B. Koltuniewicz, *J Memb Sci* **2000**, 169, 1.
- [43] B. Hu, K. Scott, *J Memb Sci* **2007**, 294, 30.
- [44] X. Feng, L. Jiang, *Advanced Materials* **2006**, 18, 3063.
- [45] M. Ge, C. Cao, J. Huang, X. Zhang, Y. Tang, X. Zhou, K. Zhang, Z. Chen, Y. Lai, *Nanoscale Horiz* **2018**, 3, 235.
- [46] C. Chen, D. Weng, A. Mahmood, S. Chen, J. Wang, *ACS Appl Mater Interfaces* **2019**, 11, 11006.
- [47] Z. Xue, Y. Cao, N. Liu, L. Feng, L. Jiang, *J Mater Chem A Mater* **2014**, 2, 2445.
- [48] A. Tuteja, W. Choi, M. Ma, J. M. Mabry, S. A. Mazzella, G. C. Rutledge, G. H. McKinley, R. E. Cohen, *Science (1979)* **2007**, 318, 1618.
- [49] R. J. Good, *J Adhes Sci Technol* **1992**, 6, 1269.
- [50] M. K. Dawood, H. Zheng, T. H. Liew, K. C. Leong, Y. L. Foo, R. Rajagopalan, S. A. Khan, W. K. Choi, *Langmuir* **2011**, 27, 4126.
- [51] Z. Chu, Y. Feng, S. Seeger, *Angewandte Chemie - International Edition* **2015**, 54, 2328.
- [52] Z. Li, B. Wang, X. Qin, Y. Wang, C. Liu, Q. Shao, N. Wang, J. Zhang, Z. Wang, C. Shen, Z. Guo, *ACS Sustain Chem Eng* **2018**, 6, 13747.
- [53] M. Ratova, P. J. Kelly, G. T. West, *Mater Chem Phys* **2017**, 190, 108.
- [54] D. Zahner, J. Abagat, F. Svec, J. M. J. Fréchet, P. A. Levkin, *Advanced Materials* **2011**, 23, 3030.
- [55] A. Marmur, **2012**, 6867.
- [56] H. Gao, Y. Jian, Y. Yan, *Soft Matter* **2021**, 17, 447.
- [57] J. Yong, Q. Yang, J. Huo, X. Hou, F. Chen, *Nano Select* **2021**, 2, 1580.
- [58] Z. Xiong, H. Lin, Y. Zhong, Y. Qin, T. Li, F. Liu, *J Mater Chem A Mater* **2017**, 5, 6538.
- [59] S. K. Sethi, G. Manik, *Polymer - Plastics Technology and Engineering* **2018**, 57, 1932.

- [60] Y. Li, F. Chen, R. He, Y. Wang, N. Tang, *Semiconductor Photocatalysis for Water Purification*, Elsevier Inc., **2018**.
- [61] K. Honda, *Nature* **1972**, 238, 38.
- [62] O. Carp, C. L. Huisman, A. Reller, *Progress in Solid State Chemistry* **2004**, 32, 33.
- [63] H. L. Nguyen, *New Journal of Chemistry* **2017**, 41, 14030.
- [64] M. Sharma, M. Joshi, S. Nigam, D. K. Avasthi, R. Adelung, S. K. Srivastava, Y. K. Mishra, *Appl Mater Today* **2019**, 17, 130.
- [65] X. Chen, W. Chen, H. Gao, Y. Yang, W. Shanguan, *Appl Catal B* **2014**, 152–153, 68.
- [66] M. Sakar, R. Mithun Prakash, D. Trong-On, *Catalysts* **2019**, 9, 1.
- [67] Dionysios D Dionysiou, Gianluca Li Puma, Jinhua Ye, Jenny Schneider, Detlef Bahnemann, *Photocatalysis Applications*, The Royal Society Of Chemistry 2016 All, **2016**.
- [68] S. Garcia-Segura, E. Brillas, *Journal of Photochemistry and Photobiology C: Photochemistry Reviews* **2017**, 31, 1.
- [69] R. Andreozzi, V. Caprio, A. Insola, R. Marotta, *Catal Today* **1999**, 53, 51.
- [70] Z. Zhang, Q. Zhou, X. Zhang, **2013**.
- [71] T. M. Pan, S. Mondal, *Structural Properties and Sensing Characteristics of Sensing Materials*, Elsevier, **2014**.
- [72] F. Caroleo, G. Magna, M. L. Naitana, L. Di Zazzo, R. Martini, F. Pizzoli, M. Muduganti, L. Lvova, F. Mandoj, S. Nardis, M. Stefanelli, C. Di Natale, R. Paolesse, *sensors Review* **2022**, 22.
- [73] C. McDonagh, C. S. Burke, B. D. MacCraith, *Chem Rev* **2008**, 108, 400.
- [74] K. A. Willets, R. P. Van Duyne, *Annu Rev Phys Chem* **2007**, 58, 267.
- [75] B. Yang, S. Jin, S. Guo, Y. Park, L. Chen, B. Zhao, Y. M. Jung, *ACS Omega* **2019**, 4, 20101.
- [76] S. C. V. RAMAN, *Science (1979)* **1930**, 69, 15.
- [77] S. Y. Ding, E. M. You, Z. Q. Tian, M. Moskovits, *Chem Soc Rev* **2017**, 46, 4042.
- [78] R. Helbig, J. Nickerl, C. Neinhuis, C. Werner, *PLoS One* **2011**, 6, 2.
- [79] R. Fürstner, W. Barthlott, C. Neinhuis, P. Walzel, *Langmuir* **2005**, 21, 956.
- [80] E. Yu. Bormashenko, *Wetting of Real Surfaces*, De Gruyter, **2013**.
- [81] K. J. M. Bishop, C. E. Wilmer, S. Soh, B. A. Grzybowski, *Small* **2009**, 5, 1600.
- [82] R. N. Wenzel, *Ind Eng Chem* **1936**, 28, 988.
- [83] W. Barthlott, C. Neinhuis, *Planta* **1997**, 202, 1.
- [84] Xuefeng Gao, Lei Jiang, *Nature* **2004**, 432, 153.
- [85] C. R. Lawrence, A. R. Parker, *Nature* **2001**, 414, 33.
- [86] Y. Zheng, X. Gao, L. Jiang, *Soft Matter* **2007**, 3, 178.
- [87] E. Bormashenko, Y. Bormashenko, T. Stein, G. Whyman, E. Bormashenko, *J Colloid Interface Sci* **2007**, 311, 212.
- [88] J. Yuan, X. Liu, O. Akbulut, J. Hu, S. L. Suib, J. Kong, F. Stellacci, *Nat Nanotechnol* **2008**, 3, 332.
- [89] P. Varshney, D. Nanda, M. Satapathy, S. S. Mohapatra, A. Kumar, *New Journal of Chemistry* **2017**, 41, 7463.
- [90] D. Tian, X. Zhang, X. Wang, J. Zhai, L. Jiang, *Physical Chemistry Chemical Physics* **2011**, 13, 14606.
- [91] M. J. Kreder, J. Alvarenga, P. Kim, J. Aizenberg, *Nat Rev Mater* **2016**, 1, DOI 10.1038/natrevmats.2015.3.

- [92] S. Lee, W. Kim, C. Yim, K. Yong, S. Jeon, *RSC Adv* **2019**, *9*, 761.
- [93] W. Barthlott, M. Moosmann, I. Noll, M. Akdere, J. Wagner, N. Roling, L. Koepchen-Thomä, M. A. K. Azad, K. Klopp, T. Gries, M. Mail, *Philosophical Transactions of the Royal Society A: Mathematical, Physical and Engineering Sciences* **2020**, *378*, DOI 10.1098/rsta.2019.0447.
- [94] J. B. Rosenholm, *Wetting of Surfaces and Interfaces: A Conceptual Equilibrium Thermodynamic Approach*, **2010**.
- [95] P. Sahoo, *Surface Topography*, Woodhead Publishing Limited, **2011**.
- [96] and Cassie A. B. D., S. Baxter, **1944**, 546.
- [97] A. B. D. Cassie, *Discuss. Faraday Soc.* **1948**, *3*, 11.
- [98] D. Öner, T. J. McCarthy, *Langmuir* **2000**, *16*, 7777.
- [99] X. Huang, D. Kim, M. Im, J. Lee, J. Yoon, Y. Choi, **2009**, 90.
- [100] O. C. Aktas, S. Schröder, S. Veziroglu, M. Z. Ghorri, A. Haidar, O. Polonskyi, T. Strunskus, K. Gleason, F. Faupel, *Adv Mater Interfaces* **2019**, *6*, 2.
- [101] T. Y. Chen, J. A. Tsamopoulos, R. J. Good, *J Colloid Interface Sci* **1992**, *151*, 49.
- [102] D. K. Owens, R. C. Wendt, *J Appl Polym Sci* **1969**, *13*, 1741.
- [103] M. Mantel, J. P. Wightman, *Surface and Interface Analysis* **1994**, *21*, 595.
- [104] A. Bondi, **1952**.
- [105] M. Kalin, M. Polajnar, *Tribol Int* **2013**, *66*, 225.
- [106] K. Song, J. Lee, S. O. Choi, J. Kim, *Polymers (Basel)* **2019**, *11*, DOI 10.3390/polym11030498.
- [107] T. Young, *Philos Trans R Soc Lond* **1805**, *1*, 171.
- [108] A. M. Vidal, E. Papirer, *Colloidal Silica: Fundamentals and Applications* **2005**, *12*, 379.
- [109] X. Cui, J. Liu, L. Xie, J. Huang, Q. Liu, J. N. Israelachvili, H. Zeng, *Angewandte Chemie - International Edition* **2018**, *57*, 11903.
- [110] Michael B. Smith, *March's Advanced Organic Chemistry Reactions, Mechanisms, and Structure*, John Wiley & Sons, Inc., Hoboken, New Jersey. Published Simultaneously In Canada., **2020**.
- [111] James R. Hanson, *Functional Group Chemistry*, The Royal Society Of Chemistry, **2001**.
- [112] W. Huang, X. Tang, Z. Qiu, W. Zhu, Y. Wang, Y. L. Zhu, Z. Xiao, H. Wang, D. Liang, J. Li, Y. Xie, *ACS Appl Mater Interfaces* **2020**, *12*, 40968.
- [113] J. Zhao, M. Wang, K. K. Gleason, *Adv Mater Interfaces* **2017**, *4*, 1.
- [114] G. Q. Shi, C. Han, Y. ming Wang, H. T. Wang, *Powder Technol* **2019**, *356*, 1077.
- [115] A. Cortez Vásquez, G. Rosales Gerónimo, R. Naupari Quiroz, H. Vega Huerta, *Smart Materials for Advanced Environmental Applications*, **2016**.
- [116] J. Guo, L. Zhang, S. Liu, B. Li, *Fuel* **2018**, *231*, 449.
- [117] Z. Liu, M. Zhu, H. Yang, D. Zhao, K. Zhang, *Fuel* **2021**, *302*, 121113.
- [118] S. Lee, J. S. Park, T. R. Lee, *Langmuir* **2008**, *24*, 4817.
- [119] G. Zhou, C. Xu, W. Cheng, Q. Zhang, W. Nie, *J Anal Methods Chem* **2015**, *2015*, DOI 10.1155/2015/467242.
- [120] G. Zhao, Z. Schwartz, M. Wieland, F. Rupp, J. Geis-Gerstorfer, D. L. Cochran, B. D. Boyan, *J Biomed Mater Res A* **2005**, *74*, 49.
- [121] M. Paven, L. Mammen, D. Vollmer, *Challenges and Opportunities of Superhydrophobic/Superamphiphobic Coatings in Real Applications*, **2016**.

- [122] Z. M. Wang, Y. F. Jia, X. C. Zhang, Y. Fu, C. C. Zhang, S. T. Tu, *Critical Reviews in Solid State and Materials Sciences* **2019**, *44*, 445.
- [123] P. Fabbri, M. Messori, *Surface Modification of Polymers: Chemical, Physical, and Biological Routes*, Elsevier Inc., **2016**.
- [124] R. Thanigaivelan, N. Rajan, T. G. Argul, *Advanced Manufacturing Techniques for Engineering and Engineered Materials*, **2022**.
- [125] S. Cavalu, I. V. Antoniac, A. Mohan, F. Bodog, C. Doicin, I. Mates, M. Ulmeanu, R. Murzac, A. Semenescu, *Materials* **2020**, *13*, 1.
- [126] S. K. Nemani, R. K. Annavarapu, B. Mohammadian, A. Raiyan, J. Heil, M. A. Haque, A. Abdelaal, H. Sojoudi, *Adv Mater Interfaces* **2018**, *5*, 1.
- [127] F. Schmidt-Stein, F. Kellner, V. Wagener, R. Hahn, J. Kunze, P. Schmuki, *Journal of The Surface Finishing Society of Japan* **2009**, *60*, 170.
- [128] A. Khassanov, H. G. Steinrück, T. Schmaltz, A. Magerl, M. Halik, *Acc Chem Res* **2015**, *48*, 1901.
- [129] M. Singh, N. Kaur, E. Comini, *J Mater Chem C Mater* **2020**, *8*, 3938.
- [130] M. Guix, J. Orozco, M. Garcia, W. Gao, S. Sattayasamitsathit, A. Merkoči, A. Escarpa, J. Wang, *ACS Nano* **2012**, *6*, 4445.
- [131] Y. Paz, *Beilstein Journal of Nanotechnology* **2011**, *2*, 845.
- [132] Daniel K Schwartz, *Annu. Rev. Phys. Chem* **2001**, *52*, 107.
- [133] B. Wang, Z. Guo, *Appl Phys Lett* **2013**, *103*, 063704.
- [134] B. Fotovvati, A. Dehghanghadikolaei, N. Namdari, *Particulate Science and Technology* **2021**, *39*, 738.
- [135] F. Wang, J.-Y. Li, J. Pi, F. Song, Y.-Q. Luo, X.-L. Wang, Y.-Z. Wang, *Chemical Engineering Journal* **2020**, 127793.
- [136] S. Schröder, T. Strunskus, S. Rehders, K. K. Gleason, F. Faupel, *Sci Rep* **2019**, *9*, 1.
- [137] M. C. Popescu, B. I. Bitu, M. A. Banu, R. M. Tomescu, *Advanced Topics in Optoelectronics, Microelectronics, and Nanotechnologies VIII* **2016**, *10010*, 100102N.
- [138] T. Tatsuma, W. Kubo, A. Fujishima, *Langmuir* **2002**, *18*, 9632.
- [139] P. M. Martin, *Deposition Technologies for Films and Coatings*, **2005**.
- [140] Dr. O. Meyer, R. Behrisch, *Sputtering by Particle Bombardment, Vol. I: Physical Sputtering of Single-Elements Solids*, **1981**.
- [141] D. Depla, S. Mahieu, J. E. Greene, *Sputter Deposition Processes*, Elsevier Ltd., **2010**.
- [142] G. Bräuer, B. Szyszka, M. Vergöhl, R. Bandorf, *Vacuum* **2010**, *84*, 1354.
- [143] Yves Huttel, *Gas-Phase Synthesis of Nanoparticles Edited by Yves Huttel*, **2017**.
- [144] H. Lang, S. Dietrich, *Metals - Gas-Phase Deposition and Applications*, Elsevier Ltd., **2013**.
- [145] K. L. Choy, *Prog Mater Sci* **2003**, *48*, 57.
- [146] A. Behera, P. Mallick, S. S. Mohapatra, *Corrosion Protection at the Nanoscale* **2020**, 227.
- [147] Karen K. Gleason, *CVD Polymers Fabrication of Organic Surfaces and Devices*, Wiley-VCH Verlag GmbH & Co. KGaA, Boschstr. 12, 69469 Weinheim, Germany, Weinheim, Germany, **2015**.
- [148] A. Goossens, E. L. Maloney, J. Schoonman, *Chemical Vapor Deposition* **1998**, *4*, 109.
- [149] A. Hozumi, O. Takai, *Thin Solid Films* **1997**, *303*, 222.
- [150] R.E. Rocheleau, S. C. Jackson., S. S. Hegedus, and B. N. Baron, *Mat. Res. Soc. Symp. Proc.* **1986**, *70*, 37.

- [151] F. H. Yang, *Modern Metal-Organic Chemical Vapor Deposition (MOCVD) Reactors and Growing Nitride-Based Materials*, Woodhead Publishing Limited, **2013**.
- [152] S. Okada, H. Sugime, K. Hasegawa, T. Osawa, S. Kataoka, H. Sugiura, S. Noda, *Carbon N Y* **2018**, *138*, 1.
- [153] A. M. Coclite, *Surf Innov* **2013**, *1*, 6.
- [154] H. Matsumura, H. Umemoto, K. K. Gleason, R. E. I. Schropp, *Catalytic Chemical Vapor Deposition*, Wiley, **2019**.
- [155] H. Moon, H. Seong, W. C. Shin, W. T. Park, M. Kim, S. Lee, J. H. Bong, Y. Y. Noh, B. J. Cho, S. Yoo, S. G. Im, *Nat Mater* **2015**, *14*, 628.
- [156] K. K. S. Lau, K. K. Gleason, *Macromolecules* **2006**, *39*, 3688.
- [157] P. J. Hotchkiss, N. Wagner, P. Theato, S. Pan, R. Guo, W. Xu, A. Olusegun, H. A. Makun, I. M. Ogara, M. Edema, K. O. Idahor, B. F. Oluwabamiwo, M. E. Eshiett, X. Zhan, Y. Yan, Q. Zhang, F. Chen, T. Darmanin, F. Guittard, D. Panchanathan, G. Kwon, T. F. Qahtan, M. A. Gondal, K. K. Varanasi, G. H. McKinley, Z. Gong, N. Yang, Z. Chen, B. Jiang, Y. Sun, X. Yang, L. Zhang, R. N. Wenzel, E. S. Gawalt, K. Brault-Rios, M. S. Dixon, D. C. Tang, J. Schwartz, M. J. Avaltroni, N. Koch, J. Schwartz, M. Textor, L. Ruiz, R. Hofer, A. Rossi, K. Feldman, G. Hähner, N. D. Spencer, X. Zhang, M. Jin, Z. Liu, D. A. Tryk, S. Nishimoto, T. Murakami, A. Fujishima, *Langmuir* **2014**, *2*, 14521.
- [158] K. Liu, M. Cao, A. Fujishima, L. Jiang, *Chem Rev* **2014**, *114*, 10044.
- [159] J. G. Kralj, H. R. Sahoo, K. F. Jensen, *Lab Chip* **2007**, *7*, 256.
- [160] D. Tian, X. Zhang, Y. Tian, Y. Wu, X. Wang, J. Zhai, L. Jiang, *J Mater Chem* **2012**, *22*, 19652.
- [161] H. Notsu, W. Kubo, I. Shitanda, T. Tatsuma, *J Mater Chem* **2005**, *15*, 1523.
- [162] Peter Schroll, C. Fehl, S. and B. K. Dankesreiter, *J. Mater. Chem. C* **2013**, *11*, 6510.
- [163] S. Veziroglu, M. Z. Ghorri, M. Kamp, L. Kienle, H. G. Rubahn, T. Strunskus, J. Fiutowski, J. Adam, F. Faupel, O. C. Aktas, *Adv Mater Interfaces* **2018**, *5*, 1.
- [164] W. Zhang, N. Liu, Y. Cao, X. Lin, Y. Liu, L. Feng, *Adv Mater Interfaces* **2017**, *4*, DOI 10.1002/admi.201700029.
- [165] I. F. Guha, K. K. Varanasi, *Curr Opin Colloid Interface Sci* **2018**, *36*, 110.
- [166] Y. Tian, J. Zhou, C. He, L. He, X. Li, H. Sui, *Processes* **2022**, *10*, DOI 10.3390/pr10040738.
- [167] F. Peters, D. Arabali, *Colloids Surf A Physicochem Eng Asp* **2013**, *426*, 1.
- [168] A. K. Kota, G. Kwon, W. Choi, J. M. Mabry, A. Tuteja, *Nat Commun* **2012**, *3*, DOI 10.1038/ncomms2027.
- [169] L. He, F. Lin, X. Li, H. Sui, Z. Xu, *Chem Soc Rev* **2015**, *44*, 5446.
- [170] J. Nriagu, *Encyclopedia of Environmental Health* **2019**, 758.
- [171] J. G. Reynolds, P. R. Coronado, L. W. Hrubesh, *Energy Sources* **2001**, *23*, 831.
- [172] Q. Ma, H. Cheng, A. G. Fane, R. Wang, H. Zhang, *Small* **2016**, *12*, 2186.
- [173] G. Li, H. Fan, F. Ren, C. Zhou, Z. Zhang, B. Xu, S. Wu, Y. Hu, W. Zhu, J. Li, Y. Zeng, X. Li, J. Chu, D. Wu, **2016**, DOI 10.1039/c6ta08231a.
- [174] V. Poliseti, S. Naidu, A. M. Kansara, P. Ray, P. S. Singh, *Environ Technol Innov* **2021**, *21*, DOI 10.1016/j.eti.2020.101322.
- [175] G. Kwon, A. K. Kota, Y. Li, A. Sohani, J. M. Mabry, A. Tuteja, *Advanced Materials* **2012**, *24*, 3666.
- [176] H. He, H. Jiang, C. Chen, L. Ouyang, W. Jiang, S. Yuan, *ACS Sustain Chem Eng* **2019**, *7*, 13815.
- [177] Y. Zhu, D. Wang, L. Jiang, J. Jin, *NPG Asia Mater* **2014**, DOI 10.1038/am.2014.23.

- [178] M. B. Tahir, T. Iqbal, M. Rafique, M. S. Rafique, T. Nawaz, M. Sagir, *Nanomaterials for Photocatalysis*, Elsevier Inc., **2020**.
- [179] S. M. Gupta, M. Tripathi, F. Möllers, H. J. Tolle, R. Memming, C. R. Everly, J. G. Traynham, D. L. Kuhn, Z. Zander, A. M. Kulisiewicz, S. M. Debow, C. Haffey, H. Fang, X. T. Kong, Y. Qian, S. D. Walck, A. O. Govorov, Y. Rao, H. L. Dai, B. G. Delacy, M. E. Simonsen, M. Sadowsky, P. D. Payne, *J Electrochem Soc* **1958**, *105*, 105.
- [180] D. Chen, Y. Cheng, N. Zhou, P. Chen, Y. Wang, K. Li, S. Huo, P. Cheng, P. Peng, R. Zhang, L. Wang, H. Liu, Y. Liu, R. Ruan, *J Clean Prod* **2020**, *268*, 121725.
- [181] H. Lim, M. Yusuf, S. Song, S. Park, K. H. Park, *RSC Adv* **2021**, *11*, 8709.
- [182] D. J. Wilson, K. Schneider, S. Hönl, M. Anderson, Y. Baumgartner, L. Czornomaz, T. J. Kippenberg, P. Seidler, *Nat Photonics* **2020**, *14*, 57.
- [183] Q. Guo, C. Zhou, Z. Ma, X. Yang, *Advanced Materials* **2019**, *31*, 1.
- [184] J. M. Herrmann, *J Photochem Photobiol A Chem* **2010**, *216*, 85.
- [185] B. Ohtani, *Catalysts* **2013**, *3*, 942.
- [186] A. Hernández-Ramírez, I. Medina-Ramírez, E. Bustos, J. Manríquez, J. M. Peralta-Hernández, *Photocatalytic Semiconductors*, **2015**.
- [187] H. Morkoç, Ü. Özgür, *General Properties of ZnO*, **2009**.
- [188] K. Sayama, H. Hayashi, T. Arai, M. Yanagida, T. Gunji, H. Sugihara, *Appl Catal B* **2010**, *94*, 150.
- [189] Z. Zhang, M. F. Hossain, T. Takahashi, *Appl Catal B* **2010**, *95*, 423.
- [190] A. Di Paola, E. García-López, G. Marcì, L. Palmisano, *J Hazard Mater* **2012**, *211–212*, 3.
- [191] D. Dambournet, I. Belharouak, K. Amine, *Chemistry of Materials* **2010**, *22*, 1173.
- [192] X. Chen, S. S. Mao, *Chem Rev* **2007**, *107*, 2891.
- [193] U. Diebold, *Surf Sci Rep* **2003**, *48*, 53.
- [194] Roel van de Krol, Michael Gratzel, *Photoelectrochemical Hydrogen Production*, Springer Science+Business Media, LLC, 233 Spring Street, New York, NY 10013, USA, **2012**.
- [195] R. Asahi, Y. Taga, W. Mannstadt, *Phys Rev B Condens Matter Mater Phys* **2000**, *61*, 7459.
- [196] X. Pan, M. Q. Yang, X. Fu, N. Zhang, Y. J. Xu, *Nanoscale* **2013**, *5*, 3601.
- [197] X. Liu, H. Xu, L. R. Grabstanowicz, S. Gao, Z. Lou, W. Wang, B. Huang, Y. Dai, T. Xu, *Catal Today* **2014**, *225*, 80.
- [198] G. Barbillon, *Materials* **2021**, *14*, DOI 10.3390/ma14164423.
- [199] Arpan Kumar Nayak, N. K. Sahu, *Nanostructured Materials for Visible Light Photocatalysis*, Elsevier Inc., **2022**.
- [200] A. Brognara, B. R. Bricchi, L. William, O. Brinza, M. Konstantakopoulou, A. L. Bassi, M. Ghidelli, N. Lidgi-Guigui, *Small* **2022**, *18*, DOI 10.1002/sml.202201088.
- [201] S. Banerjee, D. D. Dionysiou, S. C. Pillai, *Appl Catal B* **2015**, *176–177*, 396.
- [202] J. E. Greene, *Journal of Vacuum Science & Technology A: Vacuum, Surfaces, and Films* **2017**, *35*, 05C204.
- [203] Krishna Seshan, *Handbook of Thin Film Deposition Processes and Technologies*, **2002**.
- [204] M. Benelmekki, A. Erbe, *Nanostructured Thin Films—Background, Preparation and Relation to the Technological Revolution of the 21st Century*, **2019**.
- [205] J. S. Shaikh, N. S. Shaikh, A. D. Sheikh, S. S. Mali, A. J. Kale, P. Kanjanaboos, C. K. Hong, J. H. Kim, P. S. Patil, *Mater Des* **2017**, *136*, 54.

- [206] M. Z. Ghorl, S. Veziroglu, B. Henkel, A. Vahl, O. Polonskyi, T. Strunskus, F. Faupel, O. C. Aktas, *Solar Energy Materials and Solar Cells* **2018**, 178, 170.
- [207] S. Veziroglu, K. Röder, O. Gronenberg, A. Vahl, O. Polonskyi, T. Strunskus, H. G. Rubahn, L. Kienle, J. Adam, J. Fiutowski, F. Faupel, O. C. Aktas, *Nanoscale* **2019**, 11, 9840.
- [208] J. Liu, C. Wöll, *Chem Soc Rev* **2017**, 46, 5730.
- [209] A. N. Banerjee, *Nanotechnol Sci Appl* **2011**, 4, 35.
- [210] A. Vahl, S. Veziroglu, B. Henkel, T. Strunskus, O. Polonskyi, O. C. Aktas, F. Faupel, *Materials* **2019**, 12, 2840.
- [211] Mika Sillanpää, *Advanced Water Treatment Advanced Oxidation Processes*, Elsevier Inc, **2020**.
- [212] Y. Nosaka, A. Nosaka, *ACS Energy Lett* **2016**, 1, 356.
- [213] Muhammad Umar and Hamidi Abdul Aziz, in *Organic Pollutants - Monitoring, Risk and Treatment*, **2013**, pp. 195–203.
- [214] M. Boroski, A. C. Rodrigues, J. C. Garcia, L. C. Sampaio, J. Nozaki, N. Hioka, *J Hazard Mater* **2009**, 162, 448.
- [215] U. I. Gaya, A. H. Abdullah, *Journal of Photochemistry and Photobiology C: Photochemistry Reviews* **2008**, 9, 1.
- [216] T. Heckenthaler, S. Sadhujan, Y. Morgenstern, P. Natarajan, M. Bashouti, Y. Kaufman, *Langmuir* **2019**, 35, 15526.
- [217] L. Feng, S. Li, Y. Li, H. Li, L. Zhang, J. Zhai, Y. Song, B. Liu, L. Jiang, *Advanced Materials* **2002**, 1857.
- [218] C. Yu, S. Sasic, K. Liu, S. Salameh, R. H. A. Ras, J. R. van Ommen, *Chemical Engineering Research and Design* **2020**, 155, 48.
- [219] S. Veziroglu, **2021**, 16.
- [220] L. Lin, M. Liu, L. Chen, P. Chen, J. Ma, D. Han, L. Jiang, *Advanced Materials* **2010**, 22, 4826.
- [221] R. Shwetharani, H. R. Chandan, M. Sakar, G. R. Balakrishna, K. R. Reddy, A. V. Raghu, *Int J Hydrogen Energy* **2019**, DOI 10.1016/j.ijhydene.2019.03.149.
- [222] W. Rong, H. Kazuhito, F. Akira, C. Makoto, K. Eiichi, K. Astushi, S. Mitsuhide, W. Toshiya, *Nature* **1997**, 338, 431.
- [223] N. Sakai, A. Fujishima, T. Watanabe, K. Hashimoto, *Journal of Physical Chemistry B* **2003**, 107, 1028.
- [224] P. Falaras, I. M. Arabatzis, T. Stergiopoulos, M. C. Bernard, *International Journal of Photoenergy* **2003**, 5, 123.
- [225] Y. Y. Hsu, T. L. Hsiung, H. Paul Wang, Y. Fukushima, Y. L. Wei, J. E. Chang, *Mar Pollut Bull* **2008**, 57, 873.
- [226] T. Kamegawa, K. Irikawa, H. Yamashita, *Sci Rep* **2017**, 7, 1.
- [227] E. Papa, P. Gramatica, *J Mol Graph Model* **2008**, 27, 59.
- [228] Britte Erickson, *C&EN Global Enterprise* **2019**, 97, 28.
- [229] P. Rajput, P. Chakraborty, P. Devi, **2022**, 179.
- [230] H. Bi, X. Han, *Chemical Sensors for Environmental Pollutant Determination*, Elsevier Inc., **2019**.
- [231] P. LARKIN, *Infrared and Raman Spectroscopy: Principles and Spectral Interpretation*, **2011**.
- [232] Lord Rayleigh, *The London, Edinburgh, and Dublin Philosophical Magazine and Journal of Science* **1899**, 47, 375.
- [233] C. V. Raman., K. s. Krishnan, *Nature* **1928**, 122, 12.
- [234] R. L. McCreery, *Raman Spectroscopy for Chemical Analysis*, **2001**.
- [235] A. J. M. Fleischmann and, P.J. Hendra Mcquillan, *Chem Phys Lett* **1974**, 26, 163.
- [236] M. Moskovits, *J. Chem. Phys* **1978**, 9, 4159.

- [237] Y. S. Yamamoto, Y. Ozaki, T. Itoh, *Journal of Photochemistry and Photobiology C: Photochemistry Reviews* **2014**, *21*, 81.
- [238] J. Gersten, Abraham Nitzan, *J. Chem. Phys.* **1980**, *7*, 3023.
- [239] C. Zhan, X. J. Chen, J. Yi, J. F. Li, D. Y. Wu, Z. Q. Tian, *Nat Rev Chem* **2018**, *2*, 216.
- [240] E. Hutter, J. H. Fendler, *Advanced Materials* **2004**, *16*, 1685.
- [241] I. Alessandri, J. R. Lombardi, *Chem Rev* **2016**, *116*, 14921.
- [242] J. F. Li, Y. J. Zhang, S. Y. Ding, R. Panneerselvam, Z. Q. Tian, *Chem Rev* **2017**, *117*, 5002.
- [243] A. Fularz, S. Almohammed, J. H. Rice, *ACS Appl Nano Mater* **2020**, *3*, 1666.
- [244] X. X. Han, Rebeca S. Rodriguez, Christy L. Haynes, O. Yukihiro, and B. Zhao, *Nat Rev Methods Primers* **2021**, *1*, 1.
- [245] S. Schlücker, *Angewandte Chemie - International Edition* **2014**, *53*, 4756.
- [246] S. Cong, X. Liu, Y. Jiang, W. Zhang, Z. Zhao, *The Innovation* **2020**, *1*, 100051.
- [247] E. C. Le Ru, P. G. Etchegoin, *Chem Phys Lett* **2006**, *423*, 63.
- [248] P. Kambhampati, O. Song, A. Campion, *phys. stat. sol* **1999**, *233*, 233.
- [249] B. N. J. Persson, K. Zhao, Z. Zhang, *Phys Rev Lett* **2006**, *96*, 1.
- [250] Arkaprava Das, D. Singh, C. P. Saini, R. Ahuja, A. Kaur, *Proceedings of the ACM International Conference on Digital Libraries* **1996**, 45.
- [251] A. Otto, J. Timper, J. Billmann, G. Kovacs, I. Pockrand, *Surf Sci* **1980**, *92*, 55.
- [252] M. Galperin, M. A. Ratner, A. Nitzan, *Journal of Chemical Physics* **2009**, *130*, DOI 10.1063/1.3109900.
- [253] L. Zhao, L. Jensen, G. C. Schatz, *J Am Chem Soc* **2006**, *128*, 2911.
- [254] D. W. Silverstein, L. Jensen, *Journal of Chemical Physics* **2012**, *136*, 152.
- [255] J. Chowdhury, *Appl Spectrosc Rev* **2015**, *50*, 240.
- [256] J. R. Lombardi, R. L. Birke, *Journal of Physical Chemistry C* **2014**, *118*, 11120.
- [257] A. Campion, J. E. I. 111, C. M. Child, and M. Foster, *JJ. Am. Chem. SOC.* **1995**, *117*, 11807.
- [258] S. Ben-Jaber, W. J. Peveler, R. Quesada-Cabrera, E. Cortés, C. Sotelo-Vazquez, N. Abdul-Karim, S. A. Maier, I. P. Parkin, *Nat Commun* **2016**, *7*, 1.
- [259] D. Glass, E. Cortés, S. Ben-Jaber, T. Brick, W. J. Peveler, C. S. Blackman, C. R. Howle, R. Quesada-Cabrera, I. P. Parkin, S. A. Maier, *Advanced Science* **2019**, *6*, DOI 10.1002/advs.201901841.
- [260] M. Zhang, H. Sun, X. Chen, J. Yang, T. Chen, Z. Bao, J. J. Liu, Y. Y. Wu, L. Shi, T. Chen, Z. Bao, J. J. Liu, Y. Y. Wu, *ACS Sens* **2019**, *4*, 1670.
- [261] R. M. Al-Shammari, M. A. Baghban, N. Al-Attar, A. Gowen, K. Gallo, J. H. Rice, B. J. Rodriguez, *ACS Appl Mater Interfaces* **2018**, *10*, 30871.
- [262] S. Almohammed, F. Zhang, B. J. Rodriguez, J. H. Rice, *Sci Rep* **2018**, *8*, 41.
- [263] K. Abid, N. H. Belkhir, S. B. Jaber, R. Zribi, M. G. Donato, G. Di Marco, P. G. Gucciardi, G. Neri, R. Mañej, *Journal of Physical Chemistry C* **2020**, *124*, 20350.
- [264] T. Man, W. Lai, M. Xiao, X. Wang, A. R. Chandrasekaran, H. Pei, L. Li, *Biosens Bioelectron* **2020**, *147*, DOI 10.1016/j.bios.2019.111742.
- [265] D. Glass, E. Cortés, S. Ben-Jaber, T. Brick, R. Quesada-Cabrera, W. J. Peveler, Y. Zhu, C. S. Blackman, C. R. Howle, I. P. Parkin, S. A. Maier, *SPIE* **2019**, *11010*, 110100D.
- [266] S. Corby, R. R. Rao, L. Steier, J. R. Durrant, *Nat Rev Mater* **2021**, *6*, 1136.